

**GROWTH AND CHARACTERIZATION OF KDP, LAP AND
ZCTC CRYSTALS FOR NON-LINEAR OPTICAL
APPLICATIONS**

By

SUSHIL KUMAR SHARMA

(Enrolment No. PHYS03200904009)

**Raja Ramanna Centre for Advanced Technology,
Indore-452013, India**

*A thesis submitted to the
Board of Studies in Physical Sciences.
In partial fulfillment of requirements
for the Degree of*

DOCTOR OF PHILOSOPHY

of

HOMI BHABHA NATIONAL INSTITUTE



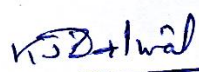
August, 2016

Homi Bhabha National Institute

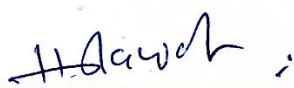
Recommendations of the Viva Voce Board

As members of the Viva Voce Board, we certify that we have read the dissertation prepared by **Shri Sushil Kumar Sharma** entitled “**Growth and Characterization of KDP, LAP and ZCTC Crystals for Non-linear Optical Applications**” and recommend that it may be accepted as fulfilling the thesis requirement for the award of Degree of Doctor of Philosophy.

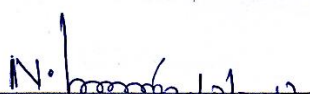

Chairperson - Dr. Rama Chari Date: 20-03-2017


Guide / Convener - Dr. K. S. Bartwal Date: 20-03-2017


Member 1 - Dr. Sangeeta Date: 20-03-2017


Member 2 - Dr. H. S. Rawat Date: 20-03-2017


Member 3 - Dr. S. Ganesamoorthy Date: 20-03-2017


External Examiner - Dr. N. Vijayan Date: 20-03-2017

Final approval and acceptance of this thesis is contingent upon the candidate's submission of the final copies of the thesis to HBNI.

I hereby certify that I have read this thesis prepared under my direction and recommend that it may be accepted as fulfilling the thesis requirement

Date: 20-03-2017

Place: RRCAT, Indore

Guide 
(Dr. K. S. Bartwal)

STATEMENT BY AUTHOR

This dissertation has been submitted in partial fulfillment of requirements for an advanced degree at Homi Bhabha National Institute (HBNI) and is deposited in the Library to be made available to borrowers under rules of the HBNI.

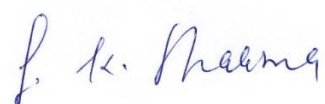
Brief quotations from this dissertation are allowable without special permission, provided that accurate acknowledgement of source is made. Requests for permission for extended quotation from or reproduction of this manuscript in whole or in part may be granted by the Competent Authority of HBNI when in his or her judgment the proposed use of the material is in the interests of scholarship. In all other instances, however, permission must be obtained from the author.



(Sushil Kumar Sharma)

DECLARATION

I, hereby declare that the investigation presented in the thesis has been carried out by me.
The work is original and has not been submitted earlier as a whole or in part for a degree
/ diploma at this or any other Institution / University.



(Sushil Kumar Sharma)

List of Publications arising from the thesis

A) International Journals: (3)

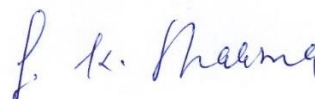
1. "Growth technique to increase the device purpose yield of KDP crystal and assessment of its quality using X-ray and optical techniques", **S. K. Sharma**, Sunil Verma, Yeshpal Singh and K. S. Bartwal, Cryst. Eng. Comm. **2013**, 15, 9955-9962. (*Impact factor 3.858*)
2. "Investigations of structural defects, crystalline perfection, metallic impurity concentration and optical quality of flat-top KDP crystal", **S. K. Sharma**, Sunil Verma, Yeshpal Singh, K. S. Bartwal, M. K. Tiwari, G. S. Lodha and G. Bhagavannarayana, Optical Materials, **2015**, 46, 329-338. (*Impact factor 2.075*)
3. "Growth of L-arginine phosphate monohydrate crystals in different orientations to achieve isometric morphology for device applications", **S. K. Sharma**, Yeshpal Singh, Sunil Verma, M. K. Singh, K. S. Bartwal and P. K. Gupta, Cryst. Eng. Comm. **2016**, 18, 6403-6410. (*Impact factor 3.858*)

B) National/ International Conferences: (10)

1. **S. K. Sharma**, "Development of shape modification techniques for KDP crystal growth to enhance cross-section and crystallization yield", 13th National Seminar on Crystal Growth, Jan. 27-29, 2009, SSN College, Chennai.
2. **S. K. Sharma**, Yeshpal Singh, K. S. Bartwal and P. K. Gupta "Growth of L-arginine phosphate monohydrate (LAP) single crystals with high rate from point seed and their characterization", National Laser Symposium-19, Dec. 1-4, 2010, RRCAT, Indore, pp.38.
3. **S. K. Sharma**, Yeshpal Singh, K. S. Bartwal and P. K. Gupta, "A simple technique for protection of seed-crystal during overheating of solution for growth of large size crystals", National Laser Symposium-20, Jan. 9-12, 2012, Crystal Growth Centre, Anna University, Chennai, pp.72.
4. Sunil Verma, **S. K. Sharma**, Yeshpal Singh, K.S. Bartwal and P. K. Gupta, "Characterization of structural defects and optical quality of large size KDP crystals using X-ray topography and optical interferometry", National Laser Symposium-22, Jan. 8-11, 2014, Manipal University, Manipal, pp.61.

5. **S. K. Sharma**, Yeshpal Singh, Sunil Verma, K. S. Bartwal and P. K. Gupta, "Rapid growth of KDP and LAP crystals by solute feeding during unidirectional growth", National Laser Symposium-22, Jan. 8-11, 2014, Manipal University, Manipal, pp.62.
6. **S. K. Sharma**, Yeshpal Singh, Sunil Verma, K. S. Bartwal and P. K. Gupta, "Investigation on growth, structural and optical properties of zinc cadmium thiocyanate (ZCTC) metal-organic crystal", National Laser Symposium-22, Jan. 8-11, 2014, Manipal University, Manipal, pp.62.
7. **S. K. Sharma**, Yeshpal Singh, Sunil Verma, K. S. Bartwal and P. K. Gupta, "Unidirectional growth of DKDP crystal along [001] direction by solute feeding technique and characterization", National Laser Symposium-23, Dec. 3-6, 2014, S. V. University, Tirupati, pp.55.
8. **S. K. Sharma**, Sunil Verma, Yeshpal Singh, K. S. Bartwal and P. K. Gupta, "Oriented growth of KDP crystal along SHG type-II phase matching direction by solute feed based unidirectional growth technique", National Laser Symposium-24, Dec. 2-5, 2015, RRCAT, Indore, pp.71.
9. **S. K. Sharma**, Sunil Verma, Yeshpal Singh, K. S. Bartwal and P. K. Gupta, "Technique for growth of SHG oriented type-II and type-I KDP crystals using natural morphology point seeds along with flat-top growth process", 20th National Seminar on Crystal Growth and Applications (NSCGA 2016), Jan. 19-21, 2016, BARC, Mumbai, pp.144.
- 10*. **S. K. Sharma**, Sunil Verma, Yeshpal Singh, K. S. Bartwal and P. K. Gupta, "Frequency convertors fabricated from type-I and type-II SHG oriented KDP crystals grown using natural morphology point seeds and flat-top growth technique", 20th National Seminar on Crystal Growth and Applications (NSCGA 2016), Jan. 19-21, 2016, BARC, Mumbai, pp.310.

**The paper was selected for "Best crystal/Device display" award.*



(Sushil Kumar Sharma)

DEDICATION

*Dedicated to my beloved Mother,
late Father, maryada purushottam
bhagawan Ram & my Family.*

*यह शोध प्रबंध मैं अपनी प्रिय माँ, स्वर्गीय
पिताजी, मर्यादा पुरुषोत्तम भगवान राम तथा
अपने परिवार को समर्पित करता हूँ.*

ACKNOWLEDGEMENTS

First of all, I thank my parents for their unconditional love, support and blessings. I also want to sincerely thank Bhagawan Ram who has been my constant source of inspiration, motivation and peace of mind during odd times of life and to face challenges during Ph. D. It is his blessings that give me strength to face tension during the span of Ph. D.

I would like to express my sincere thanks to Dr. P. K. Gupta, former Head, Laser Materials Development and Devices Division for his constant support and critical comments. I express my gratitude to Dr. P. A. Naik, Director RRCAT and former Director Dr. P. D. Gupta for their kind support during Ph. D. I am highly obliged to Dr. Rama Chari, chairperson of the Doctoral committee and Head, Materials Science Section, RRCAT for her kind support and encouragement. I also express my sincere gratitude to members of my doctoral committee Dr. Sangeeta, Dr. S. Ganesamoorthy, Dr. H. S. Rawat for their positive attitude and constructive suggestions, and also to two former members Dr. S. C. Mehendale and Dr. L. M. Kukreja for their support.

I am highly thankful to my guide Dr. K. S. Bartwal for his valuable guidance, encouragement and support during the course of this work. I am highly obliged to him for his constructive criticism, useful suggestions and motivations. I am grateful to Dr. A. K. Karnal, Head, Laser Materials Section, RRCAT for his kind support and confidence and also to my colleagues Dr. S. Verma, Dr. M. K. Singh, Dr. R. Bhatt, Dr. S. Satapathy, Dr. V. S. Tiwari, Dr. S. M. Gupta, Dr. G. Singh, Dr. I. Bhaumik, Dr. V. B. Tiwari and Dr. B. N. Upadhyay for their help at different stages of this work and for providing friendly support. I also express thanks to Dr. Arup Banerjee, Dean Academic, HBNI, RRCAT and also to the former Dean Dr. S. B. Roy for their kind support and encouragement.

I am particularly thankful to my colleagues Yeshpal Singh and S. R. Markam for setting up different experiments for crystal growth. I also thank Rachna, Sanjib, Sujana, Chiranjit, Pathak ji, S. M. Sharma, Sazith, Prem, Bagare, Amit, J. B. Rathi, J. Sisodia and Gopal for their help in different capacities. I also thank my collaborators, Dr. G. Bhagavannarayana, Dr. G. S. Lodha, Dr. M. K. Tiwari, Dr. Beena Jain, Khattak Ji, Kamath Ji, A. S. Joshi ji and colleagues of glassblowing section, laser workshop and electrical sections RRCAT for their support at different levels for the crystal growth activity. I also want to thank all the teachers of BARC training school at RRCAT who taught me different courses. I am also thankful to my project trainee M. Tech. students Parasram, Anuradha and Sachin for their help.

At last but not least, I must express my sincere thanks to my wife Manjul and son Samyak for their love and support during this journey and also to all the well-wishers.

Table of Contents

	Page No.
SYNOPSIS	xiii - xix
LIST OF FIGURES	xx- xxxi
LIST OF TABLES	xxxii - xxxiii
Chapter 1	
Introduction.....	1-1
1.1 Importance of crystals.....	1-1
1.2 Single crystals.....	1-1
1.3 Physics of crystal growth.....	1-4
1.3.1 Driving force for crystallization	1-5
1.3.2 Free energy barrier for nucleation	1-7
1.3.3 Rate of nucleation	1-9
1.3.4 Process of crystal growth.....	1-10
1.3.5 Crystal growth mechanisms.....	1-11
1.4 Techniques of crystal growth.....	1-15
1.4.1 Melt growth	1-15
1.4.2 Vapor growth	1-16
1.4.3 Solution growth	1-17
1.5 Crystal habit.....	1-23
1.6 Shape modification techniques in solution crystal growth.....	1-26
1.7 Selected materials and motivation	1-28
Chapter 2	
Characterization techniques used for crystals	2-34
2.1 Introduction.....	2-34
2.2 Characterization techniques used for crystalline materials under study..	2-34
2.2.1 X-ray diffraction	2-35
2.2.2 High resolution X-ray diffraction	2-38
2.2.3 X-ray diffraction topography.....	2-40
2.2.4 Chemical etching	2-43
2.2.5 UV-Visible-IR transmission spectroscopy	2-45
2.2.6 Mach-Zehnder interferometry for optical homogeneity	2-47

2.2.7	Birefringence interferometry: Orthoscopy and Conoscopy	2-49
2.2.8	Second harmonic generation	2-52
2.2.9	Laser-induced damage threshold	2-58
2.2.10	X-ray fluorescence studies	2-60
2.2.11	Fourier transform infrared spectroscopy	2-62
2.2.12	Differential scanning calorimetry	2-65
Chapter 3	Development of Flat-top growth technique to enhance device purpose yield of KDP crystals	3-71
3.1	Introduction	3-71
3.2	Development of a water bath and a crystallizer	3-75
3.2.1	Fabrication of a thermostatic water bath	3-75
3.2.2	Fabrication of crystallizer and platform	3-77
3.2.3	Procedure of solution preparation and its processing for KDP crystal growth	3-80
3.3	Development of a seed protection technique	3-81
3.4	Development of shape modification techniques to enhance usable volume fraction of KDP crystals	3-84
3.4.1	Three plate technique for SHG type-II oriented growth of KDP crystals	3-85
3.4.2	Flat-top technique to enhance usable volume fraction of KDP	3-86
3.4.3	Flat-top technique along with oriented seed methodology to enhance usable volume fraction for type-I and type-II SHG elements	3-90
3.5	Characterization of flat-top KDP crystals	3-94
3.5.1	Structural identification by powder X-ray diffraction	3-96
3.5.2	Crystalline perfection by high resolution X-ray diffraction	3-97
3.5.3	Defect structure and dislocation density	3-99
3.5.4	Assessment of optical quality	3-103
3.5.5	X-ray fluorescence spectroscopy for impurity distribution ...	3-109
3.5.6	Laser-induced damage threshold	3-112
3.5.7	Fabrication of Pockels element, SHG elements and cells	3-114
3.5.8	Measurement of SHG efficiency	3-115
3.6	Summary and conclusion	3-117

Chapter 4 Development of solute feed based unidirectional growth technique to enhance growth rate and crystallization yield of KDP crystals 4-123

4.1	Introduction.....	4-123
4.2	Development of solute feed based unidirectional growth technique.....	4-125
4.3	Instrumentation for unidirectional growth of crystals by solute feeding.....	4-127
4.3.1	Fabrication of a two-zone water bath	4-127
4.3.2	Axial temperature profile of the two-zone water bath.....	4-129
4.3.3	Growth ampoule, feed tube and seed mounting method	4-130
4.3.4	Imaging mass transfer and crystal growth by shadowgraphy technique	4-131
4.4	Growth of unidirectional KDP crystals by solute feeding technique along different crystallographic directions and their characterizations.....	4-132
4.4.1	Unidirectional growth of KDP crystals along [001] direction by solute feeding technique and its characterizations.....	4-133
4.4.2	Unidirectional growth of KDP along SHG type-II phase matching direction by solute feeding and its characterization	4-139
4.4.3	Unidirectional growth of KDP crystal along (101) surface...	4-146
4.4.4	Unidirectional growth of KDP along [100] direction.....	4-149
4.5	Application of solute feed based unidirectional technique for growth of DKDP and LAP crystals	4-150
4.5.1	Growth of unidirectional LAP crystal by solute feeding technique	4-150
4.5.2	Growth of DKDP crystal by solute feeding technique	4-151
4.6	Conclusion	4-152

Chapter 5 Growth, kinetics studies and characterization of LAP crystals 5-155

5.1	Introduction.....	5-155
5.2	Chemical synthesis and determination of solubility curve	5-156
5.2.1	Chemical preparation.....	5-156
5.2.2	Powder X-ray diffraction	5-157
5.2.3	Determination of solubility curve	5-158
5.3	Growth of LAP crystals using different seed orientations.....	5-159

5.4	Effect of seed orientation on growth rate and aspect ratio of LAP crystals	5-162
5.5	Characterization of LAP crystal	5-165
5.5.1	Crystalline quality and defects structure.....	5-165
5.5.2	Assessment of optical quality	5-167
5.5.3	Fourier transform infrared analysis.....	5-170
5.5.4	Laser-induced damage threshold	5-171
5.5.5	Differential scanning calorimetry for thermal stability	5-173
5.6	Growth kinetics studies of (100) faces of LAP crystal using birefringence interferometry	5-173
5.6.1	Design and fabrication of a small size growth unit for growth kinetics studies.....	5-174
5.6.2	Determination of the orientations of the principal axes by laser conoscopy	5-174
5.6.3	Growth kinetics studies of (100) face of LAP crystal using birefringence interferometry	5-177
5.7	Summary and conclusion.....	5-182
Chapter 6	Growth and characterization of ZCTC crystals.....	6-187
6.1	Introduction.....	6-187
6.2	Chemical synthesis, phase identification and determination of solubility curve.....	6-187
6.2.1	Chemical synthesis.....	6-187
6.2.2	Powder X-ray diffraction for phase identification	6-188
6.2.3	Determination of solubility curve in water	6-189
6.3	Growth of ZCTC crystals by evaporation technique	6-191
6.3.1	Seed preparation and influence of solution pH.....	6-191
6.3.2	Design and fabrication of a crystallizer to control evaporation rate of solvent	6-192
6.3.3	Growth of ZCTC crystals.....	6-193
6.4	Characterization of ZCTC crystals	6-195
6.4.1	Indexing faces of ZCTC crystal and preparation of samples plates	6-195
6.4.2	Optical quality by transmission spectroscopy.....	6-195

6.4.3	Birefringence homogeneity: Orthoscopy and conoscopy.....	6-196
6.4.4	X-ray diffraction topography for defects structures	6-197
6.4.5	Chemical etching	6-197
6.4.6	Laser-induced damage threshold of ZCTC crystal.....	6-198
6.4.7	Structural characterization by FTIR	6-199
6.4.8	Differential scanning calorimetry of ZCTC	6-200
6.4.9	Measurement of refractive indices of ZCTC and determination of Sellmeier coefficients and thermo-optic coefficients for ordinary and extraordinary waves.....	6-201
6.4.10	Determination of phase matching angles for second harmonic generation.....	6-205
6.5	Unidirectional growth of ZCTC crystals	6-208
6.6	Conclusion	6-209
Chapter 7	Summary and future scope	7-212



Homi Bhabha National Institute

SYNOPSIS OF Ph. D. THESIS

- 1. Name of the Student** : Sushil Kumar Sharma
- 2. Name of the Constituent Institution:** Raja Ramanna Centre for Advanced Technology, Indore-452013 (M. P.), India
- 3. Enrolment No.** : PHYS03200904009
- 4. Title of the Thesis:** “Growth and Characterization of KDP, LAP and ZCTC Crystals for Non-linear Optical Applications”
- 5. Board of Studies** : Physical Sciences

SYNOPSIS

Crystals have fascinated human from the ancient time due to their beauty, symmetry, clarity and rarity. They also play an important role in the development of modern science and technology because physical properties of materials depend highly on crystal structure. Single crystals are required for a wide variety of applications in the field of solid state lasers, non-linear optics, radiation detectors, monochromators, integrated optics, optical data storage etc. Laser frequency conversion is one of the important phenomena of non-linear optics widely used for generation of radiation at frequencies where other sources of coherent radiation are not available. In this context non-centrosymmetric single crystals are of particular interest as these are capable of producing second order non-linear optical (NLO) effects such as second harmonic generation (SHG). There are a large number of such materials but only a few are suitable for actual practical applications because apart from being non-centrosymmetric there are many other requirements for a material to be

suitable for SHG applications. These include high second order NLO coefficient, high transmittance at the wavelengths involved, wide phase matchable range, high laser-induced damage threshold (LDT), non-hygroscopic nature, ease in growth and processing etc.

This thesis describes the work carried out to address some important issues that hamper the growth and utilization of three important non-centrosymmetric crystals namely potassium dihydrogen phosphate (KDP), L-arginine phosphate monohydrate (LAP) and zinc cadmium thiocyanate (ZCTC).

KDP is a well-known NLO material, widely used for second harmonic generation mainly because of ease with which large size crystals of good optical quality can be grown. However, one important limitation is that its natural growth morphology greatly limits the size of the device element such as second harmonic conversion element, which can be obtained from a naturally grown crystal. Different shape modification techniques have been investigated with a view to modify the crystal shape in a manner that helps in obtaining large size device element. Investigations of the different shape modification techniques to find ways for enhancing the usable volume fraction of KDP crystals for devices was one of the objectives of this thesis. A new shape modification technique termed as ‘flat-top growth technique’ developed by us has allowed significant improvement in the usable fraction of the grown crystal. For second harmonic generation of 1064 nm laser, type-I and type-II SHG oriented KDP crystals were grown with usable volume fraction about 48% and 56% which is larger than that available with conventionally grown crystals.

LAP crystal is of interest because compared to KDP, it has a factor 1.9 higher NLO coefficient and a factor of ~ 2 higher LDT. However, a major drawback with LAP is that the large asymmetry along crystallographic axes leads to a morphology which results in low usable volume fraction for device elements. Possible approaches to reduce the growth anisotropy of LAP was another objective for the present thesis. Our studies have shown that growth with (011) oriented seed leads to significantly better aspect ratio compared to that for (100), (010) and (001) oriented seeds.

ZCTC has the advantage of having a very large NLO coefficient comparable with the best available melt grown crystals such as potassium titanyl phosphate (KTP), lithium tri borate (LBO) etc. The main difficulty with this crystal is very low growth rate of its

habit faces because of which it becomes difficult to grow good optical quality crystals. Growth of ZCTC crystals and their characterization is also presented in this thesis.

The thesis is organized into seven chapters as described below.

Chapter 1: Introduction

In this chapter we provide a brief overview of the physics of crystal growth and the different techniques used for the growth of single crystals. Since the main objective of the thesis is shape modification of crystals to enhance usable volume fraction for device applications, we provide a detailed review of the shape modification techniques reported in literature. The important physical, chemical and optical parameters of the three crystals (KDP, LAP and ZCTC) investigated as part of the thesis are summarized in this chapter.

Chapter 2: Characterization techniques used for the crystals

In this chapter we provide a brief description of the techniques used for the assessment of structural perfection, chemical impurities, optical quality and thermal stability of the grown crystals. These include powder X-ray diffraction for phase analysis, Fourier transform infrared spectroscopy for functional group identification, high resolution X-ray diffraction (HRXRD) for crystalline perfection, X-ray diffraction topography and chemical etching for defect structure imaging, X-ray fluorescence for quantifying the metallic impurities, UV-Vis-NIR transmission spectroscopy, birefringence interferometry and Mach-Zehnder interferometry for assessing the optical quality, laser induced damage threshold and second harmonic generation for characterizing the device related parameters, and differential scanning calorimetry for thermal stability.

Chapter 3: Development of flat-top growth technique to enhance device purpose yield of KDP crystals

KDP is widely used for frequency conversion and electro-optic switching of high power Nd doped solid state lasers. However, the growth morphology of this crystal is such that in order to obtain the SHG or the Pockels cell element, the crystal has to be cut in directions which are not along any of the natural habit faces. As a result, only a small volume fraction can be used for making the device elements. Various techniques have been reported in the literature to enhance the usable volume fraction of KDP. These include, use of mechanical shape modifiers in the form of parallel plates or use of shaping cell for limiting growth along certain specific directions or growing crystals in specific crystallographic directions

in cylindrical tubes. In this chapter we describe the development of a new shape modification technique named “flat-top growth technique”. In this technique solution-air interface in the crystallizer was employed as a barrier to limit the growth normal to the interface. This leads to elimination of the pyramidal cap of the KDP crystal while the growth along prismatic directions [100] and [010] continues resulting in enhancement of the crystal cross-section. Using this methodology, KDP crystals for two different applications have been grown:

(a) Electro-optic switching application, where the crystal is grown using point seed such that [001] direction is normal to the platform. As a result, the usable volume fraction for Pockels cell elements is enhanced by ~ 22% as compared to the conventionally grown KDP crystals.

(b) Frequency doubling application, where point seed oriented in type-I and type-II directions are used for growth. For SHG of 1064 nm Type-I and type-II oriented KDP crystals were grown with usable volume fraction about 48% and 56% which are higher compared to conventionally grown KDP crystals.

Using the above technique several flat-top shape KDP crystals were successfully grown without any nucleation. For this purpose, special crystal growth apparatus was designed and fabricated which included a ~150 liter capacity water bath, a ~15 liter capacity crystallizer associated with a square shape platform and a stirring mechanism.

The crystals grown by the flat-top growth technique were characterized for their optical quality, defects structure and crystalline perfection, using several different techniques. UV-Vis-NIR transmission, optical interferometry and laser induced damage threshold measurements were carried out for assessing the optical quality. High resolution XRD, X-ray topography and X-ray fluorescence studies were carried out for characterizing the crystalline perfection, defects structure imaging and metallic impurity distribution in the crystal. The analyses of the XRF spectra showed presence of iron in the range of 3 to 16 ppm, which decreases from seed to flat-top portion of the crystal. HRXRD at several point on a broad (100) face show the full width of half maxima (FWHM) of the rocking curve in the range of 6 to 9 arc sec. Dislocation defects density and their distribution imaged using X-ray diffraction topography and chemical etching were found to be in the range $10^3 - 10^4/\text{cm}^2$. The LIDT was measured using Nd:YAG laser of 7 ns pulse width and was in the range of 2.4 to 3.9 GW/cm^2 . SHG conversion efficiency measured using the

same laser and was found to be ~ 30%. The results indicated that inhibition of growth by solution - air interface does not adversely affect the quality of the grown crystals.

Chapter 4: Development of solute feed based unidirectional growth technique to enhance growth rate and crystallization yield of KDP crystal

The KDP crystals grown by “Flat-top growth technique” yields higher usable volume fraction compared to that obtained from the crystals grown by conventional platform technique. This can be further enhanced by use of unidirectional growth technique which lead to growth of crystals with circular cross section as opposed to rectangular cross section achieved using platform approach. Therefore, we also investigated the use of unidirectional growth methodology to grow cylindrical shape crystals. In this context we first analysed the existing “SR unidirectional growth method" (J. Cryst. Growth 280 (2005) 467-473) which is based on slow evaporation of solvent from the hot zone maintained at top of the growth tube. It was found that growth rate of KDP crystals obtained using this technique was low mainly due to difficulty in maintaining and controlling high supersaturation by evaporation. To circumvent this problems, we modified this technique and developed “solute-feed based unidirectional growth technique” where solute particles are fed online through a permeable membrane at the hot zone to maintain high supersaturation by optimizing temperature gradient without need for evaporation of solution. Growth of unidirectional cylindrical shape KDP crystals along [001], [101], [100] and type-II SHG direction is described in this chapter. Growth rates achieved using this technique for KDP crystal along [001] was ~10 mm/day.

A comparison of the results obtained with solute feed based unidirectional grown KDP crystals with that grown by “flat-top growth technique” revealed that: i) Solute feed based unidirectional growth technique is better compared to flat-top growth technique to obtain very long crystals of small diameter along a particular direction. ii) Flat-top growth technique is better suited for large aperture device elements. iii) Optical and structural quality of the KDP crystals grown by these two techniques were comparable.

Chapter 5: Growth, kinetics studies and characterization of LAP crystals

Major difficulty in growing LAP for NLO applications arises due to growth asymmetry along crystallographic axes which leads to a morphology that results in low volume fraction for the device elements. In order to enhance the useful volume of the grown crystal, the growth anisotropy needs to be minimized. For this purpose, we investigated

the kinetics of the slow growing (100) face in two different manners: (a) influence of supersaturation on growth rate of (100) face using birefringence interferometry, (b) effect of seed orientation on the crystal morphology. The degree of supersaturation was not found to have a significant influence on the growth rate of (100) face. However, considerable modification of crystal morphology was observed due to different seed orientations during growth, and hence this approach was followed to achieve the desired shape of the LAP crystal. LAP crystals were grown along four different seed orientations namely (100), (010), (001) and (011) faces parallel to platform. Results show that (011) oriented crystal has better aspect ratio compared to that for (100), (010) and (001) oriented crystals. The (011) oriented crystal was characterized for assessing its defects structure and optical quality using various optical and X-ray techniques described in Chapter 2. Optical transmittance was ~ 88% in the visible region for a 1.7 mm thick (100) plate with UV cut off near 230 nm. Optical homogeneity of the plate was assessed using birefringence interferometry and Mach-Zehnder interferometry. LIDT was in the range of 4.8 to 6.6 GW/cm². X-ray diffraction topograph was obtained for (811) planes for a large size (100) plates showing a broad region of low defects density. Chemical etch pit technique was used to quantify dislocation defects density in the (100) plate showing low etch pit density $10^2 - 10^3$ /cm² in the region corresponding to low defect density observed by X-ray topography.

Chapter 6: Growth and characterization of ZCTC crystals

ZCTC because of its high NLO coefficient (~ 15 times higher as compared to KDP) is an attractive NLO material for generation of coherent UV radiation by frequency doubling of low power lasers. The main difficulty in the use of this crystal is its unavailability in large sizes due to very slow growth rates of its habit faces and its lower LIDT. This chapter describe the results of our c investigations to obtain good optical quality, inclusion-free prismatic shape ZCTC crystals of ~ 15 mm length. This required taking measures like the design of a crystallizer for precise control of evaporation and optimizing the pH of the solution in order to overcome the problems of nucleation. Transparent ZCTC crystals with dimensions of about 4×2×15 mm³ were grown at a rate of about 0.5 mm/day along c-axis. The grown crystals were characterized for their defects structure and optical quality using various optical and X-ray techniques. Optical transmittance for 1 mm thick (100) plate was ~ 70 - 75% in visible-NIR region without accounting for Fresnel reflection losses. Laser

damage threshold was $\sim 0.9 \text{ GW/cm}^2$ for Nd:YAG laser. X-ray topography and chemical etching of (100) face was performed for imaging the defect structure and quantifying the dislocation density respectively. Sellmeier equations were determined by measuring the refractive index for ordinary and extra-ordinary waves at different wavelengths and the data was used for determining the phase matching angles for SHG at different wavelengths.

Chapter 7: Summary

Salient findings of the thesis are summarized in this chapter. These are as follows:

i) The first ever report on the modification of crystal shape through solution-vapor interface. It was confirmed that termination of natural facets at solution-vapor interface does not have any adverse effect on crystal quality. The technique was successfully used to grow KDP crystals along optic axis and SHG directions from natural morphology point seeds by eliminating pyramidal cap containing up to 22% of the crystal volume. Significant enhancement in usable volume fraction has been achieved for electro-optic modulators and SHG elements with this methodology.

ii) The solvent-evaporation based unidirectional growth technique was modified to solute-feed based unidirectional growth technique without the need for evaporation. With this modification almost 100% conversion efficiency of polycrystalline powder to single crystal was achieved. KDP crystals were grown from point seed with growth rate up to 10 mm/day along [001] direction which is two times higher than that reported by solvent evaporation based technique. This technique was used to grow crystals along [001], [100] and [101] directions and type-II SHG direction of different lengths and diameters.

iii) Other than KDP, two other NLO single crystals of LAP and ZCTC were also grown successfully. The usable volume for device elements from LAP was enhanced by growing the crystal from seed oriented along a specific direction, which helped in modifying the crystal aspect ratio. The study showed that (011) oriented LAP crystal results in better aspect ratio compared to (100), (010) and (001) orientations. Good optical quality ZCTC crystals of dimensions $\sim 4 \times 2 \times 15 \text{ mm}^3$ were grown at a rate of $\sim 0.5 \text{ mm/day}$ along c-axis.

LIST OF FIGURES

Fig. 1.1 Classification of materials.	1-2
Fig. 1.2 Schematic of general unit cell of crystal.	1-3
Fig. 1.3 Importance of crystals for different fields of science and technology.	1-4
Fig. 1.4 Schematic of processes of crystallization.....	1-5
Fig. 1.5 Typical Gibbs free energy curves for solid and liquid phases across melting point.	1-5
Fig. 1.6 Mechanisms of nucleation.....	1-8
Fig. 1.7 Variation of Gibbs free energy with radius of cluster.	1-9
Fig. 1.8 Schematic showing flat (F), stepped (S) and kinked (K) surfaces of a crystal.	1-11
Fig. 1.9 Kossel's model of a growing crystal surface showing flat faces/terrace, steps, kinks, surface adsorbed growth units.....	1-12
Fig. 1.10 Development of a growth spiral starting from a screw dislocation.....	1-13
Fig. 1.11 Schematic showing development of a flat face by the birth and spread model.....	1-14
Fig. 1.12 A classification of crystal growth techniques.....	1-15
Fig. 1.13 Schematic representation of typical solubility - supersolubility curves....	1-19
Fig. 1.14 Schematic of three vessel method for solution crystal growth.....	1-22
Fig. 1.15 Schematic showing effect of different relative growth rates along different axis leading to change in crystal habit.	1-25
Fig. 1.16 Schematic depiction of shape modification techniques based on mechanical barriers for growth of crystals from solution (light blue shade show barriers while yellow shade show crystal).	1-27
Fig. 2.1 Schematic for derivation of Bragg's law of X-ray diffraction by constructive interference of the beams diffracted from parallel planes of crystal spaced by distance d	2-35

Fig. 2.2 Characterization techniques based on Bragg's law of X-ray diffraction....	2-36
Fig. 2.3 Schematic of double crystal diffractometer for HRXRD.	2-39
Fig. 2.4 Origin of contrast in X-ray topograph due to misorientation of nearby lattice planes.....	2-41
Fig. 2.5 (a) Jordan Valley make digital X-ray topography system, and (b) schematic representation of its working principle.	2-42
Fig. 2.6 Schematic of etch pits seen observed by an optical microscope for calculation of etch pit density.	2-44
Fig. 2.7 Transmission of light through a sample of thickness t accounting reflection losses and absorption.....	2-47
Fig. 2.8 Schematic drawing of the Mach-Zehnder interferometer used for optical homogeneity.	2-48
Fig. 2.9 A classification of crystals based on index ellipsoid.....	2-49
Fig. 2.10 Schematic showing optical set up for orthoscopic birefringence interferometry.....	2-51
Fig. 2.11 Schematic showing optical set up for conosopic birefringence interferometry.....	2-51
Fig. 2.12 Schematic depiction of the process of SHG.	2-55
Fig. 2.13 (a) Mathematical conditions for birefringence phase matching for negative uniaxial crystals, and (b) Schematic depiction of orientation of beam propagation directions for type-I and type-II phase matching in index ellipsoid for a negative uniaxial crystal like KDP at ω and 2ω frequencies.	2-57
Fig. 2.14 Schematic layout of laser-induced damage threshold (LDT) set up. ...	2-60
Fig. 2.15 Schematic diagram depicting process of X-ray fluorescence.....	2-61
Fig. 2.16 A classification of vibrational modes of molecules.....	2-63
Fig. 2.17 Schematic line diagram of FTIR.	2-65
Fig. 3.1 Schematic line diagram showing morphology of KDP crystals.....	3-71

Fig. 3.2 KDP crystals grown by conventional method of hanging broad c-plate as seed in the solution. The central part shows capping region about seed plate.....	3-72
Fig. 3.3 Schematic diagram showing the morphology of the KDP crystals obtained by platform technique.	3-73
Fig. 3.4 Photograph of the fabricated water bath of capacity ~ 150 liter.	3-76
Fig. 3.5 Schematic line diagram of the crystal growth workstation including water bath and crystallizer.	3-77
Fig. 3.6 Variation of axial temperature inside the water bath at four different set temperatures.	3-77
Fig. 3.7 A photograph of the fabricated crystallizer having ~ 15 liter solution capacity.	3-78
Fig. 3.8 Variation of axial temperature inside the crystallizer filled with water up to 18 cm height at three different values of set temperature of the water bath.....	3-79
Fig. 3.9 Schematic of a crystal growth workstation based on platform technique... 80	3-80
Fig. 3.10 Schematic showing process of solution filtration.....	3-81
Fig. 3.11 Schematic diagram showing seed protection technique.....	3-82
Fig. 3.12 Seed holders of length 15 and 20 mm showing remaining KDP seed part in the longer tube after 47.5 hours of overheating.	3-83
Fig. 3.13 KDP crystal grown using seed protection technique.....	3-84
Fig. 3.14 (a) Schematic design of three plate platform for growth of SHG type-II oriented KDP crystals, and (b) photograph of an as- grown KDP crystal.	3-86
Fig. 3.15 Schematic showing modification of crystal shape by solution-air interface as growth proceeds from pyramidal-cap crystal (a), to the flat-top shaped crystal (b).	3-88
Fig. 3.16 Photographs of three KDP crystals grown using c-oriented point seeds employing flat-top growth methodology.	3-88

Fig. 3.17 Depiction of beam direction (θ, Φ) with respect to the principal axes (x, y, z) of KDP crystal.....	3-91
Fig. 3.18 Schematic depiction of the orientation methodology of KDP seed at the platform for growth of SHG oriented crystal.....	3-92
Fig. 3.19 (a) As-grown type-I SHG oriented KDP crystal, and (b) prepared type-I SHG element by slicing the crystal parallel to its base.....	3-93
Fig. 3.20 Slicing process of type-I SHG oriented KDP parallel to its base using Buehler make low speed saw.....	3-93
Fig. 3.21 (a) As-grown type-II SHG oriented flat-top KDP crystal, (b) cut parts normal to its base and (c) prepared type-II SHG element.....	3-94
Fig. 3.22 (a) Another view of the Flat-top KDP crystal showing different faces, seed and flat-top part for preparation of samples, (b) schematic depiction of location and orientation of six plates prepared for different characterizations.....	3-95
Fig. 3.23 Six sample plates prepared from one of the flat-top KDP crystals for characterization purpose.....	3-96
Fig. 3.24 Powder X-ray diffraction pattern of recrystallized KDP chemical prepared for crystal growth.....	3-97
Fig. 3.25 Diffraction curves for (200) diffraction planes of (100) surface of as-grown flat-top KDP crystals at successively increasing height from the bottom edge to the top edge. The distance of the diffraction point corresponding to each DC is also shown in the image.....	3-98
Fig. 3.26 Variation in relative peak positions of the diffraction curves for (200) planes of flat-top KDP crystal with respect to the linear position of beam at the crystal.....	3-99
Fig. 3.27 Internal view of digital topography system used for reflection topography.....	3-101
Fig. 3.28 X-ray topographs of three (001) sample plates for (316) diffraction planes, (a) for (001) top plate, (b) for (001) middle plate, and (c) for (001) bottom plate.....	3-101

Fig. 3.29 X-ray topographs of (101) sample plate for (732) planes (a), (010) plate for (172) planes (b), and (100) plate for (712) planes (c).....	3-102
Fig. 3.30 Optical micrographs of etch pits at three different regions of the (100) plate of flat-top KDP crystal, (a) linear chains of etch pits, (b) high defects density region, and (c) low defects density region. (Magnification 50X)	3-103
Fig. 3.31 Optical micrographs of etch pits at three different regions of the (101) plate of flat-top KDP crystal, (a) linear chains of etch pits, (b) high defects density region, and (c) low defects density region. (Magnification 50X)	3-103
Fig. 3.32 Transmission spectra of different locations at the (001) bottom, (001) middle and (001) top plates without accounting Fresnel reflection losses. The locations of the points from where the transmission was measured is marked in the schematic shown in inset.....	3-105
Fig. 3.33 Spatial variation of transmittance along X-axis at four specific wavelengths for for (001) middle plate.....	3-105
Fig. 3.34 Spatial variation of transmittance along Y-axis at four specific wavelengths for (001) middle plate.	3-106
Fig. 3.35 Transmission spectra for the four different plates of the flat-top KDP crystal namely (100), (010), (101) and (001)-bottom plates without accounting for Fresnel losses.....	3-106
Fig. 3.36 Conoscopy images of the (001) bottom (a), (001) middle (b), and (001) top plates (c) of the flat-top KDP crystal.	3-107
Fig. 3.37 Birefringence interferogram for (100) plate (a), and (010) plate (b) of flat-top KDP in orthoscopic mode.....	3-108
Fig. 3.38 Mach-Zehnder (MZ) interferograms of (100) (a), (001)-bottom (b) and (001)-top (c) plates.....	3-109
Fig. 3.39 (a) Schematic line diagram showing the geometry of XRF measurement set up, and (b) a KDP sample plate at the sample stage during the experiments.....	3-110

Fig. 3.40 The X-ray fluorescence spectra obtained for (001)-bottom plate of the flat-top KDP crystal.	3-110
Fig. 3.41 Experimental set up for measurement of laser-induced damage threshold.	3-113
Fig. 3.42 Variation of transmitted pulse energy with respect to the position of knife edge for calculation of $(1/e^2)$ beam diameter of the laser beam at the sample surface.	3-113
Fig. 3.43 (a) C-cut KDP element prepared for electro-optic modulator, and (b) conoscopic figure at screen confirming its orientation.	3-114
Fig. 3.44 (a) SHG element of size $50 \times 50 \times 25 \text{ mm}^3$ prepared from a flat top KDP crystal, (b) a housing designed for the SHG element, and (c) complete KDP type-II SHG cell with antireflection windows and index matching fluid.	3-115
Fig. 3.45 Schematic of the optical set up used for measurements of SHG efficiency of KDP samples.	3-115
Fig. 3.46 Variation of SHG efficiency with input intensity for KDP SHG type-I element.	3-116
Fig. 3.47 Variation of SHG efficiency with input intensity for KDP SHG type-II element.	3-116
Fig. 4.1 Schematic depiction of usable area at the square cross-section device elements.	4-123
Fig. 4.2 Schematic representation of solute feed based unidirectional growth technique.	4-126
Fig. 4.3 Two-zone water bath fabricated using helical shape heaters in a single glass beaker.	4-128
Fig. 4.4 Schematic line diagram of the two-zone water bath with isolated heating zones.	4-128
Fig. 4.5 (a) Photograph of the fabricated two-zone water bath with isolated heating zones, and (b) growth ampoule with feed tube.	4-129
Fig. 4.6 Axial temperature profile of the fabricated two-zone water bath at two different temperatures of the upper zone.	4-130

Fig. 4.7 Schematic line diagram showing two designs of growth ampoules for mounting point seeds for crystal growth, (a) flat bottom, and (b) conical bottom.	4-131
Fig. 4.8 (a) Schematic of the laser shadowgraphy set up used for imaging the process of mass transfer and crystal growth, and (b) photographs of typical laser shadowgraphs corresponding to mass transfer through the membrane from the feed powder, and upward movement of depleted plumes from the growing crystal shows crystal growth.	4-132
Fig. 4.9 KDP crystals grown along [001] direction by using solute-feed based unidirectional growth technique.	4-134
Fig. 4.10 Crystal growth ampoule containing a KDP crystal grown inside it. ...	4-134
Fig. 4.11 Three (001) plates prepared from the 90 mm long [001] oriented KDP crystals from bottom, middle and top portions.	4-136
Fig. 4.12 UV-Vis-NIR transmission spectra for the three sample plates of the (001) oriented unidirectional KDP crystal.	4-137
Fig. 4.13 Laser conoscopic images of (001) bottom plate (a), (001) middle plate (b), and (001) top plate (c).	4-137
Fig. 4.14 X-ray diffraction topographs for (316) planes of (001) bottom (a), (001) middle (b), and (001) top plates (c) of the [001] oriented unidirectional KDP crystal.	4-138
Fig. 4.15 SHG type-II oriented KDP crystals grown by solute feed based unidirectional technique (a) as grown KDP in the growth ampoule of 55 mm diameter, and (b) photograph of the crystal after taking out from the growth ampoule.	4-140
Fig. 4.16 (a) Type-II SHG elements prepared by slicing the KDP crystal shown in Fig. 4.15 normal to the growth direction, and (b) (100) plate prepared from the top portion of the crystal.	4-140
Fig. 4.17 UV-Vis-NIR transmission spectra for 2.6 mm thick (100) and SHG plates of SHG type-II oriented unidirectional grown KDP crystal by solute feeding technique.	4-141

Fig. 4.18 Orthoscopic birefringence interferograms for (100) plate (a), and for the SHG plate (b), prepared from SHG type-II oriented unidirectional KDP crystal.	4-142
Fig. 4.19 Mach-Zehnder interferograms for (100) plate (a), and for SHG plate (b).	4-142
Fig. 4.20 X-ray diffraction topographs, (a) for type-II SHG plates no. 1, (b) for type-II SHG plate no. 6, and (c) for (100) plates.	4-143
Fig. 4.21 High resolution X-ray diffraction curves for (100) plate (a), and for SHG plate (b).	4-144
Fig. 4.22 Optical micrographs of the chemical etch pits at the (100) plate, (a) at high defects density region, and (b) at low defect density region. (Magnification: 50 X)	4-145
Fig. 4.23 Variation of SHG efficiency with input power density for the SHG type-II plate.	4-145
Fig. 4.24 (a) Unidirectional growth of KDP crystal along (101) surface by solute feeding, technique, and (b) prepared (101) elements by slicing crystal normal to the growth direction.	4-146
Fig. 4.25 Transmission spectrum of a 3.0 mm thick (101) plate prepared from (101) oriented unidirectional grown KDP crystal by solute feeding.	4-147
Fig. 4.26 Birefringence interferogram for (101) plate prepared from the (101) oriented unidirectional KDP crystal.	4-148
Fig. 4.27 X-ray diffraction topograph for (101) plate of the (101) oriented KDP crystal.	4-148
Fig. 4.28 Unidirectional KDP crystal grown along (100) face by solute feeding technique.	4-149
Fig. 4.29 (a) Photographs of three sample plates prepared from the (100) oriented unidirectional KDP crystal from bottom, middle and top portions, (b) the corresponding X-ray diffraction topographs, and (c) corresponding birefringence interferograms for the three plates.	4-150
Fig. 4.30 LAP crystal grown along (010) direction from a point seed by solute feeding technique.	4-151

Fig. 4.31 DKDP crystal of 80 mm length and 18 mm diameter grown using solute-feed based unidirectional growth technique.....	4-151
Fig. 5.1 X-ray powder diffraction pattern of synthesized LAP chemical.....	5-157
Fig. 5.2 Solubility curve for LAP chemical in water at pH 4.3.....	5-159
Fig. 5.3 Spontaneously grown LAP seed crystals.	5-160
Fig. 5.4 Typical habit of LAP crystal viewed normal to bc – plane (a), and normal to ca-plane (b).	5-160
Fig. 5.5 Schematic diagram of the crystallizer used for growth of LAP crystals.....	5-161
Fig. 5.6 LAP crystals grown using seed crystals having (i) (100), (ii) (010), (iii) (001) and (iv) (011) planes parallel to the platform.	5-162
Fig. 5.7 Schematic showing the overall dimensions (L_a , L_b , L_c) of a LAP crystal looked along crystallographic a-axis (i), and that along b-axis (ii); for calculation of aspect ratio and average growth rates.	5-162
Fig. 5.8 (i) Microscopic image of as-grown (100) surface of LAP crystal at 50X magnification showing a series of steps elongated parallel to b-axis and spread along c-axis, (ii) atomic structure of (100) face showing chains of strong bonds between phosphate groups elongated towards b-axis.	5-164
Fig. 5.9 (i) (100) sample plate prepared from the (011) oriented LAP crystal, and (ii) its corresponding X-ray topograph for (811) planes.....	5-166
Fig. 5.10 Optical micrographs of the surface of (100) plate of the LAP crystal after chemical etching showing chains of etch pits (i), high etch pit density (ii), low etch pitch density (iii) and almost dislocation free region (iv), corresponding to the regions marked as a, b, c, d in its X-ray topograph shown in Fig. 5.9(ii). (Magnification 50X.).....	5-167
Fig. 5.11 UV-Vis-NIR transmission spectrum for (100) plate of LAP crystal without accounting for Fresnel reflection losses, for plate thickness 1.7 mm. .	5-168
Fig. 5.12 Birefringence interferogram of the (100) plate of the (011) oriented LAP crystal.....	5-169

Fig. 5.13 Mach-Zehnder interferogram of the (100) plate of the LAP crystal. .	5-170
Fig. 5.14 FTIR spectrum of the LAP crystal.	5-171
Fig. 5.15 Differential scanning calorimetric graph for LAP sample.	5-173
Fig. 5.16 Laser conoscopy set up for determination of directions of optic axes and bisectrix.....	5-175
Fig. 5.17 Laser conoscopic interferograms obtained using (100) LAP plate. (a) for beam direction along one of the optic axis (OA1), and (b) for beam direction along its acute bisectrix.....	5-175
Fig. 5.18 Schematic ray diagram showing path of the central beam in the optic plane in laser conoscopy to calculate direction of optic axis (r).....	5-176
Fig. 5.19 (a) Orientations of acute and obtuse bisectrix inside the LAP crystal calculated from the observed external directions by laser conoscopy in the optic plane relative to habit faces of the crystal. The directions of crystallographic axes in this plane were determined using SHAPE software. (b) schematic of the corresponding sections of biaxial indicatrix viewed normal to zx- plane.....	5-177
Fig. 5.20 Schematic of the optical set up used for growth rate measurement based on birefringence interferometry. The seed-crystal is shown with b-axis downward. Top view of the growth unit is depicted to show beam propagation in the optic plane with respect to its habit faces.	5-177
Fig. 5.21 Crystal growth unit (a), seed crystal at mount (b), and shadowgraph of seed showing saturation state (c).....	5-179
Fig. 5.22 (a) Image of birefringence fringes during growth, and (b) variation of transmitted intensity with time and temperature during the course of the experiment.....	5-180
Fig. 5.23 Variation of growth rate of LAP crystal normal to the (100) face with supercooling.	5-181
Fig. 5.24 Photograph of the as-grown LAP crystal at the mount after the experiment.	5-181
Fig. 6.1 Powder X-ray diffraction pattern for the prepared ZCTC chemical. ...	6-189

Fig. 6.2 Solubility curve for ZCTC chemical in water at stoichiometric pH value ~ 6.2.....	6-190
Fig. 6.3 (a) Needle shape nuclei and their aggregates formed at stoichiometric pH value 6.2, (b) an enlarged image of some aggregates.....	6-191
Fig. 6.4 (a) Prismatic shape seed crystals obtained at pH 2.3 by spontaneously nucleation by slow evaporation, and (b) a seed placed in a seed holder to mount at the platform for growth of ZCTC crystal.....	6-192
Fig. 6.5 (a) Schematic of a crystallizer based on controlled evaporation, and (b) actual photograph of the crystallizer based on controlling the rate of solvent evaporation.....	6-193
Fig. 6.6 As-grown ZCTC crystals from point seeds at low pH with approximate dimensions (a×b×c) as (i) 4×4×7 mm ³ , (ii) 4×3×11 mm ³ , (iii) 3×2×16 mm ³ , (iv) 2×2×14 mm ³ , and (v) 4×1.5×15 mm ³	6-194
Fig. 6.7 Typical growth morphology of ZCTC crystal obtained by SHAPE software.	6-195
Fig. 6.8 Transmission spectrum of 1 mm thick (100) plate of ZCTC crystal without accounting for Fresnel reflection losses. Inset show the sample plate.	6-196
Fig. 6.9 (a) (100) sample plate of ZCTC crystal used for birefringence interferometry, and (b) birefringence interferogram for the plate in orthoscopic configuration.	6-196
Fig. 6.10 (a) ZCTC sample plate used, and (b) X-ray diffraction topograph for (811) planes of (100) plate.....	6-197
Fig. 6.11 Optical micrograph of etched (100) surface of ZCTC sample plate by ethylene glycol. (Magnification:50X).....	6-198
Fig. 6.12 ZCTC crystals splitted normal to c-axis at energy above the LDT....	6-199
Fig. 6.13 FTIR spectrum of ZCTC crystal.	6-200
Fig. 6.14 DSC curve of ZCTC crystal.	6-200
Fig. 6.15 Schematic depiction of principle of prism coupling method used for determination of refractive index of a sample plate.....	6-202

Fig. 6.16	Variation of ordinary and extra-ordinary refractive indices with wavelength, measured by prism coupling method at five different wavelengths at room temperature (30 °C).....	6-203
Fig. 6.17	Temperature dependent refractive index of extraordinary wave in ZCTC crystal at four different wavelengths.....	6-204
Fig. 6.18	Temperature dependent refractive index of ordinary wave in ZCTC crystal at four different wavelengths.	6-205
Fig. 6.19	Variation of phase matching angle with wavelength for ZCTC crystal in type-I and type-II phase matching configurations.	6-207
Fig. 6.20	Some of the ZCTC crystals, grown along [001] direction by solute-feed based unidirectional growth technique.....	6-208
Fig. 6.21	Transmission spectrum for ~ 1mm thick (001) plate of ZCTC crystal grown by solute-feed based unidirectional growth technique.....	6-209
Fig. 6.22	Optical conoscopy image of ~ 1.0 mm thick (001) plate of ZCTC crystal.	6-209

LIST OF TABLES

Table 3.1 Depth of dissolution of KDP seed versus duration of overheating by 20 °C for KDP solution saturated at 45 °C.....	3-83
Table 3.2 Orientation of the normal to the device plate of KDP w.r.t. its crystallographic coordinate system for different applications with Nd:YAG laser.	3-85
Table 3.3 Growth details of the flat-top shape KDP crystals along with design parameters of the platform showing the validity of the empirical relationship 3.3 for flat-top growth.	3-89
Table 3.4 Comparison of the process conditions and crystal parameters at two different stages of growth viz. when pyramidal-cap just reaches the solution-air interface and second at the end of the growth run when the flat-top shaped KDP crystal has been grown.	3-89
Table 3.5 Values of angles α and β for orientating KDP seed crystal for SHG oriented growth	3-92
Table 3.6 Concentration of iron and nickel impurities in different plates of flat-top KDP crystal determined using X-ray fluorescence, and the UV-Vis-NIR transmittance for these plates at six different wavelengths. The transmittance values are without accounting for Fresnel reflection losses.	3-111
Table 3.7 Values of the laser-induced damage threshold for the different samples of the flat-top KDP crystal.	3-114
Table 4.1 Growth details of [001] oriented KDP crystals grown by solute feeding method.....	4-135
Table 4.2 Influence of increasing temperature gradient on growth rate of KDP along [001] direction.....	4-135
Table 4.3 Growth details of unidirectional KDP crystal grown along (101) face....	4-147
Table 5.1 Solubility data for LAP in water at pH 4.3.....	5-158

Table 5.2: Dimensions, average growth rates along crystallographic axes and aspect ratio of LAP crystals grown along four different orientations on the platform.	5-163
Table 5.3 : LDT results obtained from various locations in low EPD region. ..	5-172
Table 5.4 : LDT results obtained from various locations in high EPD region. .	5-172
Table 5.5 Growth kinetics data determined at different undercooling for LAP crystal using birefringence interferometry.....	5-180
Table 6.1 A comparison of obtained lattice parameters with that reported in the literature.	6-189
Table 6.2 Saturation concentration of ZCTC salt in water for solubility curve.	6-190
Table 6.3 Growth details of ZCTC crystal shown in Fig. 6.6(iv).....	6-194
Table 6.4 LDT results measured at various locations of different (100) plates of ZCTC crystals.	6-198
Table 6.5 Extraordinary and ordinary refractive indices of ZCTC crystal at five different wavelengths at room temperature (30 °C) and the resulted birefringence.	6-202
Table 6.6 Sellmeier coefficients for the ZCTC crystal.....	6-203
Table 6.7 Values of extraordinary and ordinary refractive indices with temperature measured by prism coupling method at four different wavelengths. ..	6-204
Table 6.8 Values of temperature coefficients of refractive indices for ordinary and extraordinary waves at different wavelengths.....	6-205
Table 6.9 Phase matching angle with wavelength for ZCTC crystal in type-I SHG configuration.	6-206
Table 6.10 Phase matching angle with wavelength for ZCTC crystal in type-II SHG configuration.	6-207

Chapter 1 Introduction

1.1 Importance of crystals

Crystals have attracted human from ancient times due to their smooth and shining faces, sharp edges, attractive colours and symmetry which have been mainly used for ornamental applications for example diamond, topaz, ruby.^{1,2} In modern era there are numerous other applications for crystals in every walk of life ranging from daily use items for food, fertilizers and pharmaceutical products to science and technology. Crystals played a significant role in the development of various fields of science and technology such as crystallography, crystal physics, crystal growth, solid state physics, lasers, non-linear optics, semiconductor physics, fiber optics and optical communication, light emitting devices, pyroelectric detectors, radiation detectors, X-ray spectroscopy, inertial confinement fusion etc. It is because of the perfect order of constituent atoms which makes it possible to quantify physical properties of materials and to fabricate devices with high order of repeatability. Crystals have unique characteristics of high chemical purity, ultra-high precision of atomic placement in three dimensions with feasibility to precisely change the chemical composition. These characteristics make them suitable to correlate structure-property relations of materials utilizing their optical, non-linear optical, thermal, mechanical, electrical and magnetic properties and tailoring the structure to obtain desired properties for device applications. The study of crystals also helped to understand defect structure and the mechanism of crystal growth.

1.2 Single crystals

The materials are usually classified in three forms solid, liquid and gas which are interconvertible under variation of physical conditions such as temperature, pressure and composition. Solids have further been classified as crystalline or amorphous depending on the length of spread of regular arrangement of atoms or molecules. Crystals have long range order of atoms or molecules due to periodic arrangement of atoms while amorphous materials have very short range order. Crystalline materials have been divided into two groups i) Polycrystalline and 2) Single crystals. Polycrystalline and single crystals are differentiated in terms of number of grains in the sample. Ideally single crystals are defined as the solids in which atoms, ions or molecules are arranged in a periodic repeating pattern up to long ranges in three dimensions up to infinity. Real crystals have finite dimensions

having surface as defect therefore on strict sense they are not perfect single crystals however having periodicity up to their extension. Fig. 1.1 shows a general classification of matter in different physical states.

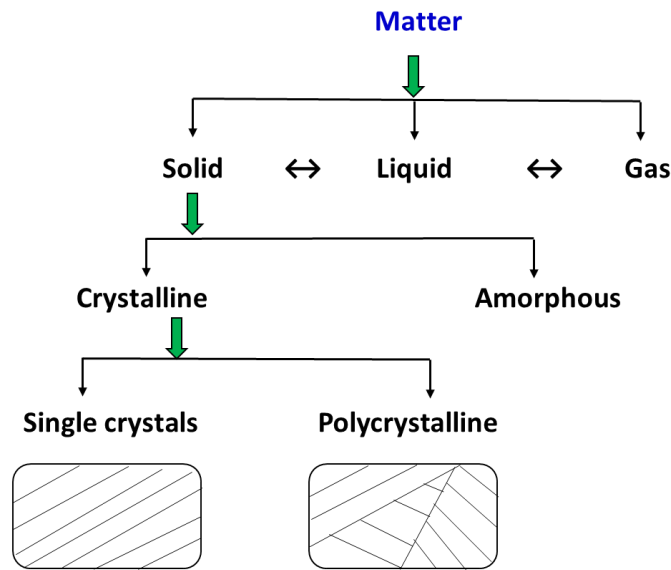


Fig. 1.1 Classification of materials.

The repeating atom or group of atoms of a crystal is called as basis. In crystallography, for simplicity the basis locations are denoted by spherical points called as lattice points and the centers of the nearby lattice points are connected by straight lines. The net type structure formed by lattice points is called crystal lattice. A lattice is thus a set of points arranged regularly in space having identical surroundings. Mathematically,

$$\text{Lattice} + \text{Basis} = \text{Crystal}$$

The periodic arrangement of atoms leads to translational symmetry in the crystals. The smallest parallelepiped shape unit of the crystal lattice which can generate the whole crystal by translation symmetry is called as unit cell. A unit cell is usually characterized by lattice parameters a , b , c and interfacial angles α , β , γ as shown in Fig. 1.2.

There are thousands of different materials which can be crystallized. All these can be grouped into seven crystal systems which further classified into 14 different types of lattices known as Bravais lattices. The periodic arrangement of atoms also leads to rotational symmetries in the crystals. There are ten different types of rotational and roto-inversion symmetries possible in crystals. Based on these symmetries crystals can be classified into 32 point groups. A crystallographic point group is defined as a group of symmetry elements (operations) that can operate on a three-dimensional lattice leaving at

least one point unmoved. The complete symmetry of a crystal includes rotational as well as translational symmetries which is represented by space group. There are 230 space groups possible in crystals. Space group operations enable one to generate complete crystal structure from a single (or group of) molecules(s) called as asymmetric unit. Details of point groups and space groups are a part of crystallography and beyond the scope of this thesis. These are nicely described in details in several books.^{3,4}

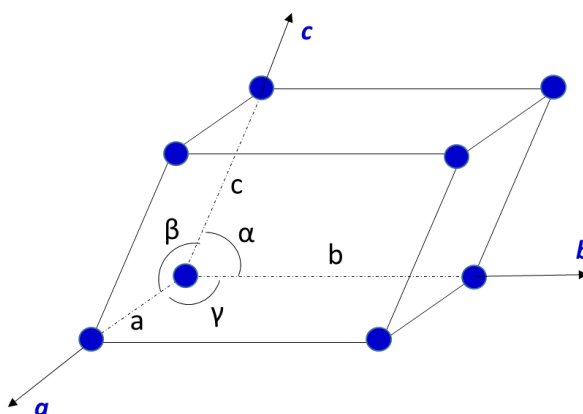


Fig. 1.2 Schematic of general unit cell of crystal.

A crystal can also be assumed or described as composed of parallel planes of lattice points. A crystal thus can be depicted independently by different sets of parallel planes distinguished by interplanar spacing and their orientation. British mineralogist W. H. Miller introduced a simple scheme in 1839 to denote a crystal face or a set of parallel lattice planes by three integers denoted in a parenthesis as (hkl) called as the Miller indices of the plane. The three numbers h, k and l for a lattice plane are defined as the reciprocals of the intercepts made by the plane in terms of unit cell parameters with the three crystallographic axes namely a , b , c as shown in Fig. 1.2. The indices are normally given as the smallest set of integers that can be obtained by division or by clearing of fractions. The distance between the parallel planes is called the interplanar spacing (or d spacing) and is designated by the symbol d_{hkl} . All symmetrically equivalent planes i.e. all faces that can be derived from hkl by symmetry operations of the crystal are represented by placing indices in a curly bracket {hkl}, represents crystallographic form. One of the important characteristics found in most of the crystals is the anisotropic character of their physical properties. Periodic arrangement of atoms in the crystals is responsible for the direction dependent variation of physical properties (except for cubic crystals). Point group symmetries have their influence on the symmetry of anisotropic properties of crystals.

According to Neumann's principle "the symmetry elements of any physical property of a crystal must include the symmetry elements of the point group of the crystal". Thus symmetry and anisotropic physical properties of a crystal are related by Neumann's principle. It is to note that a change in crystal structure has profound effect on physical properties of a material. One of the well-known examples is, carbon having two allotropes: graphite (hexagonal structure) and diamond (cubic structure) having quite different physical properties due to difference in crystal structure.

For a particular application, specific single crystals are required. Some of the crystals are found in nature while most of the crystals are grown in the laboratories. The growth of a particular crystallographic phase of a material requires knowledge of crystal growth.

1.3 Physics of crystal growth

Crystal growth is complex phenomena. It is a multi-disciplinary field, a meeting point of several branches of science such as solid state physics, crystallography, optics, thermodynamics, semiconductor physics, chemistry, material science, mineralogy and gemology, metallurgy, mechanical engineering, electronics and instrumentation, chemical engineering, fluid dynamics, mathematical modelling etc. Fig. 1.3 schematically demonstrates some of the areas of science and technology which are related with crystals.

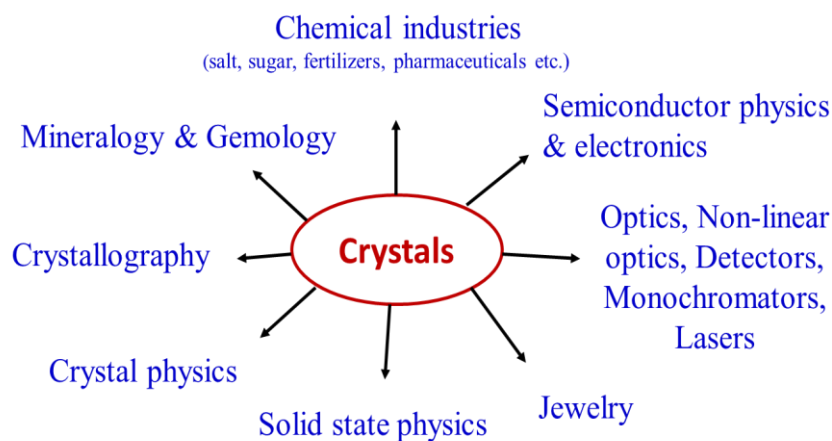


Fig. 1.3 Importance of crystals for different fields of science and technology.

Growth of large size crystals with good quality are essential for device fabrication. Crystal growth is considered as an art as well as science. A good understanding of physics of crystal growth is essential for deciding the technique of crystal growth and for growth good quality crystal at high rates.

1.3.1 Driving force for crystallization

Crystal growth is basically a process of first-order phase transition either from liquid or vapor phase to the solid phase as shown schematically in Fig. 1.4.

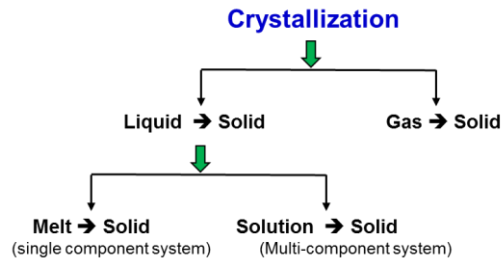


Fig. 1.4 Schematic of processes of crystallization.

Crystallization is usually achieved by reduction in temperature across phase transition temperature. However, thermodynamically the main driving force for crystallization is change in Gibbs Free energy (ΔG). Because for a spontaneous process at constant temperature and pressure, $\Delta G < 0$. It means every system spontaneously tries to minimize its Gibbs free energy. Fig. 1.5 shows the typical variation of Gibbs free energy with temperature for solid and liquid phase across melting point for a single component system. Gibbs free energy for a material at temperature T and enthalpy H is given by,

$$G = H - T S \quad \text{---- (1.1)}$$

At phase transition temperature where the two phases of a material say solid and liquid, are in thermodynamic equilibrium, the change in Gibbs free energy can be written as,

$$\Delta G = \Delta H - T \Delta S \quad \text{---- (1.2)}$$

where T is melting point, ΔH is heat of phase transition and ΔS is change in entropy on account of phase transition.

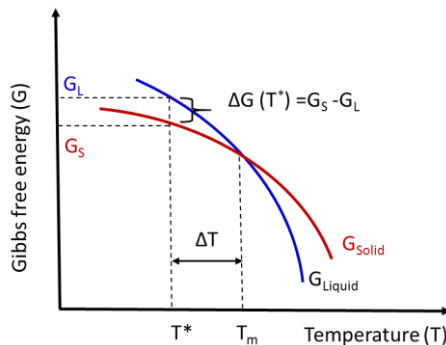


Fig. 1.5 Typical Gibbs free energy curves for solid and liquid phases across melting point.

At equilibrium of two phases $\Delta G = 0$. Therefore, the above equation becomes,

$$\Delta H - T_m \Delta S = 0 \quad \text{---- (1.3)}$$

putting value of ΔS from eq. (1.3) into (1.2),

$$\Delta G = (\Delta H \Delta T) / T_m \quad \text{---- (1.4)}$$

This equation shows that change in free energy is proportional to the change in temperature between the liquid phase and the phase transition temperature (T_m). This is referred as the driving force for crystallization in case of melt to solid transformation. It shows that driving force for phase transition is directly proportional to the undercooling.

In case of two component systems such as solutions, crystallization can be achieved by temperature variation or by evaporation. The state of solution depends not only on temperature and pressure but also on composition which is depicted by its phase diagram. Gibbs phase rule is normally used to identify number of phases in equilibrium at a given temperature, pressure and composition. In case of solutions, the fundamental driving force for crystallization is the difference between chemical potential ($\Delta\mu$) of the material in solution and in crystal phases at equilibrium temperature.⁵ Thermodynamically in case of solutions, change in Gibbs free energy is proportional to change in chemical potential at constant pressure, therefore the latter is usually treated as driving force. The chemical potential depends on absolute temperature (T) and activity a of the molecule of that material, which is given as,

$$\mu = \mu_o + k_B T \ln (a) \quad \text{---- (1.5)}$$

Where k_B is the Boltzmann constant and μ_o is the standard chemical potential of the material. The difference between the two states of the solute molecule at equilibrium can be written as.^{5, 6}

$$\begin{aligned} \Delta\mu / k_B T &= \ln (a/a^*) \\ &\approx \ln (C_a / C_s) = \ln S \end{aligned}$$

$$\text{Where, } S = C_a / C_s = (C_a - C_s + C_s) / C_s = (C_a - C_s) / C_a + 1 = \sigma + 1$$

Here, S is called fundamental supersaturation or supersaturation ratio which is also written as β in some books. σ is called as relative supersaturation and C_a and C_s are actual and saturation concentration of the solution. It gives,

$$\begin{aligned} \text{Thus, } \Delta\mu / k_B T &= \ln S = \ln (1 + \sigma) \\ \Delta\mu &= k_B T \ln (1 + \sigma) \quad \text{---- (1.6)} \end{aligned}$$

For low value of σ compared to 1;

$$\ln (1 + \sigma) \approx \sigma = (C_a - C_s) / C_a = \Delta C / C_s$$

Therefore, in such cases, one can write,

$$\Delta\mu = k_B T \ln (C_a / C_s) = k_B T \ln S = k_B T \ln (1 + \sigma) \approx R T \sigma = k_B T (\Delta C / C_s) \text{ ---- (1.7)}$$

It shows that in case of solution growth, the driving force of the crystallization is proportional to relative supersaturation σ . Therefore, supersaturation is generally considered as the driving force for solution crystal growth. Further, supersaturation depends on change in concentration ΔC which can be correlated with change in temperature or undercooling of the solution. If solubility increases linearly with temperature, supersaturation σ and hence driving force $\Delta\mu$ would depend on amount of reduction in temperature which is also known as supercooling or undercooling.

A similar expression can also be written for vapour growth. Vapour growth is applicable to those materials which directly crystallize from vapour phase without entering into liquid phase. It is like sublimation. In such cases the expression for driving force be,

$$\Delta\mu = k_B T \ln (P_a / P_s) \text{ ---- (1.8)}$$

Where P_a and P_s are actual and equilibrium vapour pressures at the Temperature T .

1.3.2 Free energy barrier for nucleation

As per the above analysis, supercooling (ΔT) or supersaturation (σ) is necessary for crystallization. However, it is not sufficient for initiation of crystallization. It is because when growth of solid phase starts by association of molecules in the liquid phase, the volume energy decreases due to formation of bonds among molecules but surface energy increases due to formation of surface. The net change in energy due to solidification depends on the amount of these two energy terms. It can be shown that initially when the size of the solid phase is very small the net change in energy is positive but after a certain critical size it turns to be negative. It shows that if the size of a solid particle in its liquid phase is below the critical size it will dissolve spontaneously while if somehow it acquires a size above the critical value it will survive and grow.

The aggregation of individual molecules or atoms is called clustering and it takes place by collisions among atoms, ions or molecules present in the liquid phase. If a cluster acquire crystalline lattice type structure is called embryo. An embryo of critical size is called nucleation which remain stable in the solution and can grow under supersaturation. Since it is a dynamic process until the formation of nucleation, it may be depicted as,



The mechanism of formation of nucleation is quite complex and not yet fully understood. If nucleation occurs spontaneously in a fluid without presence of any foreign crystalline matter is called as primary nucleation while if nucleation induced in the fluid by presence or deliberate insertion of a crystal such as seed crystal is called as secondary nucleation. The primary nucleation is further divided into two categories homogeneous and heterogeneous. If nucleation occurs by itself in the solution is called as homogeneous one while if it is initiated by some foreign particle is called as heterogeneous nucleation. A classification of mechanism of nucleation formation is shown in Fig. 1.6.⁵

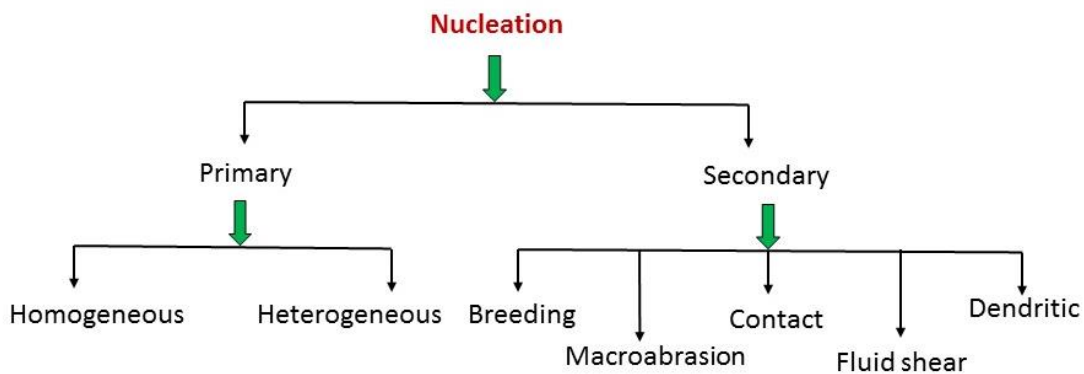


Fig. 1.6 Mechanisms of nucleation

The structure and morphology of critical nucleus is not known exactly because it is too small to be visible. However, an estimate can be made based on classical theory of nucleation. When a solid particle form in liquid by association of its molecules, its surface free energy increases while volume free energy decreases, therefore the net excess free energy can be written as,

$$\Delta G = \Delta G_s + \Delta G_v \text{ ---- (1.9)}$$

Where ΔG_s = change in Gibbs free energy due to formation of surface which is positive, and ΔG_v = change in Gibbs free energy due to volume formation which is negative.

Considering a case of homogeneous nucleation of spherical shape of nucleus of radius r in a liquid phase, the net change of free energy can be written as,⁵

$$\Delta G(r) = 4\pi r^2 \gamma + \frac{4}{3}\pi r^3 \Delta G_v \text{ ---- (1.10)}$$

Where γ = change in Gibbs free energy per unit surface area, which is positive and ΔG_v = change in Gibbs free energy per unit volume which is negative.

It has two terms of opposite nature; first one is positive which varies with r^2 while the second is negative which varies with r^3 as shown in Fig. 1.7. The value of $\Delta G(r)$ therefore will maximize at certain value of r which can be obtained by equating its first derivative to zero. This gives value of r_{crit} ,

$$r_{crit} = -2\gamma / \Delta G_v \text{ ---- (1.11)}$$

the corresponding value of net change in free energy for formation of critical size cluster be,

$$\Delta G_{crit} = -4\pi\gamma r_{crit}^3 / 3 \text{ ---- (1.12)}$$

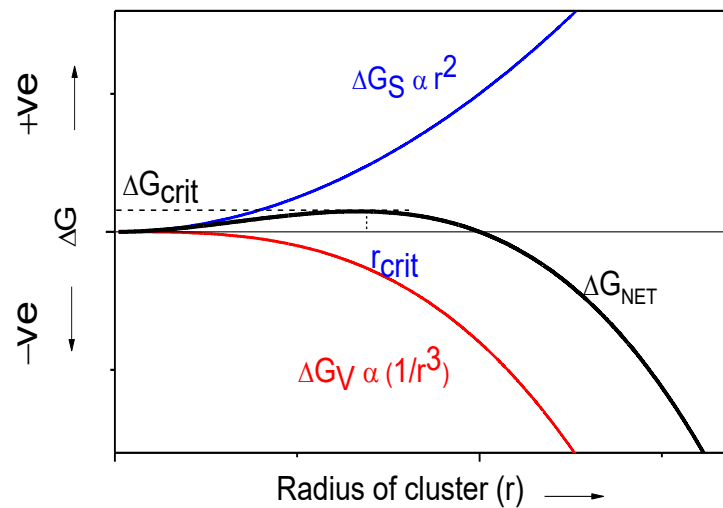


Fig. 1.7 Variation of Gibbs free energy with radius of cluster.

The above equations and Fig. 1.7 show that the clusters of radius below r_{crit} have tendency of dissolving while that above this value would survive in the liquid and grow further spontaneously. To achieve this a certain threshold of change in Gibbs free energy is warranted given as ΔG_{crit} which corresponds to certain amount of supercooling or supersaturation. This analysis is however for spherical shape homogeneous nucleation which can be extended for nucleation of different shapes and different types of nucleation.^{5,7} For nucleation of types other than homogeneous the required amount of ΔG_{crit} is lesser compared to that for homogeneous nucleation.

1.3.3 Rate of nucleation

For growth of large size single crystals, it is required to prevent nucleation other than what is inserted as a seed. However, there is always a chance of occurrence of nucleation in a

supercooled melt or supersaturated solution. Nucleation rate (J) is defined as the number of nuclei produced per unit volume per unit time. Because there is a critical barrier of free energy to form a nucleation therefore using the Arrhenius equation, it can be expressed as,

$$J = A \exp(-G_{crit} / k_B T) \text{ ---- (1.13)}$$

Where G_{crit} is a proportionality constant.

1.3.4 Process of crystal growth

Crystal growth process can be described in three basic steps,

1. *Achievement of supersaturation or supercooling,*
2. *Formation of nucleation or insertion of a seed crystal, and*
3. *Subsequent growth of seed crystal or nucleation.*

Nucleation is the initial formation of a three-dimensional crystal while subsequent growth is a two-dimensional process yields distinct faces. Crystal growth takes place due to transport of growth units from bulk solution to the interface between the solid phase and the surrounding liquid phase. The third basic step mentioned above for the crystal growth process consists of several consecutive stages which can in general be described as,

- i) Generation of growth units in the bulk,
- ii) Transport of growth units from bulk to growing surface by diffusion or convection,
- iii) Adsorption of growth units at the crystal surface and subsequent migration on the surface,
- iv) Attachment of the growth units at the energetically favourable sites at the crystal surface,
- v) Transport of unwanted products such as heat of crystallization and depleted solution away from solid-liquid interface to the bulk.

Each of these stages depends on various factors making the process further complicated. A crystal growing inside a fluid acquires faceted morphology to minimize its overall surface energy. Crystal surfaces are denoted by Miller indices as mentioned in Section 1.2 and in general have different surface structures. The growth of a particular face depends upon its structure to capture the growth units and to integrate them in the crystal lattice. This depends on the number of bonds and their strength which can form between the surface and the growth unit. Depending on the number of bonds formed by a surface with the growth unit as one, two or three, the crystal surfaces have been classified into

following three categories as shown in Fig. 1.8, which have been described by Hartman using his concept of periodic bond chains (PBC).⁸

- i) *Flat faces or F-faces*
- ii) *Stepped faces or S-faces*
- iii) *Kinked faces or K-faces*

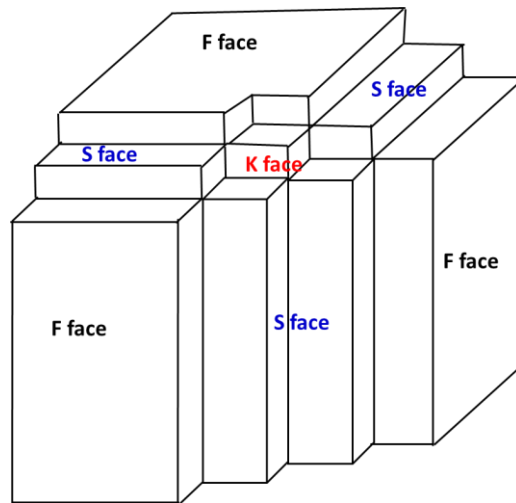


Fig. 1.8 Schematic showing flat (F), stepped (S) and kinked (K) surfaces of a crystal.

Growth rate of a face is generally considered to be proportional to the total binding energy of the growth unit to the crystal surface therefore growth rate of kinked face is highest and that of the flat faces is the lowest while that for stepped faces is in between these two. It indicates that growing crystals are bounded by flat faces because fast growing faces disappear from the morphology. The crystal growth theories are therefore related with the mechanism of growth of F faces.

1.3.5 Crystal growth mechanisms

There are several theories in the literature to explain the growth mechanism and kinetics of crystal growth. It is because there are various processes which may decide the crystal growth. Such as surface energy theory, adsorption layer theory, diffusion theory, structure of crystal-solution interface etc. Some of the prominent growth mechanisms are briefly described.

Surface energy theory was proposed by Gibbs and Curie. According to it growing crystal assumes a shape which has a minimum total surface energy for a given volume under a

given set of temperature and pressure in equilibrium. This theory was partly successful, because it could not explain many observations therefore do not have general acceptance.

Adsorption layer theory introduced by Volmer and developed with Gibbs is based on thermodynamic reasoning. According to it, solute atoms do not directly adsorb at the crystal lattice but adsorb at the surface layer and migrate over the surface until attached to a kink site where attractive forces are highest. This process leads to step by step build-up of one complete layer at crystal surface. However, for initiation of fresh layer on a complete face a two-dimensional nucleus is required to form.

Kossel model of crystal growth is based on the idea that there are many layers of monoatomic height moving one above the other parallel to the crystal surface. The layers may consist of one or more kinks where growth units most easily incorporated. The kink moved along the step thereby completing the layer at the crystal surface as depicted in Fig. 1.9. This model also requires surface nucleation for commencement of fresh layer on a completed face which demands sufficient supersaturation for crystal growth. While experimental measurement of growth rate with supersaturation showed for many crystals that crystal grows even at very low supersaturation.

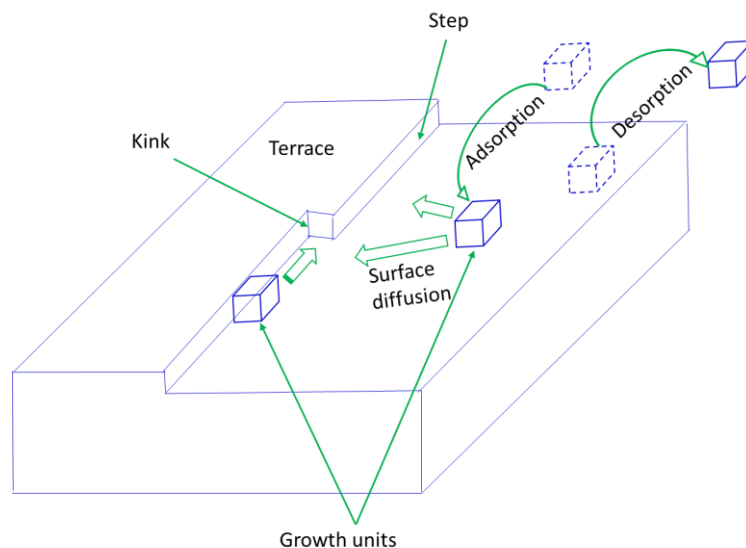


Fig. 1.9 Kossel's model of a growing crystal surface showing flat faces/terrace, steps, kinks, surface adsorbed growth units.

Burton, Cabrera and Frank model (BCF model): The above mentioned dilemma of observation of crystal growth at low supersaturation was solved by Frank (1949) who

postulated that most crystals contain screw dislocations which provide unending step for crystal growth. Due to this, growth face acquires a spiral staircase type pattern called as dislocation hillock as shown in Fig. 1.10.

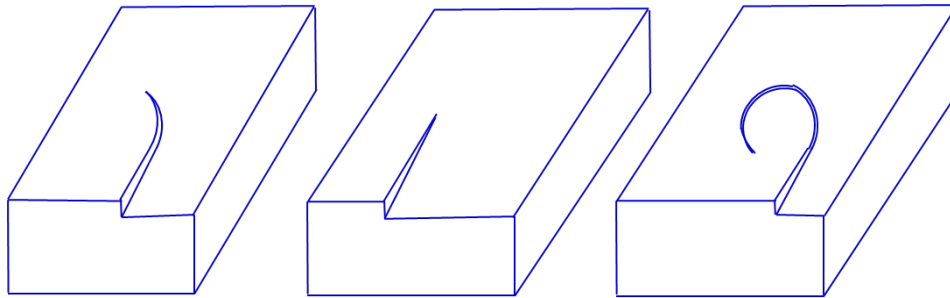


Fig. 1.10 Development of a growth spiral starting from a screw dislocation.

This model of crystal growth is also called as "spiral growth model" or "screw dislocation model" and soon confirmed by observation of spiral hillocks on crystal faces by several researchers experimentally. In 1951 Burton, Cabrera and Frank developed a kinetic growth theory⁹ of growth in which the curvature of the spiral near its origin was related to the spacing of successive turns and the level of supersaturation and using it successfully explained the experimentally observed growth rate at low supersaturations. The Burton-Cabrera-Frank (BCF) relationship may be written as,

$$R = \text{step velocity} \times \text{step height} \times \text{step density}$$

The final expression becomes as,⁵

$$R = A \sigma^2 \tanh (B/\sigma) \text{ ---- (1.14)}$$

where R is growth rate, σ is relative supersaturation, and A and B are complex temperature-dependent constants which include parameters depending on step spacing.

This relation suggests that at low supersaturation growth rate varies proportional to σ^2 while at higher supersaturation it approaches to linear relation.

Birth and spread model (B + S model): This model is based on assumption that two-dimensional nucleation arises at crystal surface which provide steps to spread monolayers on the face. The 2D nuclei may also develop on a moving monolayer thereby higher growth rate is envisaged. This model is also known as "nuclei on nuclei" (NON) or "polynuclear growth". The Fig. 1.11 shows the growth of a face by two-dimensional nucleation on the surface.

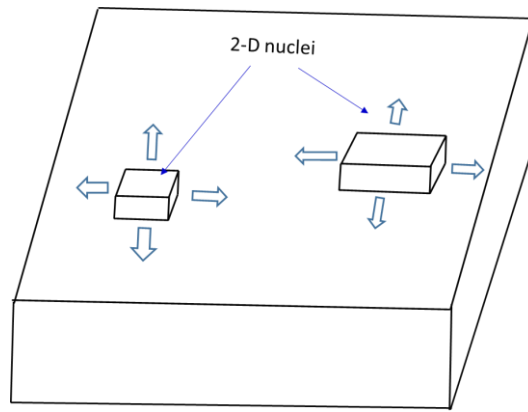


Fig. 1.11 Schematic showing development of a flat face by the birth and spread model.

The growth rate-supersaturation relationship for a flat face under B + S model can be written as,

$$R = \text{Number of critical size nuclei formed per unit time} \times \text{step height} \times \text{step velocity}$$

The simplified mathematical expression has the form,⁵

$$R = A_1 \sigma^{5/6} \exp(-A_2 / \sigma) \quad \text{---- (1.15)}$$

where A_1 and A_2 are system-related constants.

Continuous growth model: In cases where energy required for formation of step is low, the surface of the crystal will contain many kinks and step sites. In this case every growth unit arriving to the surface will find a growth site. Such growth is called continuous growth and the relation between linear growth rate and supersaturation can be written in simple form as,

$$R = k \sigma \quad \text{---- (1.16)}$$

where k is a constant. This mode of growth is applicable for kink faces over entire range of supersaturation.

In conclusion, it is also possible that there may be more than growth mechanisms influencing the growth process. In such cases one has to consider the nature of the process if they are acting parallel to promote growth rate then their nature is additive and in turn growth rate would increase and the one that gives faster rate is rate determining while if they are consecutive or serial in nature than the overall growth rate decrease and the slowest one will be rate determining.

1.4 Techniques of crystal growth

Crystal growth is basically a process of phase transition where an ordered phase is obtained from a disordered phase either from liquid to solid or vapor to solid. Based on this phenomenon the crystal growth techniques can be classified broadly into three main categories.

- i) *Liquid to Solid*
- ii) *Vapor to Solid*
- iii) *Solid to Solid*

There are various techniques under each of these category.¹⁰ Some of the important techniques are shown in Fig. 1.12.

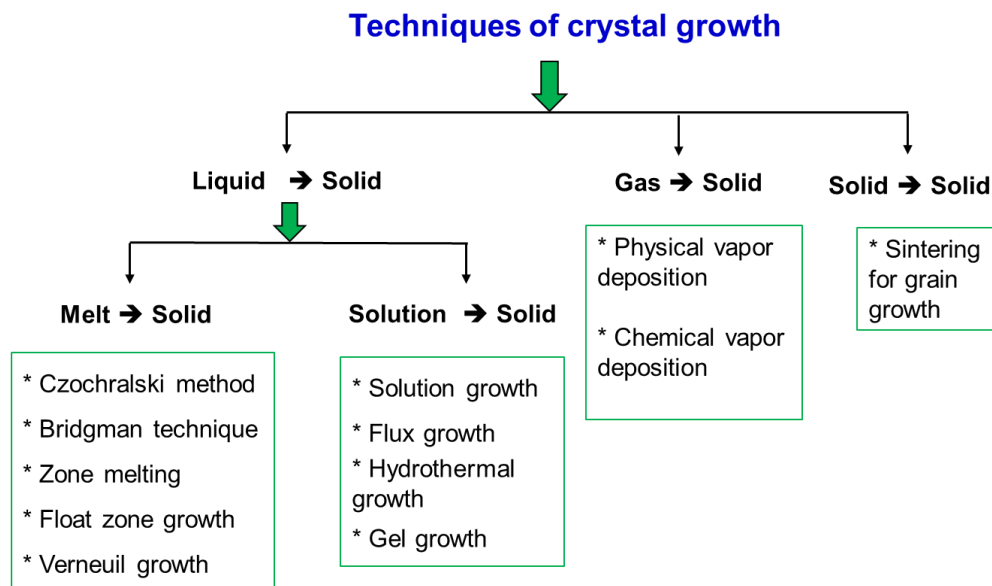


Fig. 1.12 A classification of crystal growth techniques.

Growth of good quality, large size single crystal of a particular material for a particular application requires knowledge of techniques of crystal growth. The selection of a suitable technique depends on the properties of the material. Some of the important and widely used techniques are described below.

1.4.1 Melt growth

It is suitable for those materials which melt congruently or near congruently and show absence of any phase transition below melting point to room temperature. Melt growth is process of crystallization by fusion followed by re-solidification of the pure material.

Temperature plays a very crucial role in case of this technique. This technique is relatively fast compared to solution based techniques because no second component is involved in melt growth but needs high capital input for crystal puller. There are various techniques of crystal growth from melt such as Czochralski technique (CZ), Bridgman or Bridgman-Stockbarger technique, Kyropoulos method, Floating zone technique, flame fusion or Verneuil method, skull melting, laser heated pedestal growth (LHPG) or laser float zone (LFG) etc.^{7,11} The last four techniques belong to container-less techniques, suitable for very high melting compounds. Cz technique also known as crystal pulling method is however the most widely used technique of melt growth described below in detail.

Czochralski method: In this technique material to be crystallized is taken in a crucible made of silica or platinum or iridium depending on the melting point and reactivity of the material and placed in a furnace based on resistive or inductive heating. The furnace temperature is raised slowly to melt the charge completely. The atmosphere in the growth chamber is chosen as per reactivity of the material with ambient. A suitably oriented seed crystal is slowly pulled down employing a crystal puller and touched at top surface of the melt maintained slightly above the melting point of the material. The seed rod is slightly pulled up to maintain a meniscus along with adjustment of temperature. Once the meniscus is formed the seed rod is slowly pulled up with rotation of the seed for necking and shoulder formation. By optimizing the pull rate, rotation rate and temperature single crystal can be grown. Nowadays automatic diameter control (ADC) feature is available with modern crystal pullers which made it easy to maintain constant diameter of the crystal. Many technological important single crystals with large dimensions such as silicon, lithium niobate, Nd:YAG etc. are grown by this technique.

1.4.2 Vapor growth

Vapor growth is particularly suitable for those materials which have high melting point, show appreciable dissociation at the melting point or melts at high pressure. In this technique polycrystalline starting material is sublimed under vacuum or using a suitable carrier gas or the vapor of its constituent and transported to a second region maintained at somewhat lower temperature where it gets deposited at a suitable substrate. Crystal quality is optimised by temperature and pressure gradients between the two regions, transfer rate of the material vapor and characteristics of the carrier gas, if there. There are various

techniques of vapor growth such as sublimation, physical vapor deposition, chemical vapor deposition etc.^{7,12,13} The growth rate and crystal size obtained by vapor growth is relatively low compared to melt growth and solution growth techniques. Vapor phase deposition is a suitable technique for fabrication of high purity epitaxial layers on substrates particular for multilayer deposition of semiconductors preferably by metalorganic chemical vapor deposition (MOCVD), molecular beam epitaxy (MBE) etc. It is also convenient for large-scale operation or to coat irregular shape substrates. Crystalline material like ZnS, ZnSe etc. are prepared on commercial scale by vapor based technique.

1.4.3 Solution growth

This is one of the most widely used technique for growth of large size single crystals. It is suitable for growth of wide range of materials of inorganic, organic, semi-organic, metalorganic complexes. It has tremendous applications in pharmaceuticals, food and fertilizer industry. This is the only technique suitable for growth of protein crystals. Solution growth techniques are simpler compared to melt growth and vapor growth techniques and require relatively lower temperature for operation and cheaper infrastructure. It also provides faceted crystals with full visibility making it possible to carry out growth kinetic or morphological investigations. This technique is particularly suitable for growth of those materials which do not melts congruently or have phase transition near melting temperature. The main requirements are availability of a suitable solvent where it dissolves sufficiently and growth system with high order temperature stability and uniformity.

Solution growth is divided in to two categories based on temperature involved.

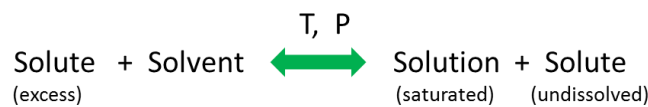
- a) *Low temperature solution growth or simply solution growth*
- b) *High temperature solution growth or flux growth*

The principle of both these techniques are similar. Since this thesis is concerned with low temperature solution growth which is commonly called briefly as solution growth, it is therefore discussed with some details in following sections.

1.4.3.1 Solution, solubility and supersaturation

A solution is defined as a homogeneous mixture of two or more substances. A solution in general may be solid, liquid or gaseous. Our concern for crystal growth is with liquid

solutions which composed of a solute and a solvent. A suitable solvent is one which is able to dissolve solute particles sufficiently. In the case of low temperature solution growth, the commonly used solvents are water, ethanol, methanol, toluene, anisole, carbon tetra chloride etc. Water is the most suitable solvent because it is cheap, stable, non-toxic, having high boiling point, high dielectric constant and low viscosity. Water is a polar solvent and hence most suitable for dissolving polar solutes such as inorganic and semi-organic compounds. While in case of organic compounds usually organic solvents are used. The amount of solute dissolved in 100g solvent is usually termed as concentration of the solution. If a solution contains maximum amount of solute at a given temperature (assuming pressure to be constant equal to the atmosphere pressure, for further discussion) is termed as saturated.



The concentration of a saturated solution is known as its solubility at that temperature. A graph of saturation concentration with temperature is called as solubility curve. Solubility is an important term used in solution crystal growth. Solubility of a given material in general depends on temperature, pressure, nature of solvent, solution pH and presence of impurities if there. Solubility curve in general may have positive, negative or zero temperature coefficient of solubility depending on materials involved. If a solution somehow contains concentration excess to that allowed by its solubility curve is called as supersolubility curve and the solution is called as supersaturated. Fig. 1.13 schematically depicts solubility and supersolubility curves for a material having positive temperature coefficient of solubility.

Fig. 1.13 consists of three important regions:

- i) Stable region: The region up to solubility curve.
- ii) Metastable region: The region in between solubility and supersolubility curves.
- iii) Unstable or labile region: The region above the supersolubility curve.

Supersolubility curve and hence metastable zone width is not fixed, it depends on various conditions such as solution stirring, presence of foreign particle, solution filtration, presence of impurities etc. The curve is therefore depicted as broken line. Metastable region is an important portion of solubility curve where crystal growth takes place. A large width of metastable region is preferable for growth of large size crystal. The region above

the supersolubility curve is unstable and immediately crystallize if one reaches there. However, a solution in metastable state has a certain lifetime before it crystallizes spontaneously. This time is called induction period. The value of supersaturation and induction period have inverse relation. For higher supersaturation induction period will be lower. Ideally we need high supersaturation and high induction period for growth of large size crystals. Due to their inverse relation one has to optimize these two to get large size crystal without nucleation.

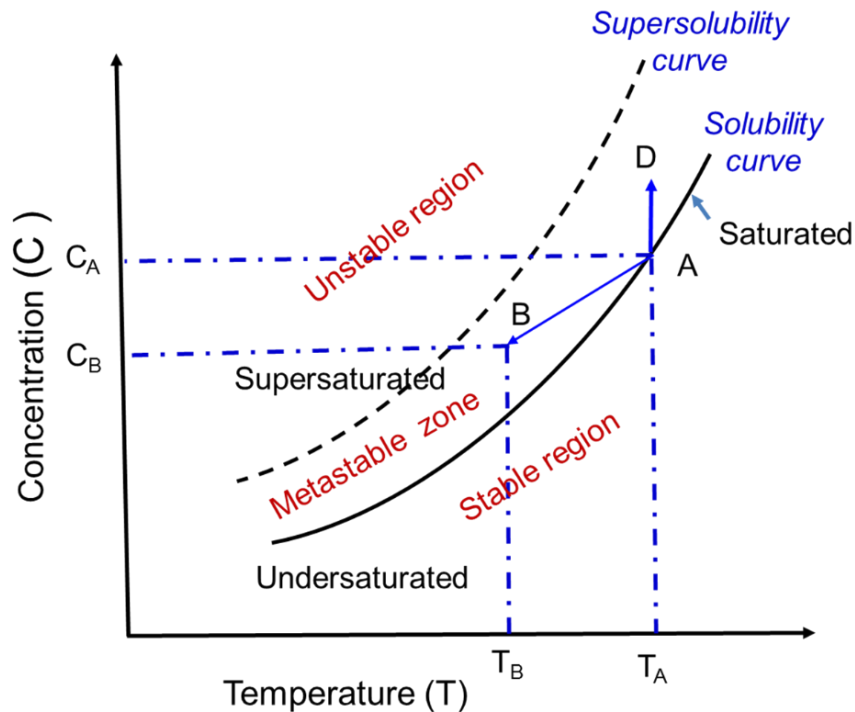


Fig. 1.13 Schematic representation of typical solubility - supersolubility curves.

Methods of achieving supersaturation:

The state of supersaturation is possible to achieve due to presence of free energy barrier as described in the Section 1.3.2. Experimentally supersaturated solution may be created by following methods¹⁴:

- i. Changing temperature (mainly cooling)
- ii. Evaporation of solvent from the solution
- iii. Changing the solvent composition (e. g. salting out)
- iv. Chemical reaction, and
- v. Creating concentration gradient for mass transfer

As discussed in earlier Section 1.3.1, supersaturation is the main driving force for crystallization. Formally, supersaturation (σ) can be defined in terms of the dimensionless difference between chemical potentials of a molecule in saturation state μ_s and that in supersaturated state or say in actual state μ_a of the solute, such that,

$$\sigma = (\mu_a - \mu_s) / RT$$

There are some other simpler ways for expressing supersaturation in terms of concentration. Among the most common expressions for the supersaturation are:

- i) Concentration driving force, $\Delta C = C_a - C_s$
- ii) Supersaturation ratio, $S = C_a / C_s$
- iii) Absolute or relative supersaturation, $\sigma = (C_a - C_s) / C_s = S - 1$
- iv) Percentage supersaturation, $\% \sigma = 100 \sigma$

It is also possible to correlate supersaturation with supercooling of the solution which is the main operational parameter to achieve supersaturation. If solubility varies linearly with temperature for example, $C_s = a + b T$, where a and b are some constants.

In such case,

$$\sigma = (T_a - T_s) / T_s = \Delta T / T_s$$

Where T_a , T_s and ΔT are called actual temperature, saturation temperature and supercooling (or undercooling) respectively.

In case of supersaturated solution prepared by cooling from state A to B in Fig. 1.13,

$$\sigma = (C_A - C_B) / C_B \approx (T_A - T_B) / T_B$$

Methods for solution growth of crystals:

For growth of crystals from solutions, it is required to create supersaturated state of the solution. Depending on the method of achieving supersaturation, some of the prominent methods of crystal growth from solution can be written as,

- a) *Slow cooling method*
- b) *Slow evaporation technique*
- c) *Temperature gradient method or three vessel method*
- d) *Gel method*
- e) *Unidirectional growth technique*

Typical procedure of solution crystal growth:

It involves following steps in sequence.

- i) Preparation of saturated solution →
- ii) Filtration and overheating →
- iii) Seeding →
- iv) Creation of supersaturation →
- v) Crystal growth.

Slow cooling method:

This is the one of the most widely used techniques in solution crystal growth. It is suitable for those materials which dissolve in a solvent preferably water at room temperature with positive temperature coefficient of solubility. Once the solubility curve is determined, the growth procedure involves preparation of saturated solution followed by ultrafine filtration through ultrafine porosity membranes and subsequently overheated to destroy unseen nuclei if there. In this technique supersaturation is created by slow cooling of saturated solution. The solution is prepared in a sealed crystallizer and subsequently placed in a water bath whose temperature is controlled by a programmable PID temperature controller. Seed is normally hanged in the solution or placed on a platform and rotated reversibly for temperature and concentration homogenisation. This method has got a great success for a variety of crystals and for growth of some of very large size crystal of crystals such as KDP and DKDP.

Main limitation of this technique is usage of a certain range of temperature which limits crystallization yield and hence crystal size because some amount of solute remains in the solution at the end of the run. The crystals grown by solution are prone to nucleation and inclusion. In addition, achievement of high growth rates and high usable yield are some another challenges of the solution crystal growth.

Slow evaporation method:

This method is particularly suitable for those materials whose temperature coefficient of solubility is very small, near to zero or negative. In such cases, solution cooling is not sufficient for creation of supersaturation. For these materials solvent evaporation is the suitable method to achieve supersaturation for crystal growth. In such case concentration increases due to evaporation of solvent as depicted by A to D in Fig. 1.13. This technique is however most suitable if the solvent is water because in case of other solvents, evaporation may contaminate the atmosphere. One of the main advantages of this

technique is being growth at a fixed temperature. The main limitation for this technique is unavailability of the control systems for achieving precise control of evaporation rate.

Temperature gradient method or three vessel method:

In this technique the materials to be crystallized is transported from a hot region containing high concentration of solute particles to a region of lower concentration, where the solution gets supersaturated. In this techniques two vessels¹⁵ or three vessels¹⁶⁻¹⁸ can be used. The three vessel method is more suitable for growth of large crystals and is therefore shown schematically in Fig. 1.14. Here a vessel called as “crystallizer” is used for crystal growth, a part of this solution is transferred regularly to the second vessel called as “Saturator”. The saturated solution from this vessel is transferred to the third vessel called as “super-heater” which overheat the solution to make it free from nuclei. This solution is then slowly transferred to the crystallizer where it gets mixed with its solution and compensate the depleted concentration. The main advantages of this method is that (i) Crystal growth takes place at a fixed temperature, (ii) It is almost insensitive to changes in temperature provided both the source and the growing crystal undergo the same change, and (iii) Economy of solvent and solute. However, the main difficulties are its complicates design and need of precise control of temperature difference between source and growth zones which otherwise have a large effect on the growth rate.

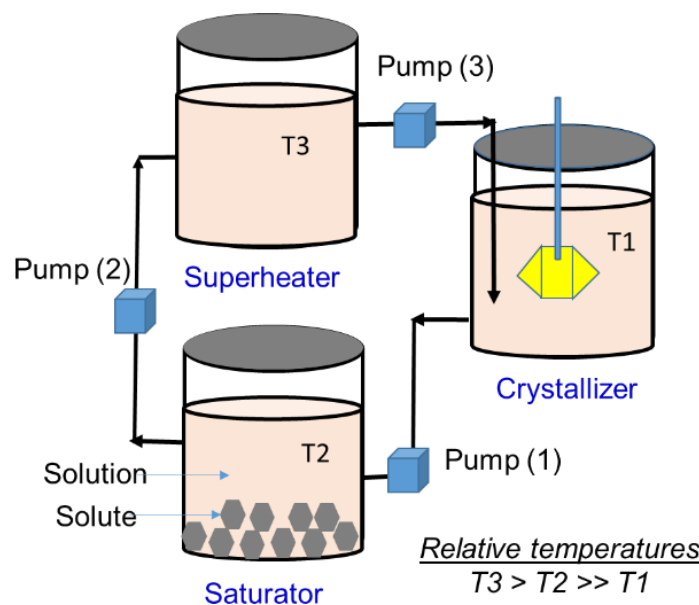


Fig. 1.14 Schematic of three vessel method for solution crystal growth.

1.5 Crystal habit

As-grown crystals from solution acquire a particular shape bounded by plane surfaces. This external shape of crystals is termed as habit or morphology. The change in shape in terms of the relative variation of crystal dimensions along different directions is called as modification of crystal habit. The change in crystal shape or habit is usually quantified in terms of aspect ratio (AR) or habit factor (H) which is defined as the ratio of crystal dimensions along its crystallographic axes. Crystal shape in general depends on relative growth rate of habit faces. Growth morphology is usually determined by the slowest growing faces. The morphological importance of a face is therefore inversely proportional to its growth rate. There are various factors which influence crystal shape that may be classified into three categories,

- i) *Internal factors*
- ii) *External factors*
- iii) *Interfacial structure*

i) Internal factors:

Ordered packing of atoms or molecules in a crystal results into regular shapes of as-grown crystals. They grow as polyhedral bounded with certain planes designated by Miller indices. The symmetry inherent in the shape of the as-grown crystal reflects the underlying packing symmetry of the crystal lattice governed by its point group symmetry. The crystal shape is thus a characteristic of a material's internal structure. Internal parameters normally include point group symmetry and lattice parameters which influence the crystal's rotational symmetry and interfacial angles. The earliest study regarding crystal morphology was made by Steno (1669). As per his law of constancy of interfacial angles, which is also considered as the law of crystal habit: The angles between corresponding habit faces of all crystals of a given material are constant.¹⁹ The crystals may vary in size and the development of the various faces may differ considerably leading to different habit or aspect ratio but the interfacial angles remains constant. Further major impetus to this field was due to works of Haüy (1784). He postulated a relation between material and shape of its crystalline forms. Gibbs (1878) and Curie (1885) described equilibrium shape of crystal based on thermodynamics.²⁰ According to their theory, a crystal growing in

equilibrium would acquire a shape which has the minimum surface energy for a given volume. This may be written for a given crystal volume as,

$$\sum_i \alpha_i A_i = \text{minimum}$$

Where α_i is the specific surface free energy of the i th face of the crystal and A_i is the surface area of that face.

Further, Wulff (1901) described equilibrium shape crystals in terms surface energy of individual faces. He showed that the above criterion is equivalent to,

$$\Sigma(\alpha_i/h_i) = \text{constant}$$

$$\text{Or } \alpha_1 : \alpha_2 : \alpha_3 \dots = h_1 : h_2 : h_3 \dots$$

Where h_i is the central distance of the i th face.

This statement is also known as Wulff theorem or Wulff rule.²⁰ According to it, the equilibrium shape can be constructed by a geometrical procedure:

- i) Consider an arbitrary point in space and draw vectors normal to the possible crystallographic planes.
- ii) The lengths of these vectors should be proportional to their respective surface free energies, and
- iii) Draw planes perpendicular to the tip of these vectors. The polyhedron thus formed would represent its equilibrium shape.

Qualitative methods of prediction of equilibrium shape of crystals were also proposed by many other scientists: Bravais (1866) connected the habit planes with high density lattice planes, Niggli (1919) related habit faces with that having few unsaturated bonds. In 1937 Donnay and Harker proposed that the lowest surface free energy will be for those planes which have highest reticular density and further related growth rate with interplanar spacing d_{hkl} . According to BFDH theory (Bravais, Friedel, Donnay, Harker theory) morphological importance is relatively higher for those planes which have higher interplanar spacing compared to those having lower value. More recently in 1955 Hartman and Perdock explained crystal surfaces in terms of their concept of periodic bond chains (PBC).²¹ A PBC was defined as an uninterrupted chain of strong bonds at the surface in a layer of d_{hkl} . A flat (F) face was defined as to contain at least two different sets of PBC's, while a step (S) face to have one and a kinked (K) face with no PBC.²² Crystal growth was considered due to formation of bonds between crystalizing units with the surface. According to Hartman-Perdock (H-P) theory, growth rate of a flat face is proportional to

its attachment energy.²³ This information can be used to predict morphology using a Wulff plot. Today it is possible to predict possible morphologies of a crystal by knowing its structure. There are many softwares available for this purpose.²⁴

ii) External factors:

Crystal shape or habit is also influenced by relative growth rates of its habit faces. It is evident that fast growing faces usually disappear from the crystal morphology. Therefore, the as-grown crystals are normally bound with slow growing faces. There are a number of external factors²⁵ which influence growth rate of habit faces such as supersaturation,²⁶ temperature, impurities, solution pH²⁷, solution flow dynamics, nature of solvent, seed orientation,²⁸ seed quality etc. By manipulation of these parameters it is possible to change crystal habit. Habit describes the overall type of the shape of a particular crystal. Depending on the external growth conditions, a crystal may grow more rapidly in one direction than the other changing a prismatic habit to platy or to a needle-shaped as shown schematically in Fig. 1.15.

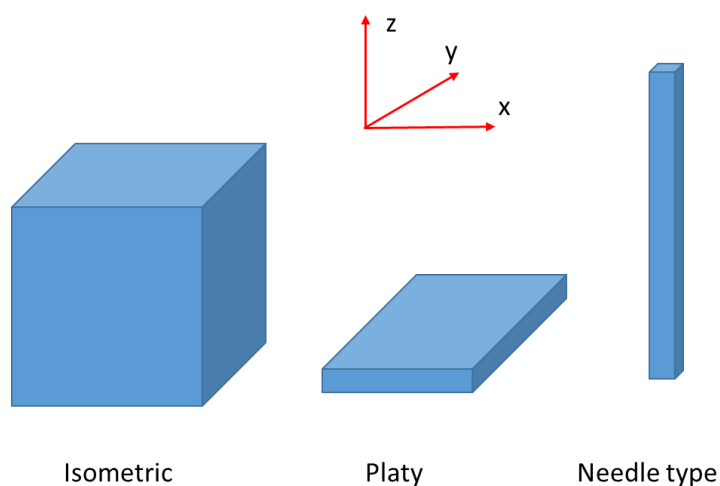


Fig. 1.15 Schematic showing effect of different relative growth rates along different axis leading to change in crystal habit.

iii) Interfacial structure:

Crystal growth takes place at the solid-surrounding media interface in near equilibrium condition. The surface structure of a crystal is in general different for different faces. In case of solution growth, surrounding media also play an important role. Solvent has isotropic nature but is influenced by the structure of surface in contact. The interfacial

structure may be different for different faces and hence influence growth rate and crystal shape. A change of solvent may influence interfacial structure differently leading to different crystal shape.^{29,30} The role played by the solvent to influence interfacial structure and growth rate is still not solved completely. It is because solvent may enhance or reduce growth rate of a particular face depending on its interaction with crystal surface. If the solvent molecules reduce interfacial energy, the surface may be rough and hence fast growth rate. On the other hand, if the solvent strongly interacts and hence adsorbed at the surface the growth rate will be reduced.

The above three factors essentially decide equilibrium crystal habit however it is difficult to eliminate certain face or to obtain some other face by using these factors. Moreover, actual crystal growth takes place usually in non-equilibrium conditions. For several device applications for example in case of laser frequency converters the crystal plate should be prepared with faces normal to phase matching direction which may not be either parallel or perpendicular to any of the crystal faces. In such cases one has to cut the crystal to prepare device elements. This leads to wastage of crystal volume. To solve such problems another method of shape modification is gaining interest in the field of solution crystal growth. It is based on the usage of mechanical constraints or mechanical shapers to alter crystal shape during growth. The shaped growth of crystals with the help of mechanical constraints is quite well established in case of melt growth of crystals,^{31,32} while investigated a little in case of solution growth. This thesis is mainly devoted for investigation of shape modification techniques for a few important solution grown crystals to enhance usable volume fraction. The following section is therefore describing a survey of existing shape modification techniques in solution crystal growth.

1.6 Shape modification techniques in solution crystal growth

Shape modification is an important aspect of crystal growth particularly to obtain specific shape, size or orientated element which not only save the duration of crystal growth but also reduce processing time. Moreover, it also enhances usable volume fraction for device elements which in turn helpful to reduce the size of the crystal growth systems. Shape modification techniques are well developed in case of melt growth where mechanical guides have been used to obtain rod shape, fiber shape, cylindrical shape or platy shape crystals using Cz technique^{33,34} Stepanov had done pioneering work in this field and proposed a technique known as Stepanov's method.³⁵ Another technique named as EFG (

Edge-defined film-fed growth) was invented by LaBelle for shaped growth of crystals from melt.^{36,37} Tatartchenko has compiled different techniques of shape modification for melt growth of crystals.³⁸

While in case of solution growth it has been difficult to insert some foreign item or structure during growth because it may lead to formation of unwanted nucleation. However, several researchers investigated this issue and developed various approaches based on mechanical barriers to alter crystal shape as per requirement or to enhance usable volume fraction. A survey was conducted showing that the available shape modification techniques based on mechanical barriers may be classified in to following three categories as shown in Fig. 1.16.

Shape modification techniques based on mechanical barriers

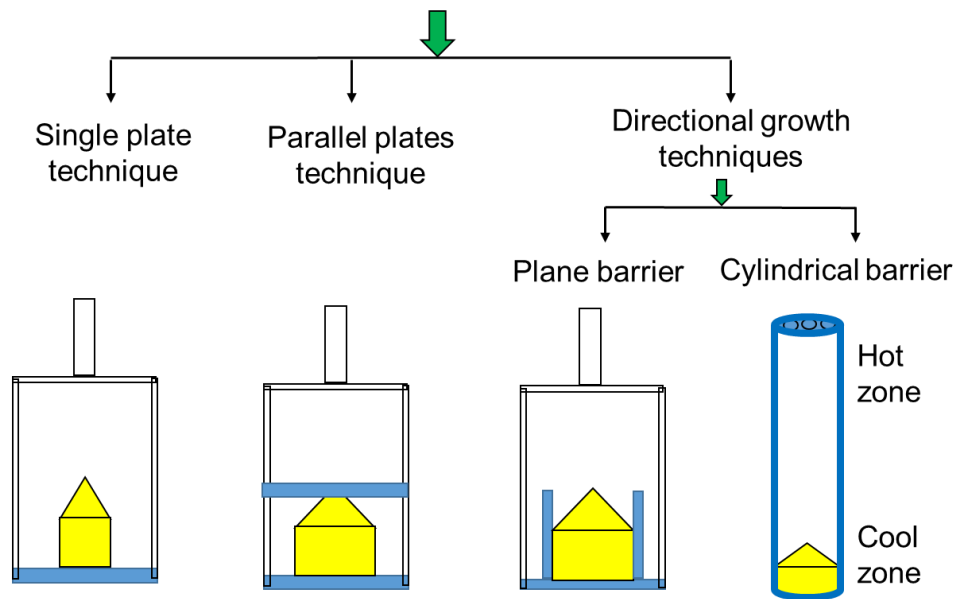


Fig. 1.16 Schematic depiction of shape modification techniques based on mechanical barriers for growth of crystals from solution (light blue shade show barriers while yellow shade show crystal).

In case of **single plate technique**, a horizontal plate is used to mount seed crystal, thereby growth of one half of the crystal is restricted. This technique has been useful to change aspect ratio of crystals. This is one of the main techniques for rapid growth of large size KDP crystals pioneered by Zaitseva et al.^{39,40}

Parallel plate technique was developed to limit growth along two directions of crystals. This technique has been useful to change aspect ratio for those crystals which grow faster

along one direction. In this technique two parallel plates are used and seed crystal is placed in between them to limit growth normal to the plates. This method thus restricts height of the crystals to a certain value while lateral growth is free making crystal to enlarge in cross section. This technique was used by Zeng et al.⁴¹ for Urea crystal and, Tatartchenko et al.⁴² and Tu et al.⁴³ for KDP crystal growth.

Directional growth technique allows to proceed crystal only along one direction by imposing restriction at all other remaining sides. This technique is suitable to obtain single crystal elements of constant cross section or diameter. Bepalov et al. used it to grow SHG oriented KDP crystal in square shape cavity.⁴⁴ An another variant of this technique was introduced by Genbo et al.⁴⁵ and Ramasamy group⁴⁶ where all the sides were restricted using cylindrical glass tube. This technique is suitable to obtain cylindrical shape crystals along a particular orientation.

1.7 Selected materials and motivation

Single crystals are required for a wide variety of applications in the field of solid state lasers, non-linear optics, radiation detectors, monochromators, integrated optics, optical data storage etc. Laser frequency conversion is one of the important phenomena of non-linear optics widely used for generation of radiation at frequencies where other sources of coherent radiation are not available. In this context non-centrosymmetric single crystals are of particular interest as these are capable of producing second order non-linear optical (NLO) effects such as second harmonic generation (SHG). There are a large number of such materials but only a few are suitable for actual practical applications because apart from being non-centrosymmetric there are many other requirements for a material to be suitable for SHG applications.^{47,48} These include,⁴⁹

- i) High second order nonlinear optical coefficient,
- ii) Wide phase matchable range preferably with non-critical phase matching,
- iii) Wide transmission band with low absorbance at the concerned frequencies,
- iv) Large value of laser - induced damage threshold,
- v) High figure of merit for SHG,
- vi) Large values of bandwidth for angular acceptance, temperature acceptance and frequency acceptance.

There are many crystals having these properties but no one is ideal with respect to all these characteristics. From commercial as well as experimental point of view there are certain

more criteria to select a particular crystal for growth. This includes following characteristics:

- i) Ease in growth up to large size,
- ii) High stability in the ambient conditions,
- iii) Non-hygroscopic,
- iv) Ease in processing for devices,
- v) Low cost of growth units,
- vi) High growth rate of the crystal,
- vii) Non-toxic solvent preferably water,
- viii) Visibility of the growth process for monitoring during growth.

This thesis describes the work carried out to address some important issues related to growth and utilization of three important non-centrosymmetric crystals namely potassium dihydrogen phosphate (KDP), L-arginine phosphate monohydrate (LAP) and zinc cadmium thiocyanate (ZCTC). These crystals are grown by aqueous solution growth.

KDP is a well-known NLO material, widely used for second harmonic generation of high power lasers mainly because of ease with which large size crystals of good optical quality can be grown.^{17, 50} However, one important limitation is that its natural growth morphology greatly limits the size of the device element such as second harmonic conversion element. We have investigated shape modification techniques for KDP crystal growth with a view to modify the crystal shape in a manner that helps in obtaining large size device element.

L-arginine phosphate monohydrate (LAP) crystal is of interest because, it has a factor of 1.9 higher NLO coefficient and a factor of ~2 higher laser-induced damage threshold compared to KDP.^{51,52} However, a major drawback with LAP is the large growth asymmetry along crystallographic axes leading to a morphology which results in low usable volume fraction for device elements. Possible approaches to reduce the growth anisotropy of LAP was another objective for the present thesis.

Zinc cadmium thiocyanate (ZCTC) is relatively new material having very large NLO coefficient comparable with the best available melt grown crystals such as potassium titanyl phosphate (KTP), lithium tri borate (LBO) etc.^{53,54} The main difficulty with this crystal is very low growth rate of its habit faces because of which it becomes difficult to grow good optical quality crystals. The solubility of this material varies slowly with

temperature therefore a crystallizer based on solvent evaporation was developed as part of the research work. The crystals were grown using this crystallizer and characterized to assess its optical and structural quality to test its suitability for device applications.

References:

- ¹ H. J. Scheel, Historical introduction, Chapter 1, in: "Handbook of Crystal Growth 1, Fundamentals, Part A: Thermodynamics and Kinetics", D. T. J. Hurle (Ed.), Elsevier Science Publishers, North-Holland, Amsterdam, 1993.
- ² K. Nassau, "Gems Made by Man", Chilton Book Company Radnor, Pennsylvania, 1980.
- ³ T. Hahn (Ed.), "International Tables for Crystallography, Vol. A", Springer, Netherlands 2005.
- ⁴ D. Schwarzenbach, "Crystallography", John Wiley & Sons, Chichester, UK, 1997.
- ⁵ J. W. Mullin, "Crystallization", 4th Edition, Butterworth-Heinemann, 2001.
- ⁶ R. Boistelle, J. P. Astier, *J. Cryst. Growth*, 90 (1988) 14-30.
- ⁷ P. SanthanaRaghavan, P. Ramasany, "Crystal Growth Processes and Methods", KRU Publications, Kumbakonam, Chennai, India.
- ⁸ P. Hartman, Structure and morphology, in: P. Hartman (Ed.) "Crystal Growth: An Introduction", North Holland Publ. Co. Amsterdam, 1973, pp. 367-402.
- ⁹ W. K. Burton, N. Cabrera, F. C. Frank, *Phil. Trans. Roy. Soc. London Ser. A*, 243 (1951) 299-358.
- ¹⁰ B. R. Pamplin, *Prog. Crystal Growth Charact.*, 1 (1977) 5-22.
- ¹¹ G. J. Sloan, A. R. McGhie, "Techniques of Melt Crystallization", John Wiley & Sons. New York, 1986.
- ¹² J. C. Brice, Chapter 9 and 10, in: "Crystal Growth Processes", John Wiley & Sons, New York, 1986.
- ¹³ A. A. Chernov, Crystal growth from the vapor phase, Chapter 8 in: "Modern Crystallography III: Crystal Growth", Springer-Verlag, Berlin Heidelberg, 1984, pp. 298-351.
- ¹⁴ A. S. Myerson, A. F. Izmailov, The structure of supersaturated solutions, Chapter 5, in: "Handbook of Crystal Growth 1, Fundamentals, Vol. 1, Part A: Thermodynamics and Kinetics", D. T. J. Hurle (Ed.), Elsevier Science Publishers, North-Holland, Amsterdam, 1993.

- ¹⁵ R. S. Feigelson, *J. Cryst. Growth*, 90 (1988) 1-13.
- ¹⁶ G. M. Loiacono, J. J. Zola, G. Kostecky, *J. Cryst. Growth*, 62 (1983) 545-556.
- ¹⁷ T. Sasaki, A. Yokotani, *J. Cryst. Growth*, 99 (1990) 820-826.
- ¹⁸ N. P. Zaitseva, J. J. de Yoreo, M. R. Dehaven, R. I. Vital, L. M. Carman, H. R. Spears, *Proc. SPIE*, 3027 (1997) 404-414.
- ¹⁹ B. S. Vainshtein, Crystalline state, Chapter 1 in: “Fundamentals of Crystals”, Springer-Verlag, Berlin Heidelberg, 1994, pp. 1-24.
- ²⁰ I. V. Markov, “Crystal Growth for Beginners: Fundamentals of Nucleation, Crystal Growth, and Epitaxy”, World Scientific, Singapore, 1998, pp. 13-15.
- ²¹ P. Hartman, Modern PBC theory, Chapter 4, in: “Morphology of Crystals, Part A”, I. Sunagawa (Ed.), Terra Scientific Publishing Co., Tokyo, 1987, pp. 269-319
- ²² I. Sunagawa, “Crystals, Growth Morphology and Perfection”, Cambridge University Press, Cambridge, 2005, pp. 60-68.
- ²³ P. Hartman, P. Bennema, *J. Cryst. Growth*, 49 (1980) 145-156.
- ²⁴ Eric Dowty, Shape Software, 521 Hidden Valley Road, Kingsport, TN 37663.
- ²⁵ I. Sunagawa, Morphology of minerals, Chapter 7 in: “Morphology of Crystals, Part B”, I. Sunagawa (Ed.), Terra Scientific Publishing Co., Tokyo, 1987, pp. 509-587.
- ²⁶ S. K. Sharma, Sunil Verma, B. B. Shrivastava, V. K. Wadhawan, *J. Cryst. Growth*, 44 (2002) 342-348.
- ²⁷ L.N. Rashkovich, G.T. Moldazhanova, *J. Cryst. Growth*, 151 (1995) 145-152.
- ²⁸ S. Satapathy, S. K. Sharma, A. K. Karnal and V. K. Wadhawan, *J. Cryst. Growth*, 240 (2002) 196-202.
- ²⁹ X. Y. Liu, P. Bennema, Growth morphology of crystals and the influence of fluid phase, in: “Crystal Growth of Organic Materials”, A. S. Myerson, D. A. Green, P. Meenan (Eds.), American Chemical Society, Washington, 1995, pp. 36-42.
- ³⁰ M. K. Singh, S. K. Sharma, Arup Banerjee, *CrystEngComm* 15 (2013) 8493-8503.
- ³¹ V. A. Tatarchenko, Shaped crystal growth, Chapter 16, in: “Handbook of Crystal Growth 1, Fundamentals, Vol. 2, Part B: Thermodynamics and Kinetics”, D. T. J. Hurle (Ed.), Elsevier Science Publishers, North-Holland, Amsterdam, 1993.
- ³² V. N. Kurlov, *J. Cryst. Growth*, 179 (1997) 168-174.
- ³³ L. Lytvynov, Shaped sapphire production, Chapter 22, in: “Crystal Growth Technology”, H. J. Scheel and T. Fukuda (Eds.), John Wiley & Sons, West Sussex, England, 2003.

- ³⁴ V. N. Kurlov, S. N. Rossolenko, N. V. Abrosimov, K. Lebbou, Shaped crystal growth, Chapter 5, in: “Crystal Growth Processes Based on Capillarity: Czochralski, Floating Zone, Shaping and Crucible Techniques”, T. Duffer (Ed.), John Wiley and Sons Ltd, 2010, pp. 277-354.
- ³⁵ P. I. Antonov, V. N. Kurlov, Crystallography Reports, Vol. 47, Suppl. 2 (2002), pp. S43-S52.
- ³⁶ H. E. LaBelle Jr., Mat. Res. Bull., 6 (1971) 581-590.
- ³⁷ H. E. LaBelle Jr., J. Cryst. Growth, 50 (1980) 8-17.
- ³⁸ Y. A. Tatartchenko, Shaped Crystal Growth, Kluwer Academic Publishers, Dordrecht, The Netherlands, 1993.
- ³⁹ N. P. Zaitseva, L. N. Rashkovich, S. V. Bogatyreva, J. Cryst. Growth, 148 (1995) 276-282.
- ⁴⁰ N. Zaitseva, L. Carman, I. Smolsky, J. Cryst. Growth, 241 (2002) 363-373.
- ⁴¹ L. Zheng, M. Zha, M. Ardoino, P. Franzosi, L. Zanotti, G. Zuccalli, C. Paoriei, J. Cryst. Growth, 166 (1996) 528-532.
- ⁴² V. Tatartchenko, E. Beriot, Proc. SPIE, 3482 (1999) 386-390.
- ⁴³ H. Tu, Y. Zhao, Y. Yue, F. Fan, Z. Hu, CrystEngComm, 17 (2015) 6669-6673.
- ⁴⁴ V. I. Bespalov, J. Nonlinear Opt. Phys. and Mater., 4 (1997) 467.
- ⁴⁵ S. Genbo, H. Youping, L. Zhengdong, J. Rihong, Z. Changwu, Y. Shangfeng, J. Cryst. Growth, 213 (2000) 99-102.
- ⁴⁶ K. Shankaranarayanan, P. Ramasamy, J. Cryst. Growth, 280 (2005) 467-473.
- ⁴⁷ P. F. Bordui, M. M. Fejer, Inorganic crystals for nonlinear optical frequency conversion, in: “Annual Review of Materials Science”, Vol. 23, Annual Reviews Inc., California, 1993, pp. 321-379.
- ⁴⁸ J. T. Lin, A critical review of high-efficiency crystals for tunable lasers, in: “Proceedings of the Topical Meeting on Laser Materials and Laser Spectroscopy”, W. Zhijiang and Z. Zhiming (Eds.), World Scientific, Singapore, 1988, pp. 66-70.
- ⁴⁹ H. S. Nalwa, T. Watanabe, S. Miyata, Organic materials for second-harmonic generation, Chapter 4, in: “Nonlinear Optics of Organic Molecules and Polymers”, H. S. Nalwa and S. Miyata (Eds.), CRC Press, Tokyo, 1997, pp.89-329.
- ⁵⁰ N. P. Zaitseva, J. J. De Yoreo, M. R. Dehaven, R. L. Vital, K. E. Montgomery, M. Richardson, L. J. Atherton, J. Cryst. Growth, 180 (1997) 255-262.
- ⁵¹ A. Yokotani, T. Sasaki, K. Yoshida, S. Nakai, Appl. Phys. Lett., 55 (1989) 2692- 2993.

⁵² D. Eimerl, S. Velsko, L. Davis, F. Wang, G. Loiacono, G. Kennedy, *J. Quantum Electronics*, 25 (1989) 179-193.

⁵³ X. Wang, D. Xu, M. Lu, D. Yuan, G. Zhang, S. Xu, S. Guo, X. Jiang, J. Liu, C. Song, Q. Ren, J. Huang, Y. Tian, *Mater. Res. Bull.*, 38 (2003) 1269-1280.

⁵⁴ C. Feng, G. Lu, X. Wang, P. Zhang, G. Zhou, H. Yang, Y. Jiao, *Phys. Status Solidi B*, 248, No. 6 (2011) 1483-1489.

Chapter 2 Characterization techniques used for crystals

2.1 Introduction

Crystal growth of a material is usually carried out for obtaining good quality single crystals for desired application. It is therefore important to assess its quality for the intended application and to analyse the parameters which influence it. This activity is called as characterization and is normally done after crystal growth. It involves determination of its structure and assessment of chemical and physical perfection and measurement of physical properties particularly those related to its application.^{1,2} It also includes investigation of structural defects and their influence on various physical properties of the crystal. This thesis is related to growth of single crystals for NLO applications. This chapter is therefore involving a brief account of the characterization techniques used for the assessment of the grown crystals for crystal structure, structural perfection, chemical impurities, molecular structure, defects structure and density, optical quality, second harmonic generation, laser-induced damage threshold and thermal stability of the grown crystals.

2.2 Characterization techniques used for crystalline materials under study

Characterization is a very important step not only to assess the quality of the grown crystal but also helps in identifying new materials. The grown crystals were characterized using various techniques, it includes

- i) Powder X-ray diffraction for phase identification,
- ii) High resolution X-ray diffraction for assessment of crystalline perfection,
- iii) X-ray diffraction topography for assessment of defect structure,
- iv) Chemical etching for dislocation defects distribution and their density,
- v) UV-Vis-NIR transmission spectroscopy for optical transmittance,
- vi) Mach-Zehnder interferometry for assessment of optical homogeneity,
- vii) Birefringence interferometry for birefringence homogeneity,
- viii) Second harmonic generation for device applications,
- ix) Laser-induced damage threshold for material strength against laser intensity,
- x) X-ray fluorescence for chemical purity/ impurities concentration,

- xi) Fourier transform infrared spectroscopy for identification of molecular functional groups,
- xii) Differential scanning calorimetry for assessment of thermal stability.

A brief outline of these techniques along with their working principle is described in the following section.

2.2.1 X-ray diffraction

X-rays are electromagnetic waves discovered by Roentgen in 1895. These are mainly produced by bombardment of high energy electrons at some metal target due to removal of inner electrons from the atom. The wavelength of most of the characteristic X-rays emitted from the excited atoms lies in the wavelength range of 0.1 to 10 nm which is shorter than the wavelengths of vacuum ultra violet region of spectrum. X-ray diffraction is one of very important phenomenon widely used for structural characterization of materials. The diffraction of X-rays by crystalline materials was first observed by Max Von Laue in 1912. Within a year of this observation W. H. Bragg and W. L. Bragg successfully explained this phenomenon and given a simple formula widely known as “Bragg’s law”.³ This was derived considering interaction of X-rays with each atom of crystal lattice which in turn scatter the beam at every direction. The scattered waves superpose and in turn gives intense diffracted beams at certain directions due to constructive interference while the other directions do not get any diffracted beam due to destructive interference.

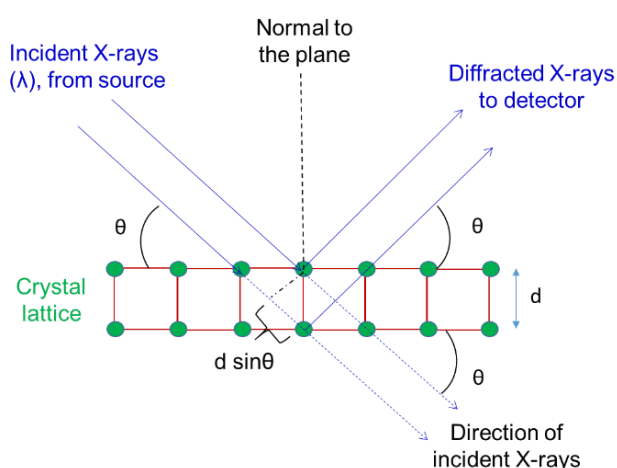


Fig. 2.1 Schematic for derivation of Bragg’s law of X-ray diffraction by constructive interference of the beams diffracted from parallel planes of crystal spaced by distance d .

Fig. 2.1 shows schematic representation of X-ray diffraction from crystal planes from which Bragg's condition can be derived. If the wavelength of incident X-rays is λ and the interplanar spacing is d , the condition of constructive interference gives a relation,

$$2d\sin\theta = n\lambda \quad \dots \quad (2.1)$$

Which is known as Bragg's law for X-ray diffraction. Here n is the order of diffraction. Bragg's law has an important place in the field of characterizations of materials.

The two other characterization techniques mentioned in the Fig. 2.2 are discussed in the next two sections in this chapter.

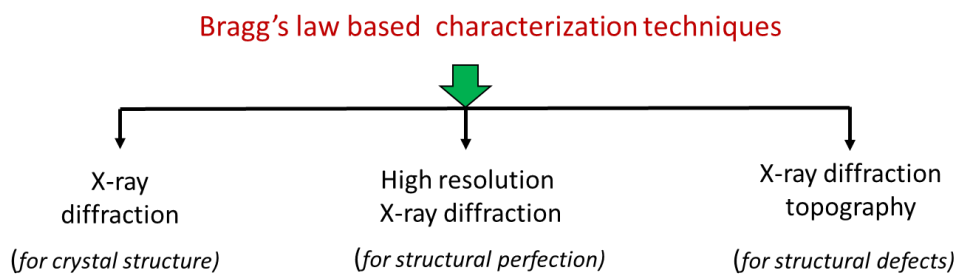


Fig. 2.2 Characterization techniques based on Bragg's law of X-ray diffraction.

Since a crystal can be considered in term of different sets of planes differing in orientation and d-spacing. These planes therefore diffract the incident X-ray beam at different angles. Hence diffraction pattern of a crystal shows discrete diffraction spots. For a given set of planes say (hkl) , if the first order diffracted X-rays are obtained at angle θ_{hkl} . Eq. 2.1 can be written as,

$$2d_{hkl} \sin\theta_{hkl} = \lambda \quad \dots \quad (2.2)$$

Since the interplanar spacing d_{hkl} depends on unit cell parameters $(a, b, c, \alpha, \beta, \gamma)$, therefore diffraction angle θ_{hkl} can be correlated with lattice parameters.⁴ Eq. 2.2 also shows that to get such diffraction, wavelength should be of the order of lattice parameter, which is met by X-rays.

Depending on the nature of crystalline sample and the geometry of measurement, X-ray diffraction methods have been classified as,^{3,5}

1. **Laue method of X-ray diffraction:** In this technique a beam of continuous wavelength radiation is shined at a fixed single crystal sample and the diffracted

spots are obtained on a broad screen. Each spot belongs to a particular set of plane satisfying the Bragg's law. This method is good for identification of crystal axes and symmetry but relatively poor for defects analysis.

2. ***Rotating-crystal method of X-ray diffraction:*** In this method monochromatic and collimated X-ray is used to shine at a single crystal mounted in particular orientation with respect to its crystallographic axes and the diffraction spots are obtained at a cylindrical detector with rotation of the crystal about the axes. The spots obtained at the screen are analysed as per Bragg's law and d-spacing of the crystal planes are calculated.
3. ***Powder method of X-ray diffraction:*** This method is simpler than the above two as it does not require single crystal for measurements. Here a monochromatic and collimated X-ray beam is used to interact powder of the crystalline material placed in the form of film or plane compressed sheet. There are thousands of small crystallites in the powder oriented in all the directions. It gives possibility of presence of every plane of the crystal to interact with X-rays. In this method the direction of X-ray beam is kept fixed and the sample and detector are rotated in steps in such a way that the angle made by diffracted beam towards detector be double to that made by incident beam with sample surface. This geometry is known as $(\theta, 2\theta)$ configuration for X-ray diffraction.

We have used the powder method of X-ray diffraction for structural characterization of our samples. The instrument used to measure X-ray diffraction is called X-ray diffractometer. There are various companies which make such instruments. We have used Rigaku make X-ray diffractometer for the purpose where the wavelength of the X-rays is copper k-alpha line. During the experiment diffraction intensities are automatically recorded by a detector with respect to its angular position (2θ) and displayed in the form of 2θ versus intensity. It shows discrete and sharp peaks corresponding to different set of planes which diffracted the X-rays as per Bragg's law. The peak positions are used to determine lattice parameters while peak intensities are used to determine positions of atoms in the unit cell. It is to note that it is not possible in general to get diffraction from each set of planes because of extinction conditions which mainly depend on type of Bravais lattice and presence of screw axis or glide planes.^{3,6}

The intensity of diffraction peaks is not uniform. It depends on following factors

- i) Structure factor,
- ii) Polarization factor,
- iii) Multiplicity factor,
- iv) Lorentz factor,
- v) Absorption factor,
- vi) Temperature factor, and
- vii) Preferred orientation.

The details about these factors is beyond the scope of this thesis. It is readily available in the literature.^{2,6,7} There are various softwares available to determine lattice parameters from the powder diffraction pattern. Powder X-ray diffraction is a non-destructive technique and gives unique diffraction pattern for a crystalline material which can be considered like fingerprint for its phase identification. There is a database of standard patterns of different crystalline materials prepared by International Centre for Diffraction Data (ICDD) earlier known as Joint Committee on Powder Diffraction Standards (JCPDS).

Powder X-ray diffraction in general a suitable technique to obtain following information of the sample under investigations,⁸

- i) To distinguish crystalline or amorphous nature of the material,
- ii) Lattice parameters determination,
- iii) Phase analysis,
- iv) Particle size from peak broadening,
- v) To study residual stress- strain inside the sample,
- vi) To determine thermal expansion coefficients,
- vii) Time resolved studies.

2.2.2 High resolution X-ray diffraction

The powder X-ray diffraction method is suitable for identification of crystal structure in terms of lattice parameters and position of atoms inside unit cell however there is a little information regarding how perfect is the ordering of lattice plane in general. The information can be obtained using basic principle of X-ray diffraction. The technique used to determine perfection of the ordering of lattice planes is called as high resolution X-ray diffraction (HRXRD).^{9,10} In this technique a highly monochromatic and collimated X-ray

beam is used to get diffraction under $(\theta, 2\theta)$ configuration and a detector is used to record the intensity of the diffracted beam. The single crystal sample under study is first oriented to get diffraction signal from a particular set of Bragg planes (θ_B) and then optimised the parameters for maximum signal intensity. From this orientation the crystal is rotated (or rocked) in very fine angular steps and diffracted intensity is recorded keeping the source and detector at fixed position. The resulting angle θ versus intensity curve is called a rocking curve or a diffraction curve. The full width of half maxima (FWHM) of this curve is a measure of the perfection of the crystal planes. A low value of FWHM indicates good crystalline perfection. If there are multiple peaks or asymmetric nature of peak indicates lattice defects in the sample due to lattice distortions caused by physical defects or impurities.

The main requirements for HRXRD set up are,

- i. Highly monochromatic X-rays,
- ii. Highly collimated X-rays, and
- iii. A goniometer with facility of very fine angular variation.

Depending upon the method used to achieve high order monochromaticity and collimation, the HRXRD set up may be called as based on double crystal, triple crystal, four crystal or five crystal diffractometers.^{11,12} Higher number of crystals are more suitable to increase resolution of the X-ray beams exploring the defects at the sample however it reduces the beam intensity. High quality single crystals of materials such as silicon or germanium are normally used for this purpose. Fig. 2.3 shows schematic of a typical double crystal diffractometer for HRXRD. It comprises a double-crystal monochromator based on double Bragg reflections and is made using two similar crystals.

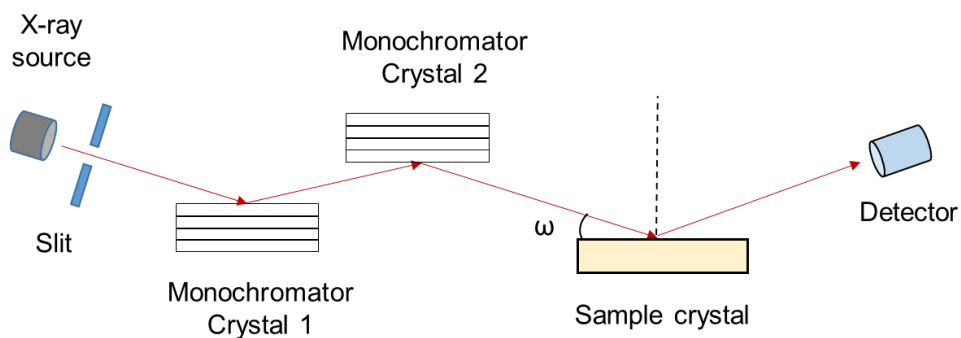


Fig. 2.3 Schematic of double crystal diffractometer for HRXRD.

There are three types of rocking scans possible:

- i. **Rocking scan or ω scan:** In this scan the crystal is rotated such that only the angle ω changes keeping source and the detector at fixed positions.
- ii. **Detector scan or 2θ scan:** In this scan source and sample are kept fixed and the detector is moved.
- iii. **Mixed scan or ω - 2θ scan:** In this scan source is kept fixed but both crystal and detector are rotated.

We have carried out rocking scan for our studies at the HRXRD facility at National Physical Laboratory, New Delhi. The rocking scan is normally used for assessing crystalline perfection of single crystals. HRXRD is useful to obtain information about stress or strain, low angle grain boundaries, lattice distortion and radius of curvature of the planes. This technique is also useful for defects analysis of crystalline thin films.

2.2.3 X-ray diffraction topography

X-ray diffraction topography is a non-destructive technique based on Bragg's law of X-ray diffraction for imaging defects at planes of single crystals. Defects or imperfection are those regions (may be small or large) of a crystal which deviates from regular periodic arrangement of its atoms or molecules. Investigation of defects and their distribution is an important part of characterization of single crystals because they influence various properties such as optical absorption, mechanical strength, electrical conductivity, laser damage threshold, luminescence etc. This study also helps in investigating the origin of defects and to establish its relation with growth history. A crystal in general may contain various types of defects which are usually classified as per their dimensions as:

- i. **Point defects or 0-dimensional defects:** such as vacancies, interstitials, substitutional presence of impurity atoms.
- ii. **Line defects or 1-dimensional defects:** such as dislocations.
- iii. **Surface defects or 2-dimensional defects:** such as growth sector boundaries, growth striations, low angle grain boundaries, stacking faults, cracks etc.
- iv. **Volume defects or 3-dimensional defects:** like inclusions, clusters of impurities, presence of second phase etc.

There are various techniques to identify crystal defects but the X-ray diffraction topography is one of the most versatile. It is based on the difference between diffracting

power of x-rays by perfect and imperfect or distorted part of the crystal as shown in Fig. 2.4. A slight mismatch of the orientation of lattice plane even though having same d_{hkl} corresponds to variation in contrast at the detector. Similarly, a small variation in lattice parameters in neighbouring regions will also be reflected in terms of change in diffracted intensity at the detector because of corresponding change in angle of diffraction. These features make the X-ray diffraction topography a suitable technique to study a wide variety of crystalline defects such as lattice strain, dislocations, growth sector boundaries, growth striations, stacking faults, cracks, inclusions or precipitates, phase boundaries, grain boundaries etc. An assessment of change in diffraction angle due to a change in interplanar spacing can be made by differentiating Bragg's law given in equation (2.1). Considering highly monochromatic X-ray beam, it gives

$$\Delta\theta = -(\Delta d/d)\tan\theta \quad \dots (2.3)$$

This is an important formula relating the observed change in diffraction angle with structural change in the crystal sample.

There are a variety of techniques for X-ray topography based on X-rays which may be classified as,^{13,14}

1. *Transmission topography or Lang method,*
2. *Reflection topography or Berg-Barrett method,*
3. *Section topography,*
4. *Double crystal topography,*
5. *Anomalous transmission or Borrmann method, and*
6. *White beam topography using synchrotron radiation*

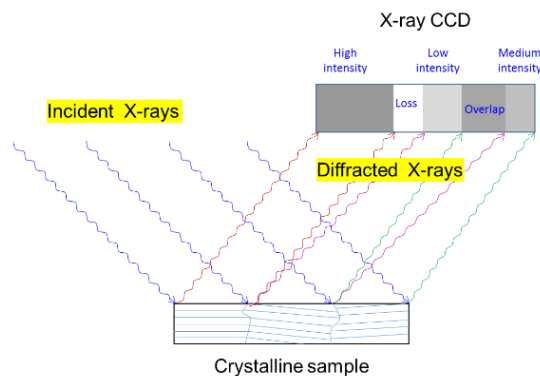


Fig. 2.4 Origin of contrast in X-ray topograph due to misorientation of nearby lattice planes.

We used a digital X-ray reflection topography system made by M/s Jordan Valley as shown in Fig. 2.5 (a). It comprises a micro-focus X-ray source with copper anode, a goniometer, a sample stage, and an X-ray CCD detector. The sample under study is mounted at the sample stage which can accommodate a sample of diameter up to 200 mm. The sample stage along with crystal is capable of translational motion along x, y, and z axis and rotational motion about the normal to the stage (ϕ) and the angle between beam direction and the stage surface, ω as shown in the Fig. 2.5 (b). The width of X-ray beam is 0.1 mm in the diffraction plane while the width normal to this plane is up to 12 mm which can be reduced using a slit depending on the dimensions of the sample under investigation. The direction of X-ray beam from the source aiming towards the sample stage is fixed irrespective of the orientation of sample stage. Therefore, the Bragg condition for a particular set of diffraction plane is achieved by rotation of ϕ and ω angle of the goniometer. The orientation of CCD detector can also be adjusted by x, y, z motions relative to the sample stage to get the diffracted beam. Once the sample is oriented for a particular set of Bragg planes, the X-ray beam automatically scans the sample and generated series of images which are stitched to form stripes these stripes are assembled by a tiling software to generate full topograph of the diffraction plane under study.

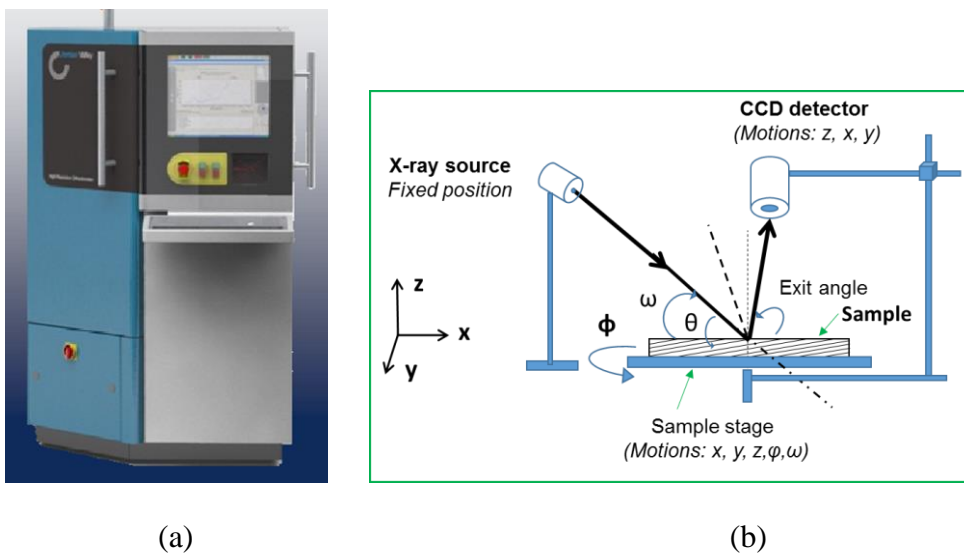


Fig. 2.5 (a) Jordan Valley make digital X-ray topography system, and (b) schematic representation of its working principle.

Sample preparation is also an important part to correctly reveal the defect structure by X-ray topography. To avoid the unwanted features of surface scratches due to polishing

errors, normally mild etching of the crystal surface is done to reduce these features so that actual information of the lattice defects could be obtained. The X-ray topography is a direct imaging system its spatial resolution is of the order of $\sim 10 \mu\text{m}$. A perfect crystal produces a uniformly intense topograph while lattice non-uniformities are reflected in term intensity contrast at the topograph. X-ray topography is suitable to obtain following information of crystalline imperfections: dislocation which cross through or near the surface and their spatial distribution, growth striations, cracks, presence of second phase, stacking faults, growth bands, twins, strain around grain boundaries, inclusions, etc.¹⁵ The visibility of a dislocation depends on the $\mathbf{g}\cdot\mathbf{b} = 0$ criterion, where \mathbf{b} is the Burger vector of the dislocation and \mathbf{g} is diffraction vector. Diffraction vector lie normal to the diffraction planes under study. Therefore, maximum visibility will be obtained when these two vectors be parallel and minimum in case they are perpendicular to each other.¹⁶

2.2.4 Chemical etching

Chemical etching is a well-established technique for qualitative and quantitative analysis of dislocations at crystal surface.¹⁷ Dislocations are linear defects normally observed in single crystals which are of two basic types: edge and screw. The region around dislocations is strained compared to defect free region and has higher localized surface energy. The locations of these sites are revealed by preferential dissolution using a suitable chemical called as etchant. The etchants are normally solvents for that material. The pit formed due to dissolution is called etch pit and normally seen by optical microscope. The crystal surface under study should be either as grown clean surface or a sample plate cut parallel to a natural face. The polished surface is first brought in contact with solvent for a certain duration called as etching duration and then dried by clean blotting paper. We have used *Olympus* (model BX 60) make upright microscope for visualization of the etch pits at the crystal surface. Total magnification (M) of the observed image with respect to the actual size at the sample is the product of three factors: the magnification of objective lens (M_o), magnification of eye piece lens (M_e) and tube factor (M_T), i.e.

$$M = (M_o) \times (M_e) \times (M_T) \quad \dots (2.4)$$

The magnification of the image can be enhanced up to 1000X as per requirement by changing eye piece and varying tube factor. The dislocation defects density is quantified in terms of etch pit density (EPD), and is defined as,

$$\begin{aligned} \text{EPD} &= (\text{No. of pits observed on a specific surface area}) / (\text{area of the surface}) \\ &= N / A \quad \dots (2.5) \end{aligned}$$

Where N is total number of etch pits observed in an area of A at eye piece.

If the area under investigation at eyepiece is rectangular shape with dimensions ΔX cm and ΔY cm as shown schematically in Fig. 2.6, therefore,

$$\begin{aligned} \text{EPD} &= N / \{(\Delta X / M) \times (\Delta Y / M)\} \\ &= (N M^2) / (\Delta X \Delta Y) \quad \dots (2.6) \end{aligned}$$

The unit of EPD is cm^{-2} . Crystals grown from solution typically have dislocation density of the order of 10^3 to 10^4 cm^{-2} . Dislocations are mainly generated due to stress, thermal fluctuations, entrapment of impurities or inclusions during growth which leads to growth rate irregularities. Dislocations are thermodynamically unstable. Annealing is normally used to reduce dislocation density.¹⁸

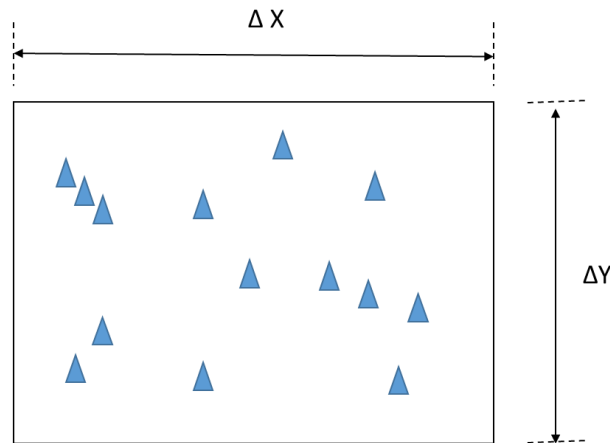


Fig. 2.6 Schematic of etch pits seen observed by an optical microscope for calculation of etch pit density.

The shape of etch pits for a particular face of a crystal mainly depends on surface symmetry and the solvent.¹⁷ However for a plate, cut at different angle to that of a habit face, the shape of etch pit be projection of the orientation of the cut on the crystal.¹⁹ Etch duration also play an important role to obtain good quality etch pit pattern. An excessive etching may lead to surface dissolution which may degrade the information of etch pits. On the other hand, etching for a very small time, hardly have time to interact at the defect sites. Therefore, there is some range of optimum time duration which depends on the nature of

chemical used, its concentration and temperature. Normally, a fast etchant is one which has relatively higher solubility for the crystal under study. For aqueous solution grown crystals water is an obvious choice. However, for those crystals which has very high solubility in water a dilute solution may be preferable to reduce etching rate. Etching technique is although simple and provide direct information of defects sites but is somewhat destructive at least to the polished surface layer. However, it is suitable to distinguish dislocation sites in X-ray topographs by one to one correlation.

2.2.5 UV-Visible-IR transmission spectroscopy

The crystals under investigations are suitable for nonlinear optical applications therefore they should have high optical quality. One of the well-known methods of assessment of optical quality of the crystals is transmission spectroscopy which gives information about transmission range, absorption coefficient, type of band gap, presence of impurities, reflection coefficients etc.^{20,21} It is a non-destructive technique suitable for assessment of bulk absorption at a particular wavelength for a crystal plate. Sample preparation is also an important part for this activity. The sample should be well polished and in the form of parallel plate. It is because when a beam passes through a material some of its part transmitted, some other reflected from its entering and exit faces and the remaining part is absorbed or scattered. As per energy conservation law, it may be represented as,

$$I_0 = I_A + I_T + I_R$$

$$\text{Or, } (I_A / I_0) + (I_T / I_0) + (I_R / I_0) = 1$$

$$\text{Or } A + T + R = 1 \quad \dots (2.7)$$

Where, A, T, and R, are absorbance, transmittance, and reflectance respectively.

The reflectance depends on refractive index of the material. For transmission studies from air to sample at normal incidence it can be written as,

$$R = \left(\frac{n-1}{n+1}\right)^2 \quad \dots (2.8)$$

The instrument used for transmission or absorption spectroscopy is called spectrophotometer. We used *Jasco* make spectrophotometer (model V-670) for our studies which has wavelength scan range from 190 nm to 2500 nm. It has scanning grating monochromators which isolates narrow bandwidth light from the broad light source which

is subsequently divided into two equal intensity beams. One beam is called the sample beam and the other as reference beam. Before placing the sample in the sample holder, baseline correction is done to account equal intensities at both the arms. Subsequently sample plate is placed in the holder to face the sample beam normally. The scan rate, wavelength resolution and wavelength range can be set as per requirement. This gives wavelength versus transmittance spectrum from which various information about material can be deduced. One of the important material parameters is absorption coefficient (α), which can be calculated from this spectrum considering Beer-Lambert law,²¹

$$I_T = I_0 e^{-\alpha.t} \quad \dots (2.9)$$

$$\alpha = \frac{1}{t} \ln(I_0 / I_T) = \frac{1}{t} \ln(1/T) \quad \dots (2.10)$$

Where, I_0 and I_T are the intensities of the incident and the transmitted beam at a particular wavelength, t is the thickness of the plate along the beam and α is absorption coefficient of the material at this wavelength.

The above formula does not account reflection losses therefore the calculated value of absorption coefficient α does not depict the correct information of material quality. Considering reflection loss to be R , a corrected formula can be derived for one-time reflection loss as shown in Fig. 2.7.

$$\text{According to it, } I_T = I_0 (1-R)^2 e^{-\alpha.t} \quad \dots (2.11)$$

$$\text{And hence, } \alpha_{corrected} = \frac{1}{t} \ln\{(1-R^2)/T\} \quad \dots (2.12)$$

Where T is obviously the transmittance measured using the spectrophotometer. The unit of absorption coefficient is cm^{-1} .

Absorption coefficient, α for a given sample is fixed but varies with wavelength. This information is used to calculate bandgap and the type of band gap of the material.^{22,23} Band gap is the energy gap between the valance band and conduction band of the material.²⁴ Direct band gap materials are those in which transition takes place without the exchange of momentum.²¹ Dielectric materials have large band gap compared to semiconductors. A large band gap indicates a larger transmission range in the UV region. Transparency region of a material is usually defined as a wavelength region in which the transmittance is more than 10% for a sample thickness of 1 mm. There are various factors

which influence optical transmittance or absorption coefficient such as surface quality, chemical impurities and bulk defects. A sample having lower value of absorption coefficient is preferable compared to that having higher.

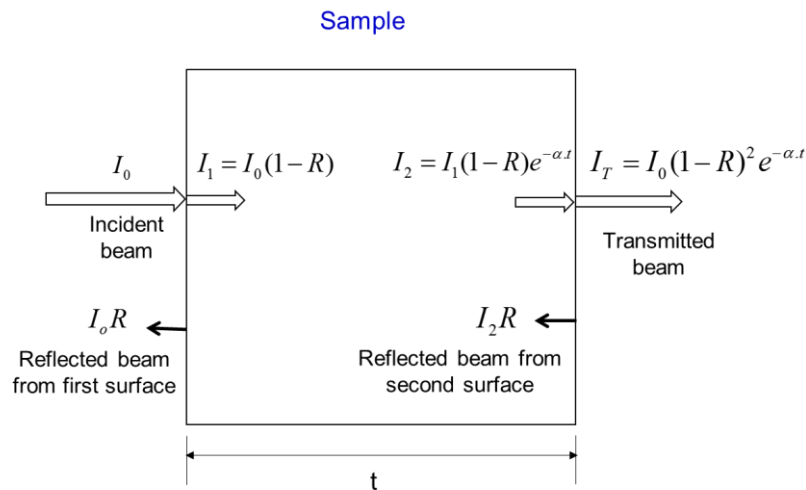


Fig. 2.7 Transmission of light through a sample of thickness t accounting reflection losses and absorption.

2.2.6 Mach-Zehnder interferometry for optical homogeneity

The transmission spectroscopy described in the earlier section provides an accurate but localized information about the optical quality of the crystal. However, for device purpose large size crystal plates are normally used which demands optical homogeneity throughout the sample volume. One of the method to assess bulk optical homogeneity is based in Mach-Zehnder interferometry.^{25,26} It is a two beam interference technique. A typical set up for Mach-Zehnder interferometry is shown in

Fig. 2.8. It consists of a He-Ne laser as a monochromatic and coherent light source. This beam is expanded and collimated using beam expander (BE) as per the sample size. The beam is then divided in to two branches at 90° to each other by a 50:50 beam splitter (BS1). One of the branch is called reference beam and the other as sample beam. These two beams are further reflected at 90° by two mirrors to meet these two at another 50:50 beam splitter (BS2) placed diagonally opposite to the first one as shown in the

Fig. 2.8. The two beams travelled from different paths interfere due to long coherence length of the He-Ne laser. A CCD camera is used to get interference image using a convex lens placed after the second beam splitter (BS2). The CCD camera is connected to a

computer for observing the interferogram at the monitor and to record it. Initially the two beams are aligned to get infinite fringe setting (for zero optical path difference) or a wedge setting using a wedge compensator. The crystal plate under study is then placed in the sample arm and a interferogram is obtained which reflects interference fringes. The shape of the interference fringes is a direct replica of the optical homogeneity of the sample plate, if it's two opposite faces are prepared perfectly parallel. An interferogram having a single fringe in case of infinite fringe setting mode or a set of equi-spaced parallel fringes in case of wedge fringe setting is an indication of good optical homogeneity of the sample.

If there are N fringes seen at the screen corresponding to sample diameter D for infinite fringe setting mode, the change in refractive index per unit length normal to fringes can be calculated from the optical path difference (OPD) between the beams at the diametrically opposite ends,

$$OPD = \Delta n d = N \lambda \quad \dots (2.13)$$

$$\delta n = (\Delta n / D) = (N \lambda / d D) \quad \dots (2.14)$$

Where d is the sample thickness and the above calculation are applicable for samples having highly uniform thickness of the order of a fraction of wavelength. It is because OPD is also depends on sample thickness. Localized distortion of fringes, fringe breaks, difference in separation between adjacent fringes, or non-uniform separation between two fringes along their length indicate variation in refractive index and hence optical inhomogeneities. Mach-Zehnder interferometry based experimental set up are very sensitive to nearby vibrations of even walking steps therefore difficult in alignment.²⁷ Therefore, experiments are carried out at the vibration isolation table.

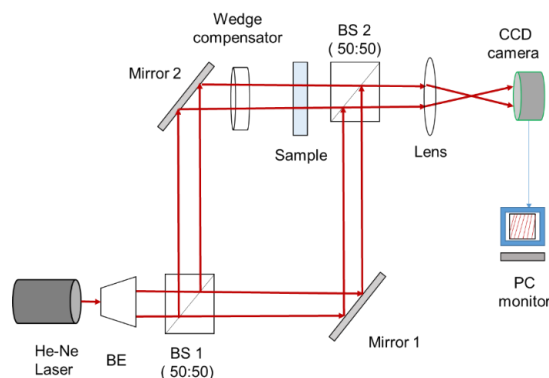


Fig. 2.8 Schematic drawing of the Mach-Zehnder interferometer used for optical homogeneity.

2.2.7 Birefringence interferometry: Orthoscopy and Conoscopy

Birefringence interferometry is another method for assessment of optical quality of bulk crystals.²⁸ It is a single beam interference technique and hence demands simpler infrastructures compared to the Mach-Zehnder interferometry. It is based on birefringence which is a property of anisotropic (non-cubic) crystals. Whenever a light beam of certain wavelength passes through a birefringent (non-cubic) crystal plate, it splits into two separate waves inside the crystal propagating with separate refractive indices and with plane of polarization perpendicular to each other. Further the refractive index of one of these two waves varies with direction and hence called as extra-ordinary wave (or e-wave) while the other beam propagates with same refractive index irrespective of direction of propagation in the crystals and hence called as ordinary wave (or o-wave). The direction dependent nature of refractive indices is depicted by index ellipsoid or indicatrix. The shape of which depends on crystal system as shown in Fig. 2.9.

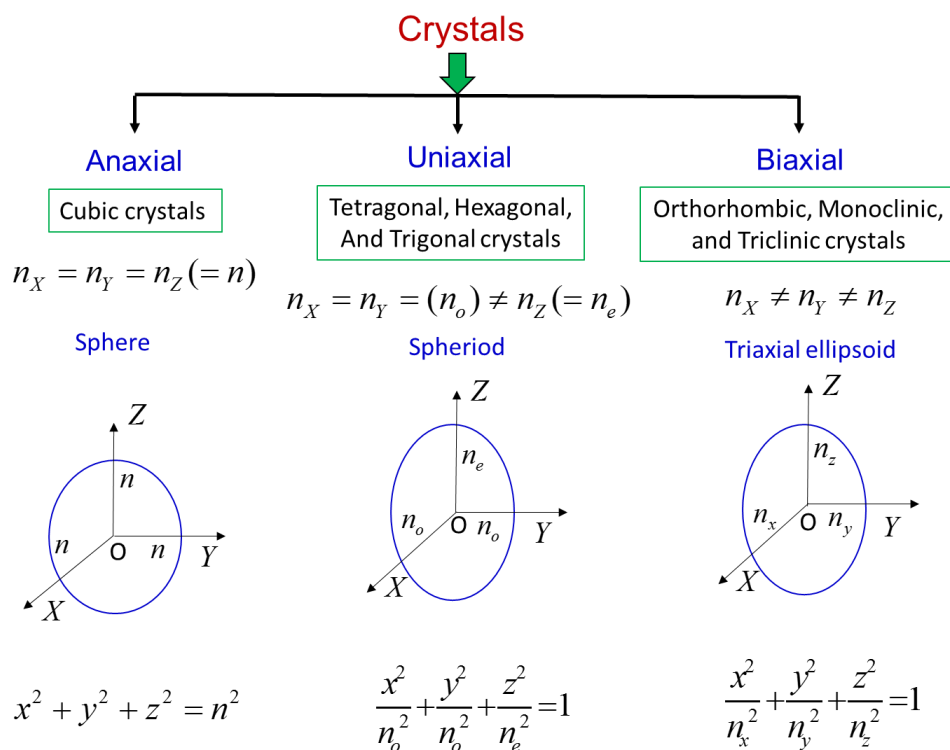


Fig. 2.9 A classification of crystals based on index ellipsoid.

The index surface (sphere, or spheroid or tri-axial ellipsoid) or indicatrix is a surface extended in 3-dimension constructed using principal refractive indices (n_x , n_y , n_z) of the crystal as shown in Fig. 2.9. The equations of index surfaces shown in the same figure

belong to principal coordinate system (x, y, z) of the crystal. Index ellipsoid can be used to determine the values of the two refractive indices and the orientation of their polarization for a given direction of beam propagation in the crystal.²⁹ The difference between the two values of the refractive indices is called the value of birefringence in that direction.

There is however certain direction(s) in non-cubic crystals called as optical axis along which birefringence is zero. To account this direction as well, the birefringence interferometry can be classified into two categories:

1. *Orthoscopy, and*
2. *Conoscopy*

Orthoscopic birefringence interferometry or orthoscopy is suitable for sample plates oriented in any directions except that prepared normal to optic axis.³⁰ On the other hand conosopic birefringence interferometry or conoscopy is suitable for those plates which are prepared normal to the optic axis. The optical set up for these two types of birefringence interferometry are shown in Fig. 2.10 and Fig. 2.11. These two set ups are quite similar except in use of a converging lens for conoscopy. The setup comprises a He-Ne laser of wavelength 632.8 μm , a beam expander, polarizer (P), analyser (A), lenses, sample mounting stage, a screen and a camera.

In case of *orthoscopy*, an expanded and collimated laser beam of wavelength λ is passed through the sample plate placed between crossed polarisers. The resulting interference pattern at the screen is a signature of birefringence homogeneity. A uniform illumination at the screen show uniform birefringence throughout the sample under study. While a set of parallel equidistant fringes also signifies good optical homogeneity, if it is due to wedge in the sample plate. If the fringes are distorted or break its continuity indicates poor birefringence homogeneity. If the sample thickness and beam diameter passing through the sample plate are known then the linear gradient of birefringence of the sample normal to fringes can be calculated using formula,^{31,32}

$$\Delta B/D = N\lambda/DL \quad \dots (2.15)$$

where N is the number of interference fringes observed through the diameter D of the sample of uniform thickness L . Low value of birefringence inhomogeneity (ΔB) indicates good optical quality of crystal, where

$$\Delta B = \delta(\Delta n) = \delta(n_e - n_o) \quad \dots (2.16)$$

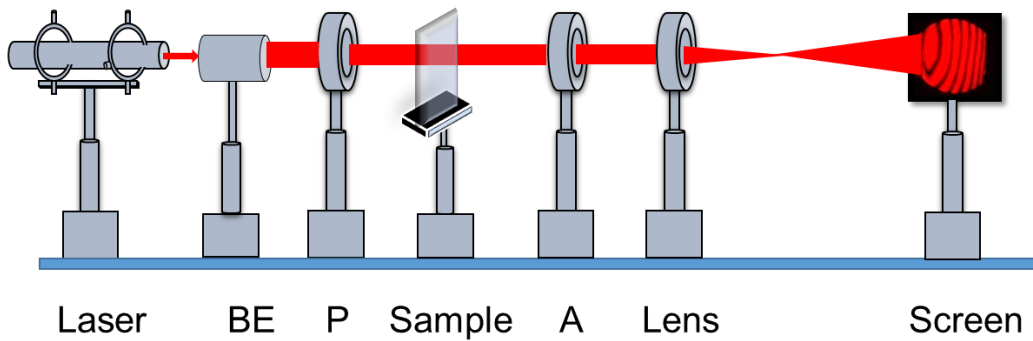


Fig. 2.10 Schematic showing optical set up for orthoscopic birefringence interferometry.

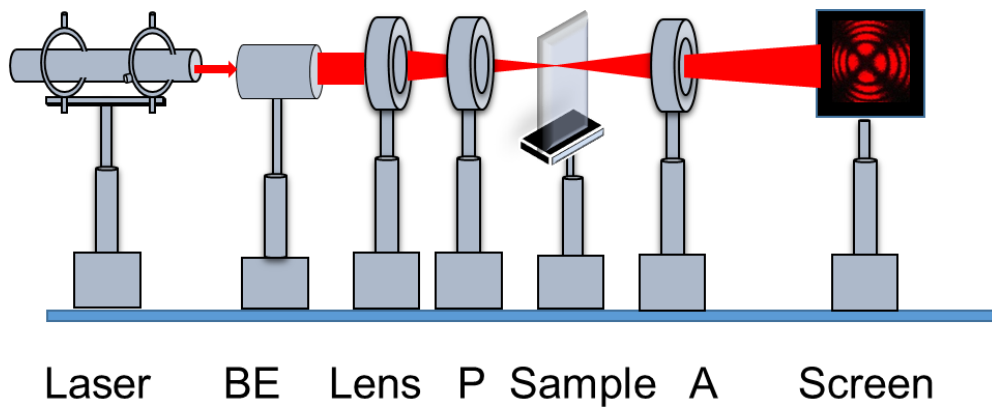


Fig. 2.11 Schematic showing optical set up for conosopic birefringence interferometry.

In case of **conoscopy**, sample is placed between crossed polarizers and a converging beam is passed. It results in a specific type of interference fringe pattern called as conosopic fringe pattern if the direction of beam propagation is along the optic axis of the plate.³³ In this case the birefringence is zero for the central beam propagating along the optic axis and hence dark while for the beams entering at an inclined angle to the optic axis find a non-zero birefringence which increases with angle from the optic axis. Therefore, optical path difference between the ordinary and extraordinary rays generated from an incident beam at an angle (say θ) from the optic axis will be same and hence form a fringe having circular ring shape about the optic axis for uniaxial crystals. These circular

fringes are called isochromes. The positions of planes of extinctions of the polarizer and analyser are dark called as isogyres. The circular shape of concentric fringes is a measure of good birefringence homogeneity. The centre of fringes shows the direction of optic axis. Conoscopy method is also used to identify direction of optic axis in uniaxial and biaxial crystals.³⁴ Distorted fringes show birefringence inhomogeneity may be due to mechanical stress or strain in the sample.³⁵

2.2.8 Second harmonic generation

Second harmonic generation (SHG) is one of the important nonlinear optical phenomenon observed in non-centrosymmetric materials at high intensities. The observation of linear or non-linear optical effect in a material depends on the strength of electric field generated by the light. The electric field (E) of an electromagnetic radiation is proportional to square root of its intensity (I). At low intensity regime of electromagnetic radiation, material properties such as transmission, absorption, refractive index etc. do not significantly depends on its intensity and hence called linear optical properties. Therefore, for ordinary light sources having $\sim 10^3$ V/cm field strength, linear optics is applicable. However, if the field strength of radiation is high enough of the order of $10^7 - 10^{10}$ V/cm means that of the order of inter-atomic fields, the response of the material become nonlinear. After the invention of laser in 1960 by Maiman³⁶, it has become possible to achieve high intensity radiation comparable to the interatomic fields mainly due to coherence nature of laser. Franken et al. were the first to demonstrated the phenomenon of second harmonic generation by focusing a Ruby laser of 694 nm wavelengths into a quartz crystal in the year 1961.³⁷ In 1962 Giordmaine³⁸ and Maker³⁹ independently discovered that for efficient conversion of laser frequency the beam is required to be passed along certain specific directions in the crystals called as phase matching directions. In this context anisotropic single crystals are important which due to having birefringence provide a method to compensate phase mismatch. One of the major applications of SHG is to obtain lasers at other frequencies simply by passing a laser through a suitable crystal. There are two categories of anisotropic crystals namely centrosymmetric and non-centrosymmetric. Out of which centrosymmetric crystal do not generate even order harmonics of fundamental laser beam because of inversion symmetry. This makes non-centrosymmetric crystals a natural choice particularly for SHG. This thesis is related to growth of three important non-centrosymmetric crystals which have capability of SHG. Non-linear optical effects such

as SHG is basically originates from the non-linear electric polarization induced in the material by intense electro-magnetic field of laser. When an electric field is applied on a dielectric material, it interacts with electrons and nuclei and change their spatial distribution, it causes creation of dipoles. The resultant dipole moment per unit volume is called as polarization (P). These dipoles oscillate due to oscillation of applied field and in turn re-radiate radiation. The scattered radiation from all the scatterers superpose and seen as transmitted or reflected radiation. At low values of applied fields, the induced electrical polarization is directly proportional to the external applied field (E),

$$P \propto E$$

$$\text{Or, } P = \epsilon_0 \chi E \dots (2.17)$$

Where ϵ_0 is electrical permittivity of the free space and χ is called linear or first order electrical susceptibility of the material. χ is related with dielectric constant (ϵ_r) and refractive index (n) of the material as,

$$n^2 = \epsilon_r = 1 + \chi \dots (2.18)$$

In case of high values of electric fields such as that in intense radiation of lasers, the induced polarization in material no longer remain linearly proportional to the applied field. Consequently, the re-radiation from the oscillating dipoles deviate in phase and amplitude from that of the sinusoidal form of applied electric field of radiation. As a result, re-radiated field contains additional frequencies. Mathematically, the nonlinear dependency of the polarization on electric field can be written as,⁴⁰

$$P = \epsilon_0 (\chi^{(1)} E + \chi^{(2)} E^2 + \chi^{(3)} E^3 + \dots) \dots (2.19)$$

where $\chi^{(1)}$, $\chi^{(2)}$ and $\chi^{(3)}$ are called first, second and third order susceptibility of the material. The material susceptibilities of order higher than the first are responsible for all the nonlinear phenomenon. However, their relative strength reduces rapidly as,

$$\chi^{(1)} \gg \chi^{(2)} \gg \chi^{(3)}$$

This suggests that a higher order field is required to observe higher order nonlinear effects. The above relations (Eq. 2.17 and Eq. 2.19) are valid only for isotropic materials such as isotropic solids, liquids or gases. In case of anisotropic materials such as non-cubic crystals, the relations are more complicated. In anisotropic materials, the induced

polarization is also not isotropic, moreover a field applied along one direction may also induce polarization in other directions. This property is normally described in term of tensors as shown in following equations.

- i) For anisotropic materials at low field or low radiation intensity, Eq. 2.17 can be written as,

$$P_i = \epsilon_o \chi_{ij} E_j \quad \dots (2.20)$$

Similarly,

- ii) For anisotropic materials at high field or high radiation intensity, Eq. 2.19 can be written as,

$$P_i = \epsilon_o (\chi_{ij}^{(1)} E_j + \chi_{ijk}^{(2)} E_j E_k + \chi_{ijkl}^{(3)} E_j E_k E_l + \dots) \quad \dots (2.21)$$

Where, $\chi_{ij}^{(1)}$, $\chi_{ijk}^{(2)}$ and $\chi_{ijkl}^{(3)}$ are called first, second and third order susceptibility tensors of the material respectively and have 9, 27 and 81 components respectively. Out of these the second order polarization or say the second rank susceptibility tensor $\chi_{ijk}^{(2)}$ is responsible for SHG and various other second order effects such as SFG (sum frequency generation), DFG (difference frequency generation), OPO (optical parametric oscillations), electro-optic effect etc. While the $\chi_{ijkl}^{(3)}$ tensor is responsible for Kerr effect, THG (third harmonic generation), SRS (stimulated Raman scattering), SBS (stimulated Brillouin scattering) etc.⁴⁰

The second order polarization term which induces SHG can be written from Eq. 2.21 as,

$$P_i^{(2)} = \epsilon_o \chi_{ijk}^{(2)} E_j E_k \quad \dots (2.22)$$

Or,

$$P_i^{(2)} = \sum_{j,k} \epsilon_o \chi_{ijk}^{(2)} E_j E_k \quad \dots (2.23)$$

The second order nonlinear susceptibility tensor $\chi_{ijk}^{(2)}$ is also depicted as d_{ijk} for optical frequency regime and is called as second-order nonlinear optical coefficient or in short as d-coefficients. They are related as $\chi_{ijk} = 2 d_{ijk}$.⁴¹ This is a 3rd rank tensor therefore having 27 components. It can also be shown using Eq. 2.23 that for centrosymmetric crystals all the $\chi_{ijk}^{(2)}$ coefficients are zero and hence centrosymmetric crystals do not show second order nonlinear optical effects such as SHG. Further, as per the Eq. 2.23, if one

interchanges of E_j to E_k the value of polarization and hence the value of d -coefficient should be same under this permutation therefore there are only 18 independent d -coefficients in the d -tensor which can be written in simple form as,

$$d_{ijk} = d_{il} = \begin{pmatrix} d_{11} & \dots & d_{16} \\ d_{21} & \dots & d_{26} \\ d_{31} & \dots & d_{36} \end{pmatrix} \dots (2.24)$$

Where l is used for last two indices jk such that,

$$11 \rightarrow 1; \quad 22 \rightarrow 2, \quad 33 \rightarrow 3; \quad 12, 21 \rightarrow 6; \quad 23, 32 \rightarrow 4; \quad 13, 31 \rightarrow 5$$

Using this form of susceptibility, the second order polarization can be written in full matrix form as,^{41,42}

$$\begin{pmatrix} P_x \\ P_y \\ P_z \end{pmatrix} = \epsilon_0 \begin{pmatrix} d_{11} & d_{12} & d_{13} & d_{14} & d_{15} & d_{16} \\ d_{21} & d_{22} & d_{23} & d_{24} & d_{25} & d_{26} \\ d_{31} & d_{32} & d_{33} & d_{34} & d_{35} & d_{36} \end{pmatrix} \begin{pmatrix} E_x^2 \\ E_y^2 \\ E_z^2 \\ 2E_y E_z \\ 2E_z E_x \\ 2E_x E_y \end{pmatrix} \dots (2.25)$$

The number of non-zero and independent d -coefficients depends on Kleinman symmetry and crystal symmetry. In case of KDP crystal there are only three non-zero d -components $d_{14} = d_{25} = d_{36}$.⁴³

SHG process can be depicted as in Fig. 2.12.

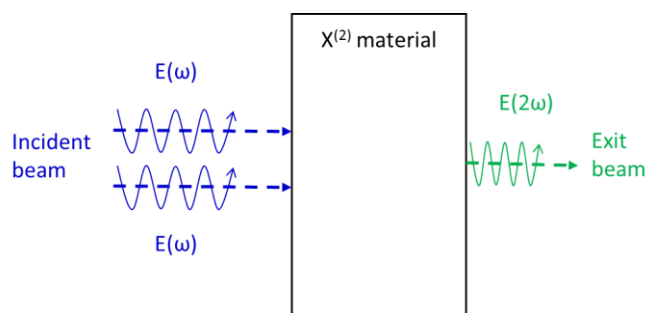


Fig. 2.12 Schematic depiction of the process of SHG.

It is originated due to second order polarization and can be given by,

$$P_i(2\omega) = \epsilon_0 \sum_{j,k} d_{ijk}(-2\omega, \omega, \omega) E_j(\omega) E_k(\omega) \dots (2.26)$$

Where ω is angular frequency of fundamental wave incident at the crystal and $P(2\omega)$ is power of second harmonic generated wave.

The efficiency of frequency doubling process is defined as SHG conversion efficiency (η). It is defined as the ratio of power generated at second harmonic frequency at exit to the laser power of fundamental frequency incident at the crystal. It is derived by solving coupled fundamental and second harmonic waves propagating in the crystal. Considering the momentum and energy conservation the expression for SHG efficiency can be written as,⁴⁴

$$\eta = \frac{P(2\omega)}{P(\omega)} = \frac{2\omega^2 d^2 L^2}{\epsilon_0 c^3 n(\omega)^2 n(2\omega)} \times \frac{P(\omega)}{A} \times \frac{\sin^2(\Delta k L/2)}{(\Delta k L/2)^2} \quad \dots (2.27)$$

Where L is the thickness of the material, A is the area of fundamental wave, $n(\omega)$ and $n(2\omega)$ are the refractive indices of the material at fundamental and second harmonic frequency, d is nonlinear optical coefficient in that direction, c is velocity of light in vacuum and Δk is called as phase mismatch between the generated and incident wave vectors given as,

$$\Delta k = 2k(\omega) - k(2\omega) \quad \dots (2.28)$$

This expression shows that conversion efficiency depends on various parameters such as power density, d coefficient, interaction length and phase mismatch Δk . It is phase mismatch on which conversion efficiency depends most critically because it is like square of sinc function whose maximum value is 1 at $\Delta k = 0$. If $\Delta k \neq 0$, the conversion efficiency oscillates as a function of propagation length. Hence it is desirable to achieve zero phase mismatch or say a condition of phase matching for efficient SHG. There are various methods of achieving phase matching for efficient frequency conversion such as,⁴⁵

- i) Angle phase matching (scalar and vector),
- ii) Temperature phase matching,
- iii) Quasi phase matching,
- iv) Cerenkov phase matching.

In case of bulk optical single crystals, the angle phase matching is most common. It is based on utilization of birefringence for phase matching.

Solution of Eq. 2.28 for $\Delta k = 0$, for SHG demands,

$$k(2\omega) = k(\omega) \quad \text{or} \quad n_{2\omega} = n_{\omega} \quad \dots (2.29)$$

It is not possible to satisfy this relation in normal dispersive materials where refractive index varies with frequency. However, it is possible to meet this condition in anisotropic crystals because there are two possible normal modes of wave propagation for each frequency which travels at different phase velocities. In case of uniaxial crystals these two waves are called as ordinary (o wave) and extra-ordinary waves (e wave) as described in Section 2.2.7. The uniaxial crystals are divided into two categories based on nature of birefringence ($\Delta n = n_e - n_o$) to be negative or positive as:

- i. Negative uniaxial, if $n_e < n_o$, and
- ii. Positive uniaxial if $n_e > n_o$,

The refractive index variation for o and e wave are conveniently depicted by index ellipsoid as shown in Fig. 2.9. There are two possible methods to meet the phase matching called as type-I and type-II phase matching as mentioned in Fig. 2.13 (a). The orientation of the beam propagation directions inside crystal is shown in Fig. 2.13(b).

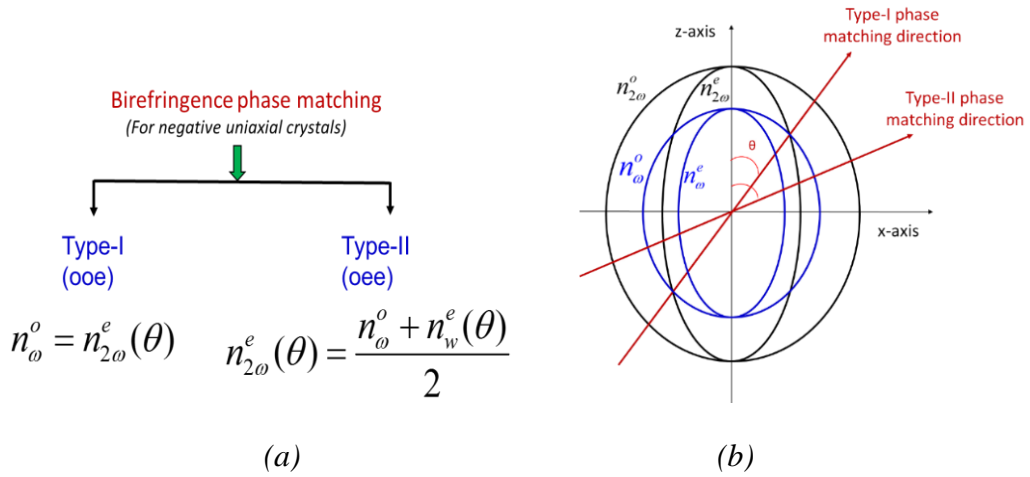


Fig. 2.13 (a) Mathematical conditions for birefringence phase matching for negative uniaxial crystals, and (b) Schematic depiction of orientation of beam propagation directions for type-I and type-II phase matching in index ellipsoid for a negative uniaxial crystal like KDP at ω and 2ω frequencies.

The condition of phase matching (Eq. 2.29) can be met finding suitable direction (θ) from z-axis at which extraordinary index matches with that the ordinary index. This can be calculated using the equation,

$$\frac{1}{n_{\omega}^e(\theta)^2} = \frac{\cos^2 \theta}{(n_{\omega}^o)^2} + \frac{\sin^2 \theta}{(n_{\omega}^e)^2} \dots (2.30)$$

Where n_{ω}^o and n_{ω}^e are principal refractive indices of the material at frequency ω .

Phase matching condition requires precise maintenance of the beam direction along specific orientations in the crystal. But there are various other parameters which influence it, such as temperature fluctuation in the ambient, beam divergence, wavelength spread of the laser. Further beam walk-off is another factor which limits the optimum length of crystal.⁴⁶ These conditions are less critical if the phase matching angle is near 90° . Such a condition is called non-critical phase matching.⁴⁷

The above expression (Eq. 2.27) for SHG efficiency was derived considering no depletion of fundamental wave intensity during propagation in the crystal. It is therefore applicable for low conversion efficiency range while in case of high SHG conversion efficiency, depletion of intensity takes place and the expression in case of perfect phase matching is modified.⁴¹

2.2.9 Laser-induced damage threshold

High laser intensity is normally required to achieve high conversion efficiency for SHG. However, there is a certain intensity threshold for the material at which it starts getting physical damages at the surface or in the bulk. The upper limit of the laser intensity which is safely handled by the material is normally described as its laser-induced damage threshold (LDT). The occurrence of damage is usually observed by CCD camera. LDT is not a physical property of a material in strict sense as it depends on various factors but is a very useful parameter to decide upper limit of intensity for safe use of the material with a particular laser. LDT is in general influenced by various factors which may be divided into two categories,⁴⁸

- i) **Laser parameters:** such as wavelength, pulse-width, polarization, pulse profile, repetition rate and laser beam size.
- ii) **Material parameters:** such as surface imperfections (scratches, digs, sleeks, chips, cracks, dust particles, stains, coating material property if there, etc.), bulk defects (inhomogeneities, liquid inclusions, voids, bubbles, chemical impurities, etc.), presence of additives or dopants, crystal plane under study etc.

It shows that LDT also influenced by surface finishing, if the surface processing is poor it may damage the crystal at low intensity even though the bulk LDT is very high. Therefore, LDT measurements may be classified as,

- a. *Surface damage, and*
- b. *Bulk damage*

There are various methods of measuring LDT which mainly depends on number of shots and number of sites used for investigations. These may be classified as,^{48,49}

1. ***Single - shot method (or “1 on 1” method):*** In this method only one shot is fired at one site, the next shot of somewhat higher energy is fired at the another site and this sequence is continued till the damage occurs.
2. ***Multiple - shot method (or “N on 1” or “S on 1” method):*** In this method a fixed number of shots of same intensity are fired at a single site of the crystal. If no damage occurs the process is repeated at another site with increased pulse intensity. This process is continued till the damage occurs.
3. ***Ramping energy - shot method (or “R on 1” method):*** In this method laser pulses are shot at a particular site with ramp increase of its pulse energy until the damage occurs.

A typical set up used for measuring LDT is shown schematically in Fig. 2.14. It comprises a Nd:YAG laser (*Quanta* make) of Gaussian TEM₀₀ mode of 7 ns pulse width and having facility of varying laser pulse energy (upto 500 mJ), a beam-splitter (BS), a converging lens, sample stage, mirror, two energy meters (*Ophir* make), a CCD camera and a computer for recording data and image from the energy meters and the camera respectively. We have used “R on 1” method for measurement of LDT. The value of LDT was calculated using the following formula,^{50,51}

$$I_{Threshold} = \frac{\frac{1}{2}(E_{no\ damage}^{max} + E_{damage}^{min})}{\tau \times A} \quad \dots (2.31)$$

where τ is the laser pulse width and A is the area of the laser beam. The area of laser pulse can be calculated from beam diameter D as, $A = \pi D^2 / 4$. The beam diameter was determined by knife edge method.⁴⁸ The unit of LDT is MW/cm² or GW/cm².

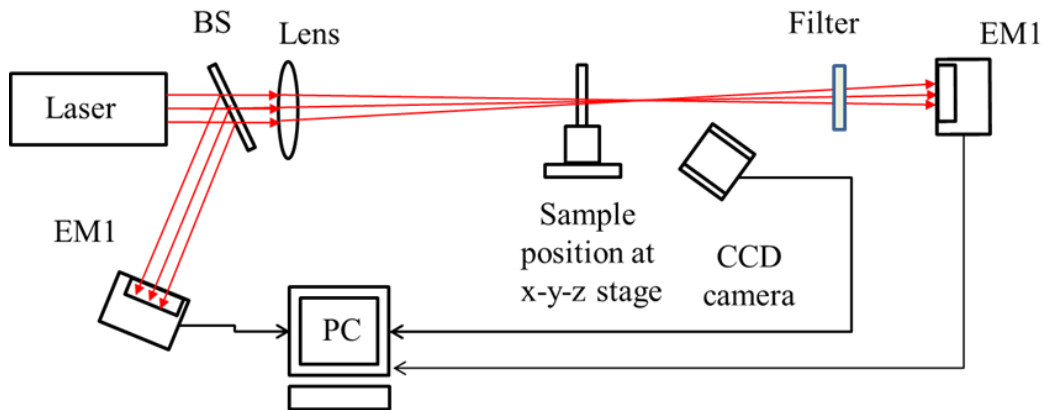


Fig. 2.14 Schematic layout of laser-induced damage threshold (LDT) set up.

There are various mechanisms of occurrence of damage at dielectrics by laser pulse energy.^{48,52} The most prominent is dielectric breakdown at surface due to presence of scratches, inclusions, pores where localized field intensity increases. It may also be induced in the bulk due to multi-photon absorption, self-focussing or electron avalanche breakdown.⁵³ The other mechanism is thermal absorption mostly at bulk due to presence of impurities or inclusions or at surface there is a layer of particulate matter or residual polishing compound. Damage threshold is probabilistic in nature and highly depends on local defects. It also varies with pulse width because damage mechanism also depends on pulse width. At short pulse of < 30 ns, multiphoton absorption and ionization is the main mechanism of damage while at longer pulse widths plasma heating and thermal effects prevails.⁵⁴

One always need a material which high LDT value. One of the ways to achieve is to grow good optical quality crystals with best possible surface finish. In addition, there are some other methods to enhance damage resistance of the crystals, such as annealing, exposure to irradiation, ultrafiltration during growth, addition of certain specific additive etc.^{18,55}

2.2.10 X-ray fluorescence studies

Determination of chemical composition and impurities present in the grown crystals is an important part of characterization. It is because impurities influence various properties of single crystals such as optical absorption, defects density and distribution, growth rate of habit faces, SHG efficiency, laser damage threshold etc. We have utilized X-ray fluorescence (XRF) spectroscopy to identify impurities and their concentration

particularly for bulk KDP crystals. XRF is a simple, non-destructive, fast and accurate technique for qualitative and quantitative analysis of elemental composition of materials up to parts per million (ppm) level or better. It is based on excitation of atoms by removal of their inner shell electrons by high energy x-rays which make them to emit characteristics X-rays due to transition of outer shell electrons to fill the inner shell vacancies. Fig. 2.15 shows the typical process of XRF. The energy of excitation X-ray photons should be higher than the binding energy of its K- shell electrons so that emission of characteristic K_{α} lines can be observed.

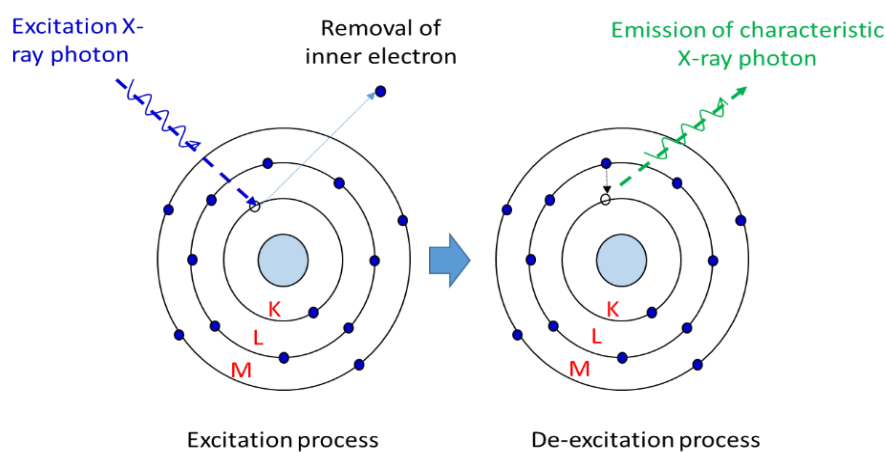


Fig. 2.15 Schematic diagram depicting process of X-ray fluorescence.

The XRF measurements can be carried out at lab source or using synchrotron source. The latter is a much intense source of radiation and hence results into less time in data collection. We have carried out these experiments at XRF beamline (BL-16) of Indus-2 synchrotron radiation source located at RRCAT, Indore.⁵⁶ Indus-2 is a 2.5 GeV, 200 mA third generation radiation source with a critical wavelength of $\sim 2 \text{ \AA}$. The XRF beamline is installed at one of its bending magnet.⁵⁷ It has photon energy in the range of 4 – 20 keV. Si (111) double crystal monochromator is used to obtain specific energy photons at the sample. The sample was placed at 45° to the incident X-rays of a particular energy and fluorescence signal was detected by a detector connected to a multichannel analyser placed at 90° to the incident beam. It is thus an energy dispersive XRF system and records all energy photon at a time. The obtained XRF spectrum is an energy versus intensity graph where peak energies correspond to the characteristics X-ray lines with mostly $K_{\alpha 1}$, $K_{\alpha 2}$ and

K_{β} lines. The obtained spectrum is analysed using softwares such as PyMCA⁵⁸ to identify the composition of elements present in the samples under investigations.

2.2.11 Fourier transform infrared spectroscopy

The XRF technique described above is suitable only for elemental identification of the material. The Fourier transform infrared (FTIR) spectroscopy is on the other hand provide information for the presence of functional groups. It is a simple technique, widely used for determination of functional groups in materials. It is based on the absorption of infrared radiation by the material. Infrared (IR) radiation is an electromagnetic radiation lying between visible and microwave spectra extended from 0.78 μm to $\sim 1000 \mu\text{m}$ wavelengths. There are two categories of IR absorption by molecules: Vibrational absorption range (0.78 μm to 50 μm) and rotational absorption in the wavelength range ($\geq 50 \mu\text{m}$). Vibrational motion is related with oscillations of bonds inside a molecule while rotational motion are oscillations of molecule as a whole. The energy involved in rotational motion is much lower than that in vibrational motion.

The IR spectra is normally divided into three regions:

- i. Near infrared (NIR) region: 0.78 μm to 2.5 μm or 12800 cm^{-1} to 4000 cm^{-1} ,
- ii. Middle infrared (MIR) region: 2.5 μm to 50 μm or 4000 cm^{-1} to 200 cm^{-1} ,
- iii. Far infrared (FIR) region: 50 μm to 1000 μm or 200 cm^{-1} to 10 cm^{-1} .

However, the mostly used IR radiation is in the range of 2.5 μm to 25 μm or say 4000 cm^{-1} to 400 cm^{-1} . Where cm^{-1} is the unit of wavenumber ($\bar{\nu}$) and is related with wavelength as,

$$\bar{\nu} = 1 / \lambda, \quad \text{or} \quad \text{cm}^{-1} = 10000 / \mu\text{m}$$

It is to note that wavenumber is proportional to frequency and can be understood as number of wavelengths in one-meter length in free space.

When IR radiation is passed through a material, it absorbs certain wavelengths which corresponds to fundamental vibrational modes of the functional groups present in the sample, and their multiples. There are in general various types of vibrations possible in molecules.⁵⁹ A classification of these motions is shown in Fig. 2.16.

Infrared radiation corresponds to vibrational energy levels of the different functional groups present in the material. There is in general two types of IR spectroscopy:

IR and Raman, which normally complement each other. IR spectroscopy is based on absorption of radiation while Raman is based on inelastic scattering. If there is a change in dipole moment for a particular vibrational mode of a molecular functional group, it absorbs corresponding IR frequency and its multiples. While those modes which accompanied with change of polarizability are called as Raman active modes. Therefore, it is not possible in general for a molecule that all the vibrational modes be IR active or Raman active. But it is true that each mode be either IR active or Raman active or both. In this case symmetry of molecule during a particular mode of vibration play an important role to decide it to be Raman active or IR or both. The total number of vibrational modes for a molecule depend its symmetry and on the number of atoms present in it. For a molecule with N number of atoms, the maximum number of fundamental vibrational modes be $(3N-5)$ in case of linear molecule and $(3N-6)$ in case of non-linear molecule.⁶⁰

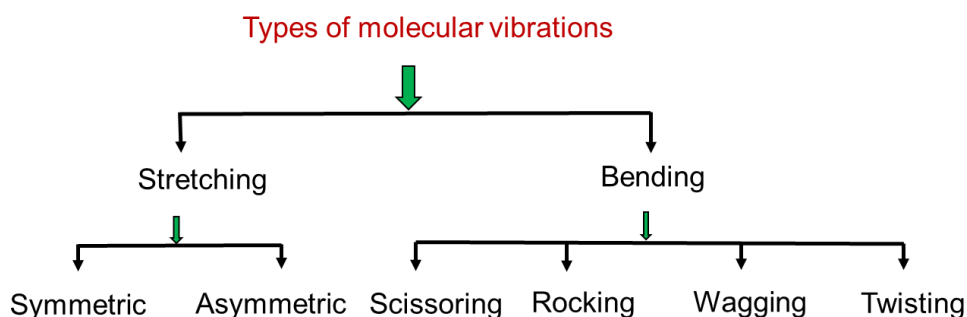


Fig. 2.16 A classification of vibrational modes of molecules.

The basic frequency of stretching vibrations of a molecular bond is called as fundamental mode. It depends on bond strength and the mass of the atoms involved. This motion normally follows Hooke's law therefore the expression for fundamental frequency of vibration can be written as,⁶⁰

$$\bar{\nu} = \frac{1}{2\pi c} \sqrt{\frac{k}{\mu}} \quad \dots (2.32)$$

Where k is called force constant which depends on strength of chemical bond and μ is the reduced mass of the atoms involved for that vibration. It is to note that a molecule cannot have zero vibrational energy which is a consequence of quantum mechanics called as zero-point energy. It means the atoms can never be completely at rest relative to each other in a molecule. In addition to the fundamental mode and its overtones, interaction between

different modes is also possible and hence combination and difference bands are also possible. This makes IR spectrum a quite complex. However sharp and intense peaks correspond to fundamental modes and characteristic of the structure of the molecule and hence commonly used to identify molecular species present in the material.

IR spectroscopy is nowadays done using an instrument called as Fourier transform infrared spectrometer rather than spectrophotometer type dispersive element based systems where scanning monochromator was used to send wavelengths one by one. FTIR technique is an advanced technique for IR spectroscopy compared to conventional dispersive systems because of rapid scanning, low signal to noise ratio, high sensitivity, high resolution and high accuracy. Moreover, it collects data simultaneously that can be used to study for time dependent variation of material properties. FTIR spectrometer is based on the Michelson interferometer. It consists of a beam splitter which separates the incoming IR wave and send at the two flat mirrors located at 90° to each other. One of the mirrors is kept fixed while the other can be translated to and fro maintaining the precision alignment relative to the fixed mirror. Due to this change of optical path difference (OPD) between the two arms the incoming optical radiation from the source is modulated continuously in a smooth or step scan mode as per the design of the FTIR. The change in OPD is done at a constant velocity over a fixed distance which is governed by the required spectral resolution. During this motion of the mirror each wavelength of the collected radiation is modulated at a unique frequency that is a function of the wavelength of the radiation and the velocity of the moving mirror. The obtained spectrum is an interferogram containing the information of the required spectrum. The Fourier transform of this interferogram is used to decode the required spectrum of the material.

We have used *Jasco* make FTIR model 660+ for investigation. It has wavelength range of 4000 cm^{-1} to 400 cm^{-1} with resolution 4 cm^{-1} . The sample under study was crushed and mixed with KBr in humidity free atmosphere and used for measurements. Initially the wavelength scan was done for background correction for air which was followed by scans for sample. The measurements are generally repeated many times and average spectrum was considered for further analysis. The Fig. 2.17 shows typical layout of the FTIR.^{61,62}

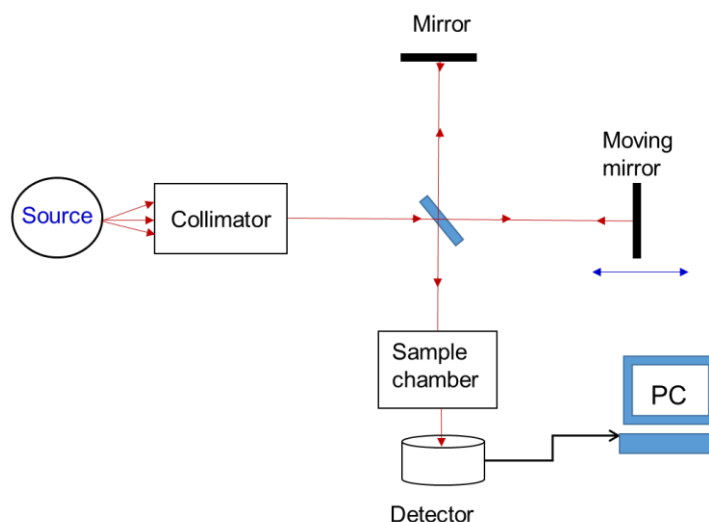


Fig. 2.17 Schematic line diagram of FTIR.

2.2.12 Differential scanning calorimetry

Assessment of thermal stability of the grown crystals is an important exercise to decide the safe range of temperature for its post growth processing and utilization. There are various thermochemical methods to analyze thermal properties of the material such as differential scanning calorimetry (DSC), differential thermal analysis, thermogravimetric analysis.^{63,64} We have employed DSC for determination of phase stability of the material grown as part of this thesis. In DSC, difference in amount of heat required to increase the temperature of the sample relative to a reference material is measured as a function of temperature and time. There are two types of DSC's: Heat flux type and power-compensation type. We have used *Setaram* make DSC system for our experiments. In this measurement two similar and small size pans of aluminum are used. A small piece of the material under study is placed in one of the pan and the other is kept empty to act itself as reference. The reference material is chosen such that it should have much higher melting point compared to the sample under study and should not have any phase transition temperature up to melting point. There is a common heater for both the pan. Both the pans are set for identical temperature programs simultaneously and actual temperature difference is monitored and corresponding heat is calculated. DSC results are in the form of heat flux as a function of temperature and time. It gives endothermic (positive peak during heating) or exothermic peak (negative peak during cooling) peaks depending on melting or solidification of the material under study. These curve can be used to

calculate enthalpies of transitions. This can be done by integration of area of corresponding peak. The enthalpy of transition is obviously proportional to the peak area. DSC measurement gives information about solid to solid phase transition temperature and temperature, glass transition temperature, melting point, crystallization temperature, enthalpy of phase change, an assessment of sample purity, heat capacity, phase diagrams of the sample and give an information about the applicable temperature range for the material for processes like annealing and for anti-reflection type protective coatings etc.

References:

- ¹ A. R. West, Characterization of inorganic solids: Applications of physical techniques, Chapter 3 in: "Solid State Chemistry and its Applications", John Wiley & Sons, Singapore, 2007, pp. 47-101.
- ² J. C. Brice, Crystal Growth Processes, Blackie & Son Ltd., Glasgow, 1986, Chapter 12, pp. 261-287.
- ³ B. D. Cullity, Elements of X-ray Diffraction, Addison-Wesley Publishing Co., Philippines, 1978, pp. 81-87.
- ⁴ B. D. Cullity, Elements of X-ray Diffraction, Addison-Wesley Publishing Co., Philippines, 1978, Appendix 3, pp. 501-503.
- ⁵ D. Schwarzenbach, "Crystallography", John Wiley & Sons, Chichester, 1997, pp.120-129.
- ⁶ R. Jenkins and R. L. Snyder, "Introduction to X-ray Powder Diffractometry", John Wiley & Sons, New York, 1996, pp.74-75.
- ⁷ A. R. West, "Solid State Chemistry and its Applications", John Wiley & Sons, Singapore, 2007, Chapter 5, pp.115-186.
- ⁸ V. K. Pecharsky, P. Y. Zavalij, "Fundamentals of Powder Diffraction and Structural Characterization of Materials, Second Edition, Springer Science, New York, 2009, pp. 159-160.
- ⁹ D. K. Bowen and B. K. Tanner, "High Resolution X-ray Diffractometry and Topography", Taylor and Francis, 1998, Chapter 2, pp.14-48.
- ¹⁰ K. Lal, High-resolution X-ray diffraction techniques for structural characterization of silicon and other advanced materials, Chapter 5, in: "Crystal Growth Technology", H. J. Scheel and T. Fukuda (Eds.), John Wiley & Sons, West Sussex, England, 2003, pp. 93-112.

- ¹¹ G. Margaritondo, "Introduction to Synchrotron Radiation", Oxford University Press, 1988, pp. 59-73.
- ¹² K. Lal, Structural characterization of single crystals, in: "Crystalline Materials: Growth and Characterization", R. Rodriguez and C. Paorici (Eds.), Trans Tech Publications, Switzerland, 1991, pp. 205-228.
- ¹³ E. S. Meieran, Industrial implications of crystal growth, Chapter 1, in: "Characterization of Crystal Growth Defects by X-ray Methods", D. K. Bowen and B. K. Tanner (Eds.), Plenum Press, New York, 1980, pp. 1-27.
- ¹⁴ D. K. Bowen, Principles of X-ray diffraction topography, in: "Applications of Synchrotron Radiation" H. Winick, D. Xian, M. Ye and T. Huang (Eds.), Gordon and Breach Science Publishers, New York, 1989, pp. 77-89.
- ¹⁵ A. Kvik, Material science applications of X-rays diffraction, in: "Encyclopedia of Spectroscopy and Spectrometry, Part 1", J. C. Lindon, G. E. Tranter, J. L. Holmes (Eds.), Academic Press, 2000, pp. 1248-1257.
- ¹⁶ B. D. Cullity, Elements of X-ray Diffraction, Addison-Wesley Publishing Company, Philippines, 1978, pp. 268-277.
- ¹⁷ K. Sangwal, "Etching of Crystals: Theory, Experiment, and Application", North Holland, Amsterdam, 1987.
- ¹⁸ K. Fujioka, S. Matsuo, T. Kanabe, H. Fujita, M. Nakatsuka, J. Cryst. Growth, 181 (1997) 265-271.
- ¹⁹ E. K. Wheeler, P. K. Whitman, T. A. Lad, J. De. Yoreo, C. B. Thorsness, J. H. McWhirter, M. L. Hanna, E. L. Miller, Appl. Phys. A 74 (2002) 813-823.
- ²⁰ D. K. Schroder, Semiconductor Materials and Device Characterization, IEEE Press, John Wiley and Sons, 2006, pp. 585-593.
- ²¹ J. G. Sole, L. E. Bausa, D. Jaque, An Introduction to the Optical Spectroscopy of Inorganic Solids, John Wiley & Sons, Chichester, 2005, pp. 113-146.
- ²² M. Razeghi, Fundamentals of Solid State Engineering, Springer Science, 2009, pp. 419-469.
- ²³ J. H. Simmons, K. S. Potter, Optical Materials, Academic Press, San Diego, US, 2000, pp. 220-229.
- ²⁴ P. Bhattacharya, Semiconductor Optoelectronic Devices, Second Edition, Prentice Hall, New Delhi, India, 2004, 118-130.
- ²⁵ Sunil Verma, P. J. Shlichta, Prog. Cryst. Growth & Charact. Mater., 54 (2008) 1-120.
- ²⁶ S. Dinakaran, Sunil Verma, S. Jerome Das, G. Bhagavannarayana, S. Kar, K. S. Bartwal, Appl. Phys. A, 99 (2010) 445-450.

- ²⁷ D. Malacara, Interference, Chapter, in: “Physical Optics and Light Measurements”, D. Malacara (Ed.), Academic Press Inc., San Diego, 1988, pp. 12-15.
- ²⁸ F. D. Bloss, An Introduction to the Methods of Optical Crystallography, Holt, Rinehart and Winston, Inc., New York, 1961.
- ²⁹ K. Lizuka, Elements of Photonics, Vol. 1, John Wiley and Sons, New York, 2002, pp. 288-290.
- ³⁰ T. Heinningsen, N. B. Singh, J. Cryst. Growth, 96 (1989) 114-118.
- ³¹ A. M. Prokhorov, Yu. S. Kuz'minov, Physics and Chemistry of Crystalline Lithium Niobate”, Adam Hilger, Bristol, UK, 1990, pp. 344-345.
- ³² S. K. Sharma, Yeshpal Singh, Sunil Verma, M. K. Singh, K. S. Bartwal, P. K. Gupta, CrystEngComm, 18 (2016) 6403-6410.
- ³³ B. N. Grechushnikov, Optical properties of crystals, Chapter 7, in: “Modern Crystallography V: Physical Properties of Crystals” L. A. Shuvalov (Ed.), Springer-Verlag Berlin, Heidelberg, 1988, pp. 405-430.
- ³⁴ M. J. Guardalben, Supplement to Optics & Photonics News, Vol. 8, No. 8, 1997.
- ³⁵ A. I. Kolesnikov, R. M. Grechishkin, S. A. Tretiakov, V. Ya., Molchanov, A. I. Ivanova, E. I. Kaplunova, E. Yu. Voronstova, Materials Science and Engineering, 49 (2013) 012037.
- ³⁶ T. H. Maiman, Nature 187 (1960) 493-494.
- ³⁷ P. A. Franken, A. E. Hill, C. W. Peters, G. Weinreich, Phys. Rev. Lett., 7 (1961) 118-119.
- ³⁸ J. A. Giordmaine, Phys. Rev. Lett., 8 (1962) 19-21.
- ³⁹ P. D. Maker, R. W. Terhune, M. Nisenoff, C. M. Savage, Phys. Rev. Lett., 8 (1962) 21-23.
- ⁴⁰ M. Fox, Optical Properties of Solids, Oxford Press, 2001, pp. 227-253.
- ⁴¹ R. L. Sutherland, D. G. McLean, S. Kirkpatrick, Handbook of Nonlinear Optics, Marcel Dekker, Inc., New York, 2003, pp. 18-47.
- ⁴² V. G. Dmitriev, G. G. Gurzadyan, D. N. Nikogosyan, Handbook of Nonlinear Optical Crystals, 2nd Edition, Springer Series in Optical Sciences, Berlin, 1997, pp. 22-25.
- ⁴³ E. Ebrahimzadeh, A. I. Ferguson, Chapter 6, in: Nonlinear optical phenomena, Chapter 6, in: “Principles and Applications of Nonlinear Optical Crystals”, R. W. Munn, C. N. Ironside (Eds.), Blackie Academic & Professional, London, 1993, pp. 99-142.

- ⁴⁴ T. Watanabe, H. S. Nalwa, S. Miyata, Phase-matched second-harmonic generation in organic materials, Chapter 5, in: *Nonlinear Optics of Organic Molecules and Polymers*, Editors H. S. Nalwa and S. Miyata, CRC Press, Tokyo, 1997, pp. 351-358.
- ⁴⁵ R. L. Sutherland, D. G. McLean, S. Kirkpatrick, *Handbook of Nonlinear Optics*, Marcel Dekker, Inc., New York, 2003, pp. 53-95.
- ⁴⁶ L. K. Cheng, W. R. Bosenberg, C. L. Tang, *Prog. Cryst. Growth Charact. Mater.*, 20 (1990) 9-57.
- ⁴⁷ W. Koechner, *Solid State Laser Engineering*, 6th Edition, Springer-Verlag, Berlin Heidelberg, 2006, pp. 602-612.
- ⁴⁸ R. M. Wood, *Laser-induced Damage of Optical Materials*, Institute of Physics Publishing, Bristol, UK, 2003.
- ⁴⁹ Marvin J. Weber (Ed.), *CRC Handbook of Laser Science and Technology*, Supplement 2: *Optical Materials*, CRC Press Inc., Boca Raton, 1995, pp. 768-776.
- ⁵⁰ K. H. Guenther, T. W. Humpherys, J. Balmer, J. R. Bettis, E. Casparis, J. Ebert, M. Eichner, A. H. Guenther, E. Kiesel, R. Kuehnel, D. Milam, W. Ryseck, S.C. Seitel, A. F. Stewart, H. Weber, H. P. Weber, G. R. Wirtenson, R. M. Wood, *Appl. Opt.*, 23 (1984) 3743-3752.
- ⁵¹ R.T. Bailey, F.R. Cruickshank, P. Kerkoc, D. Pugh, J.N. Sherwood, *Appl Opt.*, 37 (1985) 1239-124.
- ⁵² B. C. Stuart, M. D. Feit, A. M. Rubenchik, B. W. Shore, M. D. Perry, *Phys. Rev. Lett.*, 74 (1995) 2248-2251.
- ⁵³ W. Koechner, *Solid State Laser Engineering*, 6th Edition, Springer-Verlag, Berlin Heidelberg, 2006, pp. 680-688.
- ⁵⁴ F. Gan, *Laser Materials*, World Scientific, Singapore, 1995, pp. 155-160.
- ⁵⁵ P. DeMange, C.W. Carr, R. A. Negres, H. B. Radousky, S. G. Demos, *Opt. Lett.* 30 (2005) 221-223.
- ⁵⁶ <http://www.rrcat.gov.in/technology/accel/srul/beamlines/xrf.html>
- ⁵⁷ M. K. Tiwari, P. Gupta, A. K. Sinha, S. R. Kane, A. K. Singh, S. R. Garg, C. K. Garg, G. S. Lodha and S. K. Deb, *J. Synchrotron Rad.*, 20 (2013) 360-389.
- ⁵⁸ V. A. Sole, E. Papillon, M. Cotte, Ph. Walter, J. Susini, *Spectrochim. Acta Part B*, 62 (2007) 63-68, and PyMCA software website <http://pymca.sourceforge.net/>
- ⁵⁹ R. M. Silverstein, F. X. Webster, *Spectrometric Identification of Organic Compounds*, John Wiley and Sons, New Delhi, India, 2002, pp.71-81.
- ⁶⁰ C. N. Banwell, E. M. McCash, *Fundamentals of Molecular Spectroscopy*, Tata McGraw-Hill Publishing Co., New Delhi, India, 1994, pp. 55-98.

⁶¹ G. Aruldas, *Molecular Structure and Spectroscopy*, PHI Learning Pvt. Ltd., Delhi, India, 2007, pp. 200-207.

⁶² J. G. Sole, L. E. Bausa, D. Jaque, *An Introduction to the Optical Spectroscopy of Inorganic Solids*, John Wiley & Sons, Chichester, 2005, pp. 33-36.

⁶³ C. Keatch, D. Dollimore, *An Introduction to Thermogravimetry*, Heydon and Sons Ltd, London, 1975, pp. 23.

⁶⁴ P. J. Haines, *Thermal Methods of Analysis: Principles, Applications and Problems*; Blackie Academic and Professional, London, 1995, pp. 63-122.

Chapter 3 Development of Flat-top growth technique to enhance device purpose yield of KDP crystals

3.1 Introduction

Potassium dihydrogen phosphate (KDP) and its deuterated analogue (DKDP) are well known crystals for frequency conversion and electro-optic modulation of high power Nd doped YAG or Glass lasers.^{1,2} It is because of their high optical quality, high laser damage threshold, transmission down to UV region and ease in growth up to large dimensions.^{3,4} KDP is one of the few rare crystals being used worldwide for inertial confinement fusion programs⁵⁻⁷ and for X-ray generation and plasma physics experiments.^{8,9} KDP crystal was discovered in 1935 by Busch and Scherrer.¹⁰ It crystallizes in tetragonal structure¹¹ at room temperature with a non-centrosymmetric point group $\bar{4}2m$ and acquires a shape or morphology known as tetragonal bipyramidal as shown in Fig. 3.1.^{12,13}

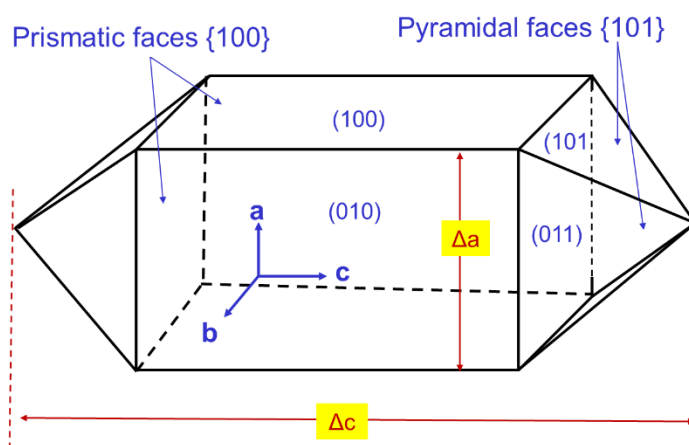


Fig. 3.1 Schematic line diagram showing morphology of KDP crystals.

It was initially used as a ferroelectric material, its growth however got an impetus after the advent of laser in 1961 when phase matched second harmonic conversion was realized in this crystal.¹⁴ However, the main challenge was to grow good optical quality crystals in large dimensions so that large size device elements could be fabricated to handle high energy lasers. KDP is an incongruently melting compound therefore melt growth is not a suitable technique for this crystal however it is sufficiently soluble in water with positive temperature coefficient of solubility. Therefore, slow cooling technique of aqueous solutions is one of the suitable techniques for its growth. Initially this crystal was

grown by suspending seed crystals in saturated solutions.¹⁵ This technique was known as conventional technique for KDP growth where a large size c-plate was used as seed. The main difficulty with this technique was the low growth rates of the order of 1-2 mm/day along *c*-axis and practically nil along *a* and *b*-directions. Therefore the crystal usually end up as elongated along *c*-axis. A few of such KDP crystals grown in our laboratory are shown in Fig. 3.2.¹⁶ The central pyramidal part about both sides of the seed plate is called as capping region and contain full of inclusions and defects. Therefore, each half part of the crystal was usable for device purposes leaving the capping part.

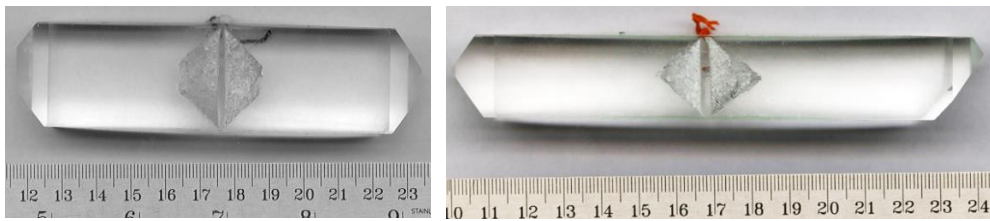


Fig. 3.2 KDP crystals grown by conventional method of hanging broad c-plate as seed in the solution. The central part shows capping region about seed plate.

This technique suffers with limited growth along cross section i.e. along *a* and *b*-axis of the crystal. The shape of the KDP crystal is usually quantified in terms of aspect ratio, defined as the ratio of the dimensions of the crystal along *c*-axis to that along *a*-axis,^{17,18}

i.e.
$$AR = \frac{\Delta c}{\Delta a} \quad \text{---- (3.1)}$$

Where Δc and Δa are the dimensions of the as-grown crystal along *c*- and *a*-axis respectively assuming growth rate along *a*- and *b*-axis to be similar due to crystallographic symmetry. The aspect ratio in case of conventionally grown KDP was therefore very high while isometric shape i.e. $AR = 1$ was preferable for large size device elements for laser applications.

To enhance the cross-section of KDP crystal various methods were developed by different researchers to modify crystal shape or aspect ratio. To circumvent this problem one of the methods known as “*seed splicing technique*” was developed by various researchers where four numbers of identical size (001) oriented plates were joined in a 2x2 array to make broad seed plate to be able to increase crystal cross section.¹⁹⁻²¹ However, this technique suffers with the strict demand of high order similarity of crystallographic orientation of all the seeds involved. Moreover, it resulted in a large capping region of no

use. Alternative approaches were developed by Sasaki et al.² and Loiacono et al.²² where they used “*three vessel method*” to grow KDP crystals at constant temperature and supersaturation for long time typically up to months and thereby grown large size crystals at a rate of 1 to 5 mm/day along c-axis from broad seeds.

In early 1990’s a major breakthrough was achieved by Zaitseva et al. when they developed “*rapid growth technique*” also known as platform technique.²³ This technique enabled to achieve approximately one order higher growth rate along all the three crystallographic axes of KDP compared to that achieved by the conventional techniques. The main features of this technique were, use of a point size seed at a horizontal platform rotating in highly supersaturated solution. The stability of the highly supersaturated solution was achieved by employing high purity chemicals, ultrafiltration, overheating of solution, and improving the design of the crystallizer.²⁴ The typical morphology of KDP crystal obtained⁴ by this technique was as shown in the Fig. 3.3.

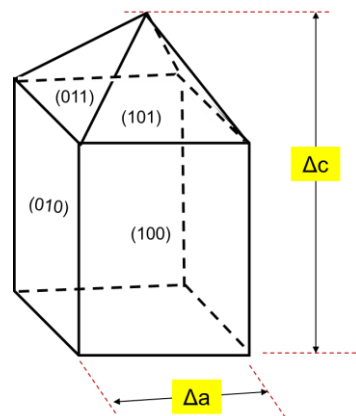


Fig. 3.3 Schematic diagram showing the morphology of the KDP crystals obtained by platform technique.

Further, it was found that this technique however solved the problems of low growth rate particularly along prismatic faces and formation of capping region. But the usable volume fraction for the devices such as laser frequency doublers, triplers and Pockels elements was very low.²⁵ Particularly the pyramidal cap portion which contains about 22% volume in case of isometric growth is of least use for the large size devices due to their specific crystallographic orientation⁴ This leads to wastage of material if a particular size element is required. Therefore, a demand was there to enhance usable volume fraction. Because it would not only reduce the amount of solution involved for

processing but correspondingly also reduce the sizes of crystallizer and water bath and demand of electrical power and growth duration as well. For this purpose, different researchers investigated on habit modification of KDP by optimization of growth influence parameters. Crystal habit in case of solution growth in general depends on relative growth rate of its habit faces. The relative growth rate of habit faces depends on several physicochemical parameters such as pH,^{17,26} supersaturation,¹⁷ temperature, impurities or additives,^{18,27} hydrodynamics,^{28,29} seed orientation,^{30,31} seed quality,³¹ nature of solvent etc. These factors however influenced relative growth rate of habit face but could not eliminate certain portion like pyramidal cap in case of KDP. Therefore, mechanical methods of shape modification are gaining importance in the field of solution crystal growth. In this context, Zeng et al. had reported “*mechanical direction limitation method*” or so called “parallel-plate method” where they successfully grown urea and its derivatives.³² Tatartchenko et al. employed similar design of parallel platform in multiple stacks and successfully grown large size KDP crystals in between them in the form of plates.^{25,33} This method however provided ~ 30-50 % volume usable for the preparation of frequency converters, but is prone to inclusions and nucleation due to difficulty in proper solution flow in between the plates. Further seed mounting in between the plates and removal of the grown crystal after growth are also practically difficult. Kim et al.³⁴ and Tu et al.³⁵ used this technique to grow *c*-oriented crystal without pyramidal cap in between parallel plates from a point seed. Youping et al.³⁶ and Salo et al.^{37,38} reported use of single-plate platform for oriented growth of KDP using large size (101) seed plate as seed to reduce capping portion. But it needs preparation of large size plate as seed with accurate orientation otherwise capping region may arise which would act as a source of defects. Bupalov *et al.* used a special chamber to restrict growth along all the undesired directions except one to grow mono-sectorial KDP crystal of desired shape with enhanced usable volume fraction.^{39,40} This method provided higher usable volume fraction in KDP compared to the pyramidal shape crystal for laser applications, but it requires to prepare large size seeds oriented along specific direction and high flow rate of the solution at the growing face. Ramasamy and co-workers developed another method called as “*unidirectional growth technique*” or so called “SR technique” based on solvent evaporation where crystal growth was confined in cylindrical glass tubes at all directions except one.⁴¹ This technique is suitable for growth of long crystals along a particular direction but growth of large aperture KDP crystals with suitable aspect ratio is difficult

due to low growth rate along a and b - directions.⁴² Verma et al reported unidirectional growth of KDP in cylindrical tubes by using slow cooling method to enhance usable volume fraction for SHG elements.⁴³ However, it suffers with low growth rate as compared to rapid growth technique due to free convection conditions during growth.

We have developed another methodology for shape modification of KDP crystals during growth to enhance usable volume fraction for devices. The crystals grown with technique resulted in to flat-top hence called as “flat-top technique”.⁴⁴ In this chapter we have described the flat-top growth technique and its application to grow KDP crystals with high usable volume fraction for electro-optic modulators and SHG elements. The work is associated with following experimental works:

A) Development of a water bath and a crystallizer

B) Development of a seed protection technique

3.2 Development of a water bath and a crystallizer

KDP crystals are grown by low temperature solution growth technique due to its sufficient solubility in water. For solution growth of a crystal various items are required. Such as water bath, crystallizer, filtration unit, water purification unit, heaters, high purity chemicals, temperature controllers for the bath, pH meter, stepper motor and its controller etc. Among these we have mainly designed and fabricated water bath and crystallizer for growth of KDP crystals as described below.

3.2.1 Fabrication of a thermostatic water bath

Water bath is an important part of crystal growth workstation from solutions. It is because high order of temperature stability and uniformity is required around the crystallizer to prevent unsteady growth and chances of nucleation in the solution. Water is not only cheap and safe in handling but also has high specific heat therefore suitable liquid for use in thermostatic baths for temperature up to about 95 °C. We have used a cylindrical shape tank of high density polyethylene (HDPE) of diameter 60 cm and height ~ 60 cm for making a thermostatic water bath. It had capacity of storing water more than 150 liter. To heat this water, we fabricated four number L-shape resistive heaters of almost equal resistance and similar dimensions. These were mounted equispaced at the periphery of the tank to heat the water. The heaters were joined in series and connected to a programmable

PID temperature controller (*Eurotherm 902P*) and a thyristor unit (*Eurotherm 425A*) along with a Pt-100 RTD (resistance temperature detector) temperature sensor placed in the bath. The heater has power capacity of maximum 800 W. The bath was also provided with cooling tubes for fast cooling purposes. The cooling tubes were made using stainless steel tubes of 12 mm diameter and symmetrically placed in the bath. A water chiller associated with a water pump was connected to the cooling tubes. Two viewing ports of diameter about 100 mm were designed and fabricated at two opposite ends of the bath. Perspex sheets were used for fabrication of the windows. The bath was insulated with a layer of foam sheet of about 10 mm thickness around it for reducing influence of temperature fluctuation of surroundings. The bath was also provided with a stainless steel make stand to place crystallizer. Fig. 3.4 shows a photograph of the fabricated water bath. A detail of the design of the bath and the associated crystallizer is given schematically in Fig. 3.5.

The bath was tested for several days up to 80.0 °C and found no leakage at windows. The short term (~ 1 hour) localized temperature stability of the bath was within ± 0.02 °C and the long term (~ 24 hours) localized temperature stability was ± 0.05 °C. The axial temperature profile of the bath was measured at four different set temperature as shown in Fig. 3.6, showing almost uniform temperature in the bath with slightly lower temperature at top layer of water in the bath due to evaporation.

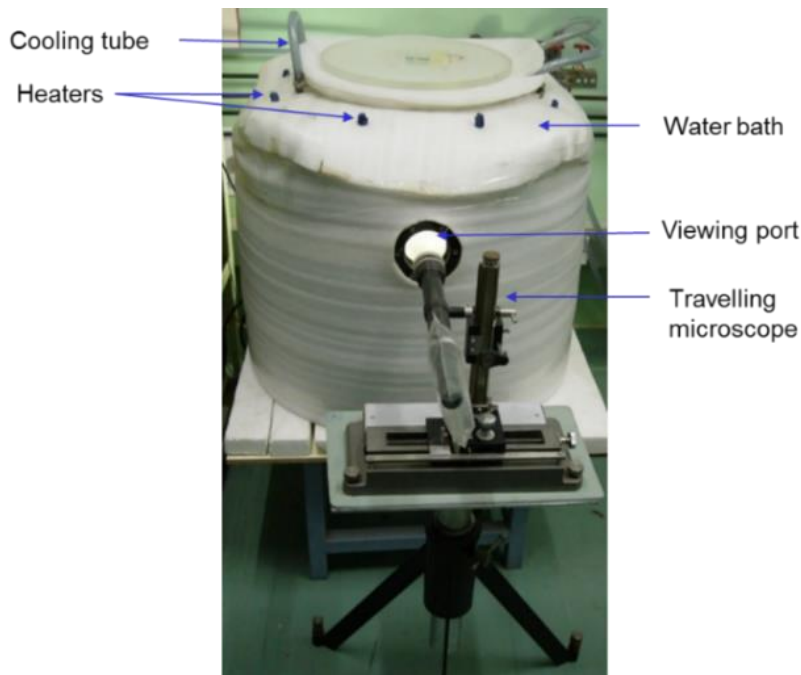


Fig. 3.4 Photograph of the fabricated water bath of capacity ~ 150 liter.

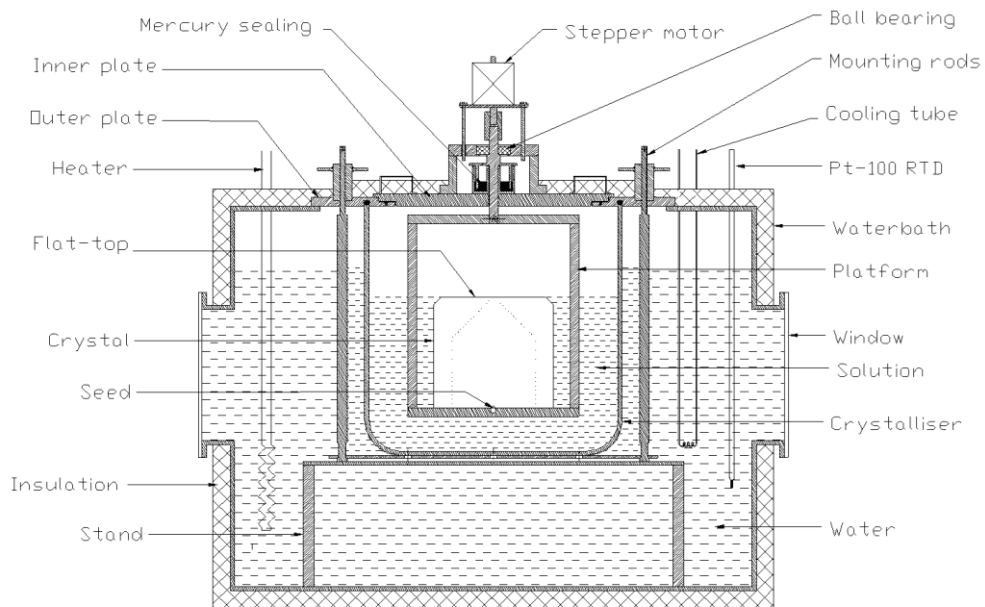


Fig. 3.5 Schematic line diagram of the crystal growth workstation including water bath and crystallizer.

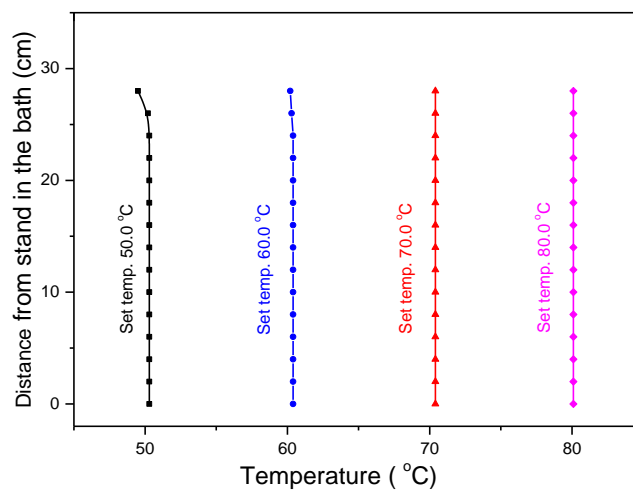


Fig. 3.6 Variation of axial temperature inside the water bath at four different set temperatures.

3.2.2 Fabrication of crystallizer and platform

Crystallizer is an important part of solution crystal growth. It contains the prepared solution and a seed-platform assembly for crystal growth. Some of the important features of a good crystallizer are high visibility, leak proof against vapours, facility of smooth

rotation of the seed-platform assembly and use of inert material for construction of all the contact part with solution. We have designed and fabricated a crystallizer as shown in Fig. 3.7. It consists of a borosilicate glass beaker of diameter ~ 30 cm and height ~ 28 cm, to store solution, two concentric lids of Perspex at top called as outer lid and inner lid, a Perspex make platform which is connected with a stepper motor via a ball bearing assembly and sealing mechanisms for the lids at the top of beaker. The outer lid was provided with a circular groove of about 10 mm depth to fit on the glass beaker where a silicone rubber make gasket was placed in between. The lid was locked at the beaker using eight numbers of stainless steel make long nuts and bolts placed equi-spaced around the beaker as shown in Fig. 3.7. The inner lid rests on the outer lid with a silicone rubber make circular gasket in between the two lids. A Perspex make square shape platform was fabricated having four vertical posts at four corners. A nylon make shaft was used to connect the platform with the stepper motor. A ball bearing assembly was fitted around the shaft of the platform and below the stepper motor for smooth rotation of the platform. A mercury seal in the form of a cup-socket mechanism was provided around the shaft to prevent leakage of solvent from the solution. The stepper motor was connected to a controller called as ACRT (accelerated crystal rotation technique) for reversible rotation of the platform in accelerated and decelerated manner.⁴⁵ It is useful to minimize the chances of jerks to the growing crystal relative to the platform during the reversal of rotational motion of the platform in the solution.

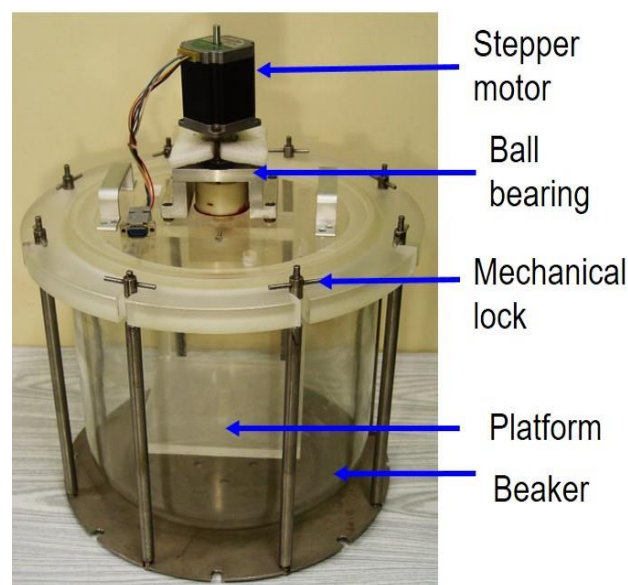


Fig. 3.7 A photograph of the fabricated crystallizer having ~ 15 liter solution capacity.

Axial temperature profile inside the crystallizer

Measurement of temperature profile inside the water bath and crystallizer is an important activity for solution crystal growth. It is like a test of the quality of the growth system. A uniform temperature is desirable to avoid concentration and temperature gradient at the growing crystal. Therefore, the axial temperature profile inside the 20 liter capacity crystallizer was measured at different set temperatures of the water bath namely 40.0 °C, 50.0 °C and 60.0 °C using a *Eurotherm* make programmable PID temperature controller. The crystallizer was filled with water up to ~ 18 cm height and placed in the water bath. The axial variation of temperature of the water placed in the crystallizer was measured using a Pt-100 RTD sensor associated with a display of resolution 0.01 °C. The temperature stability of the water bath was about ± 0.02 °C. The profile was measured from the bottom of the crystallizer to that above the water surface as well inside the crystallizer. Fig. 3.8 shows the obtained axial temperature profile at three different set temperature of the water bath. The results show that the temperature inside the water of the crystallizer is almost uniform while there was a small negative gradient of ~ 1 °C in 20 mm length at the solution-air interface region above which the temperature is again uniform in the air inside the crystallizer. This results show that the designed and fabricated water bath and crystalliser are suitable for solution growth of crystals.

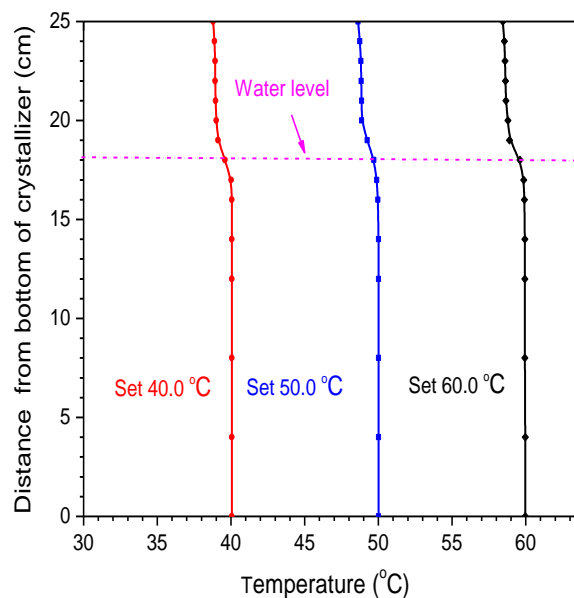


Fig. 3.8 Variation of axial temperature inside the crystallizer filled with water up to 18 cm height at three different values of set temperature of the water bath.

Schematic of a solution growth workstation:

A complete crystal growth workstation based on platform technique comprises various components such as water bath, crystallizer, temperature controllers, etc. as shown schematically in Fig. 3.9.

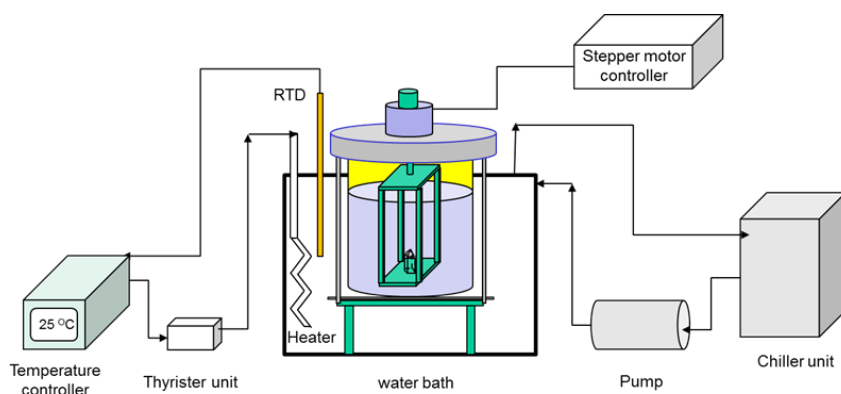


Fig. 3.9 Schematic of a crystal growth workstation based on platform technique.

3.2.3 Procedure of solution preparation and its processing for KDP crystal growth

KDP chemical was synthesised by reacting potassium carbonate (*Merck* 99.9 % pure) and phosphorous pentaoxide (*Fluka* 98 % pure) in 1:1 molar ratio in high purity demineralized water (resistivity 18.2 M Ω .cm) obtained from *Millipore* make water purification system. It involves following steps:

- i) $\text{K}_2\text{CO}_3 + \text{H}_2\text{O} \rightarrow \text{K}_2\text{CO}_3 (\text{aq.})$
- ii) $\text{P}_2\text{O}_5 + 3\text{H}_2\text{O} \rightarrow 2\text{H}_3\text{PO}_4 (\text{aq.}) + \text{heat}$
- iii) $\text{K}_2\text{CO}_3 (\text{aq.}) + 2\text{H}_3\text{PO}_4 (\text{aq.}) \rightarrow 2\text{KH}_2\text{PO}_4 (\text{aq. soln.}) + \text{CO}_2 (\text{g}) + \text{H}_2\text{O}$

The preparation of ortho-phosphoric acid (step ii) requires special care as it is highly exothermic reaction and that lead to formation of acidic fumes. To reduce the generation of fumes, first we prepared a small amount of viscous paste of P_2O_5 , keeping the quantity of the water as low as possible. It helped to reduce generation of fumes. Later we added P_2O_5 powder and mixed it in the prepared paste with the help of a glass rod. Once the viscous whitish paste was formed water was added slowly in drops. This procedure helped to reduce the generation of hazardous acidic fumes a lot. Further we placed the beaker in a tray of running water to control the temperature. Once both the aqueous solutions were prepared in two separate beakers. The acid was slowly poured into the basic solution under strong stirring using a magnetic stirrer. In this process carbon dioxide gas releases in the

form of bubbles. After completion of the reaction pH was checked and adjusted for the stoichiometric value ~ 4.2 . Subsequently the solution was heated under stirring for many hours and filtered and subsequently evaporated to obtain KDP salt. The prepared salt was first tested for phase by powder X-ray diffraction technique and then recrystallized in fresh water. About 50 % of mass was recrystallized to use for crystal growth.

For preparation of the solution for crystal growth, first the crystallizer and its lids were thoroughly cleaned using acetone for any oily material at surfaces and then with *Extran* neutral solution (*Merck* make) in general with demineralised water. Saturated solution was prepared as per standard solubility curve of KDP.¹⁴ The solution was filtered through 0.2 μm porosity and 47 mm diameter nylon membrane filter sheets using a vacuum filtration unit. The filtered solution was carefully transferred to the crystallizer through silicone rubber tube to avoid entry of dust particles from the atmosphere. A schematic of this process is shown in Fig. 3.10.

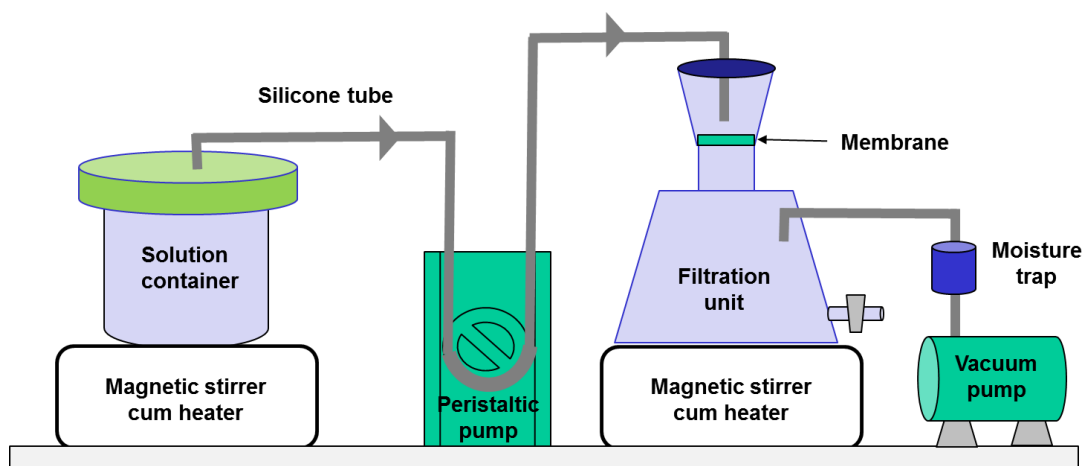


Fig. 3.10 Schematic showing process of solution filtration.

3.3 Development of a seed protection technique

In case of seeded growth of a material from solution, a small size seed crystal of preferably same material is inserted in the saturated solution. Followed by maintenance of solution temperature in the metastable zone for growth of single crystal without nucleation. However, there are various factors which may cause nucleation. Once a nuclei formed in the solution, it hampers seriously the further growth and quality of the crystal and therefore one has to normally terminate the growth run. Some of the reasons of formation of nuclei after the insertion of the seed or seed-platform assembly is the temperature mismatch

between the solution and the materials inserted, and detachment of some wear and tear from the seed surface due to rapid dissolution or growth at the time of insertion to attain equilibrium with solution. One of the remedies to this problem is to overheat the solution for sufficient time after the insertion of the seed so that minute unseen nuclei can be destroyed by the thermal energy.⁴⁶ However, overheating after the insertion of seed is not advisable because it may dissolve the seed itself. Some of the researchers have proposed a few techniques to overcome the problem of seed dissolution during overheating. Montgomery et al. designed and fabricated a mechanical structure called as “seed protector” to entirely cover the seed, placed at the platform during overheating.⁴⁷ Karnal et al. used mercury to completely cover the seed during overheating state.⁴⁸ The former technique is complicated as it requires insertion and removal of a specific type mechanical assembly which is itself prone to nucleation. The latter technique is based on adding mercury in the solution to keep submerge the seed. However, presence of mercury in many cases may itself act as an impurity or may react with chemicals involved. Our approach is different; it does not require to add any foreign item or chemical in the solution. It is based on mounting a long seed in a hole made at the centre of the platform. For this purpose, special seed holder was fabricated using glass tubes or teflon tubes as shown schematically in Fig. 3.11.

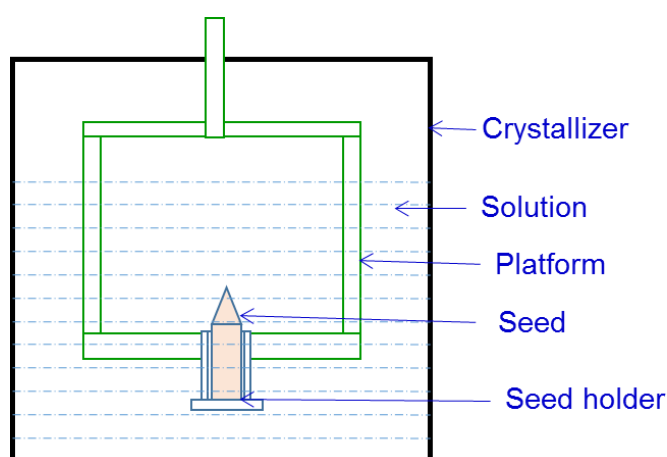


Fig. 3.11 Schematic diagram showing seed protection technique.

The principle of this technique is based on the role of gravity to delay diffusion of solute concentration at upward direction. In our case the solution in the vicinity of seed in the seed holder tube has very little effect of rotation of the platform due to its small diameter and large depth. We used a glass tube of 5 mm inner diameter and length ~ 20 mm to use

as seed holder and obtained KDP seed life ~ 2 days at an overheating by 20 °C for a solution saturated at 45 °C. Table 3.1 shows the observations made on dissolution of KDP in seed holder with duration of overheating. Fig. 3.12 shows the image of seed holders of 15 mm and 20 mm length after an overheating duration of 47.5 hrs.⁴⁹

Table 3.1 Depth of dissolution of KDP seed versus duration of overheating by 20 °C for KDP solution saturated at 45 °C.

Sr. No.	Duration of overheating (hr)	Depth of dissolution of seed (mm)
1	0.0	0.0
2	24.3	14.6
3	47.5	17.4
4	61.5	18.0



Fig. 3.12 Seed holders of length 15 and 20 mm showing remaining KDP seed part in the longer tube after 47.5 hours of overheating.

We tested this technique for growth of KDP and LAP crystals. One of the KDP crystal grown using this “seed safety technique” in the crystal growth system described above is shown in Fig. 3.13.



Fig. 3.13 KDP crystal grown using seed protection technique.

The growth parameters for this crystals were:

- * Saturation temperature: 55 °C.
- * Seed size: $3 \times 3 \times 14 \text{ mm}^3$
- * Depth of seed in the seed holder: ~ 12 mm
- * Overheating of the solution by 10 °C for 24 hrs
- * Dimensions: $75 \times 78 \times 125 \text{ mm}^3$
- * Mass: 1280 g
- * Growth duration: 25 days
- * R_c (avg.) = 5.0 mm/day, R_a (avg.) = 1.5 mm/day
- * Yield of crystallization: ~ 24 %
- * No nucleation and inclusion during growth

Where the yield of crystallization in percentage is defined as,

$$\% \text{ Yield of crystallization} = \frac{\text{Mass of grown crystal}}{\text{Mass of solute used for solution preparation}} \times 100 \quad \text{---- (3.2)}$$

3.4 Development of shape modification techniques to enhance usable volume fraction of KDP crystals

KDP, if freely grown in solution, acquires its natural morphology of tetragonal bipyramidal shape as shown in Fig. 3.1, while platform technique provides a shape of tetragonal pyramidal type as shown in Fig. 3.3. A major concern of shape of KDP is there

because none of its natural faces either (100) or (100) is directly usable for any of its three major applications namely Pockels elements, SHG type-I and SHG type-II elements for Nd:YAG laser.^{4,25} It therefore requires cutting and processing of the grown crystal as per the required elements that leads to a wastage of a large portion with respect to the intended dimensions of the elements. Table 3.2 shows the orientation of plates for different applications of the KDP to use with Nd:YAG or Nd:Glass lasers.

Table 3.2 Orientation of the normal to the device plate of KDP w.r.t. its crystallographic coordinate system for different applications with Nd:YAG laser.

Device element	Θ_{PM} (degree)	Φ_{PM} (degree)
<i>Pockels element</i>	0	--
<i>SHG type-I</i>	41	45
<i>SHG type-II</i>	59	90

We analysed these issues and developed some techniques to enhance usable volume fraction of as grown KDP crystal starting from natural morphology c-oriented seeds.

These are listed as follows,

- a. Three - plate method for SHG type-II oriented growth of KDP crystals,*
- b. Flat - top technique to enhance usable volume fraction of KDP particularly for Pockels elements, and*
- c. Flat - top technique along with oriented seed methodology to enhance usable volume fraction for type-I and type-II SHG elements.*

3.4.1 Three plate technique for SHG type-II oriented growth of KDP crystals

We initially designed a three plate platform as shown schematically in Fig. 3.14 (a) to obtain type-II SHG oriented KDP crystal. The angle between the horizontal plate and that of slanting plate was kept $(90 - \theta_{PM})$, where θ_{PM} is the phase matching angle for type-II SHG. This makes the crystal shape of the grown crystal such that every plate parallel to the slant face be a SHG type-II plate. A KDP crystal of dimensions $(a \times b \times c)$ $60 \times 40 \times 40$ mm³ was grown successfully as shown in Fig. 3.14 (b) from a point seed, but it was found that the plates of the platform restrict smooth flow of solution in between the plates where

seed was placed and in addition removal of the grown crystal was also difficult as it was covered from three sides by perspex plates. So we thought for some other better design. This led to development of the flat-to technique.⁴⁴

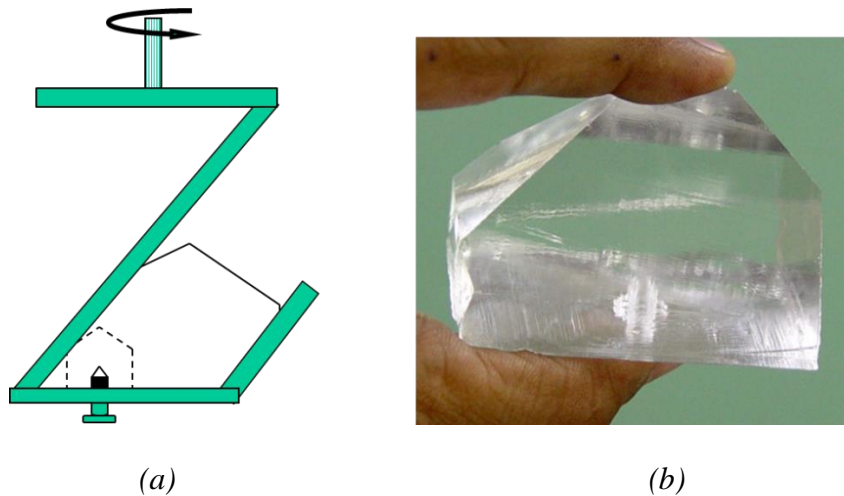


Fig. 3.14 (a) Schematic design of three plate platform for growth of SHG type-II oriented KDP crystals, and (b) photograph of an as-grown KDP crystal.

Salient features of this technique:

*Three-plate structure oriented at a specific angle was designed and fabricated for SHG type-II oriented growth of KDP crystal.

*Small size, naturally grown c-oriented seed without any processing was used for SHG oriented growth of KDP crystal.

*Higher material yield was obtained compared to single platform grown KDP crystals for type-II SHG element.

*Lesser number of cuts are required for preparation of SHG element compared to single platform grown crystals.

*Phase matching direction was within $\pm 2^\circ\text{C}$ from the exact normal to the crystal surface which can be improved further by improved mounting of the seed crystal.

3.4.2 Flat-top technique to enhance usable volume fraction of KDP

Flat-top technique of crystal shape modification is based on utilization of solution-air interface present in the solution for modification of crystal shape during growth.⁴⁴ The

interface is almost horizontal and acts as a barrier to restrict the growth of crystal beyond it. We tried this methodology for shape modification of KDP crystals and successfully grown KDP crystals between a single horizontal plate of perspex and solution-air interface without any nucleation, crack or visible inclusions. It is somewhat like growth between two flat barriers at opposite sides where one of the barriers is soft. Therefore, chances of thermal stresses are somewhat lower during variation of growth temperature of the solution. It is a different growth methodology for shape modification of crystals compared to the use of two rigid parallel plates as reported by several other research groups.^{32,33} A schematic illustration of this technique is shown in Fig. 3.15. The seed crystal is placed as facing c-axis upward and grow under slow cooling scheme of solution. Once its apex reaches at the solution-air interface (crystal 'a' in yellow), it ceases to grow upward as there is no solution but the submerged parts of the prismatic and pyramidal faces keeps growing continuously normal to the habit faces. This led to broadening of flat-top part as shown in crystal 'b' in light blue colour and hence broadening of crystal cross section. If the growth is kept continued further it led to reduction of pyramidal cap portion of the KDP crystal which is the least usable portion for large size devices. An empirical relation can be derived between the relative growth rates of the KDP along horizontal direction (R_x) and vertical direction (R_z) at the platform with the dimension of the platform 'w' and the gap between the platform and the solution-air interface 'h' for obtaining a flat-top crystal in case growth kept continued. It is based on the fact that if the time taken by the seed cap to reach at the interface is less than the time taken by its side face to reach the edge of the platform, the crystal will acquire a flat top. This condition can be written mathematically as,⁴⁴

$$\frac{h}{R_z} < \frac{(w/2)}{R_x}$$

simplified to, $\left(\frac{R_z}{R_x}\right)_{average} > \frac{2h}{w}$ ---- (3.3)

It shows that achievement of flat-top crystal is related with the ratio of average growth rates along vertical and horizontal directions of the crystal and the dimensions of the platform and its positioning in the solution. As these are independent parameters, therefore the inequality 3.3 can easily be satisfied. The left part of the inequality 3.3 shows relative growth rate of habit faces which depends on growth condition such as supersaturation, pH

value, additives and impurities, hydrodynamics etc., While the right side part of the inequality 3.3 shows design parameter of the platform and its location in the solution.

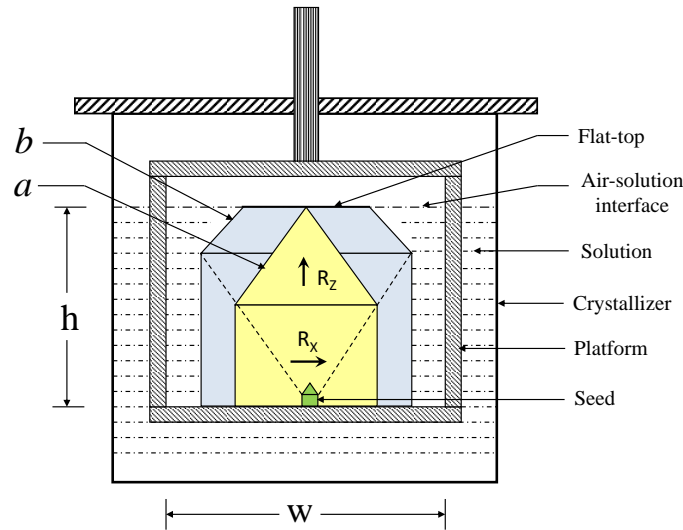


Fig. 3.15 Schematic showing modification of crystal shape by solution-air interface as growth proceeds from pyramidal-cap crystal (a), to the flat-top shaped crystal (b).

Some of the KDP crystals grown using the flat-top technique are shown in the Fig. 3.16, where small size c-oriented naturally grown KDP crystals were used as seeds. The growth details of these crystals with respect to the platform parameters in the crystallizer are shown in the Table 3.3 satisfying the inequality 3.3.

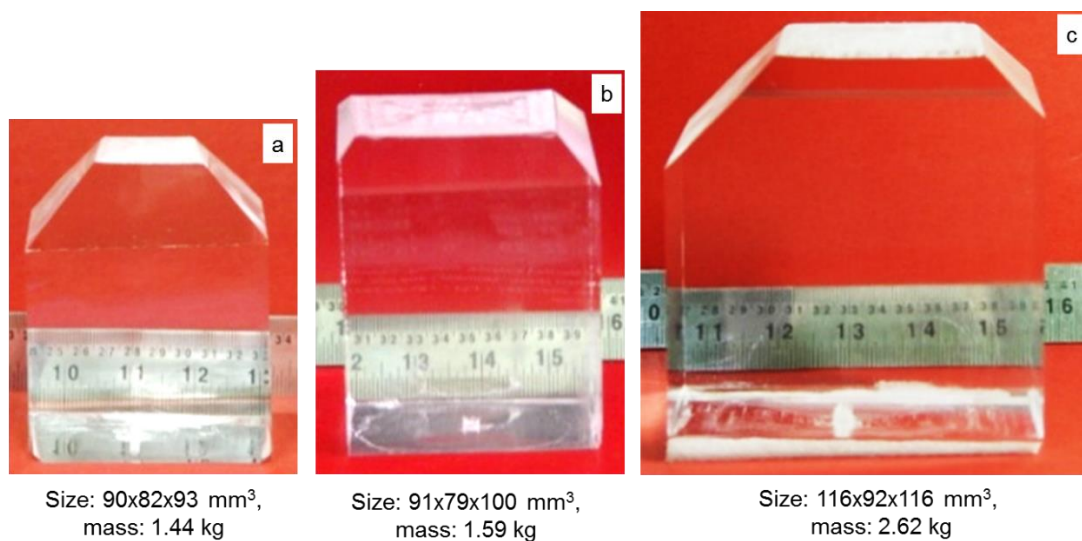


Fig. 3.16 Photographs of three KDP crystals grown using c-oriented point seeds employing flat-top growth methodology.

Table 3.3 Growth details of the flat-top shape KDP crystals along with design parameters of the platform showing the validity of the empirical relationship 3.3 for flat-top growth.

Soln.-air interface level above platform h (mm)	width of the platform w (mm)	$\frac{2h}{w}$	Saturation temp. T_{sat} °C	Average cooling rate in the expt. $\left(\frac{T_f - T_i}{\text{Time}}\right)$ °C/day	Average growth rate along [001]; R_z (mm/day)	Average growth rate along [100]; R_x (mm/day)	Ratio of growth rates $\frac{R_z}{R_x}$	Flat-top growth condition $\frac{R_z}{R_x} > \frac{2h}{w}$	Crystal image Fig no.
93	140	1.33	48.5	0.95	4.6	1.5	3.07	Yes	3.16 (a)
100	140	1.43	66.8	0.82	5.2	1.6	3.25	Yes	3.16 (b)
116	140	1.66	63.0	0.78	4.1	1.1	3.72	Yes	3.16 (c)

Further a comparative analysis was carried out to demonstrate the relative benefits of flat-top growth of KDP comparative to the case if the growth would be stopped at the time of the pyramidal cap just touched the solution-air interface. This comparison is listed in Table 3.4 for the large size crystal shown at Fig. 3.16 (c).

Table 3.4 Comparison of the process conditions and crystal parameters at two different stages of growth viz. when pyramidal-cap just reaches the solution-air interface and second at the end of the growth run when the flat-top shaped KDP crystal has been grown.

Growth stage	Process conditions and parameters of the grown crystals					
	Cooling range (°C)	Total super-cooling (°C)	Crystal mass (Kg)	Crystallization Yield (%) $\frac{\text{Mass of xtal grown}}{\text{Mass of solute in soln}}$	Crystal size $a \times b \times h$ (mm ³)	Volume of device element for Pockels cell
When the pyramidal cap just touches the solution-air interface	63 → 48	15	1.27	~ 24 %	85×68×116	~ 89 %
Final stage when the flat-top shaped crystal is grown	63 → 28	35	2.62	~ 50 %	116×92×116	~ 100 %

Salient features of flat-top technique:

* Higher material yield for fabrication of SHG elements and Pockels elements compared to the pyramidal shape KDP because the pyramidal cap portion reduces as the flat-top area increases. Thus the mass corresponding to the pyramidal portion is diverted to prismatic faces leading to enlargement of the cross section of the crystal. Thereby usable volume fractions for SHG elements and Pockels elements increase compared to that in pyramidal shape KDP of similar mass or similar cross section. In case of rapid growth of KDP where usually isometric growth takes place the volume contained by pyramidal portion may as high as 22%, which can be diverted to prismatic sector by proper design of experiment. It is thus possible to obtain ~ 100% material usable for Pockels elements by the flat top technique.

* Cross-section can easily be enlarged even in case of low relative growth rate along prismatic faces compared to that along pyramidal faces.

* It imparts higher crystallization yield compared to the case if the growth run was terminated up to pyramidal shape KDP.

* No nucleation and no inclusion was observed during growth indicates that flattening of the crystal top by solution-air interface do not act a source of nucleation or inclusion.

* There is no need to terminate growth run if the crystal apex reaches to the solution-air interface. It shows that the growth can be continued till room temperature or below until the size of the platform allows. This also facilitates to eliminate the chances of thermal cracks in the crystal by continuing growth down to room temperature because there is now no compulsion to terminate the growth run if crystal cap reached at the solution-air interface.

3.4.3 Flat-top technique along with oriented seed methodology to enhance usable volume fraction for type-I and type-II SHG elements

Growth of flat-top KDP crystal with c-oriented natural seed at the platform is suitable to enhance usable volume fraction particularly for fabrication of Pockels elements up to ~ 100%. While it is not the case for SHG elements. It is because the orientation of SHG plates either for type-I or type-II phase matching configuration is not parallel or perpendicular to any of the habit faces of KDP. To enhance the usable volume fraction for SHG elements, the geometry of the platform and the phase matching angles for SHG were

analysed and devised a method for orientation of natural unprocessed c-oriented seed at the platform. We know that phase matching direction for a particular type of interaction (type-I or type-II) is defined by two angle (θ , φ) with respect to principle axes of a crystal (x , y , z) which in case of KDP corresponds to the crystallographic axes (a , b , c). The values of these angles for Nd:YAG laser is shown in Table 3.2. θ is called polar angle made by the direction of laser beam with c -axis while φ is called azimuthal angle, made by the projection of the beam direction with respect to the x -axis as shown by line diagram in Fig. 3.17.

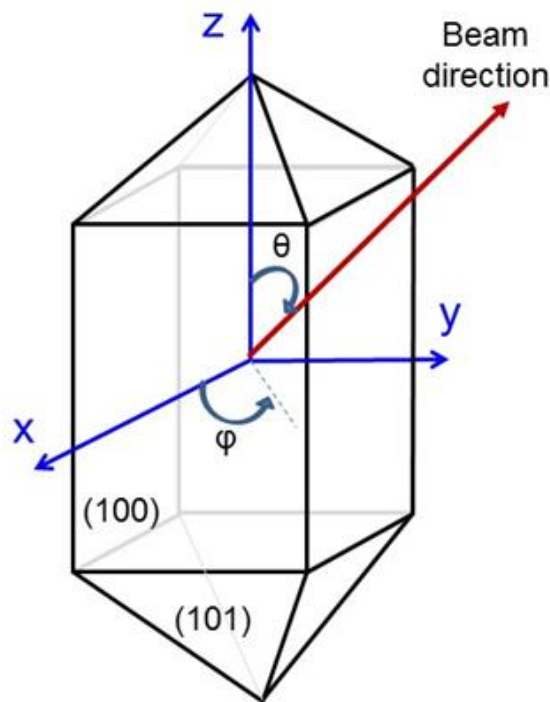


Fig. 3.17 Depiction of beam direction (θ , Φ) with respect to the principal axes (x , y , z) of KDP crystal.

To find a solution, we thought that SHG element has a certain plane to face the beam normally, if that plane is made either parallel or perpendicular to the platform by properly orienting the seed then it would be possible to have directly usable face for entering beam for SHG applications. Further if we apply flat-top methodology, the opposite face can be made parallel and hence the usable volume fraction can be further enhanced compared to the pyramidal cap or flat-top shape KDP crystals. The method of orienting KDP seed crystal is shown schematically in Fig. 3.18.⁵⁰

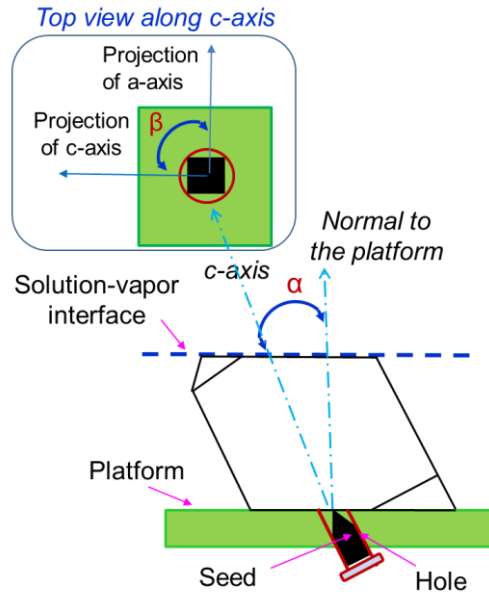


Fig. 3.18 Schematic depiction of the orientation methodology of KDP seed at the platform for growth of SHG oriented crystal.

There are two specific angles α and β for orienting the seed. ' α ' is the angle made by the c-axis of the seed with that of the normal to the platform while ' β ' is the angle of rotation of the seed about c-axis after aligning one of 'a' or 'b' edge of the seed with that of the edge of the square shape platform. The angle ' α ' can easily be achieved by drilling a hole in the perspex platform at that angle keeping its projection along one of the edge of the platform. The values of these angles for particular type of SHG elements and its orientation whether parallel or perpendicular to the platform is given in Table 3.5.

Table 3.5 Values of angles α and β for orientating KDP seed crystal for SHG oriented growth

SHG type	Seed orientation (α, β) for SHG elements			
	Normal to the platform		Parallel to the platform	
	α	β	α	β
Type-II	31°	90°	59°	90°
Type-I	49°	45°	41°	45°

3.4.3.1 Growth of type-I SHG oriented KDP crystals by flat-top technique

Employing the above methodology of seed orientation, we first fabricated a perspex platform of $100 \times 100 \text{ mm}^2$ size and drilled a hole at angle of 41° from the perpendicular at the centre for type-I SHG oriented growth to obtain SHG type-I plates parallel to the platform keeping the projection along one of the edge of the platform. For this purpose, a mount was made to hold the plate at the specific angle at the drill machine. For placement of the seed a glass tube make seed holder was used, wherein a small size seed of c-oriented KDP was mounted using teflon tape. The seed holder was inserted in the hole made at the platform and rotated by 45° to satisfy the β angle as mentioned in Table 3.5. The crystal growth was conducted by slow cooling method. Fig. 3.19 (a) shows the as-grown KDP crystal of dimensions $40 \times 47 \times 65 \text{ mm}^3$ ($a \times b \times c$). The crystal was sliced parallel to its base using *Buehler* make low speed saw as shown in Fig. 3.20. The plates were subsequently polished using fine alumina powder with dehydrated ethylene glycol at the polishing cloths mounted on the *Buehler* make polishing machine. Fig. 3.19 (b) shows one of the type-I SHG elements of size $41 \times 53 \times 12 \text{ mm}^3$ (base area \times thickness) obtained from the crystal.

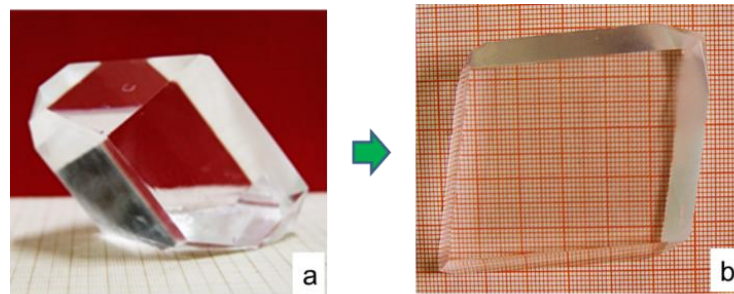


Fig. 3.19 (a) As-grown type-I SHG oriented KDP crystal, and (b) prepared type-I SHG element by slicing the crystal parallel to its base.



Fig. 3.20 Slicing process of type-I SHG oriented KDP parallel to its base using Buehler make low speed saw.

The prepared elements were tested for SHG orientation at Nd:YAG laser and the experimentally observed direction of optimum SHG was within 2° tilt with respect to the normal to its face. The fine tuning of the orientation for SHG can be obtained using a mechanical orienter. A comparison of masses of the prepared plates with that of the grown crystal showed that nearly 48% volume of the crystal was usable for the SHG elements which is higher than that reported (30 %) by Tatartchenko et al.²⁵ This ratio can further be enhanced by achieving complete flat-top.

3.4.3.2 Growth of type-II SHG oriented KDP crystals by flat-top technique

In order to grow directly SHG oriented KDP of type-II configuration, we prepared a platform and drilled a hole at 31° from the normal to the surface to obtain the SHG element normal to the platform. For fabrication of the platform a similar procedure was followed as described in the earlier section. Seed was placed in the seed holder and it was rotated in the platform so as to match its one of $\{100\}$ face exactly normal to the platform. This was done to match the angle β to be 90° as mentioned in the Table 3.5. The crystal growth was conducted by standard slow cooling method with reversible rotation in ACRT mode. Fig. 3.21 (a) shows the as grown flat-top type-II SHG oriented KDP crystal of size $57 \times 60 \times 66 \text{ mm}^3$ ($a \times b \times c$). Fig. 3.21 (b) shows the pieces cut from the crystal by cutting normal to its base using a wet thread cutter and Fig. 3.21 (c) shows the polished type-II SHG element of size $57 \times 57 \times 30 \text{ mm}^3$. The usable volume fraction in terms of mass ratio was $\sim 56\%$ which is higher than that reported (50 %) by Tatartchenko et al.²⁵

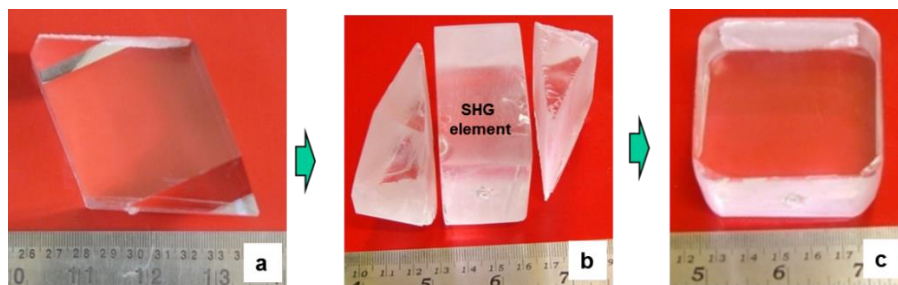


Fig. 3.21 (a) As-grown type-II SHG oriented flat-top KDP crystal, (b) cut parts normal to its base and (c) prepared type-II SHG element.

3.5 Characterization of flat-top KDP crystals

The grown KDP crystals were characterized by different techniques for optical quality, crystalline perfection, defects structure and chemical impurities distribution by various technique.⁵¹ The main concern was to investigate the influence of the abrupt termination

of growth in the solution by solution-air interface. To analyse it in detail, we prepared various samples from different parts of a flat-top KDP crystal. For this purpose, we took the crystal shown in Fig. 3.16 (a). The crystal is again shown from a different viewing angle at Fig. 3.22 (a). It clearly shows the flat-top part, (100) and (101) faces and seed positions in the crystal. Fig. 3.22 (b) shows schematic of locations of six plates namely (001) bottom, (001) middle, (001) top, (100), (010) and (101) plates prepared for assessment of crystal quality at different parts of the crystal. The crystal was cut carefully using a wet thread cutter using ethylene-water mixture at 1:1 ratio. The obtained plates were grinded carefully at 600 grit number emery papers and then lapped at 1200 grit number emery papers using ethylene glycol as a lubricant cum coolant. The plates were subsequently polished using 0.3 μm and 0.05 μm particle size alumina abrasives in sequence at polishing cloth mounted at the Buehler make polishing machine with dehydrated ethylene glycol. An image of these plates is shown in Fig. 3.23.

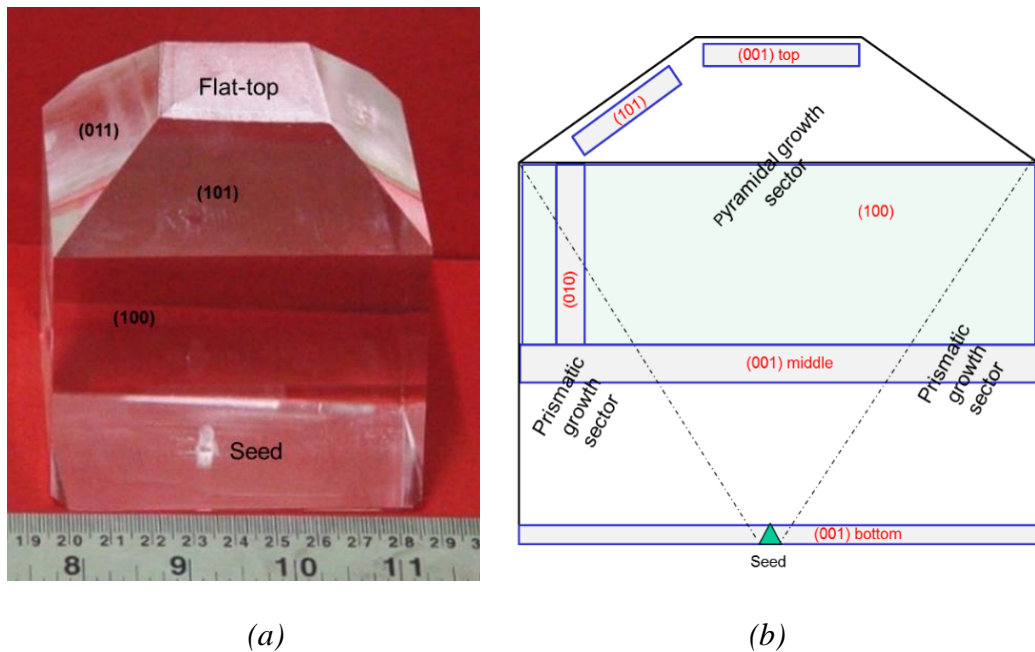


Fig. 3.22 (a) Another view of the Flat-top KDP crystal showing different faces, seed and flat-top part for preparation of samples, (b) schematic depiction of location and orientation of six plates prepared for different characterizations.

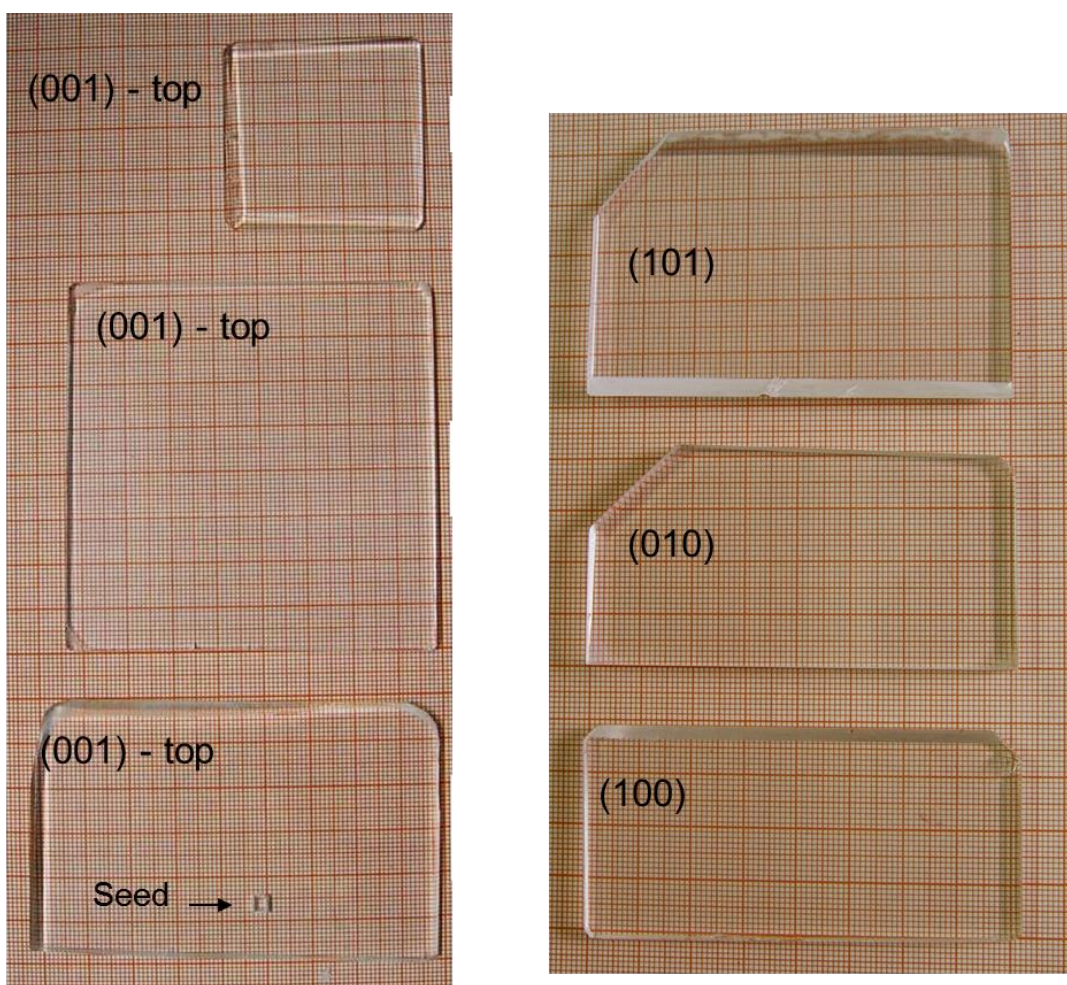


Fig. 3.23 Six sample plates prepared from one of the flat-top KDP crystals for characterization purpose.

3.5.1 Structural identification by powder X-ray diffraction

The synthesised KDP chemical was characterized by powder X-ray diffraction technique for phase identification. Fig. 3.24 shows the powder X-ray diffraction pattern of recrystallized KDP chemical in the range of $10^\circ - 60^\circ$ with angular steps of 0.01° using Rigaku make X-ray diffractometer with copper K_α radiation. The diffraction peaks positions were in good agreement with that reported in the literature and at JCPDS card 84-0520 confirming the phase to be KDP for the prepared chemical.

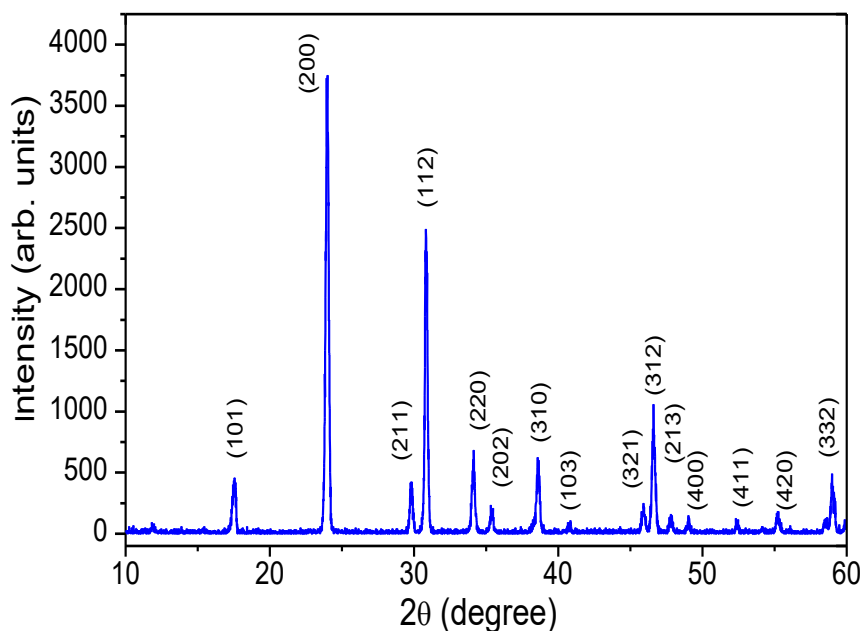


Fig. 3.24 Powder X-ray diffraction pattern of recrystallized KDP chemical prepared for crystal growth.

3.5.2 Crystalline perfection by high resolution X-ray diffraction

Crystalline perfection was investigated using high resolution X-ray diffraction (HRXRD) facility at the National Physical Laboratory, New Delhi.⁵² The characterization facility consists of a multi-crystal diffractometer to obtain a well-collimated and monochromatic Mo-K α X-ray beam for analysis of crystalline perfection of samples. The spectral purity ($\Delta\lambda/\lambda$) and divergence of the exploring Mo-K α beam were $< 10^{-5}$ and $\ll 3$ arc sec respectively. The minimum angular resolution for rotational stage containing sample about the plane of diffraction was 0.4 arc sec. We used the as-grow KDP crystal as such for this particular characterization. The (100) face of the crystal was aligned to get maximum diffraction intensity from the (200) diffracting planes and then ω -scan was carried out about this position keeping the positions of the source and detector as fixed. This experiment was conducted at eight different locations of the KDP crystal surface to have an idea of crystalline quality of the whole plane. The results are shown in Fig. 3.25. It shows that the diffraction curves (DC) are quite sharp without satellite peaks and the full width of half maxima (FWHM) from bottom edge near seed to top edge near flat-top is quite low and in a narrow range of 6 to 9 arc sec. This shows that crystal is free from internal structural grain boundaries and the crystal quality is comparable to that reported

in the literature.³⁸ The FWHM of DC's near crystal edges are slightly higher compared to that at the middle region. It is attributed to the abrupt termination of diffraction planes there which is indicated in terms of low intensities of the DC peaks there.

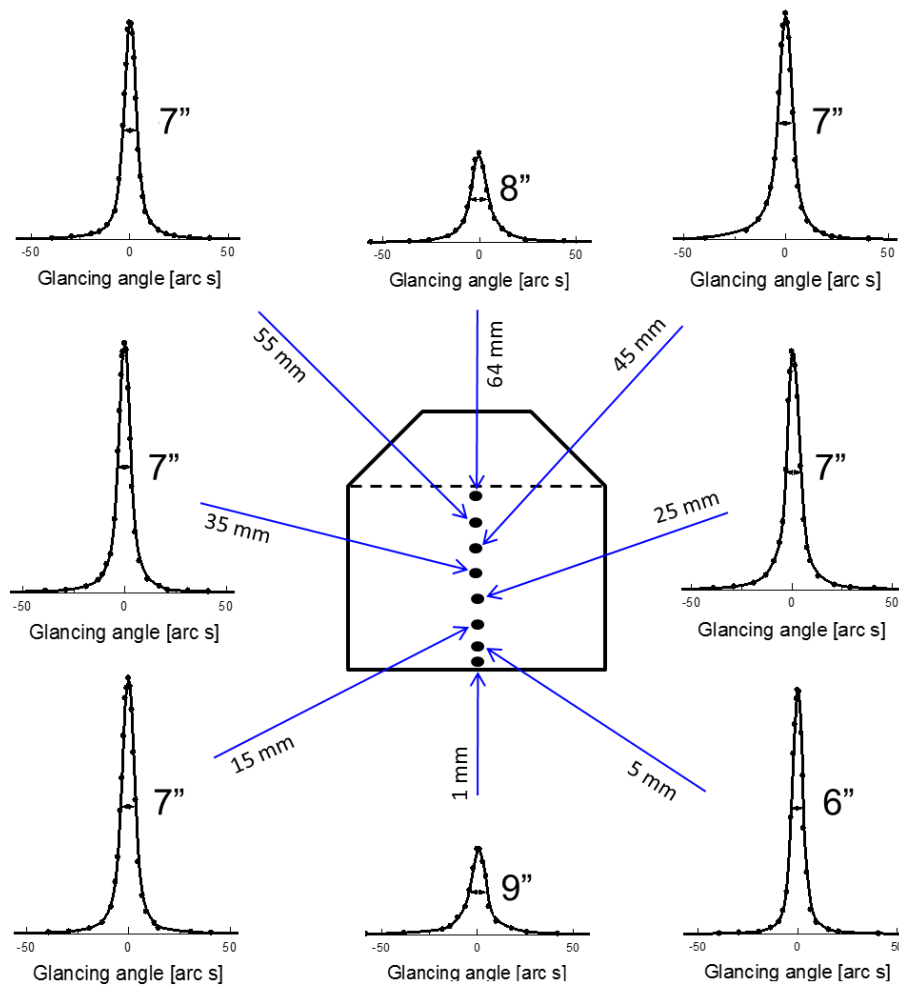


Fig. 3.25 Diffraction curves for (200) diffraction planes of (100) surface of as-grown flat-top KDP crystals at successively increasing height from the bottom edge to the top edge. The distance of the diffraction point corresponding to each DC is also shown in the image.

Experiments were also conducted for calculation of the flatness of the (200) planes in terms of the radius of curvature (ROC) of these planes. For this purpose, peak positions of the DC's were determined at different positions at 50 mm height from the base of the crystal. It was done by translating the crystal as a whole in steps of 2 mm horizontally and measured the peak position of DC at each position. Fig. 3.26 shows the results obtained for the crystal. The peak positions were plotted and calculated the slope of the curve. The reciprocal of this slope is a measure for ROC of the diffracting planes. The results show

that the ROC for the (200) planes of KDP is ~ -1 km. The high value of ROC indicates high degree of flatness and hence high crystalline quality of the crystal.⁵³ The negative sign of ROC indicates that the (200) planes are slightly concave.

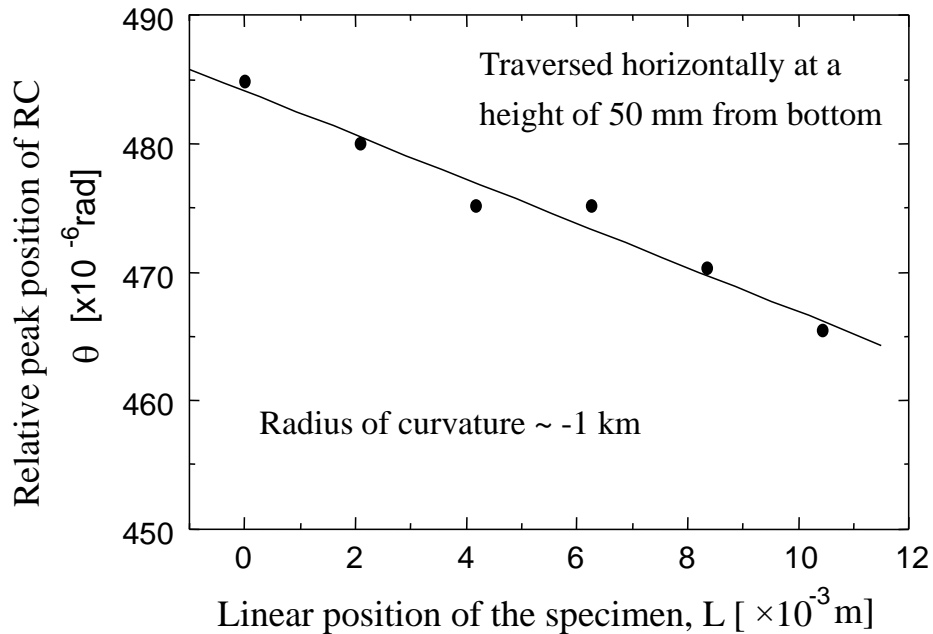


Fig. 3.26 Variation in relative peak positions of the diffraction curves for (200) planes of flat-top KDP crystal with respect to the linear position of beam at the crystal.

3.5.3 Defect structure and dislocation density

3.5.3.1 X-ray diffraction topography

X-ray diffraction topography is a useful non-destructive technique based on Bragg's law for imaging defect structures and their distribution at the crystalline samples. It is useful technique to get information about spread of defects over full surface area of the of sample plate. We used Jordon Valley make digital X-ray topography systems based on reflection topography. Fig. 3.27 is an internal view of the system showing positions of the X-ray source, sample stage with sample and CCD detector. X-ray topography is a sensitive technique for the scratches and physical damages occurred at the surface due to polishing errors. Therefore, mild etching was found useful to differentiate dislocation defects from scratches and cracks. The X-ray topographic investigations were carried out for all the six sample plates using copper $K\alpha$ radiation. Fig. 3.28 shows the X-ray diffraction topographs obtained for the three (001) oriented plates prepared from bottom, middle and top portions

of the flat-top KDP along with the photographs of the corresponding plates. This study was carried out for (316) diffracting planes. It shows that there are mainly three types of defects features, linear chains of dislocations defects, curved dislocations and localized defects. The topograph of the (001) bottom plate (Fig. 3.28 (c)) shows that the region near seed is most defective, showing features of inclusion at its vicinity due to regeneration of seed during initial stage of growth. This defective region also becomes a source of dislocations lines emanating from it. In addition, there are chains of dislocations defects in the topograph. The topograph of this plate is more or less of similar features due to belonging to single growth sector (prismatic in this case). On the other hand, the topograph of the middle plate (Fig. 3.28 (b)) shows relatively lesser defects in the central region belonging to the pyramidal growth sector compared to that in the peripheral region belonging to the prismatic sector of KDP. It is evident that there is high localized density of defects in the prismatic sector which may be due to preferential absorption of metallic impurities at the prismatic faces compared to that at pyramidal faces. There are mostly arc shape dislocations compared to linear chain dislocations. These are so called Frank-Reid type of dislocations⁵⁴ formed due to hydrodynamic stress⁵⁵ at the crystal surface due to reversible rotation of the crystal-platform assembly in the solution. The topograph of the (001) top plate (Fig. 3.28 (a)) show lesser defect density compared to the middle and the bottom plate. This comparison indicated that crystal quality improves away from seed and did not deteriorated due to flat-top portion near the top plate. Fig. 3.29 shows X-ray diffraction topographs for the three other sample plates namely (101), (010) and (100) where the diffracting planes were (732), (172) and (712) respectively. The (100) and (010) plates are crystallographically similar and therefore similar type of defects features are in their X-ray topographs. There are long chains of dislocations while the region between these chains is almost defects free. It has been observed that these chains are oriented between 60° to 75° with respect to the [100] direction and these arise due to metallic impurities and stress field.⁵⁶ The topograph for (101) plate (Fig. 3.29 (a)) shows linear and arc type dislocations chains with large region of low defects. There is no particular feature of defects due to vicinity to flat-top. This study indicates that defects structure observed at the KDP plates are due to stress field and chemical impurities and no indication was observed of defects getting introduced due to flat-top growth technique.⁵¹

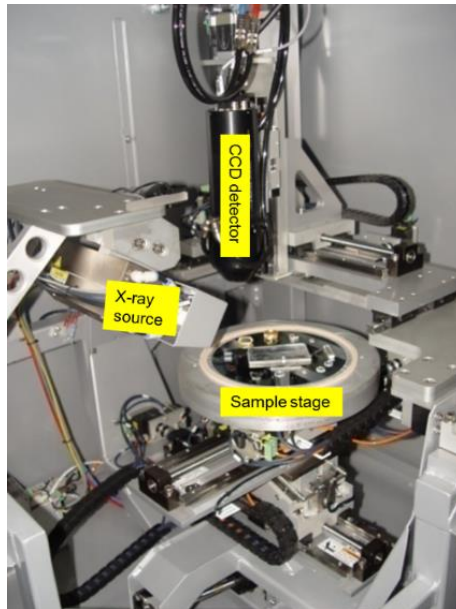


Fig. 3.27 Internal view of digital topography system used for reflection topography.

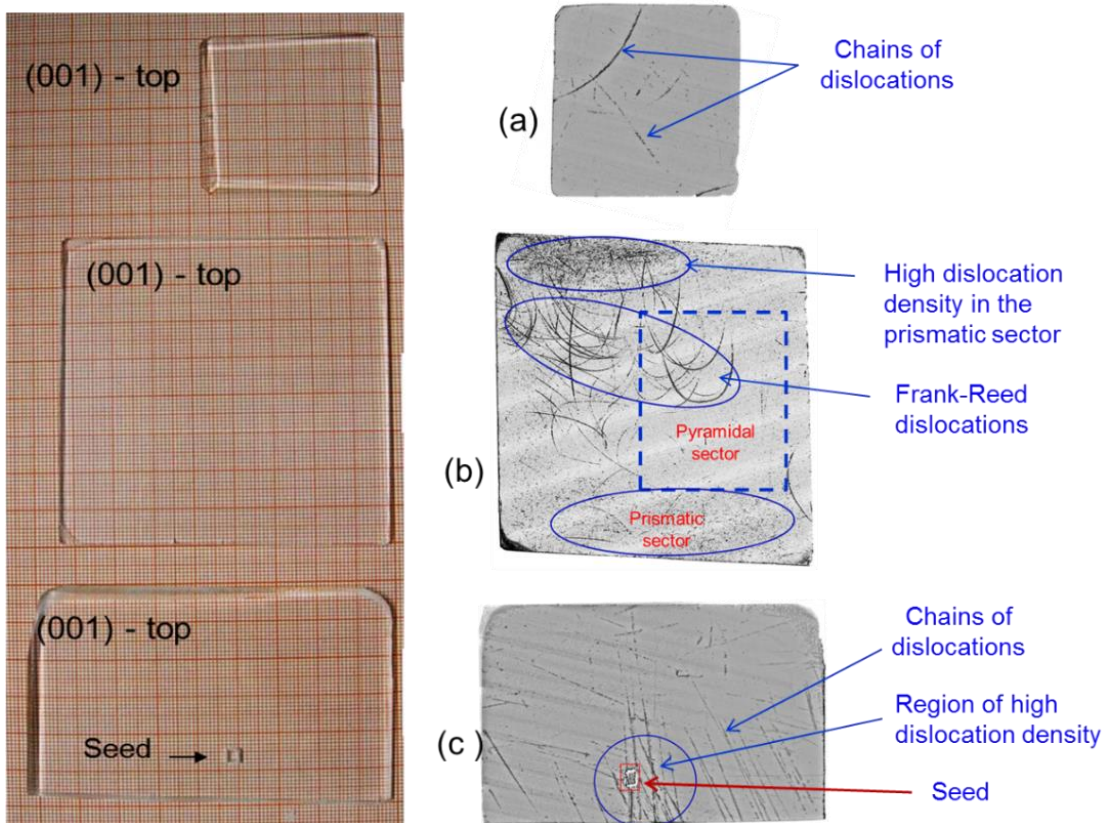


Fig. 3.28 X-ray topographs of three (001) sample plates for (316) diffraction planes, (a) for (001) top plate, (b) for (001) middle plate, and (c) for (001) bottom plate.

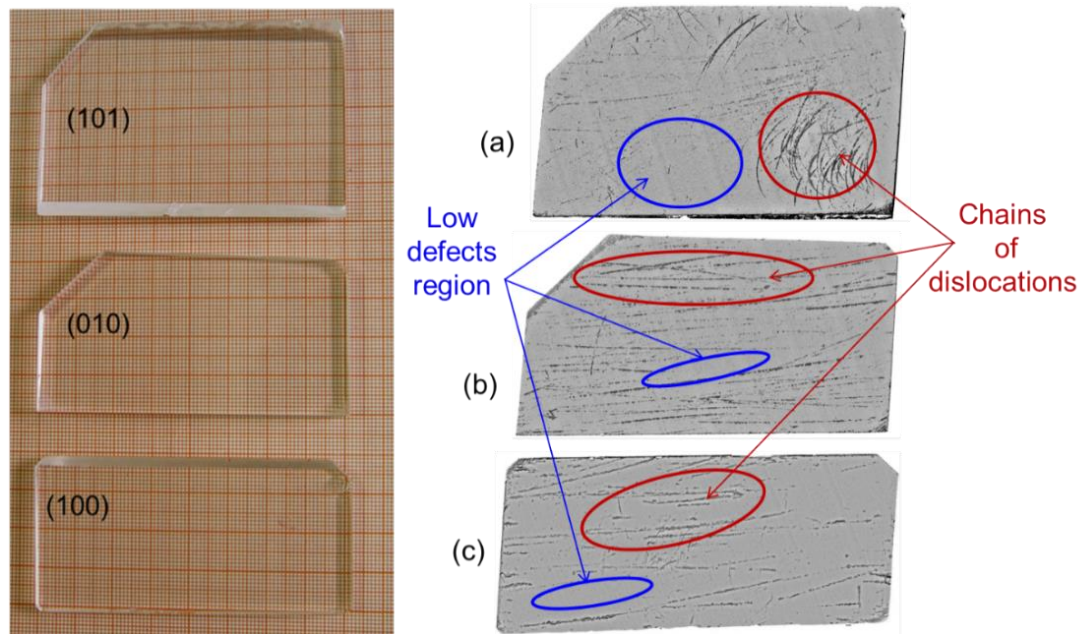


Fig. 3.29 X-ray topographs of (101) sample plate for (732) planes (a), (010) plate for (172) planes (b), and (100) plate for (712) planes (c).

3.5.3.2 Chemical etching

To correlate the observed defects features at the X-ray topographs and to quantify dislocation defects density, chemical etching studies was carried out for the same plates which were slightly etched for X-ray topography. The imaging was carried out for the plates which corresponds to the natural faces of KDP namely for (100) and (101) plates. It is because etch pits are relatively clearly visible at the slow growing faces which finally arise at the crystal surface. The etched plates were imaged using *Olympus* make optical microscope. The etch pit imaging was carried out at the regions of linear chains, low and high defects density regions corresponding to the X-ray topographs of the plates. Fig. 3.30 shows three optical micrographs for three different regions of the (100) plate corresponding to region of long chains of dislocations, high defects density and low defect density. The etch pits having parallelogram like shape conforming to the surface symmetry of the crystal plate. The chains of etch pits seen at the X-ray topograph can easily be identified here in the form of linear chain of similar shape etch pits. The etch pit density was calculated for the regions of the high and low defect density regions were 10^3 - $10^4/\text{cm}^2$ and $<10^3/\text{cm}^2$ respectively.

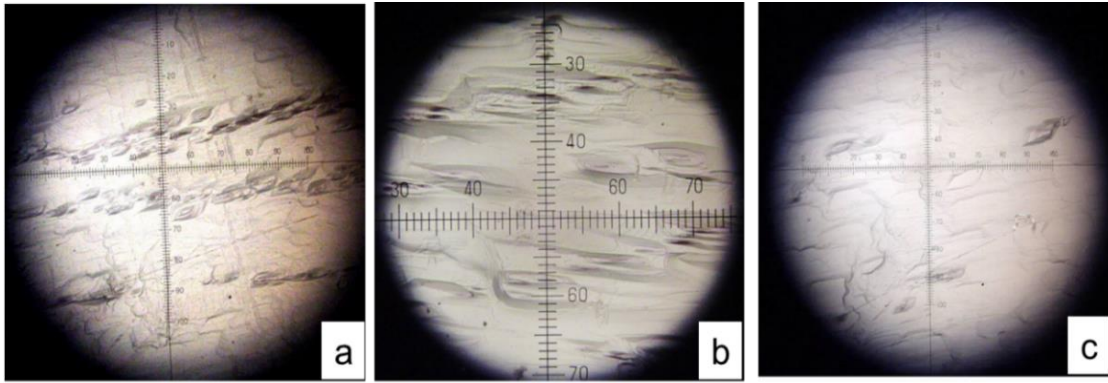


Fig. 3.30 Optical micrographs of etch pits at three different regions of the (100) plate of flat-top KDP crystal, (a) linear chains of etch pits, (b) high defects density region, and (c) low defects density region. (Magnification 50X)

Fig. 3.31 also shows three optical micrographs of the three different regions of the (101) plate corresponding to linear chains, high and low defect density regions. The micrographs show that there are triangular shape etch pits at the (101) surface. The etch pit density in the high and low defects density regions were of the order of 10^3 - $10^4/\text{cm}^2$ and $<10^3/\text{cm}^2$ respectively.

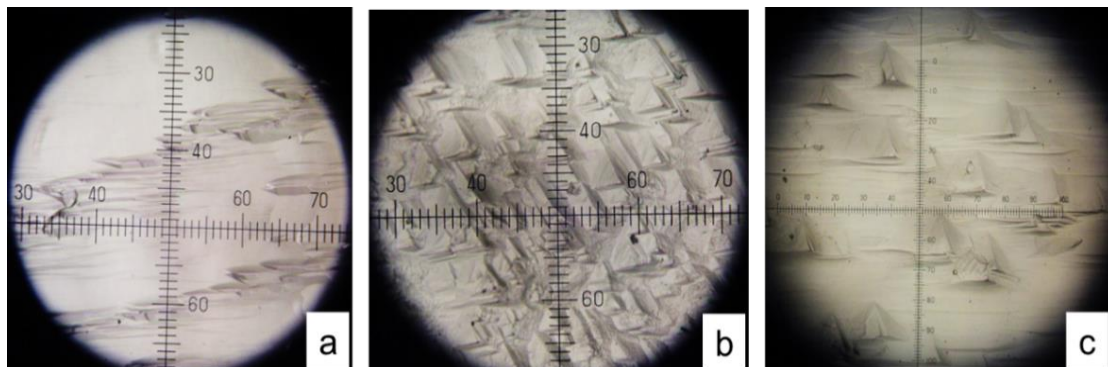


Fig. 3.31 Optical micrographs of etch pits at three different regions of the (101) plate of flat-top KDP crystal, (a) linear chains of etch pits, (b) high defects density region, and (c) low defects density region. (Magnification 50X)

3.5.4 Assessment of optical quality

Assessment of optical quality of KDP crystals is important due to its application with high intense lasers. The optical quality of the prepared sample plates was determined using three techniques namely UV-Vis-NIR spectroscopy, birefringence homogeneity and Mach-Zehnder interferometry.

3.5.4.1 UV-Vis-NIR transmission measurement

Optical transmittance measurements were carried out for the six KDP plates using *Jasco* make spectrophotometer. For this purpose, well-polished plates were used without etching of the surfaces. The experiments were conducted in the wavelength range of 190 nm to 1700 nm. For the (001) middle plate where two growth sectors namely prismatic and pyramidal lies the experiments were conducted at these two sectors to have a comparison of sectorial effect as was seen in case of x-ray topographs. Fig. 3.32 shows a comparison of transmission spectra of three (001) plates prepared from bottom, middle and top portions of the flat-top KDP. It shows that transmittance for all the plates is ~ 90% for 400 nm to 1300 nm region without accounting for Fresnel reflection losses. The effect of sample to sample thickness variation was accounted mathematically and the spectra show the results for normalized thicknesses of 1mm. The spectra show a marked difference at UV side which is attributed to the sectorial distribution of trivalent metallic impurities in KDP as has been reported by various investigators.^{57,58} To further analyse the sectorial nature of optical transmittance, spatial variation of transmittance was measured for the (001) middle plate. Fig. 3.33 and Fig. 3.34 show the spatial variation of optical transmittance at four specific laser wavelengths namely 1064 nm, 532 nm, 355 nm and 266 nm across X and Y-directions. The results show that the optical transmittance for 1064 nm and 532 nm is the highest among the four wavelengths and is also almost uniform throughout the plate. While there is a little decrease in the transmittance of 355 nm at the edge region of the plate compared to that at the central region. This difference in transmittance is more severe in case of 266 nm wavelength. It is attributed to the relatively higher concentration of metallic impurities at the peripheral region of the plate which belongs to the prismatic growth sector. While the central region belongs to pyramidal growth sector and having lower content of metallic impurities and hence relatively higher transmittance as compared to that at the prismatic growth sector.

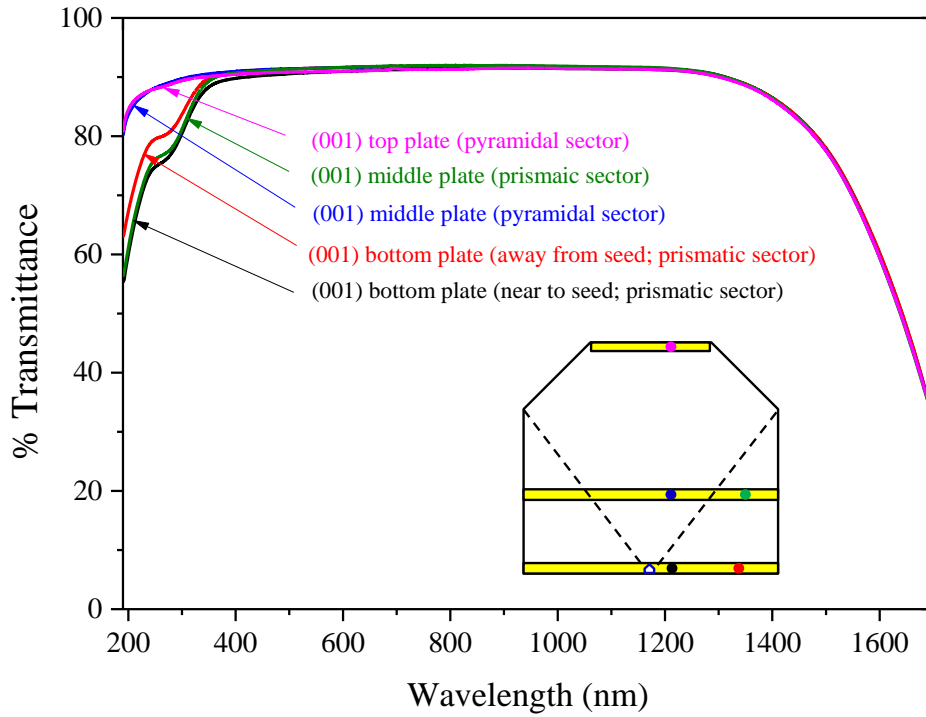


Fig. 3.32 Transmission spectra of different locations at the (001) bottom, (001) middle and (001) top plates without accounting Fresnel reflection losses. The locations of the points from where the transmission was measured is marked in the schematic shown in inset.

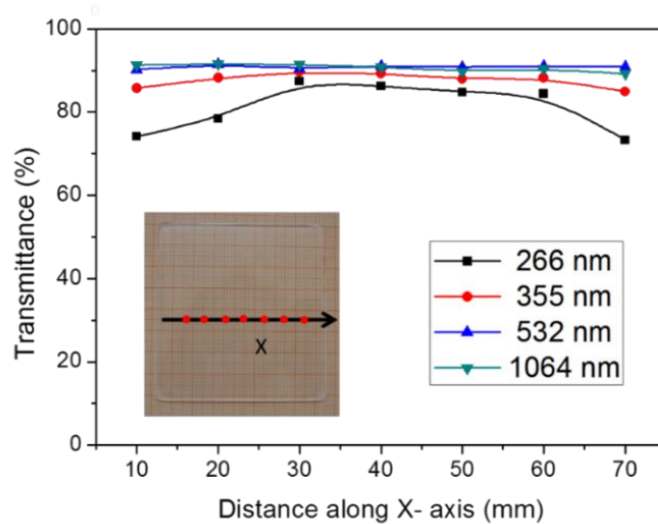


Fig. 3.33 Spatial variation of transmittance along X-axis at four specific wavelengths for (001) middle plate.

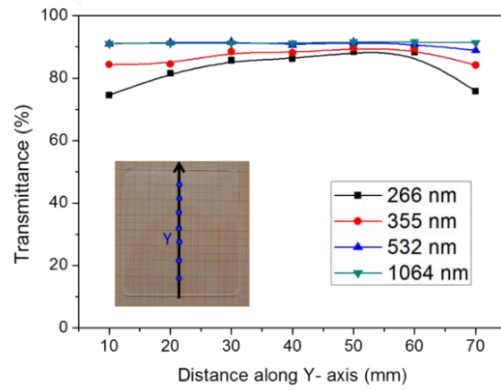


Fig. 3.34 Spatial variation of transmittance along Y-axis at four specific wavelengths for (001) middle plate.

Further, a comparison in optical transmittance among the four differently oriented plates i. e. for (100), (010), (101) and (001) is made. The results are shown in Fig. 3.35. This also confirm the sectorial nature of optical transmittance for KDP crystal. It is because (100) and (010) plates lie completely in prismatic sector while (101) plate lies in pyramidal growth sector. It may be concluded that the value of transmittance at the UV region particularly near 266 nm gives an indication about the relative chemical purity of the KDP crystal plates. The results also indicate that the metallic impurity concentration is highest near seed at prismatic sector which decreases away from it as growth proceeds. These observations are corroborated with x-ray fluorescence measurements discussed in the next section.

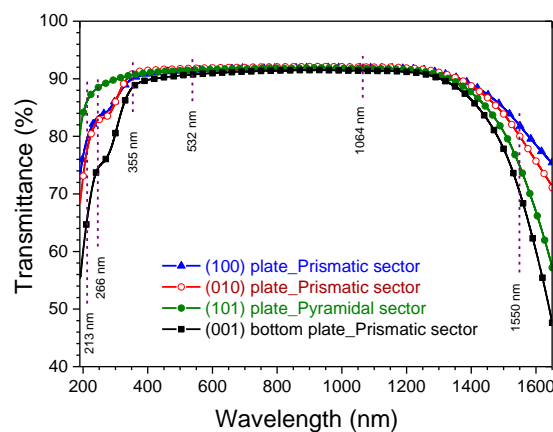


Fig. 3.35 Transmission spectra for the four different plates of the flat-top KDP crystal namely (100), (010), (101) and (001)-bottom plates without accounting for Fresnel losses.

The quantitative values of transmittance measured at six different wavelengths as marked in Fig. 3.35 are listed in Table 3.6 along with corresponding impurity content measured by X-ray fluorescence technique in Section 3.5.5.

3.5.4.2 Birefringence homogeneity: Orthoscopy and conoscopy

The KDP sample plates were further characterized using birefringence interferometry technique for assessment of bulk optical homogeneity using a particular wavelength. There are two mode of birefringence interferometry: conoscopy and orthoscopy.⁵⁹ The plates having zero birefringence normal their faces were analysed using conoscopic method while that have non-zero birefringence were assessed by orthoscopy. We used He-Ne laser (633 m) for this study. The (001) bottom, middle and top plates were assessed using laser conoscopy method due to being normal to optic axes. In this experiment, the sample plate under investigation was mounted between the crossed polarizers and a converging beam of He-Ne laser was passed through it. The sample plate was rotated about the beam to get good contrast at the screen. The transmitted intensity pattern was obtained at a screen and its image was recorded using a digital camera. Fig. 3.36 shows the conoscopic images for the three (001) plates of the flat-top KDP crystal. Concentric fringes called as isochromes are without localised distortion indicate good birefringence homogeneity about the c-axis. The dark cross is slightly shifted from the centre indicates slight error in cutting and polishing of these plates.

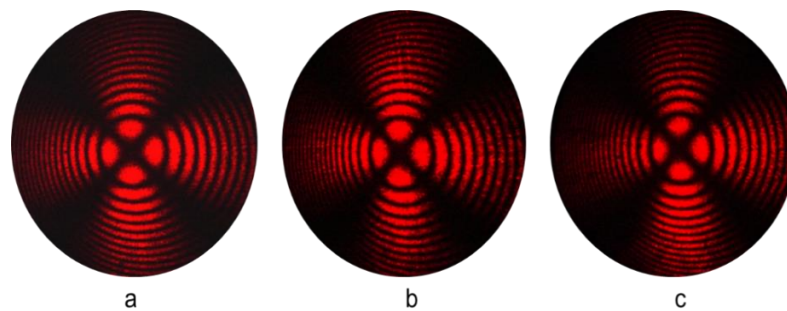


Fig. 3.36 Conoscopy images of the (001) bottom (a), (001) middle (b), and (001) top plates (c) of the flat-top KDP crystal.

Orthoscopic birefringence interferometry was carried out for (100) and (010) plates which have maximum birefringence for beam propagating normal to their surface. The experiment was conducted with 10 mm diameter He-Ne laser beam. Fig. 3.37 (b) shows

the obtained interferograms for the two plates. In case of perfectly flat plate the number of fringes is considered proportional to the birefringence inhomogeneity. There are almost equal number of fringes for both the plates indicating similar optical homogeneity of the two plates. The parallel equi-spaced fringes are a signature of good birefringence homogeneity.

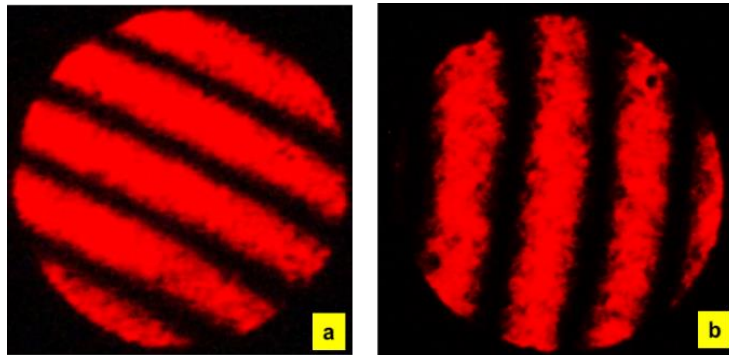


Fig. 3.37 Birefringence interferogram for (100) plate (a), and (010) plate (b) of flat-top KDP in orthoscopic mode.

3.5.4.3 Optical homogeneity by Mach-Zehnder interferometry

Mach-Zehnder interferometry is a sensitive technique for variation in optical path lengths between adjacent locations of optical plates. It gives an assessment of bulk defects which cause localized variation in refractive index and hence a net relative change in optical path difference between the nearby points of the sample. We have carried out this study for (100), (001) bottom and (001) top plates. The interferometer uses a broad collimated beam of He-Ne laser which was first aligned for infinite fringe setting mode. The sample plate was mounted in the sample arm of the interferometer and a interferogram was obtained at the CCD due to path difference created by the sample with respect to the reference arm. Fig. 3.38 show the interferogram obtained by this experiments. Parallel equi-spaced interference fringes obtained in case of (100) and (001) top plate show that the sample have good optical homogeneity the large number of fringes are related to wedge in the sample plates due processing errors. In case of (001) bottom plate we were particularly interested to know the features near the seed. Fig. 3.38 (b) shows the image observed near the seed portion of the plate, it indicates distorted fringes due to high defect density near seed. It conforms to the defected region observed near seed by X-ray diffraction topography at this plate.

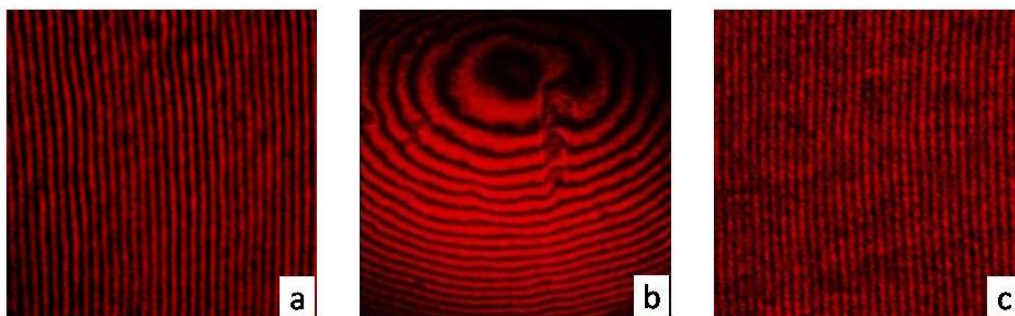


Fig. 3.38 Mach-Zehnder (MZ) interferograms of (100) (a), (001)-bottom (b) and (001)-top (c) plates.

3.5.5 X-ray fluorescence spectroscopy for impurity distribution

Determination of chemical impurities and their distribution is an important part of characterization of crystal plates to find out chemical reasons for variation in optical properties of the crystals. We have used X-ray fluorescence (XRF) technique for qualitative and quantitative analysis of chemical impurities present in the single crystal plates. XRF is particularly suitable for single crystals because it is non-destructive in nature and suitable for studying spatial variation in large size samples. We have carried out these experiments at XRF beamline (BL-16) at Indus-2 synchrotron radiation facility at RRCAT Indore which is a 2.5 GeV, 200 mA third generation radiation source.⁶⁰ XRF gives elemental information because it is based upon fluorescence due to transition of inner electrons. It happens due to removal of inner shell electrons by striking specific energy X-ray photons obtained from synchrotron radiation through a monochromator. The energy of fluorescence emitted from a particular atom is its characteristic. For detection of a particular impurity atom, the excitation photon energy should be kept higher than its binding energy for K shell electrons. We studied all the six KDP plates using 10 keV radiation to analyse the distribution of metallic impurity concentration with particular focus on Fe, Ni, Cr, Cu which are detrimental to the optical quality of KDP crystals. Fig. 3.39 (a) shows schematic of the experimental geometry. A sample holder was fabricated using perspex plates to mount the crystal plates. The sample holder was oriented such that the sample face the synchrotron radiation at 45° . The fluorescence was recorded by an energy dispersive detector connected with a multi-channel analyser. The detector was placed at 90° to the incident beam as shown schematically in Fig. 3.39 (b). The beam size and the exposure time were kept $5 \times 5 \text{ mm}^2$ and 1000s respectively for each measurement

for comparison purpose. While the distance of the detector from the sample surface where beam strike was kept 125 mm. Fig. 3.40 shows the XRF spectrum obtained for (001)-middle plate of the flat-top KDP crystal. It shows fluorescence peaks corresponding to iron and nickel as impurities in addition to atmospheric argon and potassium of the sample as the main ingredient of the sample. Similarly, the experiments data was collected for different sample plates. The data was analysed using PyMCA software.^{61,62} The potassium present in the KDP was used as a reference to calculate relative concentration of Fe and Ni impurities in the sample plates. The results are shown in the Table 3.6. The results of the optical transmittance at six different wavelengths have also been given in the same table for correlating optical properties with impurity concentration.

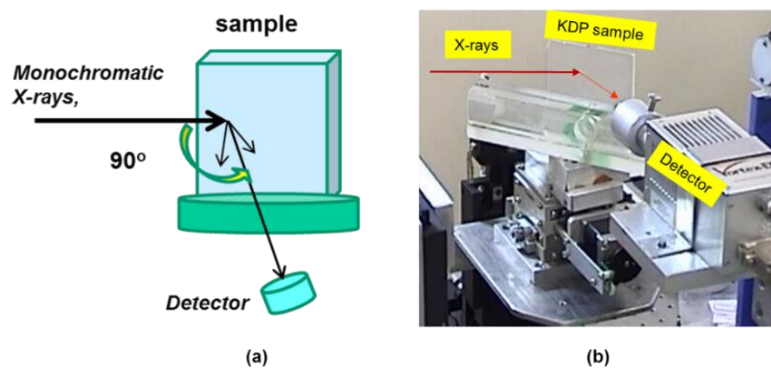


Fig. 3.39 (a) Schematic line diagram showing the geometry of XRF measurement set up, and (b) a KDP sample plate at the sample stage during the experiments.

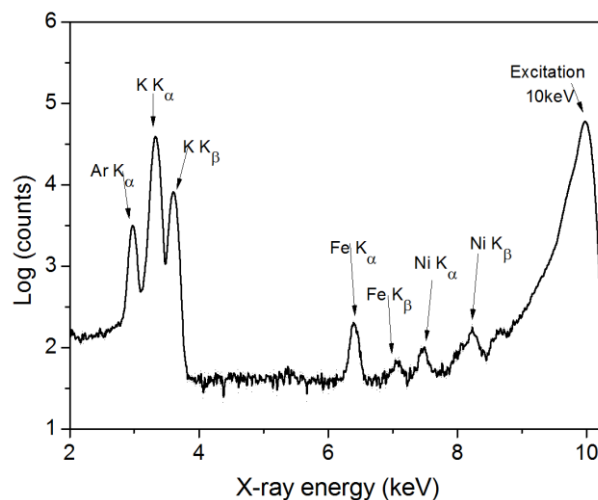


Fig. 3.40 The X-ray fluorescence spectra obtained for (001)-bottom plate of the flat-top KDP crystal.

Table 3.6 Concentration of iron and nickel impurities in different plates of flat-top KDP crystal determined using X-ray fluorescence, and the UV-Vis-NIR transmittance for these plates at six different wavelengths. The transmittance values are without accounting for Fresnel reflection losses.

Crystal plate	Growth sector	Metallic impurity (ppm \pm 10%)		Transmittance (%) at wavelengths					
		Fe	Ni	1550 nm	1064 nm	532 nm	355 nm	266 nm	213 nm
(001)-bottom	Prismatic	16	3	70.2	91.4	90.7	88.6	75.7	65.8
(001)-middle	Prismatic	12	2	69.7	91.7	91.4	89.6	76.9	67.0
(001)-middle	Pyramidal	6	2	70.0	91.7	91.4	90.5	88.6	85.1
(001)-top	Pyramidal	3	3	69.7	91.4	90.9	90.1	88.4	86.2
(100)	Prismatic	7	2	81.9	91.9	91.5	90.1	84.0	79.7
(010)	Prismatic	6	3	79.9	92.0	91.9	91.0	84.1	79.0
(101)	Pyramidal	4	2	72.6	91.5	90.9	89.7	87.8	84.7

These results show that there is a variation in the concentration of Fe impurity in the samples while the concentration of Ni is more or less uniform. The concentration of Fe is highest at the prismatic sector of the (001) bottom plate and decrease as growth proceed to (001) middle plate. There is sectorial variation in the Fe concentration which is evident from its concentration in (001) middle plate which contains both the sectors. The Fe concentration is almost half in the pyramidal sector compared to that at the prismatic sector of the (001) middle plate. The (001) top located near the flat top has lowest concentration of Fe. It indicates that formation of flat-top does not anyway act as a source of impurities in the crystal.

A comparison of the optical transmittance of the KDP plates with Fe concentration shows that the transmittance at UV region (266nm, 213nm) is the lowest where Fe concentration is higher while transmittance at other wavelengths are more or less unaffected by the variation in Fe concentration. It indicates that one of the prime cause of UV absorption by KDP crystals is the presence of high concentration of Fe impurity.⁶³

3.5.6 Laser-induced damage threshold

Laser-induced damage threshold (LDT) sets the upper limit of laser intensity for safe utilization of a material with a particular laser. It depends on various features of laser as well as on material quality and its processing. On laser side, LDT for a particular material depends on its wavelength, pulse width, repetition rate, pulse profile, polarization and beam diameter while at material side it depends upon its surface finishing, bulk defects, absorption coefficient for the laser wavelength, nature of impurities and their concentration, and orientation of sample plate in case of anisotropic crystals.^{64,65} KDP is an important material for frequency conversion of high power Nd: YAG laser, where LDT is one of the prime concern that limits the power that can be safely transferred through a given crystal. We have therefore carried out LDT measurements for the six different plates of the flat-top KDP crystal using a Nd:YAG laser. It was a Q-switched TEM₀₀ mode Nd:YAG laser (*Quanta* make) having ~ 7 ns pulse width and variable pulse energy maximum upto 500 mJ. The schematic of the experimental set is shown in Chapter 2. The experimental setup for measurements of LDT is shown in Fig. 3.41. It includes a beam splitter (BS), energy meter 1 (EM1), a converging lens, a XYZ translational stage, energy meter 2 (EM2), ND filters of different optical density, a CCD camera along with a computer. Initially the BS was set at ~ 45° angle with respect to the incident laser beam and the EM1 was aligned to measure the reflected energy of the laser pulse. The converging lens was placed ahead of BS and the transmitted energy after the lens was measured using EM2 and ND filters with respect to the reflected energy at EM1 and an average value of the transmission factor was calculated. Subsequently the position of the sample holder was fixed at ~ 46 cm away from the lens somewhat before its focal point and beam diameter ($1/e^2$) was determined using knife edge method.⁶⁶ The Fig. 3.42 shows calculated beam diameter to be 1.25 mm. After it the razor blade used as a knife edge was replaced by the sample and measured the laser induced damage by varying laser pulse energy in a ramped manner by “R on 1 method” as described in Chapter 2. A CCD camera was used to determine the state of damage at the crystal surface. The LDT measurements were repeated at various points of the plates however we could not find any systematic relation between high and low defect density regions therefore the lowest value calculated was considered as the LDT for that plate. The results of the LDT measurements are summarised in the Table 3.7. The LDT values of the different sample plates of flat-top KDP lies in the range of 2.4 GW/cm² to 3.9 GW/cm² for 7 ns pulse width Nd:YAG laser.

It was however observed that LDT value for (001) plates gradually increases as one moves up from bottom plate (2.7 GW/cm^2) to the top plate (3.9 GW/cm^2). It also shows that flat-top technique did not result into deterioration of the optical quality of the KDP. This result implies that LDT for KDP is more strongly influenced by defects density rather than concentration of Fe impurity.

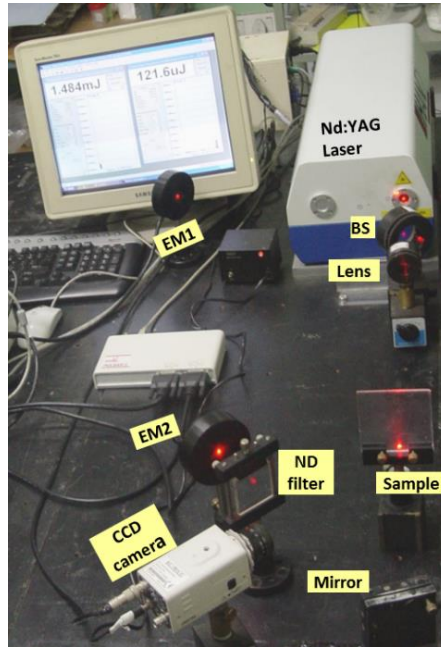


Fig. 3.41 Experimental set up for measurement of laser-induced damage threshold.

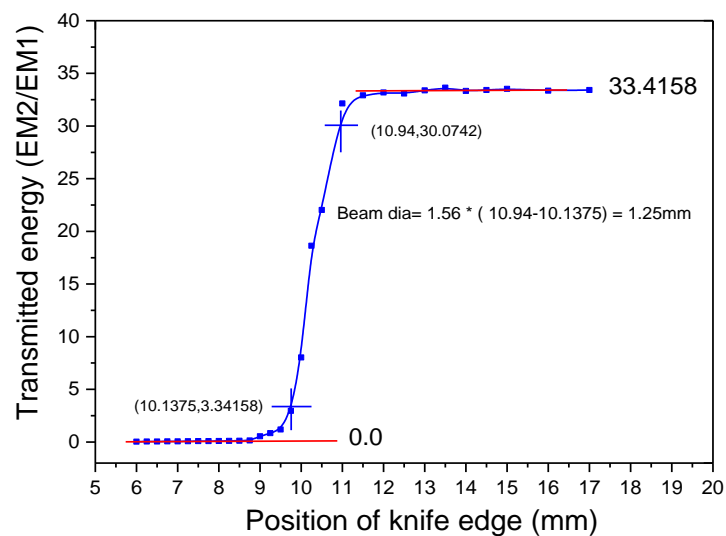


Fig. 3.42 Variation of transmitted pulse energy with respect to the position of knife edge for calculation of $(1/e^2)$ beam diameter of the laser beam at the sample surface.

Table 3.7 Values of the laser-induced damage threshold for the different samples of the flat-top KDP crystal.

Crystal plate	LDT (GW/cm²) ±10%
(001) bottom	2.7
(001) middle	3.1
(001) top	3.9
(100)	2.8
(010)	3.4
(101)	2.4

3.5.7 Fabrication of Pockels element, SHG elements and cells

Some of the flat-top grown KDP crystals were utilized for fabrication of elements for electro-optic modulation and SHG of Nd:YAG laser. Fig. 3.43 (a) shows c-cut element of size 90×82×19 mm³ prepared for electro-optic modulator. It was characterised for its orientation by laser conoscopy as shown in Fig. 3.43 (b). Fig. 3.44 (a) shows an SHG type-II element of size ~ 50×50×25 mm³ prepared from a smaller size flat-top KDP crystal. Fig. 3.44 (b) shows aluminium make housing designed and fabricated for this element. Fig. 3.44 (c) shows the complete SHG cell with index matching fluid (FC43) and one side anti-reflection coated BK7 glass windows for 1064 nm and its second harmonic for each side of the SHG cell. The SHG cell was provide with four grooves at inner surface and one taped hole at its periphery to fill the index matching fluid. A metallic screw at the tapped hole was provided with a small size rubber O-ring to make it leak proof.

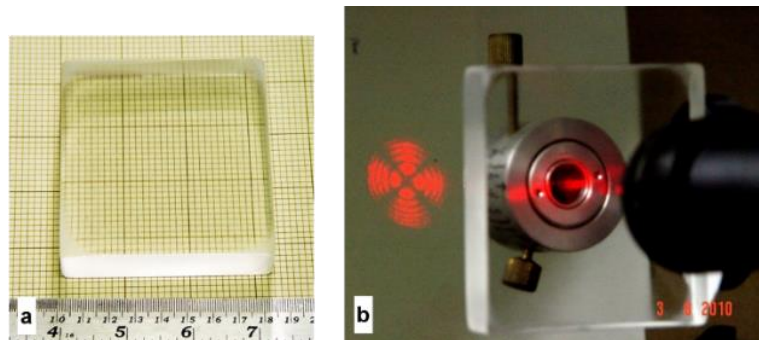


Fig. 3.43 (a) C-cut KDP element prepared for electro-optic modulator, and (b) conoscopy figure at screen confirming its orientation.



Fig. 3.44 (a) SHG element of size $50 \times 50 \times 25 \text{ mm}^3$ prepared from a flat top KDP crystal, (b) a housing designed for the SHG element, and (c) complete KDP type-II SHG cell with antireflection windows and index matching fluid.

3.5.8 Measurement of SHG efficiency

SHG efficiency for the SHG type-I and type-II elements prepared from SHG oriented KDP crystals were measured using Q-switched Nd:YAG laser of 7 ns pulse width. The sample plates were mounted at the mechanical orienter having facilities of rotation about beam, controlled by a fine thread screw and two tilt screw motions normal to the beam. The optical set up used for SHG measurement is shown schematically in Fig. 3.45.

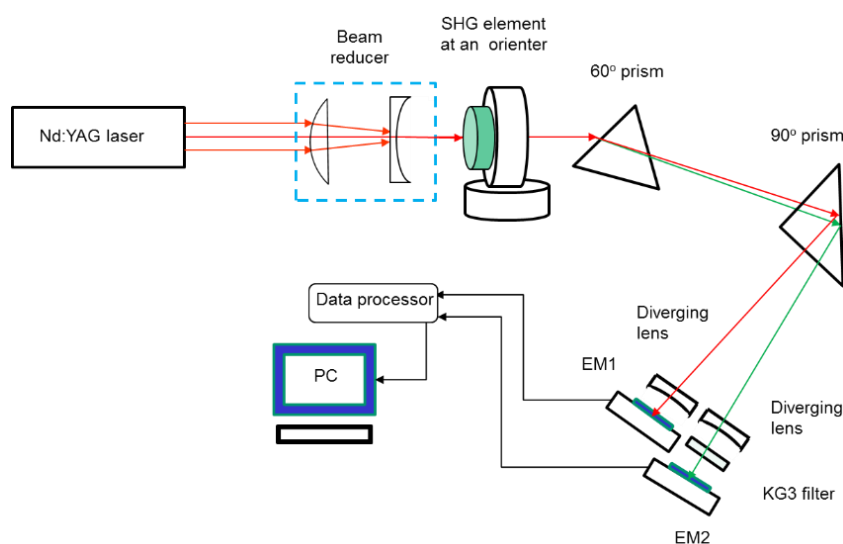


Fig. 3.45 Schematic of the optical set up used for measurements of SHG efficiency of KDP samples.

It consists of an Nd:YAG laser, a beam reducer of 0.25X made using a pair of a plano-convex and a plano-concave lenses, a mechanical orienter for the crystal having facilities of fine rotation about the beam direction say Z-direction and two tilt motions

about X- and Y- axis, two prisms to isolate the two harmonics by dispersion, two energy meters EM1 and EM2 and diverging lenses, ND filters and KG3 filter. We have carried out experiments for SHG efficiency measurement for type-I and type-II sample plates prepared from the type-I and type-II SHG oriented crystals. Fig. 3.46 and Fig. 3.47 show the variation of SHG efficiency with respect to fundamental laser power for KDP type-I and type-II SHG elements. These graphs show that SHG efficiency increases with laser intensity and reaches near to 30% at an intensity of $\sim 900 \text{ MW/cm}^2$ for type-I plate while the efficiency is slightly lower for type-II SHG plate.

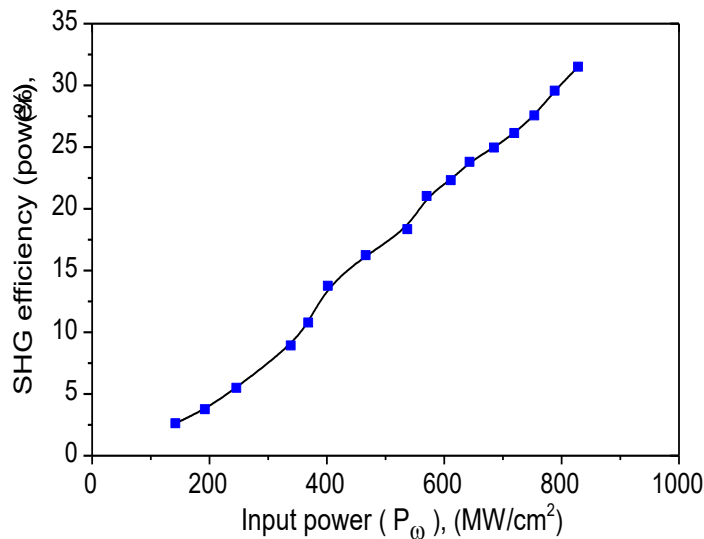


Fig. 3.46 Variation of SHG efficiency with input intensity for KDP SHG type-I element.

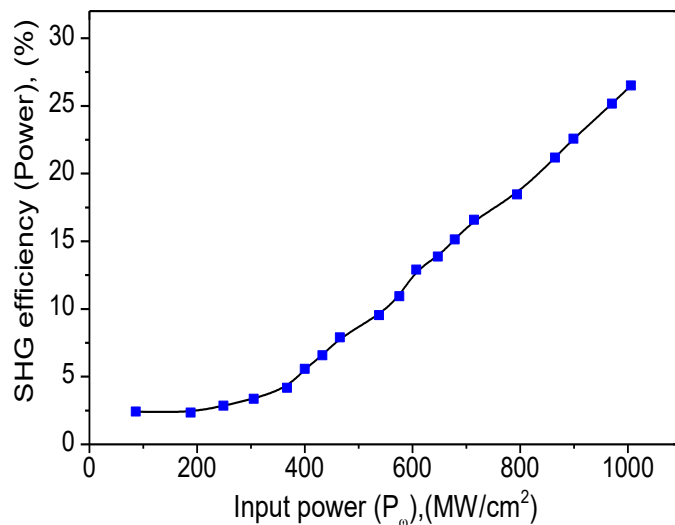


Fig. 3.47 Variation of SHG efficiency with input intensity for KDP SHG type-II element.

3.6 Summary and conclusion

1. A new methodology called as “*flat-top technique*” has been developed for shape modification of KDP crystals to enhance usable volume fraction for device elements. The technique is based on utilization of solution-air interface for elimination of pyramidal cap to get flat-top shape crystal.
2. Using this methodology several flat-top shape KDP crystals have been grown without nucleation for two different applications:
 - (a) Electro-optic switching application, where the crystal is grown using point seed such that [001] direction is normal to the platform. As a result, the usable volume fraction for Pockels cell elements can be enhanced up to ~ 22% as compared to the conventionally grown pyramidal shape KDP crystals. One of the flat-top KDP crystal of dimensions 116x92x116 mm³ was grown with ~ 50 % crystallization yield. The usable volume fraction for Pockels cell elements in this crystal was 11 % higher compared to that obtained from a pyramidal shape crystal of similar cross-section.
 - (b) Frequency doubling application, where a method was developed to orient natural morphology point seeds at the platform to grow SHG type-I and type-II oriented KDP crystals. Application of flat-top technique along with the specific way of seed orientation further enhances the usable volume fraction for SHG elements. KDP crystals were grown with usable volume fraction about 48% and 56% for SHG type-I and type-II elements respectively for Nd:YAG laser which is much higher compared to conventionally grown KDP crystals and also higher than that reported (30% and 50%) by parallel plate technique.
3. A water bath of capacity 150 liter and a crystallizer of capacity 15 liter were designed, fabricated, tested and used for the growth of flat-top shape KDP crystals
4. A technique was developed for seed protection during overheating stage of solution and used for growth of KDP crystals.
5. The flat-top KDP crystals were characterized for optical quality by various techniques showing that formation of flat-top does not deteriorate the crystal quality.
6. The analysis of the XRF spectra showed presence of iron in the range of 3 to 16 ppm, which decreases from seed to flat-top portion of the crystal.

7. HRXRD at several point on a broad (100) face show the full width of half maxima (FWHM) of the rocking curve in the range of 6 to 9 arc sec.
8. Dislocation defects density and their distribution imaged using X-ray diffraction topography and chemical etching were found to be in the range $10^3 - 10^4/\text{cm}^2$.
9. The LDT was measured using Nd:YAG laser of 7 ns pulse width and was in the range of 2.4 to 3.9 GW/cm².
10. SHG conversion efficiency measured using the same laser was found up to about 30 % at fundamental laser intensity of $\sim 900 \text{ MW}/\text{cm}^2$.
11. The results indicated that modification of KDP crystal growth by solution-air interface does not adversely affect the quality of the grown crystals.

References:

- ¹ G. J. Linford, B. C. Johnson, J. S. Hildum, W. E. Martin, R. D. Boyd, W. L. Smith, C. L. Vercimak, D. Eimerl, J. T. Hunt, *Appl. Opt.*, 20 (1982) 3633-3643.
- ² T. Sasaki, A. Yokotani, *J. Cryst. Growth*, 90 (1990) 820-826.
- ³ D. Eimerl, *Ferroelectrics* 72 (1987) 95-139.
- ⁴ N. P. Zaitseva, J. J. de Yoreo, M. R. Dehaven, R. L. Vital, K. E. Montgomery, M. Richardson, L. J. Atherton, *J. Cryst. Growth*, 180 (1997) 255-262.
- ⁵ W. H. Lowdermilk, *J. Nonlinear Opt. Phys. Mater.*, 6 (1997) 507-533.
- ⁶ K. Walter, *Science and Technology Review*, Lawrence Livermore National Laboratory, UCRL-52000-03-9, 2003, pp 4-14.
- ⁷ C. Maunier, P. Bouchut, S. Bouillet, H. Cabane, R. Courchinoux, P. Defossez, J. C. Poncetta, N. Ferriou-Daurios, *Opt. Mater.*, 30 (2007) 88-90.
- ⁸ B. Zhu, T. Zhan, Z. Gu, T. Wang, L. Qian, in, "Growth, Fabrication, Devices and Applications of Laser and Nonlinear Materials", J. W. Pierce, K. I. Schaffers (Eds.) *Proc. SPIE*, 4268 (2001) pp. 36-41.
- ⁹ S. G. Garanin, A. I. Zaretskii, R. I. Il'kaev, G. A. Kirillov, G. G. Kochemasov, R. F. Kurunov, V. M. Murugov, S. A. Sukharev, *Quantum Electronics*, 35 (4) (2005) 299-301.
- ¹⁰ G. Busch and P. Scherrer, *Naturwiss.*, 23 (1935) 737.

- ¹¹ M. E. Lines A. M. Glass, Principles and Application of Ferroelectrics and Related materials, Oxford Uni. Press, Oxford, pp. 293-296.
- ¹² J. W. Mullin, A. Amatavivadhana, J. Appl. Chem., 17 (1967) 151-156.
- ¹³ D. Xu, D. Xue, H. Ratajczak, J. Molecular Structure, 740 (2005) 37-45.
- ¹⁴ L. N. Rashkovich, KDP-Family Single Crystals, The Adam Hilger Series on Optics and Optoelectronics, Adam-Hilger, New York, 1991
- ¹⁵ Y. Xu, Ferroelectric Materials and Their Applications, North Holland, Amsterdam, 1991, pp. 284-286.
- ¹⁶ S. K. Sharma, A. Saxena, Arun Kumar, Yeshpal Singh, H. O. Mahawar, A. K. Karnal, V. K. Wadhawan, 10th AGM-MRSI, RRL, Bhopal, February 8-10, 1999, pp.31.
- ¹⁷ L. N. Rashkovich, G. T. Moldazhanova, J. Cryst. Growth, 151 (1995) 145-152.
- ¹⁸ N.A. Booth, T. Land, P. Erhmann, P. G. Vekilov, Cryst. Growth Des., 5 (2005) 105-110.
- ¹⁹ P. F. Bordui, J. J. Zola, G. Kostecky, G. M. Loiacono, J. Cryst. Growth, 71 (1985) 269-272.
- ²⁰ W. Y. Shui, P. Benema, W. H. V. D. Linden, J. Boshaar, H. Klapper, J. Cryst. Growth, 83 (1987) 471-480.
- ²¹ P. Feng, L. Jinkui, S. Genbo, H. Youping, H. B. Rong, H. Yisen, Z. Qinglan, Cryst, Rec. Technol., 26 (1991) 289-295.
- ²² G. M. Loiacono, J. J. Zola, G. Kostecky, J. Cryst. Growth, 63 (1983) 545-556.
- ²³ N. P. Zaitseva, I. L. Smol'skii, L. N. Rashkovich, Sov. Phys. Crystallogr., 36(1) (1991) 113-115.
- ²⁴ N. P. Zaisteva, L. N. Rashkovich, S. V. Bogatyreva, J. Cryst. Growth, 148 (1995) 276-282.
- ²⁵ V. Tatartchenko and E. Beriot, Proc. SPIE, 3492 (1999) 384-390.
- ²⁶ S. K. Sharma, Sunil Verma, B. B. Shrivastava, V. K. Wadhawan, J. Cryst. Growth, 244 (2002) 342-348.
- ²⁷ G. Li, L. Xue, G. Su, Z. Li, X. Zhuang, Y. He, Cryst. Res. Technol., 40(9) (2005) 867-870.
- ²⁸ P. F. Bordui, J. Cryst. Growth, 85 (1987) 199-205.
- ²⁹ W. R. Wilcox, J. Cryst. Growth, 65 (1983) 133-142.

- ³⁰ S. Satapathy, S. K. Sharma, A. K. Karnal, V. K. Wadhawan, *J. Cryst. Growth*, 240 (2002) 196-202.
- ³¹ N. Zaitseva, L. Carman, I. Smolsky, *J. Cryst. Growth*, 241 (2002) 363-373.
- ³² L. Zeng, M. Zha, M. Ardoino, P. Franzosi, G. Zuccalli, C. Paorici, *J. Cryst. Growth*, 166 (1996) 528-532.
- ³³ V. Tatartchenko, United States Patent no. 6,929,693 dated August 16, 2005.
- ³⁴ E. I. Kim, V. I. Katsman, V. V. Vorontsov, V. N. Portnov, V. N. Trushin, K. A. Markov, *Inorganic Materials*, 44 (2008) 870-875.
- ³⁵ H. Tu, Y. Zhao, Y. Yue, F. Fan, Z. Hu, *CrystEngComm.*, 17 (2015) 6669-6673.
- ³⁶ H. Youping, Z. Jinbo, W. Dexang, S. Genbo and Y. Minghan, *J. Cryst. Growth*, 169 (1996) 196-198.
- ³⁷ V. I. Salo, *Semiconductor Physics, Quantum Electronics & Optoelectronics*, 3(2) (2000) 200-202.
- ³⁸ V. I. Salo, A. P. Voronov, V. F. Tkachenko, G. N. Babenko, A. V. Makoveev, *J. Cryst. Growth*, 337 (2011) 13-19.
- ³⁹ V. I. Bepalov, V. I. Bredikhin, V. P. Ershov, V. V. Zil'berberg, V. I. Katsman, S.Y. Potapenko, *Proc. SPIE*, 1995, 2633, 732-739.
- ⁴⁰ V.I. Bepalov, *J. Nonlinear Opt. Phys. and Mater.*, 4 (1997) 467-472.
- ⁴¹ K. Sankaranarayanan, P. Ramasamy, *J. Cryst. Growth*, 337 (2011) 13-19.
- ⁴² S. Balamurugan, P. Ramasamy, S. K. Sharma, Y. Inkong, P. Manyum, *Mater. Chem. Phys.*, 117 (2009) 465-470.
- ⁴³ S. Dinakaran, Sunil Verma, S. Jerome Das, S. Kar, K. S. Bartwal, P. K. Gupta, *Physica B*, 405 (2010) 1809-1812.
- ⁴⁴ S. K. Sharma, Sunil Verma, Yeshpal Singh, K. S. Bartwal, *CrystEngComm.* 15 (2013) 9955-9962.
- ⁴⁵ A. K. Karnal, H. O. Mahawar, V. K. Wadhawan, *Indian J. Pure Appl. Phys.* 36 (1998) 587.
- ⁴⁶ M. Nakatsuka, K. Fujioka, T. Kanabe, H. Fujita, *J. Cryst. Growth*, 171 (1997) 531-537.
- ⁴⁷ K. E. Montgomery, N. P. Zaitseva, J. M. DeYoreo, R. K. Russell, US Patent No. 5904772, 18 May 1999.

- ⁴⁸ A. K. Karnal, A. Saxena, H. L. Bhat, V. K. Wadhawan, T. P. S. Nathan, *J. Cryst. Growth*, 289 (2006) 617-620.
- ⁴⁹ S. K. Sharma, Yeshpal Singh, K. S. Bartwal, P. K. Gupta, National Laser Symposium-20, January 9-12, 2012, Crystal Growth Centre, Anna University, Chennai, pp.72.
- ⁵⁰ S. K. Sharma, Sunil Verma, Yeshpal Singh, K. S. Bartwal, P. K. Gupta, 20th National Seminar on Crystal Growth and Applications (NSCGA 2016), Jan. 19-21, 2016, BARC, Mumbai, pp.144.
- ⁵¹ S. K. Sharma, Sunil Verma, Yeshpal Singh, K. S. Bartwal, M. K. Tiwari, G. S. Lodha and G. Bhagavannarayana, *Optical Materials*, 46 (2015) 329-338.
- ⁵² K. Lal and G. Bhagavannarayana, *J. Appl. Cryst.*, 22 (1989) 209-215.
- ⁵³ K. Lal, S. N. N. Goswami, J. Wurfl, H. L. Hartnagel, *J. Appl. Phys.*, 67 (1990) 4105-4113.
- ⁵⁴ F. C. Frank, W. T. Read, *Phys. Rev.*, 79 (1950) 722-723.
- ⁵⁵ M. Runkel, M. Yan, J. De Yoreo, N. Zaitseva, *Proc. SPIE*, 3244 (1998) 211-222.
- ⁵⁶ T. A. Eremina, V. A. Kuznetsov, N. N. Eremin, T. M. Okhrimenko, N. G. Furmanova, E. P. Efremova, M. Rak, *J. Cryst. Growth*, 273 (2005) 586-593.
- ⁵⁷ I. M. Pritula, M. I. Kolybayeva, V.I. Salo, Y. N. Velikhov, *J. Optoelectro. Adv. Mater.*, 2 (2000) 459-464.
- ⁵⁸ S. Dinakaran, Sunil Verma, S. Jerome Das, S. Kar, K. S. Bartwal, *Physica B*, 405 (2010) 3919-3923.
- ⁵⁹ Sunil Verma, S. Kar, K. S. Bartwal, in *Interferometry Principles and Applications*, Mark. [15] E. Russo (Ed.), Nova Science Publishers, New York, USA, 2012, Chap. 19, pp. 537-560.
- ⁶⁰ M. K. Tiwari, P. Gupta, A. K. Sinha, S. R. Kane, A. K. Singh, S. R. Garg, C. K. Garg, G. S. Lodha, S. K. Deb, *J. Synchrotron Rad.*, 20 (2013) 360-389.
- ⁶¹ V.A. Sole, E. Papillon, M. Cotte, Ph. Walter, J. Susini, *Spectrochim. Acta Part B* 62, (2007) 63-68; PyMCA software website <http://pymca.sourceforge.net/>
- ⁶² G.A. Leonard, V.A. Sole, A. Beteva, J. Gabadinho, M. Guijarro, J. McCarthy, D. Marrocchelli, D. Nurizzo, S. McSweeney, C. Mueller-Dieckmann, *J. Appl. Cryst.*, 42 (2009) 333-335.
- ⁶³ E. Dieguez, A. Cintas, P. Hernandez, J. M. Cabrera, *J. Cryst. Growth*, 73 (1985) 193-195.
- ⁶⁴ M. Runkel, M. Yan, J De Yoreo, N. Zaitseva, *Proc. SPIE*, 3244 (1998) 211-222.

⁶⁵ H. Yoshida, T. Jitsuno, H. Fujita, M. Nakatsuka, M. Yoshimura, T. Sasaki, K. Yoshida, *Appl. Phys.* B70 (2000) 195-201.

⁶⁶ Roger M. Wood, *Laser-Induced Damage of Optical Materials*, Institute of Physics Publishing, Bristol, 2003.

Chapter 4 Development of solute feed based unidirectional growth technique to enhance growth rate and crystallization yield of KDP crystals

4.1 Introduction

The “*Flat-top growth technique*” described in the previous chapter is suitable to enhance usable volume fraction of KDP crystals compared to the crystals grown using single-plate platform technique for fabrication of elements for electro-optic switching and SHG elements. However, it was noticed that still there is a scope to enhance the usability of KDP crystal by further modification of crystal shape. It is because the shape of elements prepared from the KDP crystals grown by single-plate or two-plate or by flat-top technique yield crystal element at best with square cross-section. Whereas for fabrication of devices, circular cross-section of device elements is most preferable because the laser beams involved in the operation with crystals have circular cross-section. Therefore, even though one uses an element of square cross-section of say side length ‘L’, the usable area of the sample will be considerably low as shown schematically in Fig. 4.1.

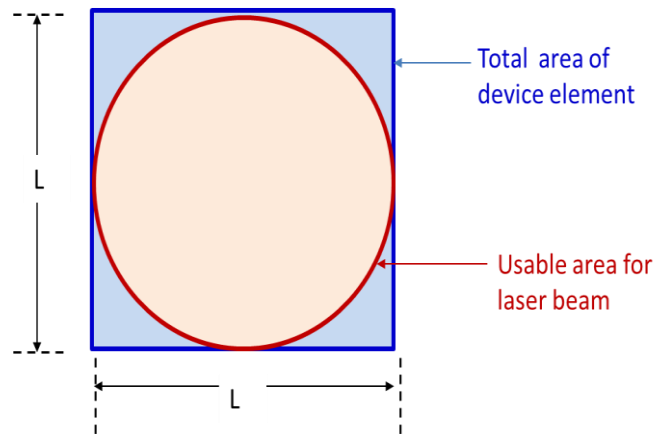


Fig. 4.1 Schematic depiction of usable area at the square cross-section device elements.

Mathematically it can be shown that,

$$\begin{aligned} \text{Usable area in square shape element (in \%)} &= \frac{\text{Area of a circle of diameter } L}{\text{Area of a square of side } L} \times 100 \\ &= \frac{(\pi L^2/4)}{L^2} \times 100 = 78.5 \end{aligned}$$

Additional benefit of using circular cross-section or say cylindrical shape device elements is that it would also reduce the required diameter of the housing and glass windows involved, compared to that needed for square or rectangular cross-section elements for handling the same size of laser beam.

We therefore investigated techniques for growth of cylindrical shape crystals from solution. In this context, we first analyzed the existing techniques for growth of cylindrical shape crystals in solution crystal growth. In the year 2000, Genbo et al. reported growth of cylindrical shape crystals of nickel sulphate from solution.¹ They used small size cylindrical shape glass tubes to guide growth of crystals along one direction. The tubes were mounted at a horizontal platform rotating in bulk solution where growth was achieved using slow cooling method. This method was probably the first indication of cylindrical shape growth of crystals from solution, however it was difficult to grow longer cylindrical shape crystals by using this technique. It was because of difficulty in mass transfer from bulk solution to the seed placed inside lengthy tubes. In 2005, Ramasamy and co-workers developed a different approach called as “*Sankaranarayanan-Ramasamy unidirectional growth technique*” or in short “*SR method*” for growth of cylindrical shape crystals.^{2,3} In this technique the entire solution was placed inside a cylindrical shape glass tube and growth takes place at the seed placed at the bottom by slow evaporation of the solution from its top. This technique is essentially based on creation of supersaturation by slow evaporation of the solvent from the solution located at top. The rate of evaporation is controlled by raising temperature at the top of the solution while the lower zone where seed is mounted, is kept near to room temperature to avoid mechanical stresses at the growing crystal. This technique is however suitable for growth of cylindrical shape crystals but suffering with low growth rate of nearly 1 to 5 mm/day particularly for KDP crystals.⁴⁻⁷ It has been attributed to the low supersaturation due to difficulty in controlling and maintaining high and uniform evaporation rate. Moreover, it was required to refill the evaporated part of the solution regularly or to move down the ring heater located at top of the solution as the solution level falls down due to evaporation, but this process is prone to nucleation. In order to enhance growth rates, Dinakaran et al. reported influence of forced convection inside the growth ampoule and obtained enhanced growth rate ~ 4.2 mm/day for KDP along [001] direction.⁸ Ghane et al. studied influence of EDTA to enhance growth rate of KDP and obtained an average growth rate ~ 2.5 mm/day along [001] direction.⁹

To circumvent the problems of low growth rates and the difficulty in controlling evaporation rate in “*SR method*”, we modified the way of producing supersaturation in SR method from evaporation to solute feeding and developed “*solute-feed based unidirectional growth technique*”. In this technique solute is fed online through a semi permeable membrane in the hot zone located at the top rather than to evaporate the solution.¹⁰ The basic driving force is concentration convection under gravity. Concentration-induced convection or so called temperature gradient method is well reported in the literature where it has been used for growth of crystals in free hanging geometry,¹¹ top hanging geometry¹² or on a horizontal platform¹³. The shape of KDP crystals grown by these techniques was tetragonal pyramidal.¹² To obtain cylindrical shape crystals we applied concentration convection method to create supersaturation in the cylindrical shape growth ampoules where the seed was placed at the bottom of the tube as used in the SR method.

In this chapter, we described the solute feed based unidirectional growth technique in detail and its application for growth of cylindrical shape KDP crystals. The KDP crystals were grown successfully along different crystallographic directions such as [001], [101], [100] and type-II SHG directions. The growth rates achieved using this technique for KDP crystals was up to ~ 10 mm/day. To further verify the validity of this technique for growth of other crystals, a glimpse of some other crystals such as DKDP, LAP etc. grown using this technique is also provided at the end of this chapter for the purpose of completeness.

4.2 Development of solute feed based unidirectional growth technique

Solute feed base unidirectional growth technique is based on creation of supersaturation difference along vertical direction in a solution placed in a cylindrical glass tube called as growth ampoule. It is created in such a way that the supersaturation be almost zero at the top of the solution while highest at the bottom where seed crystal is placed. A feed of solute is made at top to compensate the material deposited at the seed crystal. The material transport from top to bottom takes place due to gravity if the concentration is maintained higher at the top compared to that at the lower end of the solution in the ampoule. It is achieved by maintaining two conditions:

- i) Creating a temperature difference between the upper and lower zones of the ampoule. For chemicals having positive temperature coefficient of solubility the upper region is kept at higher temperature compared to that at the lower region of the ampoule.
- ii) Keeping a constant feed of solute at the upper zone so that saturation concentration is maintained corresponding to the higher temperature of the upper zone. This is done by keeping excess solute in contact of the solution at top through micro-porous membrane so that it maintains mass transfer without falling solute particles into the bottom of the ampoule.

If these two conditions are maintained, solute transfer automatically takes place from the upper zone to the lower zone under gravity due to being higher concentration at the upper zone. The process continues until the density of the solution become uniform. In this situation the solution at the upper zone be near to the saturation concentration to its temperature while that at lower zone becomes supersaturated. If a seed crystal would have been placed at the lower end of the ampoule it would start growing due to being in supersaturated solution. As the crystal grows the concentration depletes nearby it which would be compensated from the upper zone to maintain density equilibrium. The water molecules having higher temperature and hence lower density at the top zone could not move downward under gravity and hence the difference of temperature can be maintained. Thereby crystal growth continues for growth of large size crystals. A schematic of the functioning of the solute feed based unidirectional growth technique is shown in Fig. 4.2

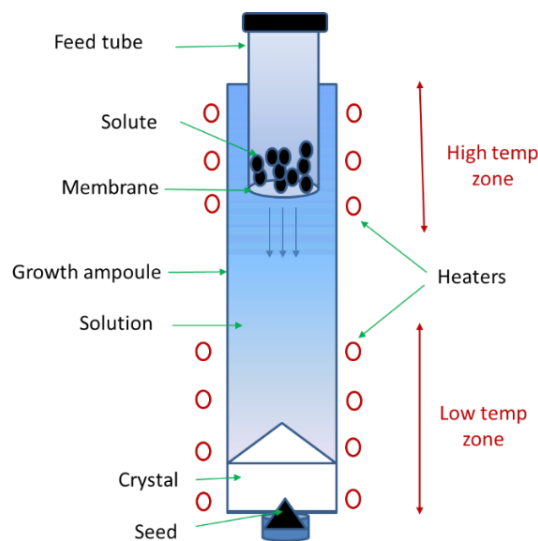
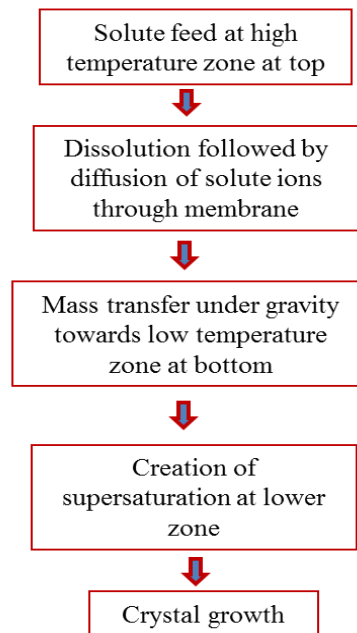


Fig. 4.2 Schematic representation of solute feed based unidirectional growth technique.

The step wise processes of crystal growth in short can be described as,

Process of mass transfer



4.3 Instrumentation for unidirectional growth of crystals by solute feeding

The experimental workstation for growth of KDP crystals by the solute feed based unidirectional technique has been developed in-house. It is relatively simpler and compact compared to that used for conventional or platform based techniques of KDP crystal growth. It consists of mainly a two-zone water bath associated with two separate PID temperature controllers and two Pt-100 RTD sensors, a growth ampoules and a feed tube with microporous membrane fitted at its lower end.

4.3.1 Fabrication of a two-zone water bath

To achieve temperature gradient across a long cylindrical growth ampoule a two zone water bath was fabricated. Initially it was fabricated by mounting two helical shape glass tubes containing resistive heaters at upper and lower portions of a 10 liter capacity borosilicate beaker as shown in Fig. 4.3. The heaters were controlled by two separate PID temperature controllers via individual Pt-100 RTD sensors. Axial temperature profile of this bath was measured and found that there was a temperature gradient in the lower zone of this bath. While ideally we need uniform temperature at the lower zone so that the growth conditions i.e. the driving force remain uniform during the growth of the crystal.

Therefore, an improved version of the two-zone water bath was designed and fabricated where the two heaters were kept isolated. It is shown schematically in Fig. 4.4. The actual photograph of the fabricated two-zone water bath is shown in Fig. 4.5 (a). It consists of a central glass tube of 50 mm diameter and about 300 mm length, around which helical shape resistive heaters were provided at top and bottom regions. The two heaters are submerged in separate water bodies which were isolated from each other by about 50 mm distance called as buffer zone. Fig. 4.5 (b) shows the photograph of a growth ampoule above which feed tube is mounted with a nylon make connector to avoid any leakage of water vapour of the solution. The growth ampoule is mounted in the central glass tube of the two-zone bath with the help of a clamp for growth of crystals.

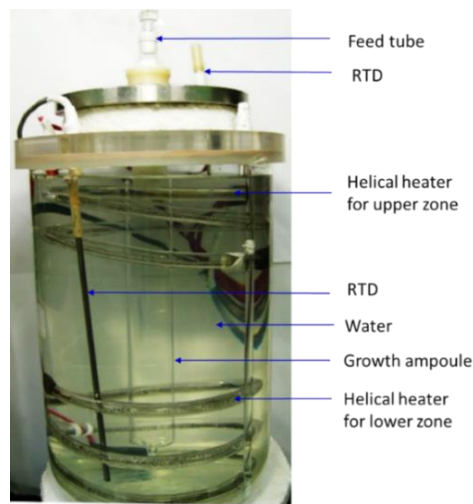


Fig. 4.3 Two-zone water bath fabricated using helical shape heaters in a single glass beaker.

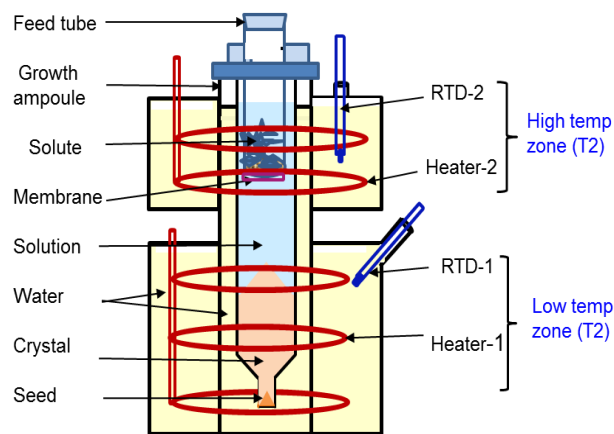


Fig. 4.4 Schematic line diagram of the two-zone water bath with isolated heating zones.

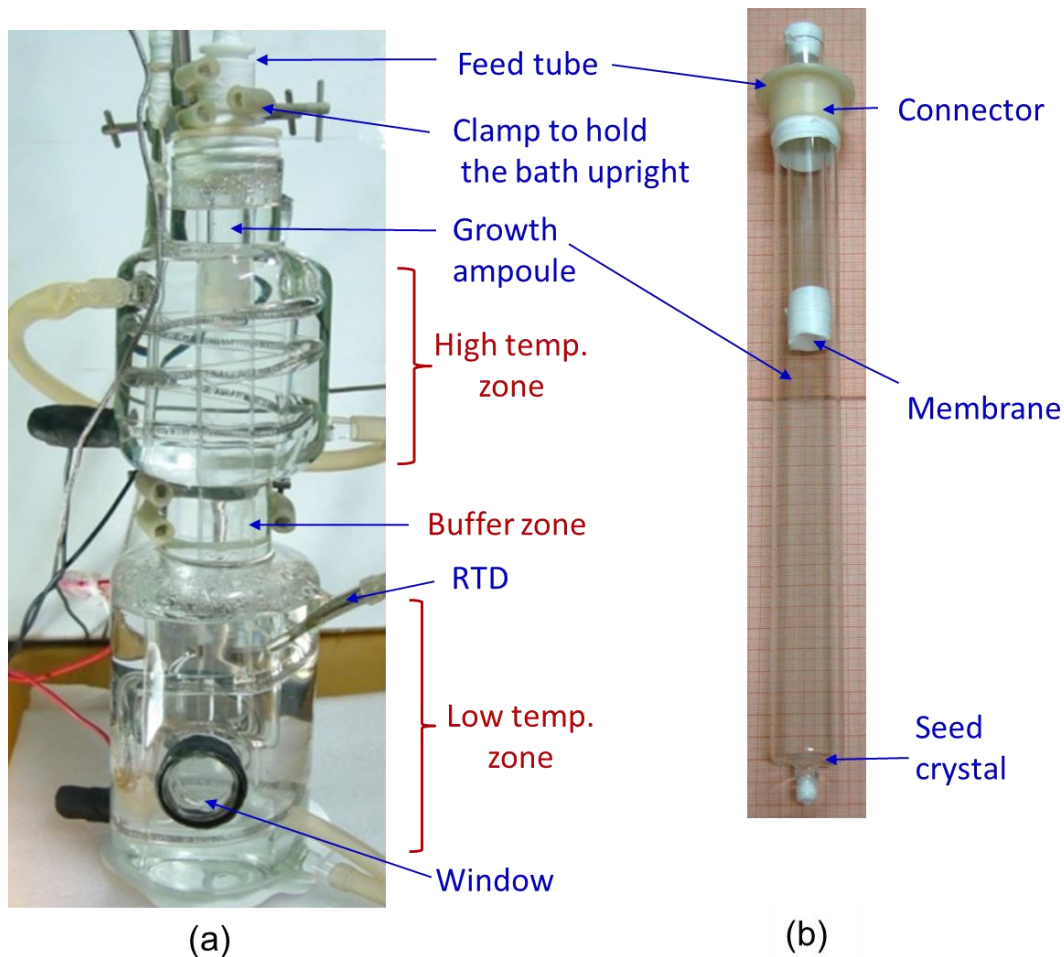


Fig. 4.5 (a) Photograph of the fabricated two-zone water bath with isolated heating zones, and (b) growth ampoule with feed tube.

4.3.2 Axial temperature profile of the two-zone water bath

The axial temperature profile of the above bath was measured at different set temperatures of the upper zone keeping the temperature of the lower zone fixed at 30 °C. Fig. 4.6 shows the axial temperature profile of the fabricated two-zone water bath. It shows that the temperature gradient of the lower zone is quite low of the order of ~ 0.2 °C/cm and extended up to ~ 16 cm length. The temperature profile of the lower zone is almost independent to the change in the temperature of the upper zone. The bath is thus suitable for crystal growth in constant temperature and constant supersaturation conditions. The temperature of the upper zone can be varied to enhance supersaturation without affecting the temperature of the lower zone where crystal growth takes place.

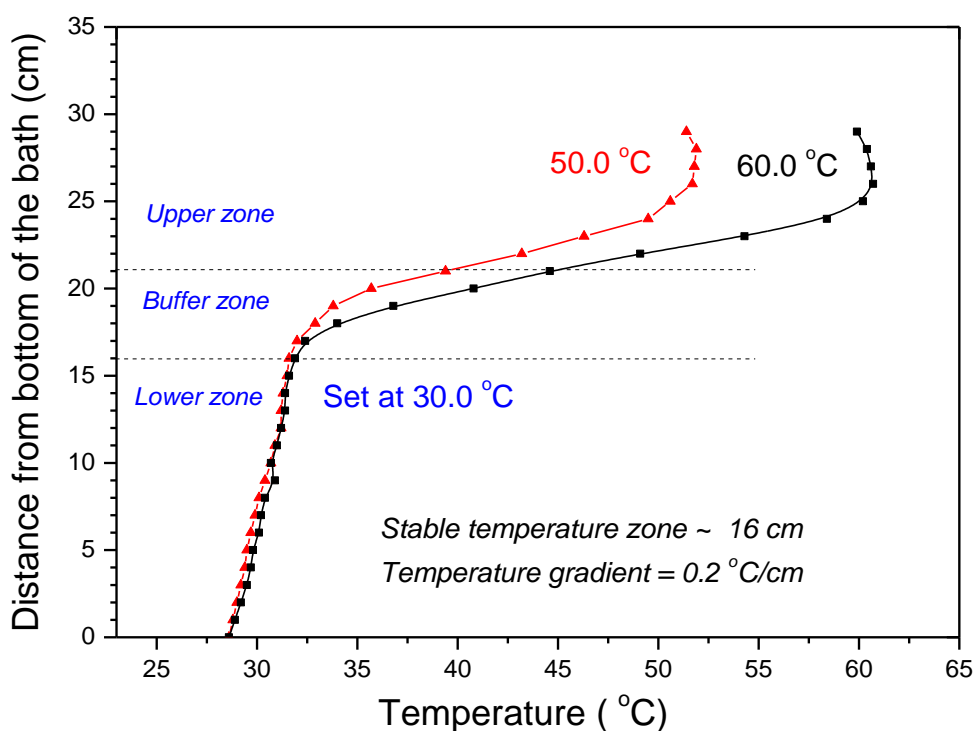


Fig. 4.6 Axial temperature profile of the fabricated two-zone water bath at two different temperatures of the upper zone.

4.3.3 Growth ampoule, feed tube and seed mounting method

Growth ampoule is normally made using a borosilicate glass tube where top end is kept open for fitting feed tube while the lower end has a small opening of diameter ~ 5 mm for placement of seed crystal. We used two designs of the lower ends to mount small size natural seed crystal for initiation of crystal growth as shown schematically in Fig. 4.7. The flat-bottom ampoule is suitable to obtain uniform diameter crystals but it need to cut the glass tube to take out the grown crystal. While conical-bottom ampoule gives tapered crystal but it is easier to take out the grown crystal without breaking the glass ampoule. The seed was mounted with help of Teflon tape and silicone sealant to avoid leakage of solution from the lower end. The upper end of the growth ampoule was fitted with a nylon or teflon make connector in which another glass tube of lesser diameter than the growth ampoule called as the feed tube was fitted tightly so that no chances of solvent leakage be there. The lower end of the feed tube was provided with 0.2 μm porosity membrane filter of nylon with tight fitting to avoid any leakage. The use of 0.2 μm porosity membrane is equivalent to the online filtration of solution and hence avoid the chances to pass any solid

particle through the membrane and therefore chances of nucleation due to online feed of the powder is restricted. The upper end of the feed tube has a lid from where solute particles are fed regularly into the feed tube during growth. As crystal grows, it pushes up the solution upward through the membrane in the feed tube which act like flushing of the pores of the membrane and hence avoid choking of pores.

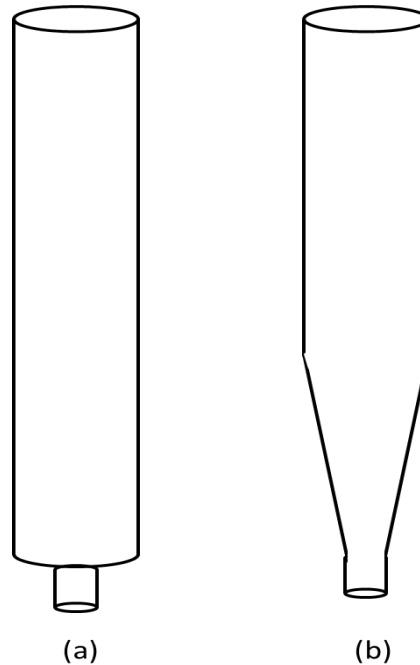


Fig. 4.7 Schematic line diagram showing two designs of growth ampoules for mounting point seeds for crystal growth, (a) flat bottom, and (b) conical bottom.

4.3.4 Imaging mass transfer and crystal growth by shadowgraphy technique

In order to confirm the mass transfer through the membrane and growth of crystal, laser shadowgraph technique was employed.¹⁴ It is also useful to determine the state of saturation or growth of the seed crystal and to visualize the rate of mass transfer through the membrane. Fig. 4.8 (a) shows the typical optical layout for this experiment where a He-Ne laser was used. The laser beam was expanded by a beam expander (BE) and passed through the growth ampoule from where the membrane or the growing crystal is there and imaging at the screen was done using a converging lens. Fig. 4.8 (b) shows the typical shadowgraphs for mass transfer and growth. The downward plumes emanating from the membrane confirms the mass transfer of solute through the membrane and the depleted plumes moving upward from the crystal top shows that the crystal is growing. The intensity of these two plumes signifies the rate of the two processes.

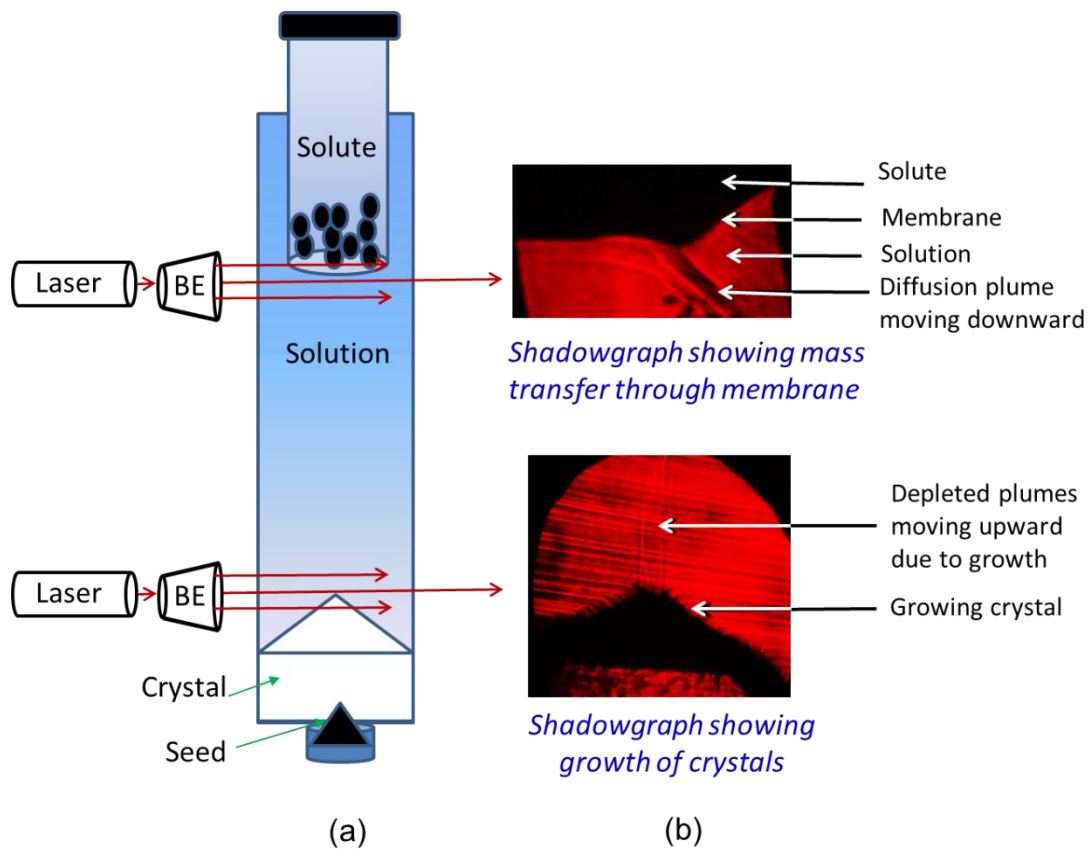


Fig. 4.8 (a) Schematic of the laser shadowgraphy set up used for imaging the process of mass transfer and crystal growth, and (b) photographs of typical laser shadowgraphs corresponding to mass transfer through the membrane from the feed powder, and upward movement of depleted plumes from the growing crystal shows crystal growth.

4.4 Growth of unidirectional KDP crystals by solute feeding technique along different crystallographic directions and their characterizations

For unidirectional growth of KDP crystals, KDP chemical was prepared as described in the Chapter 3. The chemical was used to prepare saturated solution at room temperature. The solution was filtered and overheated and again cooled to room temperature and then transferred in to a growth ampoule where seed was already fixed at the bottom. Subsequently the ampoule was fitted with the feed tube at the top. The whole growth unit was then mounted in the two-zone water bath where the lower zone temperature was set a few degrees above the room temperature. The solution was kept a few hours as such to get dissolved a few atomic layers of seed to reduce surface defects. Subsequently the feed tube

was filled with fine and purified solute powder and the temperature of the upper zone was optimized to get mass transfer. This process slowly leads to creation of supersaturation at the lower zone where the seed was placed. After about one or two day, it looks growing depending on the rate of mass transfer. The rate of mass transfer and hence growth rate of crystal depend on several parameters such as, value of the temperature gradient ($\Delta T = T_{\text{Upper zone}} - T_{\text{Lower zone}}$), growth temperature at the lower zone, porosity, area and thickness of the membrane, viscosity of the solution and solubility curve of the material, diameter and length of the growth ampoule etc.

We have grown several cylindrical and conical shape KDP crystals using this method to demonstrate the working of the “*solute feed based unidirectional technique*”. The shape of the crystal depends on the shape of the growth ampoule at the bottom. We have grown KDP crystals along [001], [101], [100] and SHG type-II orientations. The growth and characterization of crystals grown along two important directions namely [001] and SHG type-II orientations is described in details because these are particularly useful for device applications. The [001] oriented KDP crystal is useful for fabrication of elements for electro-optic modulation and switching while the SHG oriented crystal is useful for making circular shape SHG elements by just slicing the crystals normal to the growth ampoule.

4.4.1 Unidirectional growth of KDP crystals along [001] direction by solute feeding technique and its characterizations

4.4.1.1 Growth of [001] oriented unidirectional KDP crystals

We have grown KDP crystals along [001] direction using both the conical bottom and flat bottom growth ampoules. Fig. 4.9 shows some of the KDP crystals grown along [001] direction by solute feed based unidirectional technique. While Fig. 4.10 shows a complete growth unit for the crystal shown in Fig. 4.9 (c), when it was taken out from the two-zone bath. The growth details of these crystals is given in the Table 4.1. It shows that growth rate depends on temperature gradient and diameter of the crystal.

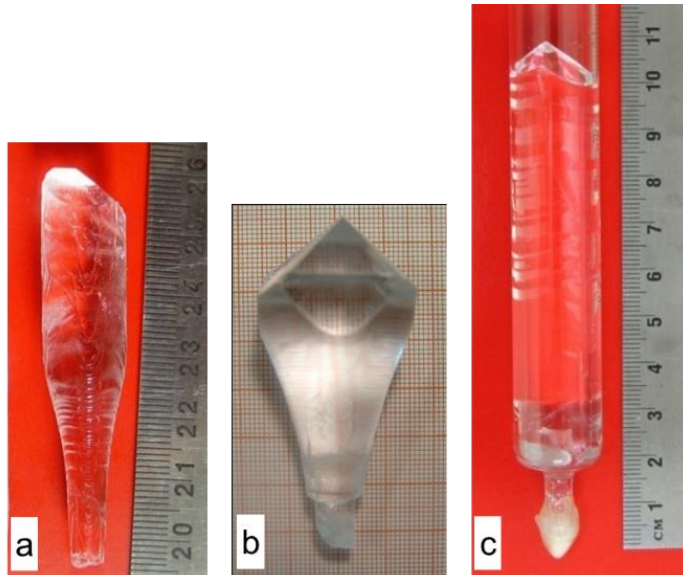


Fig. 4.9 KDP crystals grown along [001] direction by using solute-feed based unidirectional growth technique.

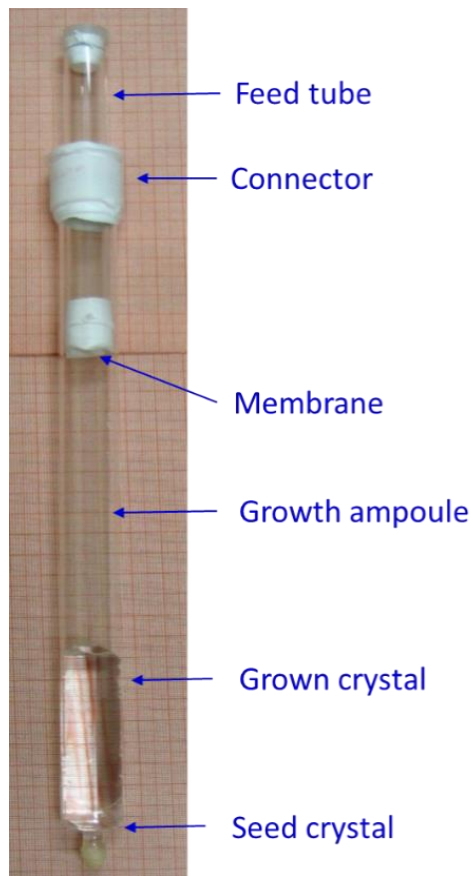


Fig. 4.10 Crystal growth ampoule containing a KDP crystal grown inside it.

Table 4.1 Growth details of [001] oriented KDP crystals grown by solute feeding method.

Crystal	Dimensions: Dia. × Height (mm)	Temperature gradient: ΔT ($T_2 - T_1$) (°C)	Growth duration (days)	Average growth rate, $R_{[001]}$ (mm/day)
Fig. 4.9 (a)	4 - 13 × 65	10 (38 - 28)	11	6
Fig. 4.9 (b)	8 - 29 × 56	21 (55 - 34)	8	7
Fig. 4.9 (c)	3 - 17 × 90	Variable: 10 to 30	18	2 to 10

In one of the growth runs, we studied influence of temperature gradient on the growth rate of KDP along [001] direction. The temperature gradient was kept low until the seed acquired the diameter (17 mm) of the glass tube after that the temperature gradient was varied in steps and the growth of the crystal was monitored. We have studied influence of temperature gradient on the growth rate of KDP crystal along [001] direction for a growth tube of internal diameter of 17 mm and the membrane diameter of ~ 12 mm exposed to the solution. The length of solution column was ~ 300 mm. The results are summarized in the Table 4.2. It shows that, it is possible to achieve high growth rate of KDP crystal without nucleation and without visible inclusions by solute feed based unidirectional growth technique.

Table 4.2 Influence of increasing temperature gradient on growth rate of KDP along [001] direction.

Temp. of the lower zone (T_1) (°C)	Temp. of the upper zone (T_2) (°C)	Temp. gradient (ΔT) (°C)	Average growth rate along [001] direction (mm/day)
30	40	10	2
30	45	15	3
30	50	20	5
30	55	25	7
30	60	30	10

The crystal was grown from point seed, indicating that crystal cross section can be enlarged in this technique which was difficult in case of solvent feed based unidirectional growth techniques.⁵ The growth rate along the tube axes mainly depends on temperature gradient but also influenced by the diameter of the growing crystal, area of the membrane and length of the growth ampoule.

4.4.1.2 Characterization of the crystal grown along [001] direction

The 90 mm long, [001] oriented KDP crystals was characterized in details for assessment of its optical quality, optical homogeneity, defects structure and laser damage threshold with particular interest of how these properties varies as growth proceeds. For this purpose, the crystal was cut using *Buehler* make diamond coated disc cutter. Three plates of similar thickness ~ 2 mm were prepared from its bottom, middle and top portions as shown in Fig. 4.11 and subsequently polished for characterization.

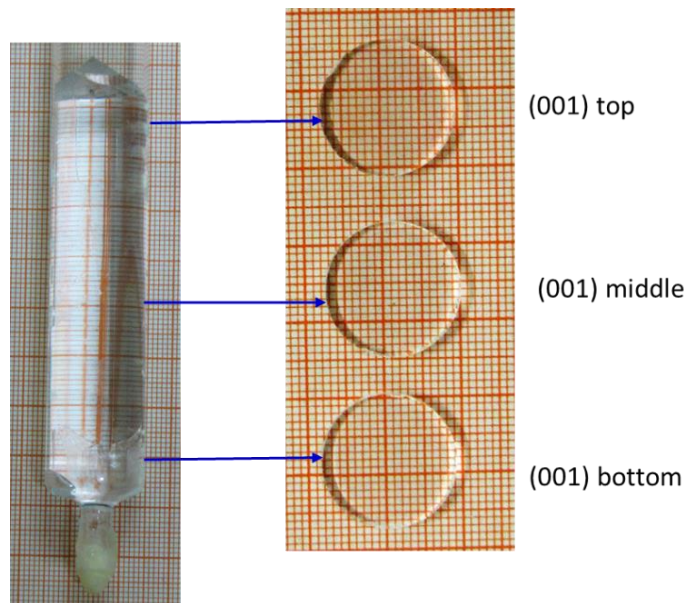


Fig. 4.11 Three (001) plates prepared from the 90 mm long [001] oriented KDP crystals from bottom, middle and top portions.

UV-Vis-NIR transmission measurement

The UV-Vis-NIR transmission spectroscopy was carried out for the prepared plates using *Jasco* make spectrophotometer in the wavelength range of 190 nm to 1900 nm range. Fig. 4.12 shows the obtained spectra without accounting the Fresnel losses. It shows that all the three plates have 88 to 89 % transmittance in the visible-NIR region. There is no absorption peak in the UV region indicating the crystal has very low content of trivalent metallic

impurities such as Fe which is known to show absorption peak near 270 nm. A closer look shows that (001) middle plate have slightly lower absorption than the other two plates. It may be due to relatively higher defects density in this plate due to some scatterers rather than absorption by metallic impurities.

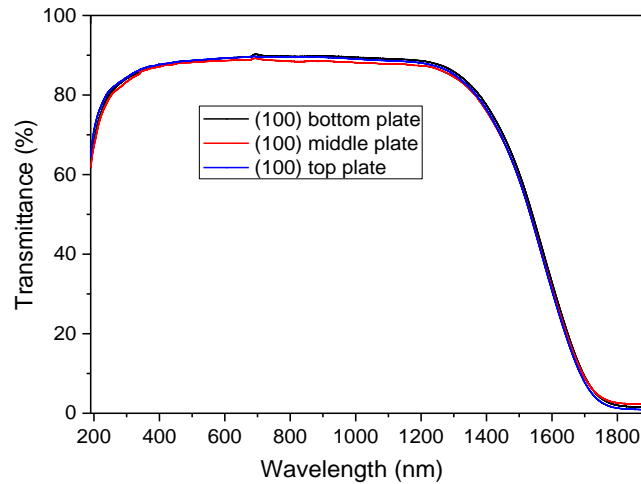


Fig. 4.12 UV-Vis-NIR transmission spectra for the three sample plates of the (001) oriented unidirectional KDP crystal.

Birefringence homogeneity by laser conoscopy

Birefringence homogeneity was tested by laser conoscopy for the three (001) plates. It was done by placing the sample plates between crossed polarizers where an expanded beam of He-Ne laser converged by a lens of 50 cm focal length was passed. Fig. 4.13 shows the characteristic conoscopic interferograms for (001) plates of uniaxial crystals. The concentric fringes show good optical homogeneity of the crystal plates. The location of isogyres is almost at the centre indicating the direction of c-axis is normal to the sample plates.

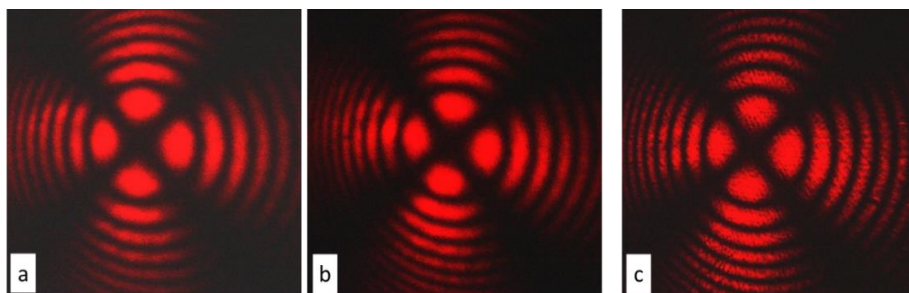


Fig. 4.13 Laser conoscopy images of (001) bottom plate (a), (001) middle plate (b), and (001) top plate (c).

X-ray diffraction topography

X-ray diffraction topography for the three sample plates was carried out to analyse defect structure and their distribution in the unidirectional grown crystals. Fig. 4.14 shows the X-ray diffraction topographs by Cu_K α radiation in Berg - Barrett reflection geometry for the three plates for (316) diffraction planes. It shows very clearly that defects do not get introduced due to the glass container. Further hydrodynamic stress induced defects such as linear chains of dislocations and Frank-Reid type dislocation loops are also not observed. It is because the growth takes place at a constant temperature and that is near to room temperature. However, there are defects due to growth rate instability between {101} pyramidal faces. There are also localized defects and some inclusions. The dark patches mainly in the middle and top plates are attributed to the difference in growth rates among {101} faces which may lead to difference in impurities concentration. Overall the defects density is low, however crystal quality may be further improved by employing high purity chemicals and choosing single sector growth.

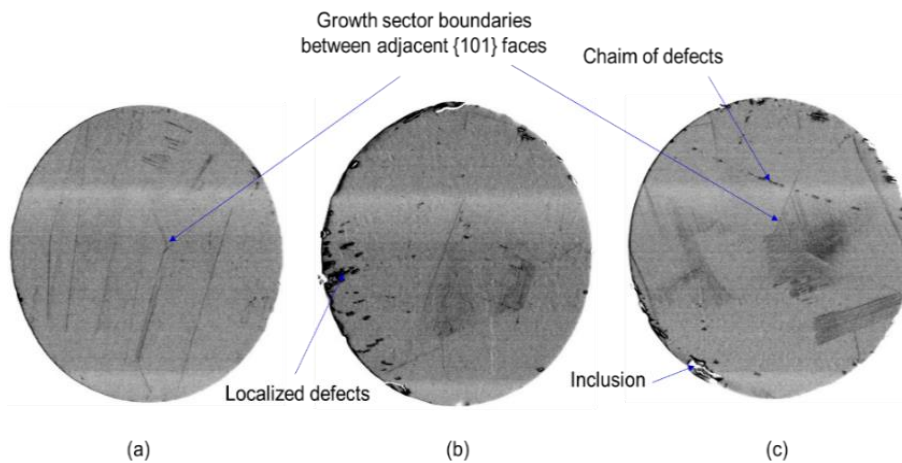


Fig. 4.14 X-ray diffraction topographs for (316) planes of (001) bottom (a), (001) middle (b), and (001) top plates (c) of the [001] oriented unidirectional KDP crystal.

Laser damage threshold measurements

The laser induced damage threshold was measured using 7 ns pulse width Nd:YAG laser described in chapter 3. The laser beam diameter ($1/e^2$) was 1.25 mm at the sample surface. The experiment was conducted by “R on 1 method” at three point of each plate at the central region. We could not find any major variation due to location of the plates in the crystal. The calculated value of the LDT for (100) plates of the solute feed based

unidirectionally grown KDP was $4.12 \text{ GW/cm}^2 (\pm 10 \%)$. This shows that LDT of these crystals is comparable to that reported in the literature.^{15,16} The high LDT of these crystals is attributed to less number of stress induced defects.¹⁷

4.4.2 Unidirectional growth of KDP along SHG type-II phase matching direction by solute feeding and its characterization

4.4.2.1 Growth of SHG type-II oriented unidirectional KDP crystals

One of the main applications of KDP is for laser frequency conversion but the usable volume fraction is quite low in the natural morphology crystals.¹⁸ Unidirectional technique is useful to provide directly cylindrical shape crystals with high usable volume fraction. Dinakaran et al. reported growth of small size KDP crystal along SHG type-II direction in cylindrical tube using evaporation technique.¹⁹ We used solute feed based unidirectional technique for SHG type-II oriented growth of KDP crystals. The growth was conducted in a 55 mm internal diameter glass make growth ampoule. Seed crystal was prepared by cutting a small size conventionally grown KDP crystal for SHG type-II phase matching direction for Nd:YAG laser. The seed was mounted at the bottom of the ampoule using silicone sealant. The growth vessel was made with conical end so that seed cross section enlarges smoothly. Fig. 4.15 shows the KDP crystal grown along the SHG type-II phase matching direction by solute feeding method.²⁰ The crystal has conical shape as per the shape of the tube. The crystal was grown in the two-zone bath of the 10 liter capacity. The crystal was $\sim 100 \text{ mm}$ long with maximum diameter $\sim 55 \text{ mm}$. The diameter of the feed tube was $\sim 20 \text{ mm}$ where $0.2 \mu\text{m}$ porosity membrane filter was fitted. The temperature gradient was increased from 5 to $25 \text{ }^\circ\text{C}$ as per the crystal size. The initial growth rate was $\sim 4 \text{ mm/day}$, later it decreased as the diameter of the crystal increased. It resulted into appearance of $\{100\}$ facets in the crystal as in crystal at Fig. 4.15 (b). It happens due to relatively lower growth rate of $\{100\}$ faces compared to that along $\{101\}$ faces at low supersaturation.^{21,14} The crystal contains a few localized inclusions mainly parallel to the slow growing (100) surface at top and at growth sector boundaries while the major part of the crystal is transparent. There was however no nucleation observed during growth. The overall growth rate of the crystal was $\sim 2 \text{ mm/day}$. The crystal was grown without cooling and without evaporation just by solute feeding and hence converts $\sim 100\%$ material fed at top into single crystal.

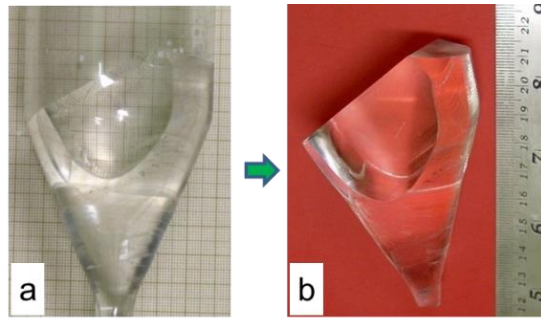


Fig. 4.15 SHG type-II oriented KDP crystals grown by solute feed based unidirectional technique (a) as grown KDP in the growth ampoule of 55 mm diameter, and (b) photograph of the crystal after taking out from the growth ampoule.

4.4.2.2 Characterization of SHG type-II oriented unidirectional grown KDP crystal

For assessment of the quality of the grown crystal for laser applications, the grown crystal was cut perpendicular to the growth direction using the diamond coated disc cutter. The prepared samples were polished using fine alumina powder at soft polishing cloth with ethylene glycol as lubricant. Fig. 4.16 (a) shows the prepared SHG elements and Fig. 4.16 (b) shows (100) plate prepared from the top most part of the crystal. We have mainly characterized one of the SHG plates namely no.1, located near to the seed region and the (100) plate from the topmost region for assessment of quality of the crystal in detail. The thickness of both these plates was ~ 2.6 mm. The sample plates were characterized for optical quality by transmission spectroscopy, birefringence interferometry, Mach-Zehnder interferometry. The structural quality was analysed by high resolution X-ray diffraction, X-ray topography and chemical etching techniques, and device usability was tested by SHG efficiency measurements and laser-induced damage threshold measurements.

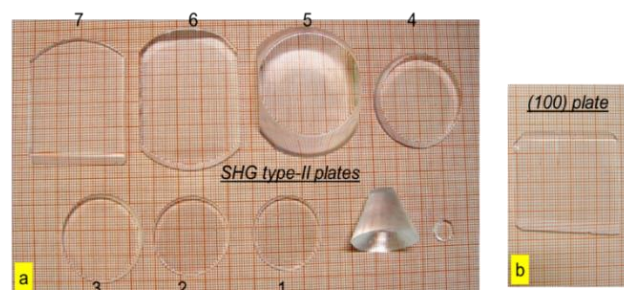


Fig. 4.16 (a) Type-II SHG elements prepared by slicing the KDP crystal shown in Fig. 4.15 normal to the growth direction, and (b) (100) plate prepared from the top portion of the crystal.

UV-Vis-NIR transmission measurement

The UV-Vis-NIR transmittance measurements was carried out for the well-polished (100) plate and the SHG plate using *Jasco* make spectrometer in the wavelength range of 190 nm to 1250 nm. Fig. 4.17 shows the obtained spectra showing that optical transmittance is nearly 90 to 92 % range for both the plates for 465 nm to 1250 nm without accounting for Fresnel reflection losses. Both the plates show absorption peak near 270 nm which is attributed to the presence of trivalent metallic impurities particularly iron in the crystal.^{22,23} SHG plate is having relatively lesser absorption near 270 nm as compared to that for (100) plate indicating that the concentration of trivalent metallic impurities is lesser in the SHG plate as compared to that in (100) plate. It is because {100} faces are relatively more prone to trap these trivalent metallic impurities compared to {101} faces due to their atomic structure.²⁴

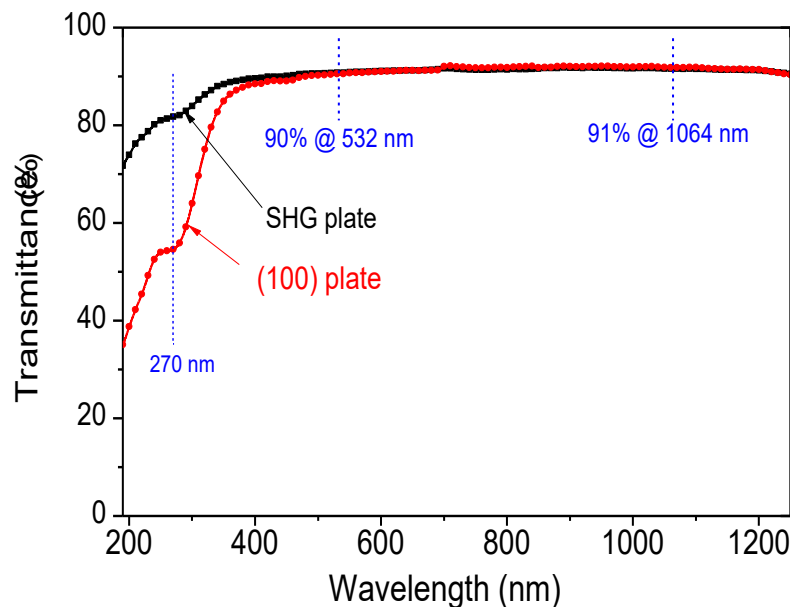


Fig. 4.17 UV-Vis-NIR transmission spectra for 2.6 mm thick (100) and SHG plates of SHG type-II oriented unidirectional grown KDP crystal by solute feeding technique.

Birefringence homogeneity

Birefringence homogeneity was assessed by orthoscopic set up of birefringence interferometry, where a collimated laser beam is passed through a crystal placed between a pair of crossed polarizers.²⁵ The interference fringes are formed due to optical path difference between extraordinary and ordinary waves inside the crystal.²⁶ A single fringe shows the spatial location at the crystal where the optical path difference is uniform. Fig.

4.18 (a) and Fig. 4.18 (b) show the birefringence interferograms for (100) and SHG plates respectively from the 10 mm diameter region of the central part of the crystal. Equispaced fringes without localized distortion indicate good birefringence homogeneity of the sample plates. The fringes indicate the wedge and slight curvature in the crystal plates due to processing errors.

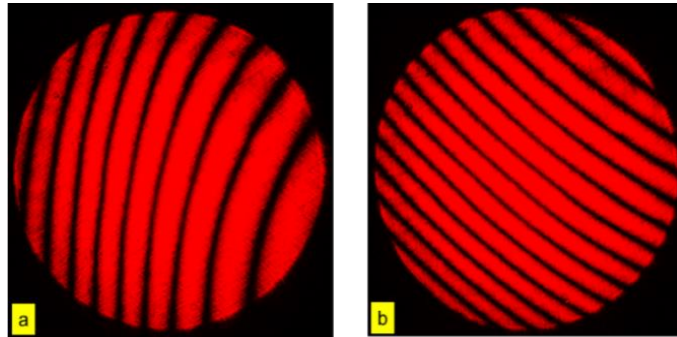


Fig. 4.18 Orthoscopic birefringence interferograms for (100) plate (a), and for the SHG plate (b), prepared from SHG type-II oriented unidirectional KDP crystal.

Mach-Zehnder interferometry

Optical homogeneity is an important characterization to indicate optical quality of the sample plates. It was determined using Mach-Zehnder interferometry for the both plates using He-Ne laser beam.²⁷ The interferometer was first aligned for infinite fringe setting by compensating optical path difference between the two arms using a wedge plate and then the sample plate was introduced in the path of one of the arms of interferometer. The obtained interferogram was captured using a CCD camera. Fig. 4.19 (a) and (b) show the obtained Mach-Zehnder interferograms for the (100) and SHG plates respectively. Both the interferograms show equi-spaced parallel fringes without distortion and inter crossing indicating good optical homogeneity of the crystal plates. Each fringe corresponds to equal optical path difference and hence parallel fringes indicates that there is wedge in the prepared samples

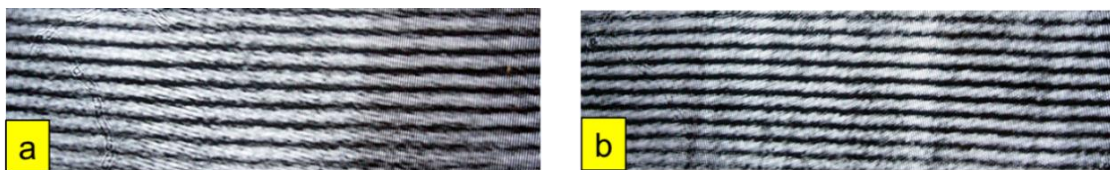


Fig. 4.19 Mach-Zehnder interferograms for (100) plate (a), and for SHG plate (b).

X-ray diffraction topography

The samples plates were further investigated using X-ray diffraction topography to determine defect structures and distribution. The plates were slightly etched using demineralized water for about 10 s to dilute features of surfaces scratches due to polishing errors. Fig. 4.20 (a) and (b) show X-ray diffraction topographs for (732) planes of SHG plate 1 and 6 and Fig. 4.20 (c) shows that for (712) planes of (100) plate. It is evident that a large portion of both the plates have low defect density however localized defects have been observed preferably at growth sector boundaries which may arise due to variation in relative growth rate of {101} and {100} faces. SHG plate show relatively higher defects compared to that for (100) plate which is attributed to the presence of {100} and {101} growth sector boundary in the SHG plates. This results corresponds to that observed in rocking curve FWHM in the next section.

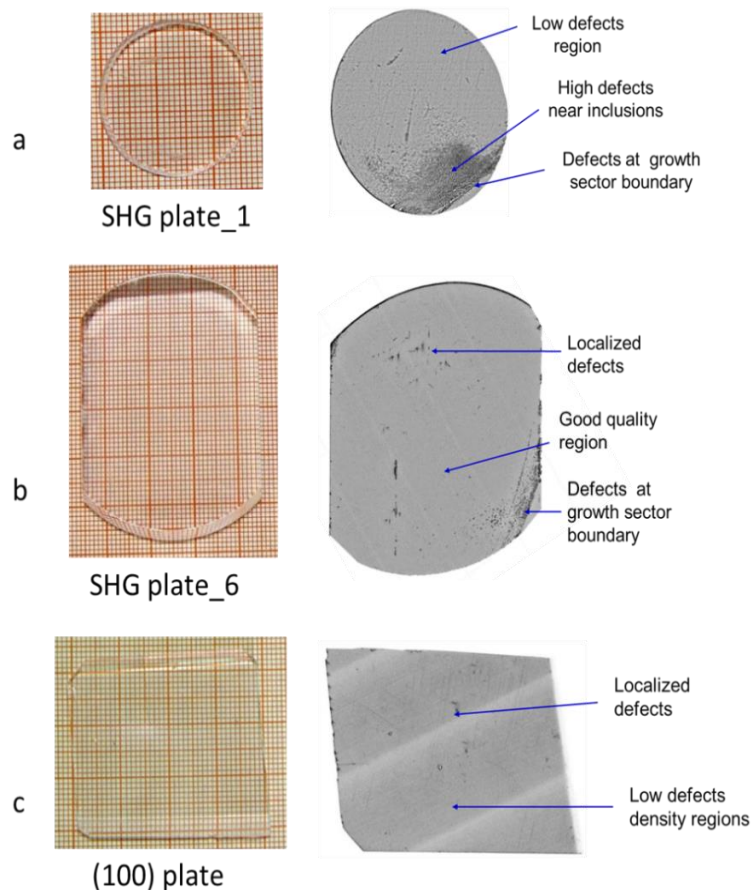


Fig. 4.20 X-ray diffraction topographs, (a) for type-II SHG plates no. 1, (b) for type-II SHG plate no. 6, and (c) for (100) plates.

High resolution X-ray diffraction

High resolution X-ray diffraction is an important technique for qualitative and quantitative assessment of crystalline perfection. It is based on Bragg's law of X-ray diffraction and sensitive for a very small change in lattice parameters due to defects. Fig. 4.21 (a) and (b) show that HRXRD curves or so called rocking curve for the (100) and SHG type-II plates obtained by ω -scan about x-ray diffraction peak for (200) and (101) planes. The rocking curve FWHM is lying in the range of 6 to 8 arc second confirming high crystalline quality of the crystal. A closer look reveals that rocking curve FWHM is slightly higher for SHG plate and also the peak is asymmetric compared to that for (100) plate indicates that localised defect density is higher in the SHG plate compared to the (100) plate.²⁸ It is attributed to the defects observed at the growth sector boundaries as observed in the X-ray topograph of the SHG plate in the earlier section.

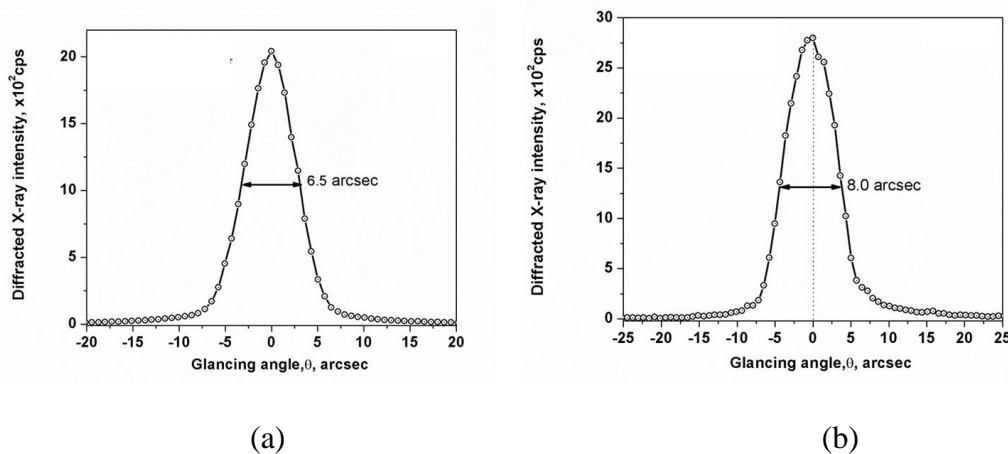


Fig. 4.21 High resolution X-ray diffraction curves for (100) plate (a), and for SHG plate (b).

Chemical etching

Chemical etching investigations were carried out to image surface defects particularly the distribution of dislocation defects at (100) plate. The etched plate prepared for X-ray diffraction topography was visualized under an optical microscope. Fig. 4.22 shows the optical micrographs corresponding to the high and low etch pit density regions. The shape of the etch pits is near to parallelograms similar to that observed by other researchers.²⁹ It revealed that crystal in general has low etch pit density (EPD) while near localised defects a group of dislocations was observed. The EPD for (100) plate is of the order of $\sim 10^3$ per

cm². In case of SHG plates inclusion were observed as chains of fine drops near growth sector boundaries which are attributed to the asymmetrical growth rates along the different faces which cause asymmetric hydrodynamic conditions due to movement of growth plumes.³⁰

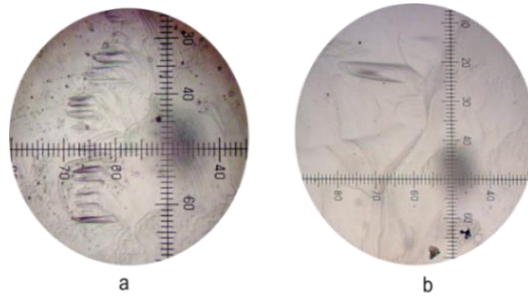


Fig. 4.22 Optical micrographs of the chemical etch pits at the (100) plate, (a) at high defects density region, and (b) at low defect density region. (Magnification: 50 X)

SHG efficiency measurements

SHG efficiency measurements were carried out for the type-II SHG plate of diameter about 35 mm and thickness 2.6 mm. Initially the plate was mounted at an orienter and aligned for the optimum phase matching direction for the beam passing through the central region of the crystal. It showed that SHG orientation was within $\pm 2^\circ$ from normal to the plate surface. Measurements of second harmonic pulse energy was measured by varying fundamental laser pulse energy of Nd:YAG laser and calculated the power efficiency. Fig. 4.23 shows the variation of the efficiency of second harmonic power with respect to the fundamental laser power. The SHG power efficiency was $\sim 21\%$ at laser pulse intensity $\sim 300 \text{ MW/cm}^2$.

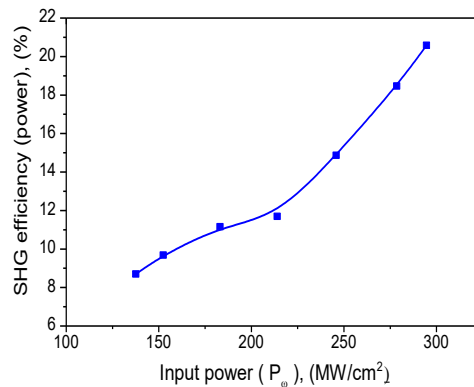


Fig. 4.23 Variation of SHG efficiency with input power density for the SHG type-II plate.

Laser damage threshold measurements

Laser induced damage threshold was determined using Nd:YAG laser of 7 ns pulse width for assessment of laser resistance of the KDP sample plates. Measurements were also carried out for both the (100) and SHG plates at three different locations in their central regions using “R on 1” methodology showing that surface damaging intensity lying in the range of 2.4 to 3.6 GW/cm².

4.4.3 Unidirectional growth of KDP crystal along (101) surface

The solute feed based unidirectional technique was also tested for growth of KDP crystals along (010) pyramidal face. For this purpose a small size seed prepared and mounted at the bottom of a growth ampoule of ~22 mm diameter. Fig. 4.24 (a) and (b) show the grown crystal and elements prepared by cutting normal to its growth direction. It shows inclusion in between, which was appeared when we changed the temperature gradient drastically. It happened due to shift of growth sector boundary of {100} and {101} surfaces as we changed the temperature gradient. Once the temperature gradient is kept stable, the growth again started to be inclusion free as evident from the upper portion of the crystal shown in Fig. 4.24 (a). It shows that one of the reasons of the formation of inclusions at the growth sector boundaries is the change in the relative growth rates due to change in supersaturation. The details of crystal growth are given in Table 4.3.

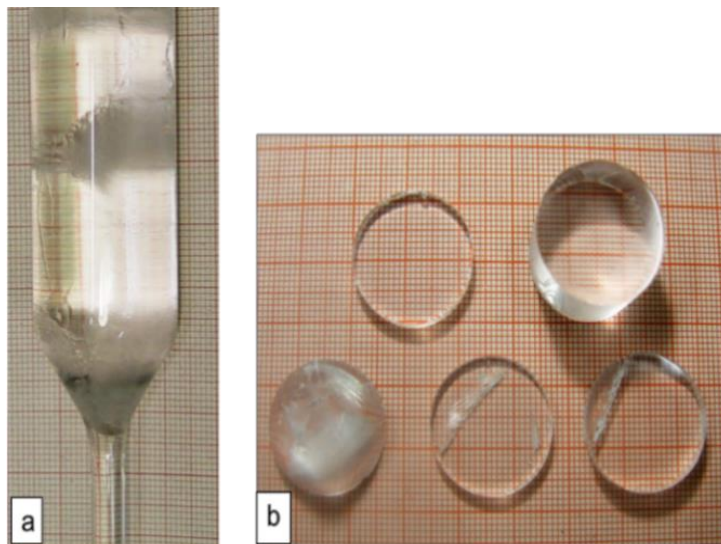


Fig. 4.24 (a) Unidirectional growth of KDP crystal along (101) surface by solute feeding, technique, and (b) prepared (101) elements by slicing crystal normal to the growth direction.

Table 4.3 Growth details of unidirectional KDP crystal grown along (101) face.

Crystal	Dimensions: Dia.× Height (mm)	Max. temperature gradient, ΔT ($T_2 - T_1$) (°C)	Growth duration (days)	Average growth rate (mm/day)
Fig. 4.24 (a)	4 - 22 x 75	24 (52 -28)	7	10

One of the prepared (101) plates of good optical quality from this crystal was characterized for optical transmittance, birefringence and chemical etching.

4.4.3.1 UV-Vis-NIR transmission measurement

The UV-Vis-NIR transmittance measurement was carried out for a 3.0 mm thick (101) plate as shown in Fig. 4.25. The inset shows the sample plate used for this investigation. The spectrum shows that the sample plate has > 90 % transmittance for the wavelength range 341 nm to 1243 nm without accounting for Fresnel losses. It also does not show any indication of absorption at UV region near 270 nm. It is attributed to the growth front i.e. to the {101} pyramidal faces which absorb relatively lesser quantity of trivalent metallic impurities compared to {100} prismatic faces and hence high transmittance at UV region.²⁴

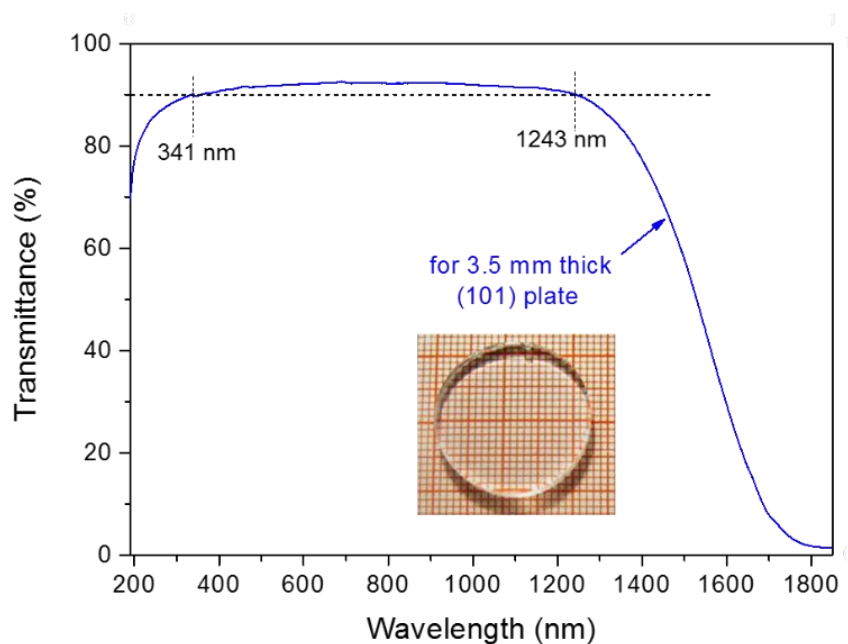


Fig. 4.25 Transmission spectrum of a 3.0 mm thick (101) plate prepared from (101) oriented unidirectional grown KDP crystal by solute feeding.

4.4.3.2 Birefringence homogeneity of (101) plate

Birefringence interferogram was obtained by placing sample plate between cross polarizers. Fig. 4.26 shows birefringence interferogram obtained for the plate using He-Ne laser. It shows only two fringes in the 15 mm diameter of the central region of the plate, indicating good birefringence homogeneity, however the region nearby to the fringe indicates presence of some defects which scatter the light.

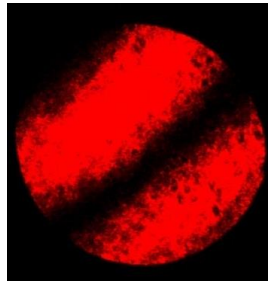


Fig. 4.26 Birefringence interferogram for (101) plate prepared from the (101) oriented unidirectional KDP crystal.

4.4.3.3 X-ray diffraction topography of (101) plate

X-ray diffraction topograph was carried out for the (101) plate for (732) diffraction planes using the *Jasco* make digital X-ray topography system. The sample surface was etched by placing it in a wet *Whatman* make filter paper for about 5-10 s and immediately dried at an another filter paper. Fig. 4.27 shows the obtained X-ray topograph. It shows features like chains of inclusion and localised high and low defect density regions. The high defects density regions are associated to prismatic growth sector. While the defects density in the pyramidal sector is relatively lower than that at the prismatic sector.

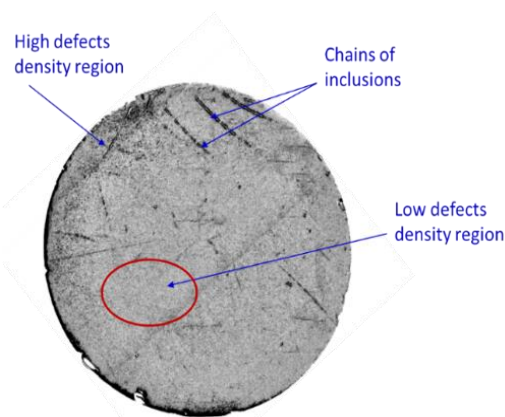


Fig. 4.27 X-ray diffraction topograph for (101) plate of the (101) oriented KDP crystal.

4.4.4 Unidirectional growth of KDP along [100] direction

We have also grown (100) oriented KDP crystal from the point seed in a borosilicate glass make growth ampoule by solute feeding technique. Fig. 4.28 shows the obtained crystal of length 40 mm and diameter 29 mm. It was grown in 14 days at a maximum upper zone temperature 50 °C while keeping the lower zone fixed at 36 °C. The growth run completed without any nucleation however a few inclusions were observed. The crystal was cut normal to the growth direction and prepared three plates from its bottom, middle and top portions as shown in Fig. 4.29 (a) for comparison of their defects structures and bulk optical quality. Fig. 4.29 (b) and (c) shows the X-ray diffraction topographs and birefringence interferograms of the samples corresponding to the (100) bottom, (100) middle and (100) top plates. It shows that, i) overall defects density is low, ii) growth sector boundary acts a source of defects as seen in the bottom plate, and iii) crystal quality improves away from the seed crystal. Further it indicates that growth of a crystal with single horizontal face filling the full cross section of the growth ampoule imparts lesser defects because there would not be any growth sector boundary.



Fig. 4.28 Unidirectional KDP crystal grown along (100) face by solute feeding technique.

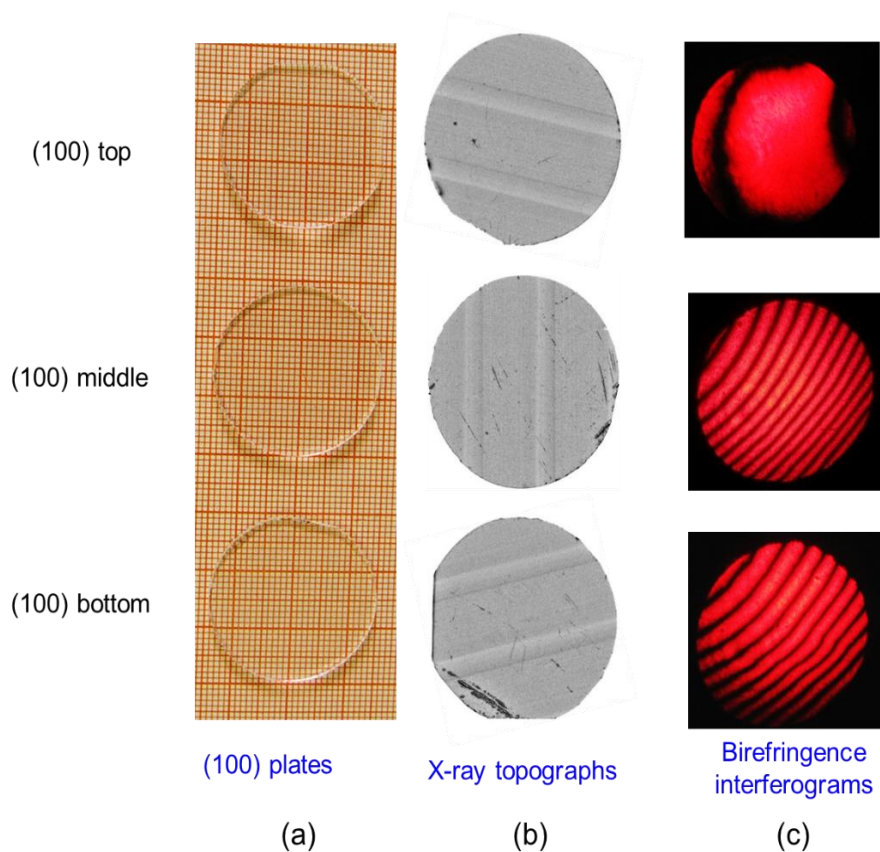


Fig. 4.29 (a) Photographs of three sample plates prepared from the (100) oriented unidirectional KDP crystal from bottom, middle and top portions, (b) the corresponding X-ray diffraction topographs, and (c) corresponding birefringence interferograms for the three plates.

4.5 Application of solute feed based unidirectional technique for growth of DKDP and LAP crystals

To validate the solute feed based unidirectional growth technique for other solution grown crystals. We have also grown a few other solution grown crystals by using this technique such as DKDP (deuterated potassium dihydrogen phosphate), LAP (L-arginine phosphate monohydrate), etc. A few representative crystals of these materials are depicted here for completeness purpose.

4.5.1 Growth of unidirectional LAP crystal by solute feeding technique

Fig. 4.30 show a LAP crystal of diameter ~ 15 mm and length ~ 15 mm from a point seed facing (010) direction along the axis of the growth ampoule. The crystal is transparent showing the applicability of the solute feed based technique for LAP crystal growth.

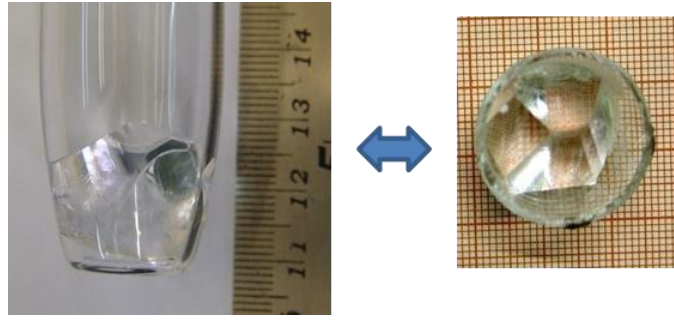


Fig. 4.30 LAP crystal grown along (010) direction from a point seed by solute feeding technique.

4.5.2 Growth of DKDP crystal by solute feeding technique

Solute feed based unidirectional growth technique is particularly useful for those material where solvent is highly economic such as heavy water or hazardous such as organic solvents whose evaporation is harmful for personnel health and environment. Therefore, solute feed based unidirectional technique is particularly useful for unidirectional growth of organic crystals. In this case we have grown DKDP crystals from a small amount of heavy water because heavy water is rarely available due to its strategic applications. Fig. 4.31 show a DKDP crystal of ~ 80 mm length grown using solute feeding technique. The crystal was having 18 mm diameter and grown along [001] direction from small amount of solution.³¹

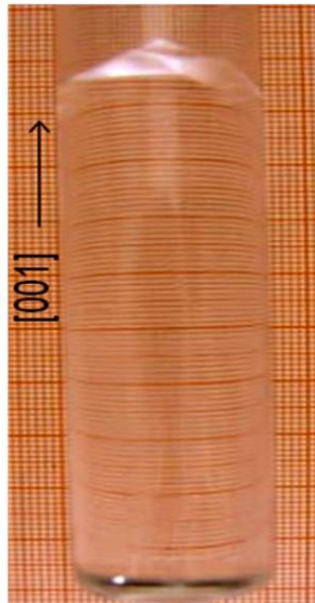


Fig. 4.31 DKDP crystal of 80 mm length and 18 mm diameter grown using solute-feed based unidirectional growth technique.

4.6 Conclusion

In conclusion, a solute feed based unidirectional growth technique is developed for rapid unidirectional growth of KDP crystals from solutions. It imparts cylindrical shape crystals with ~ 100% material crystallization yield and ~ 90 to 100% volume usable for Pockels elements or for SHG elements which is much higher compared to that obtained from the conventional and platform grown techniques. The mass transfer takes place due to gravity from high concentration zone to the to lower concentration zone. The supersaturation is maintained during growth by online feeding of solute through a 0.2 μm porosity membrane. The technique was applied for rapid unidirectional growth of cylindrical shape KDP crystals along [001], [100], [101] and SHG type-II phase matching directions for Nd:YAG laser. The crystals were characterized by various techniques for their optical quality, crystalline perfection and defect structures. Results indicate that quality of KDP crystals obtained by this technique is comparable to that grown by conventional or platform techniques. Studies suggest that growth along single face imparts better crystal quality compared to multifaceted growth in the solution. The technique was applied for a few other crystals to prove its validity for solution crystal growth in general.

References:

- ¹ S. Genbo, H. Youping, L. Zhengdong, J. Rihing, Z. Changwu, Y. Shangfeng, *J. Cryst. Growth*, 213 (2000) 99-102.
- ² K. Sankaranarayanan, P. Ramasamy, *J. Cryst. Growth*, 280 (2005) 467-473.
- ³ N. Balamurugan, P. Ramasamy, *Crys. Growth Des.*, 6(7) (2006) 1642-1644.
- ⁴ S. Balamurugan, G. Bhagavannarayana, P. Ramasamy, *Mater. Lett.*, 62 (2008) 3963-3965.
- ⁵ S. Balamurugan, P. Ramasamy, S. K. Sharma, Y. Inkong, P. Manyum, *Mater. Chem. Phys.*, 117 (2009) 465-470.
- ⁶ R. Robert, C. J. Raj, S. Krishnan, S. J. Das, *Physica B*, 405 (2010) 20-24.
- ⁷ P. Rajesh, S. Sreedhar, K. Boopathi, S. V. Rao, P. Ramasamy, *Current Applied Physics*, 11 (2011) 1343-1348.

- ⁸ S. Dinakaran, Sunil Verma, S. J. Das, S. Kar, K. S. Bartwal, *Physica B*, 405 (2010) 3919-3923.
- ⁹ A. Ghane, H. R. Dizaji, *Chinese J. Phys.*, 50(4) (2012) 652-658.
- ¹⁰ S. K. Sharma, Yeshpal Singh, Sunil Verma, K. S. Bartwal, P. K. Gupta, National Laser Symposium-22, January 8-11, 2014, Manipal University, Manipal, pp.62.
- ¹¹ A. A. Chernov, Crystal growth from the vapor phase, Chapter 8 in: “Modern Crystallography III: Crystal Growth”, Springer-Verlag, Berlin Heidelberg, 1984, pp. 365-367.
- ¹² I. A. Batyerva, V. I. Bepalov, V. I. Bredikhin, G. L. Galushkina, V. P. Ershov, V. I. Katsman, S. P. Kuznetsov, L. A. Lavrov, M. A. Novikov, N. R. Shvetsova, *J. Cryst. Growth*, 52 (1981) 832-836.
- ¹³ R. S. Feigelson, *J. Cryst. Growth*, 90 (1988) 1-13.
- ¹⁴ S. K. Sharma, Sunil Verma, B. B. Shrivastava, V. K. Wadhawan, *J. Crystal Growth*, 244 (2002) 342-348.
- ¹⁵ X. Zhuang, L. Ye, G. Zheng, G. Su, Y. He, X. Lin, Z. Xu, *J. Cryst. Growth* 318 (2011) 700–702.
- ¹⁶ S. K. Sharma, Sunil Verma, Yeshpal Singh, K. S. Bartwal, M. K. Tiwari, G. S. Lodha, G. Bhagavannarayana, *Optical Materials*, 46 (2015) 329-338.
- ¹⁷ M. Runkel, M. Yan, J. De Yoreo, N. Zaitseva, *SPIE*, 3244 (1998) 211–222.
- ¹⁸ V. Tatartchenko and E. Beriot, *Proc. SPIE*, 3492 (1999) 384-390.
- ¹⁹ S. Dinakaran, Sunil Verma, S. J. Das, S. Kar, K. S. Bartwal, P. K. Gupta, *Physica B*, 405 (2010) 1809-1812.
- ²⁰ S. K. Sharma, S. Verma, Y. Singh, K. S. Bartwal, P. K. Gupta, National Laser Symposium-24, Dec. 2-5, 2015, RRCAT, Indore, pp.71.
- ²¹ V. I. Bredikhin, V. P. Eeshov, V. V. Korolikhin, V. N. Lizyakiya, S. Yu. Potapenko, N. V. Khlyunev, *J. Cryst. Growth*, 84 (1987) 509-514.
- ²² N. Y. Garces, K. T. Stevens, L. E. Halliburton, M. Yan, N. P. Zaitseva, J. J. Yoreo, *J. Cryst. Growth*, 225 (2001) 435-439.
- ²³ E. Dieguez, A. Cintas, P. Hernandez, J. M. Cabrera, *J. Cryst. Growth*, 73 (1986) 193–195.
- ²⁴ G. Li, Y. He, G. Su, Z. Li, X. Zhuang, J. Ma, X. Huang, *Cryst. Res. Technol.*, 40 (2005) 217-221.
- ²⁵ T. Henningsen, N.B. Singh, *J. Cryst. Growth*, 96 (1989) 114–118.

²⁶ Sunil Verma, S. Kar, K. S. Bartwal, Chapter 19 in: Mark E. Russo (Ed.), *Interferometry Principles and Applications*, Nova Science Publishers, New York, USA, 2012, pp. 537–560.

²⁷ Sunil Verma, P.J. Shlichta, *Prog. Cryst. Growth Charact. Mater.* 54 (2008) 1–120.

²⁸ R. V. A. Murthy, M. Ravikumar, A. Choubey, K. Lal, L. Kharachenko, V. Shleguel, V. Guerasimov, *J. Cryst. Growth*, 197 (1999) 865-873.

²⁹ K. Sangwal, M. Szurgot, J. Karniewicz, W. Kolasinski, *J. Cryst. Growth*, 58 (1982) 261-266.

³⁰ B. Teng, D. Zhong, Z. Yu, X. Li, D. Wang, Q. Wang, Y. Zhao, S. Chen, T. Yu, *J. Cryst. Growth*, 311 (2009) 716-718.

³¹ S. K. Sharma, Yeshpal Singh, Sunil Verma, K. S. Bartwal, P. K. Gupta, *National Laser Symposium-23*, December 3-6, 2014, S. V. University, Tirupati, pp.55.

Chapter 5 Growth, kinetics studies and characterization of LAP crystals

5.1 Introduction

L-arginine phosphate monohydrate ($C_6H_{14}N_4O_2H_3PO_4 \cdot H_2O$; called as LAP) is an important material for nonlinear optical applications. It has several attractive features for frequency conversion of high power Nd:YAG laser compared to KDP such as higher NLO coefficient, higher laser damage threshold, and less hygroscopicity.¹⁻⁴ The LAP chemical was first synthesized by Aoki et al.⁵ in 1971 and twelve years later its phase matchability for second harmonic generation was first reported in 1983 by Xu et al.⁶ LAP crystal is grown from aqueous solution consist of several habit faces such as {100}, {101}, {110}, {011}, {001}, {111}. It also shows growth asymmetry across *b*-axis due to being polar direction.^{7,8} The habit of the conventionally grown crystal is usually such that the usable volume fraction for device applications is low. Crystal habit is usually described in terms of aspect ratio and is an important parameter for determination of the usable volume fraction of the grown crystals for a particular application. It depends on the relative growth rates of habit faces which depends in general on several physico-chemical parameters of the solution such as, pH,^{8,9} supersaturation,¹⁰ impurities or additives^{11,12} and hydrodynamics¹³ and orientation of seed^{14,15}. Several researchers attempted to change the aspect ratio of LAP using these parameters. Dhanaraj et al. studied influence of pH on growth and morphology of LAP crystals and found that pH influences relative growth rates along *b* axis compared to that along *c*-axis.⁸ At low pH values (< 4) growth rate along *b*-axis was higher compared to that along *c*-axis while at high pH values (> 5) growth rate along *c*-axis exceeded to that along *b*-axis. Aggarwal et al. investigated influence of Li^+ ions and found that it acts as a habit modifier to increase the growth yield along the rectangular prismatic habit, which is desirable for device fabrication¹⁶. Hameed et al. used KSCN (potassium thiocyanate) and Na_2SO_3 (sodium sulphite) as additives and obtained enhanced relative growth rate along *c*-axis compared to those along *a* and *b*-axis.¹⁷ Riscob et al. used another approach of modifying crystal shape by growing a crystal inside a tube and demonstrated growth of cylindrical shape LAP crystal along [010] direction.¹⁸ The reported results in the literature on the relative growth rates along the crystallographic axes (*a*, *b*, *c*) are also ambiguous. Kavitha et al.¹⁹ reported higher growth rate along *c*-axis in

comparison to that along b -axis while Hameed et al.²⁰ and Arunmozhi et al.¹⁰ reported the reverse trend of their relative growth rates. All these however reported that the slowest growth rate is along the a -axis. As isometric shape crystal is usually desirable for the efficient use of crystals for device applications, therefore relative growth rates along the three axes need to be modified.

In this chapter, we report two aspects of LAP crystal growth aimed at modification of growth rate and aspect ratio to obtain isometric morphology so that to enhance the usable volume fraction for device applications.

- A) Investigated the influence of seed orientation on growth rate and aspect ratio of LAP crystals.²¹ For this purpose, initially the chemical was synthesized and its crystallographic phase was confirmed by powder X-ray diffraction. Subsequently solubility of the prepared chemical was determined in water. The crystals were grown along four different orientations at an acrylic platform and their average growth rates along the three crystallographic axes, and aspect ratios were calculated. The crystal having a shape most closely to the isometric shape was characterized in detail by several techniques for assessment of optical quality, defect structure and thermal stability density.
- B) The above studies indicated lowest growth rate along (100) plane. Therefore, we investigated influence of supersaturation on the growth kinetics of (100) face of LAP. For this purpose, birefringence interferometry technique was employed which is suitable to conduct online measurements. This investigation includes,
- i. Determination of directions of principal axes relative to its crystallographic axis for proper alignment of seed crystal, and
 - ii. Development of an experimental workstation for growth kinetics studies of LAP using birefringence interferometry and carried out online measurements for growth kinetics.

5.2 Chemical synthesis and determination of solubility curve

5.2.1 Chemical preparation

LAP chemical was synthesised using equi-molar quantities of AR grade L-arginine amino acid and orthophosphoric acid in high purity demineralised water (~ 18 M Ω -cm resistivity) obtained from Milli-Q Advantage A10 water purification system. The chemical reaction involving two steps were as follows:

Step 1: (a) $\text{P}_2\text{O}_5 + \text{H}_2\text{O} \rightarrow \text{H}_3\text{PO}_4 (\text{aq.})$

(b) $\text{L-arg} + \text{H}_2\text{O} \rightarrow \text{L-arg} (\text{aq.})$

Step 2: $\text{L-arg} (\text{aq.}) + \text{H}_3\text{PO}_4 (\text{aq.}) \rightarrow \text{L-arg. H}_3\text{PO}_4 \cdot \text{H}_2\text{O} (\text{aq.})$

The prepared solution was overheated and filtered using membrane filters, first through 0.45 μm and then through 0.2 μm pore size using vacuum filtration system. Subsequently the solvent was evaporated to obtain the crystallized salt. The crystalline phase of the synthesized material was determined using powder X-ray diffraction technique.

5.2.2 Powder X-ray diffraction

Fig. 5.1 shows the powder X-ray diffraction pattern of the LAP chemical, obtained using Cu-K α radiation in the range 5° - 45° at an angular resolution of 0.01°. Peak positions were in good agreement with those reported in the JCPDS data, 50-1921, confirming the phase of the synthesized material to be LAP. The peak positions of the diffraction spectra were used to calculate values of lattice parameters using Reflex software. The results are $a = 10.796 \text{ \AA}$, $b = 7.855 \text{ \AA}$, $c = 7.280 \text{ \AA}$ and angle $\beta = 98^\circ$ close to that reported in the literature.⁵

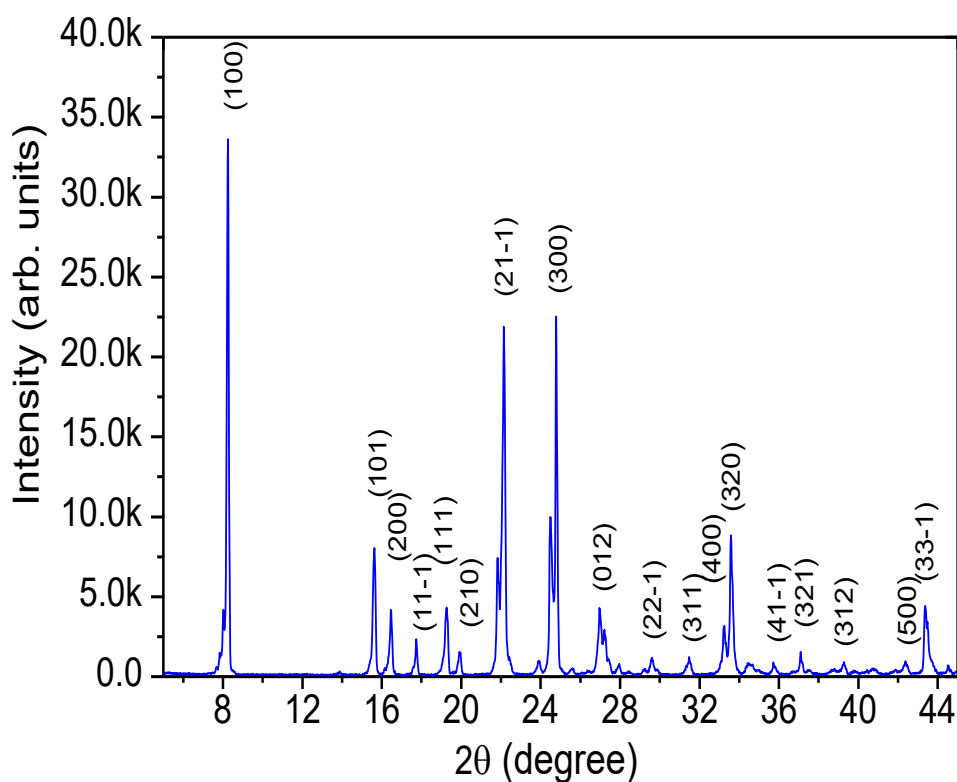


Fig. 5.1 X-ray powder diffraction pattern of synthesized LAP chemical.

5.2.3 Determination of solubility curve

Determination of solubility curve is an important part of solution crystal growth. We have measured solubility of prepared LAP salt in high purity water by gravimetric method. The pH of the prepared solution in fresh LAP salt was measured using *Hanna* make pH meter and found to be 4.3 at room temperature. The measurements were carried out for 34 °C to 66 °C range in steps of 4 °C. The results are shown in the Table 5.1.

Table 5.1 Solubility data for LAP in water at pH 4.3.

S. No.	Temperature (°C)	Saturation concentration (g/100g water)
1	34	19.57
2	38	22.67
3	42	28.29
4	46	34.18
5	50	40.92
6	54	49.85
7	58	56.78
8	62	68.04
9	66	78.52

The same data is plotted as shown in Fig. 5.2. It shows that solubility of LAP increase nonlinearly with temperature. The results are in good agreement with that reported in the literature.^{8,22} The solubility data was fitted in second order polynomial using Origin software as depicted in Fig. 5.2 and can be written mathematically as,

$$C = 25.196 - 1.219T + 0.031T^2 \quad \text{---- (5.1)}$$

where C is concentration in g solute /100g water and T in °C.

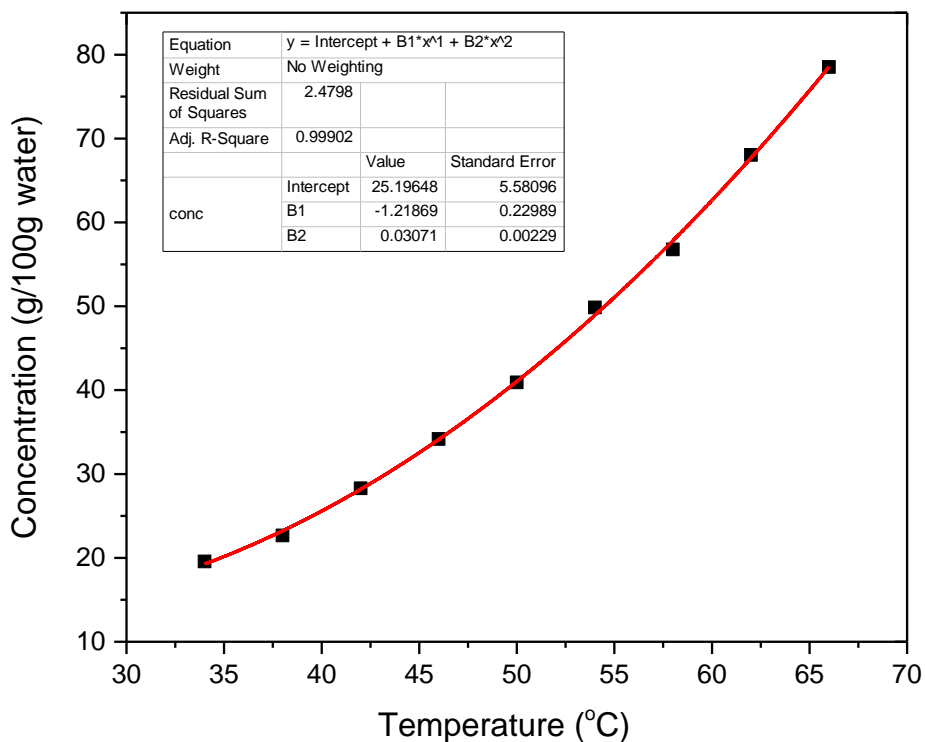


Fig. 5.2 Solubility curve for LAP chemical in water at pH 4.3.

5.3 Growth of LAP crystals using different seed orientations

In order to elucidate the influence of seed orientation on the growth of LAP crystals, following experimental works were carried out.

- i. Preparation of seed crystals of LAP for oriented growth and indexing crystal faces,
- ii. Fabrication of crystal growth unit and testing, and
- iii. Solution processing and crystal growth.

LAP seed crystals were prepared by spontaneous nucleation in small amount of saturated solution by evaporation technique. Optically clear crystals without visible defects were isolated to use as seed for growth. Some of the moderate size seed crystals are shown in Fig. 5.3 which were used to identify crystal faces and crystallographic axes with the help of SHAPE software by correlating symmetry and interfacial angles. Fig. 5.4 (a) and (b) show the morphology of LAP crystal made using SHAPE software viewed along *bc* and *ca*-planes respectively.^{23,24}

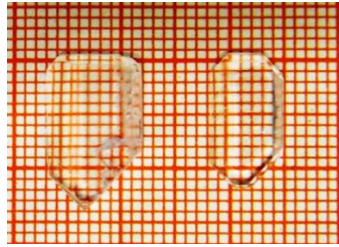


Fig. 5.3 Spontaneously grown LAP seed crystals.

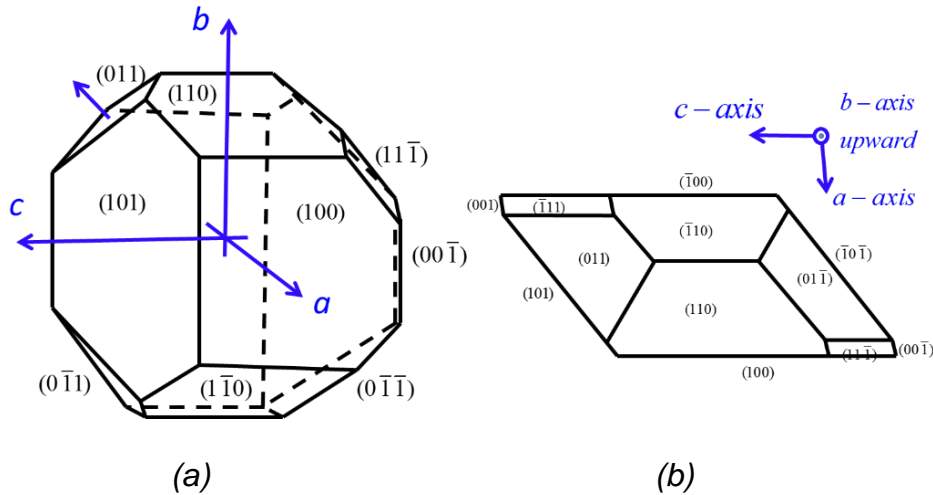


Fig. 5.4 Typical habit of LAP crystal viewed normal to bc – plane (a), and normal to ca – plane (b).

For seeded growth of LAP crystals a growth unit was fabricated. It mainly comprises of a 20-liter capacity water bath, a 2-liter capacity crystallizer and a stepper motor driver. The water bath was made using a borosilicate glass beaker which was covered at top by a perspex lid having a big hole at center to insert the crystallizer. To heat the water of this bath, a pair of U-shape resistive heaters were fabricated and mounted symmetrically at the periphery in the bath with the support of the perspex lid. The heaters were made using U-shape borosilicate glass tubes of diameter ~ 12 mm wherein helical coil of nichrome wire was inserted and the tubes were filled with silicone oil. These two U- shape heaters were connected in series and linked to a *Eurotherm (model 902P)* make PID programmable temperature controller. A Pt-100 RTD sensor covered in a stainless tube was used as a temperature sensor and mounted at the lid of the bath with its lower tip in contact with water. A thyristor unit operated by the controller was used for power transfer to the heater. The bath was tested for temperature up to 75 °C showing localized

temperature stability of the order of ± 0.02 °C. A crystallizer unit was fabricated to accommodate solution for growth of LAP crystal from a seed. It consists of a 2-liter capacity glass beaker associated with a Perspex made lid and locking mechanism for keeping solution without any leakage of solvent due to evaporation. It was provided with a platform made using perspex sheet and with two vertical posts as shown schematically in Fig. 5.5.

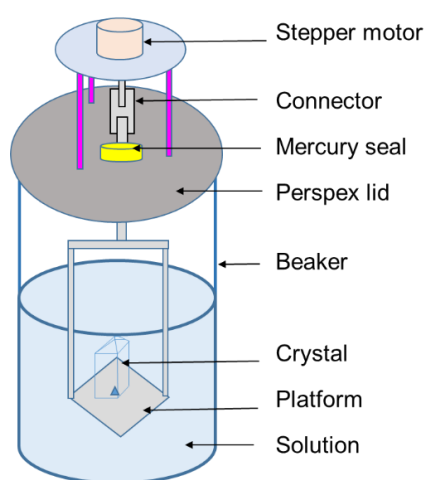


Fig. 5.5 Schematic diagram of the crystallizer used for growth of LAP crystals.

Nearly 1 liter saturated solution was prepared using the synthesised salts as per the solubility at ~ 47 °C for each growth experiment at stoichiometric pH 4.3. The solution was overheated using a magnetic stirrer cum heater and filtered through 0.2 μm porosity nylon membrane by using a vacuum filtration unit. The solution was subsequently transferred to the crystallizer which was then placed in the water bath. The solution was overheated by 10 °C for about 24 hours to overcome the problem of spurious nucleation and microbial growth and then brought down to slightly above the saturation temperature. Seed crystal in the desired orientation was placed at the centre of the platform.²⁵ The platform accompanying the seed crystal on it was preheated and subsequently gently inserting in to the solution. The initial stage of growth is very important to achieve saturation temperature. This has been done by manipulating the temperature of the bath. After slight dissolution of the seed surface the temperature was adjusted to stop the dissolution. This was done with the help of laser shadowgraph technique, where a He-Ne laser was used to image the dissolution or growth plumes from the seed crystal. After stabilization of the plumes. The platform was set in reversible rotation at low RPM in an accelerated manner to achieve uniformity of solute concentration.^{26,27} Crystal growth was

conducted by slow cooling technique of solution growth. Four different growth experiments were performed using seed crystals oriented at four different orientations such that (100), (010), (001) and (011) habit faces were parallel to the platform and facing upward. These faces are clearly identifiable from the growth morphology as shown in Fig. 5.4. Fig. 5.6 (i – iv) show the LAP crystals grown from four different seeds mounted in such a way to have (100), (010), (001) and (011) faces parallel to the platform.²¹

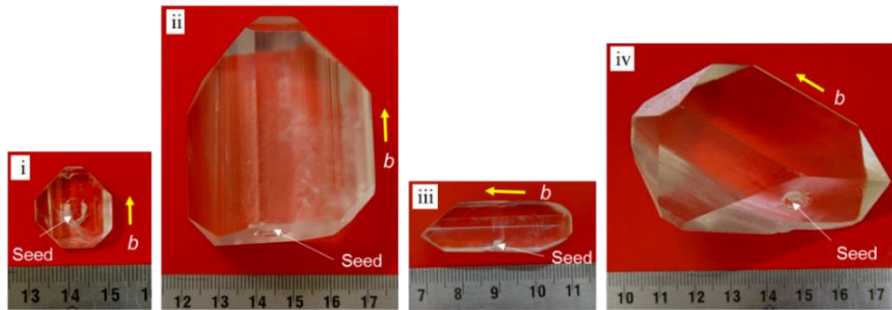


Fig. 5.6 LAP crystals grown using seed crystals having (i) (100), (ii) (010), (iii) (001) and (iv) (011) planes parallel to the platform.

5.4 Effect of seed orientation on growth rate and aspect ratio of LAP crystals

Growth morphology of LAP crystal exhibits a large number of faces (Fig. 5.4), its aspect ratio can be defined as the ratio of dimensions of the crystal along its crystallographic axes (a, b, c) i.e. $L_a : L_b : L_c$ as shown in Fig. 5.7.^{14,28,29}

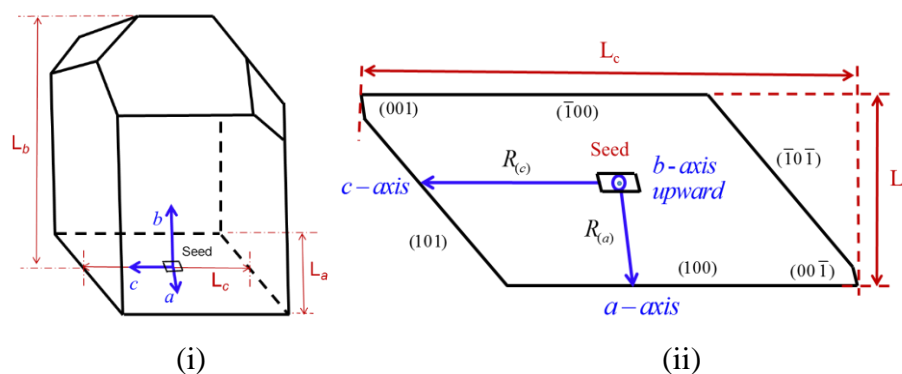


Fig. 5.7 Schematic showing the overall dimensions (L_a, L_b, L_c) of a LAP crystal looked along crystallographic a -axis (i), and that along b -axis (ii); for calculation of aspect ratio and average growth rates.

For isometric habit, $L_a : L_b : L_c$ should be as close to 1:1:1 as possible. Growth rate of LAP along a , b and c -axes is defined as the average rate of advancement of the crystal along these directions with reference to the seed crystal. Since the angle between the crystallographic a -axis and normal to (100) face is small ($\sim 8^\circ$), the growth rate of (100) face was taken as that measured along a -axis.³⁰ Table 5.2 shows the dimensions of the grown crystals, their average growth rates along the three crystallographic axes and the calculated aspect ratios.²¹

Table 5.2: Dimensions, average growth rates along crystallographic axes and aspect ratio of LAP crystals grown along four different orientations on the platform.

Photograph of crystal	Habit face parallel to platform	Crystal dimensions ($L_a \times L_b \times L_c$) mm^3	Seed dimensions ($L_a \times L_b \times L_c$) mm^3	Growth duration (days)	Average growth rates along crystallographic axes (mm/day)			Aspect ratio $L_a : L_b : L_c$
					R_a	R_b	R_c	
Fig. 5.6 (i)	(100)	$5 \times 20 \times 15$	$1 \times 5 \times 3$	5	0.8	1.5	1.2	1 : 3.8 : 3
Fig. 5.6 (ii)	(010)	$22 \times 60 \times 35$	$1 \times 2 \times 3$	12	0.9	4.8	1.3	1 : 2.8 : 1.5
Fig. 5.6 (iii)	(001)	$10 \times 42 \times 16$	$1 \times 2 \times 2$	8	0.6	2.5	1.8	1 : 4.4 : 1.6
Fig. 5.6 (iv)	(011)	$25 \times 50 \times 39$	$1 \times 2 \times 3$	13	0.9	3.7	1.4	1 : 2 : 1.5

Following important observations were made by comparison of the growth rates and aspect ratio:

- (i) growth rate along b -axis (R_b) is maximum and that along a -axis is minimum for each individual crystal irrespective of its orientation. R_b is about two to five times higher than R_a , depending on the seed orientation.
- (ii) Growth rate along b -axis is highly sensitive to seed orientation compared to those along a and c -axis.

The growth rate trend as observed in the Table 5.2 follow the order $R_a < R_c < R_b$ for all the seed orientations. This is in agreement with the results reported by Hameed et al.²⁰ and Arunmozhi et al.¹⁰

In the last column of the Table 5.2, aspect ratio of the grown crystals is displayed. The results show that (011) oriented crystal is the nearest to being in the isometric shape as the aspect ratio is 1:2:1.5, followed by (010) oriented crystal having the aspect ratio of

1:2.8:1.5. The other two orientations namely (100) and (001) are very off from the isometric shape and are not suitable for obtaining the large size device elements. These variations in aspect ratios are attributed to the following factors: i) due to the application of the platform, the growth along downward direction was restricted^{15,25} and ii) due to change in the seed orientation at the platform, the flow dynamics around the individual faces changes from one experiment to another, leading to variation in the surface supersaturation and hence growth rates of habit faces.³¹

The high growth rate observed along b -axis can be attributed to the surface micromorphology observed on the (100) face. As per the literature on LAP surface morphology, there exists long parallel macrosteps elongated along b -axis and spread along c -axis on (100) faces.^{8,32,33} Fig. 5.8 (i) shows such steps obtained on as-grown (100) surface of LAP crystal. The specific orientation of step faces is attributed to the crystal structure of (100) slice of LAP. Fig. 5.8 (ii) shows the atomic structure of the (100) slice of LAP and bonding arrangement among arginine, phosphate and water molecules present in the slice.³⁴

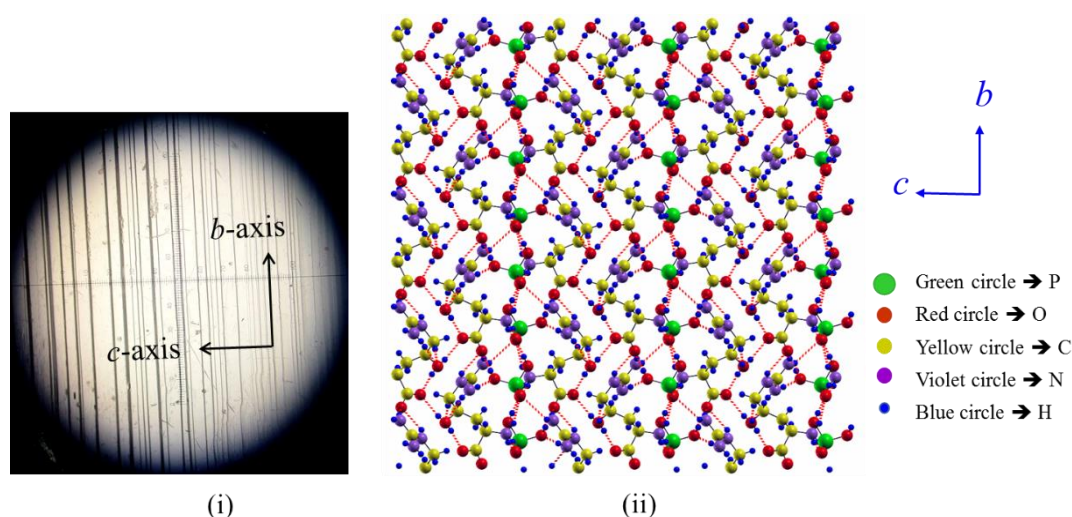


Fig. 5.8 (i) Microscopic image of as-grown (100) surface of LAP crystal at 50X magnification showing a series of steps elongated parallel to b -axis and spread along c -axis, (ii) atomic structure of (100) face showing chains of strong bonds between phosphate groups elongated towards b -axis.

The structure (Fig. 5.8(ii)) was prepared by CRYSTAL09 software³⁵ and visualized using XCrySDen software³⁶. It shows that there is a single periodic bond chain (PBC) in this plane along b -axis corresponding to strong bonds in between phosphate groups.³⁷

Consequently, step energy along b -axis is much higher compared to that along c -axis in the (100) plane. This implies in higher growth rate along b -axis compared to that along c -axis and results in to formation of long parallel macrosteps on this face. These macro steps degrade crystal quality as they are prone to trap solution or impurities and hence become source of inclusions and defects. Relatively lower growth rate of (100) faces compared to that along (010) and (001) directions is attributed to two factors: (i) the interplanar distance of {100} planes is relatively larger compared to that for the other faces which as per Bravais-Friedel-Donnay-Harker (BFDH) law leads to lower growth rate³⁸ and, (ii) relatively lower bond strength between (100) cleavage planes.

5.5 Characterization of LAP crystal

As per the growth details in Table 5.2, the crystal grown along (011) orientation was closest to the isometric morphology, therefore investigated in detail using various techniques for defects structures, optical quality, laser damage resistance and temperature stability. For this purpose, samples were prepared from the grown crystal. The (011) oriented LAP crystal was cut parallel to its broad (100) face by Buehler make low speed saw using diamond coated disc cutter and sample plates were prepared. Ethylene glycol was used as coolant and lubricant during this operation. The plates were subsequently polished carefully using fine alumina powder in sequence of 0.5 μm and 0.03 μm particle sizes on soft polishing cloth at Buehler make polisher at low speed. One of the prepared sample is shown in Fig. 5.9 (i). The sample plate was used for various characterization described in subsequent sections.

5.5.1 Crystalline quality and defects structure

5.5.1.1 X-ray diffraction topography of LAP sample

X-ray diffraction topography is used to get images of defects structures and their distribution.³⁹ The digital X-ray topography system described in Chapter 2 was used for this investigations.⁴⁰ The sample plate (Fig. 5.9 (i)) was first slightly etched using water for about 5-10 s duration to remove surface defects such as scratches introduced due to cutting and polishing. Fig. 5.9 (ii) shows the X-ray diffraction topograph corresponding to (811) diffracting planes in the (100) plate. It was observed that most common defects are dislocations, localized strain, growth striations and growth sector boundary. It was found that the portion of crystal near to the seed and platform has relatively higher defects density

compared to that away from it.⁴¹ Dark contrast localized at certain portions are attributed to strain field generated due to high density of dislocation defects particularly at growth striations and growth sector boundaries.^{41,42} The large area of uniform intensity of the topograph shows the crystal in general has low defects density and hence suitable for device application.

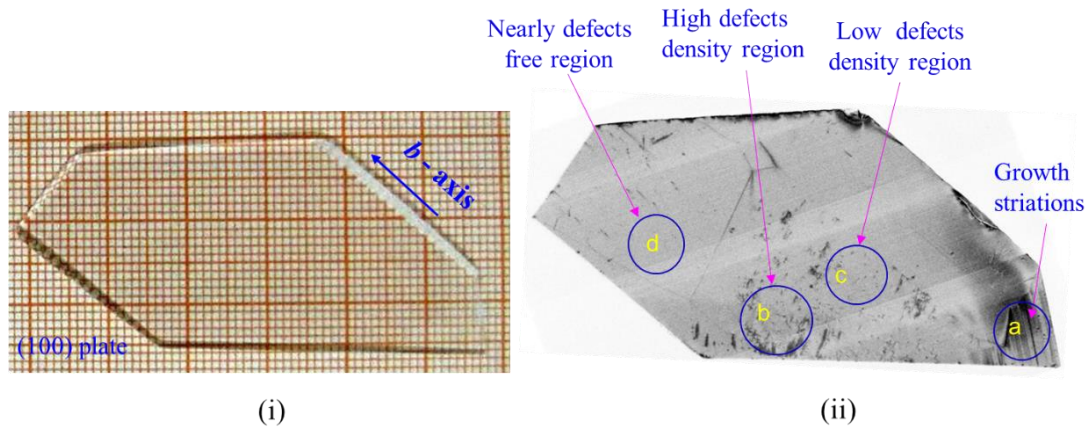


Fig. 5.9 (i) (100) sample plate prepared from the (011) oriented LAP crystal, and (ii) its corresponding X-ray topograph for (811) planes.

5.5.1.2 Chemical etching

To quantify the dislocation density at different regions of the (100) LAP crystal plate, chemical etching studies were carried out at four different locations at crystal plate corresponding to regions marked as a, b, c, d in the topograph (Fig. 5.9(ii)). It was done just after the X-ray topographic studies because the surface was already etched by water, so chances of one to one correlation of defects were possible. The surface imaging of the etched plate was done using an optical microscope at 50X magnification. Fig. 5.10 (i) to (iv) show optical micrographs of dislocation etch pits corresponding to the four regions encircled at the topograph. It shows that the shape of the etch pits is somewhat trapezium having unequal parallel sides elongated along *b*-axis.⁴³ The *b*-axis has been marked by arrow in each of the optical micrograph. Fig. 5.10 (i) shows group of dislocations corresponding to region of growth striations. Fig. 5.10 (ii) and Fig. 5.10 (iii) show high (10^3 - $10^4/\text{cm}^2$) and low (10^2 - $10^3/\text{cm}^2$) etch pit density regions corresponding to regions b and c at the X-ray topograph respectively. Fig. 5.10 (iv) shows the region having very low

etch pit density ($< 10^2/\text{cm}^2$) corresponding to almost dislocation free region *d* at the X-ray topograph.

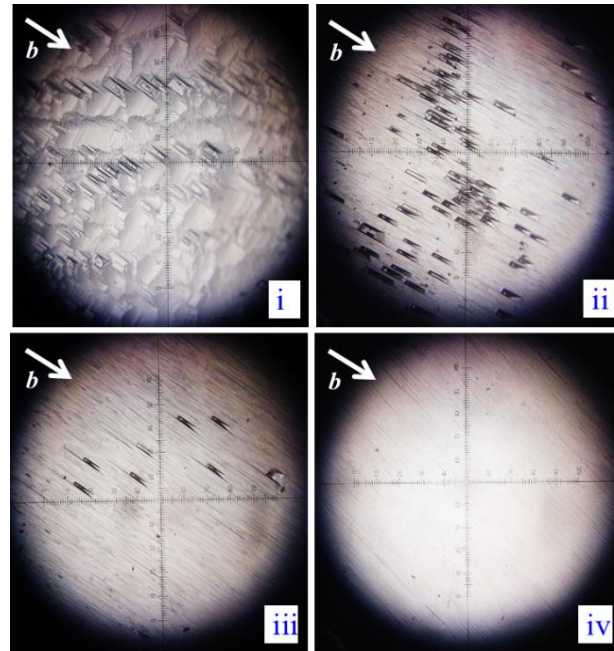


Fig. 5.10 Optical micrographs of the surface of (100) plate of the LAP crystal after chemical etching showing chains of etch pits (i), high etch pit density (ii), low etch pit density (iii) and almost dislocation free region (iv), corresponding to the regions marked as a, b, c, d in its X-ray topograph shown in Fig. 5.9(ii). (Magnification 50X.)

This study indicates that one of the main sources of defects is dislocation which may introduce during seed regeneration and due to uneven growth at growth sector boundaries. However, the orientation of etch pits along b-axis, indicates that long parallel growth steps along b-axis (Fig. 5.8(i)) may be another possible source of defects in the crystal.

5.5.2 Assessment of optical quality

Optical quality of the prepared sample plate was assessed using UV-Vis_NIR spectrophotometer, Mach-Zehnder interferometer and birefringence interferometer as described in the following sections.

5.5.2.1 UV-Vis-NIR transmission studies

Optical transmission spectroscopy is a sensitive technique to find out influence of defects such as inclusions, impurities and structural imperfections on optical quality and hence usability of the material for laser applications. The transmission measurement was carried

using *Jasco* make spectrophotometer in the wavelength range for 190 nm to 1900 nm for the (100) plate prepared from (011) oriented LAP crystal. The experiments were carried out for freshly polished plate. Fig. 5.11 shows UV-Vis-NIR transmission spectrum obtained for the 1.7 mm thick (100) plate.

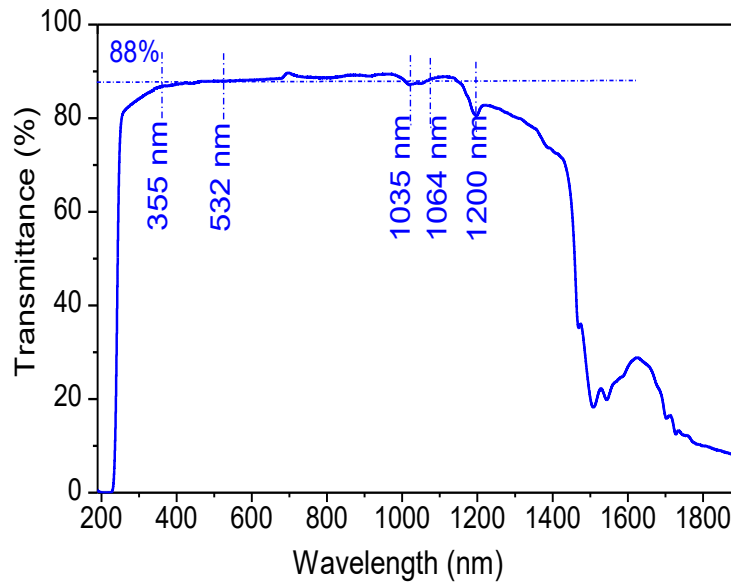


Fig. 5.11 UV-Vis-NIR transmission spectrum for (100) plate of LAP crystal without accounting for Fresnel reflection losses, for plate thickness 1.7 mm.

It shows a broad transparency range from 245 nm to 1460 nm with > 50 % transmittance without accounting for Fresnel reflection losses. For specific wavelengths such as fundamental (1064 nm), second harmonic (532 nm) and third harmonic (355 nm) of the Nd:YAG laser the transmittance was more than 88% as shown in the Fig. 5.11. The spectrum shows a sharp UV cut off at 230 nm indicating LAP to be a direct band gap material with its value ~ 5.4 eV. The weak absorption bands observed near 1035 nm and 1200 nm are attributed to the overtones of stretching vibrations of O-H and N-H bonds, and C-H bond present in the LAP molecules respectively.³ The results show that crystal has good optical quality, suitable for nonlinear optical applications.

5.5.2.2 Birefringence interferometry

Birefringence interferometry is useful technique for qualitative and quantitative assessment of birefringence homogeneity of anisotropic crystals which may be introduced due to defects such as inclusions, dislocations, stress or cracks or chemical

inhomogeneities inside the crystal. The (100) LAP sample plate under study was mounted between crossed polarizers in orthoscopic geometry.⁴⁴ Fig. 5.12 shows the obtained birefringence interferogram by passing 10 mm diameter collimated He-Ne laser beam through the central region of the plate. Equispaced and parallel interference fringes indicates that the LAP sample has good birefringence homogeneity. The linear gradient of birefringence of the sample normal to fringes was calculated using the formula,

$$\left(\frac{\Delta B}{D}\right) = \frac{N\lambda}{DL} \quad \text{---- (5.2)}$$

Where ΔB is variation in birefringence, N is the number of interference fringes observed using collimated laser beam covering diameter D at the sample, λ is the wavelength of the laser and L is the thickness of the sample plate along the beam. The above formula was derived considering uniform thickness of the sample.

For the LAP sample plate under study: $D = 10$ mm, $L = 1.7$ mm, $N = 5$ and $\lambda = 0.6328 \times 10^{-3}$ mm. This gives the birefringence gradient to be 1.86×10^{-4} / mm normal to fringes. The value is well matches with that reported in the literature.⁴⁵ Low value of birefringence inhomogeneity indicates good optical quality of crystal in accordance with x-ray topograph image of the same region.

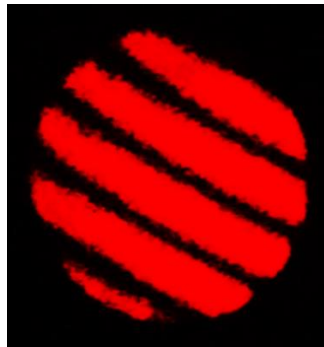


Fig. 5.12 Birefringence interferogram of the (100) plate of the (011) oriented LAP crystal.

5.5.2.3 Mach-Zehnder interferometry

This characterization was intended to assess the refractive index homogeneity of the LAP sample.⁴⁶ A He-Ne laser of wavelength 0.633 μm was used for this investigations. The Mach-Zehnder interferometer was first aligned in infinite fringe mode for this study subsequently the LAP plate was mounted in the sample arm. Fig. 5.13 shows the obtained

interferogram for the (100) plate of LAP passing the broad beam through the central portion of the sample. The interference fringes are equidistant and almost parallel without break or distortion showing good refractive index homogeneity of the sample. The large number of fringes are attributed to small wedge in the sample due to cutting and polishing errors because Mach-Zehnder interferometer is more sensitive to the sample thickness compared to the birefringence interferometer. As there is no localized distortion in the fringes, this study show that sample has good refractive index homogeneity.⁴⁷



Fig. 5.13 Mach-Zehnder interferogram of the (100) plate of the LAP crystal.

5.5.3 Fourier transform infrared analysis

Fourier transform infrared (FTIR) analysis gives information about the functional groups present in the material under study. LAP molecule consists of three species: L-arginine, phosphate group and water molecules. Each of these has various functional groups which absorb specific wavelengths in the IR region depending on their fundamental vibrational modes. FTIR measurement was carried out using Jasco make FTIR for the LAP chemical in the wave number range of 400 cm^{-1} to 4000 cm^{-1} . Fig. 5.14 shows the obtained FTIR spectrum for LAP chemical. It shows several absorption peaks as marked in this Figure. The absorption peaks located at 1453 cm^{-1} , 3332 cm^{-1} and 3448 cm^{-1} belong to three vibrational modes of water of hydration. L-arginine is a large molecule having several functional groups showing IR vibrational mode. The peaks located at 536 cm^{-1} , 770 cm^{-1} , 1410 cm^{-1} and 1573 cm^{-1} belong to vibrational modes of COO^- group and those at 1179 cm^{-1} , 1527 cm^{-1} and 3163 cm^{-1} belong to NH_3^+ group; 699 cm^{-1} , 790 cm^{-1} and 1136 cm^{-1} belong to NH_2 group; 1653 cm^{-1} belong to NH_2^+ group, 1335 cm^{-1} for CH_2 wagging; and 1691 cm^{-1} for $\text{C}=\text{N}$ stretching modes. 877 cm^{-1} , 952 cm^{-1} , 1040 cm^{-1} and 1287 cm^{-1} are related to vibrational modes of P-O-H group and 615 cm^{-1} for OH deformation mode; These values are in good agreement with that reported in the literature.^{19,20,48}

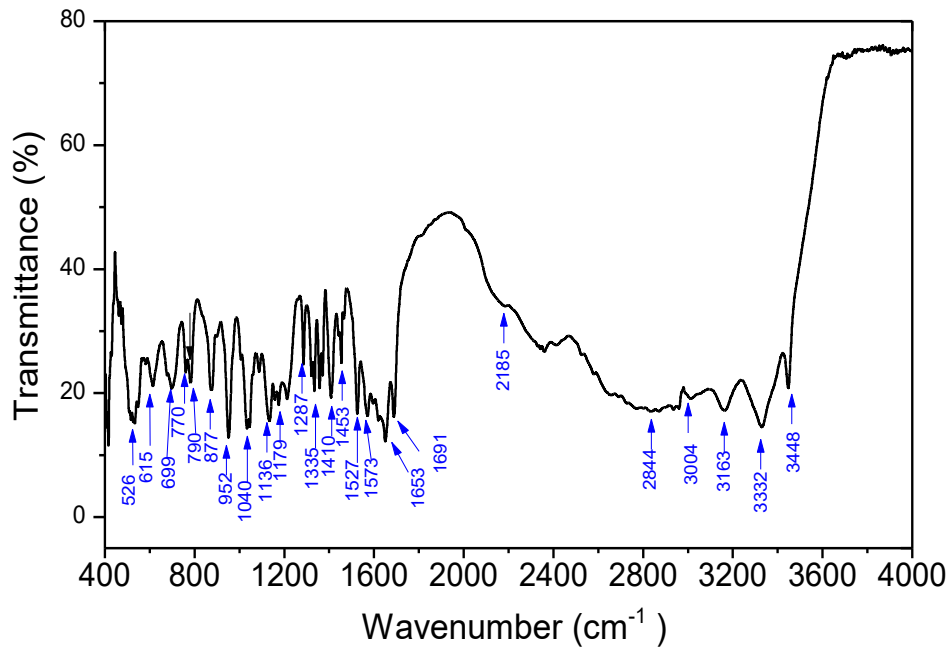


Fig. 5.14 FTIR spectrum of the LAP crystal.

5.5.4 Laser-induced damage threshold

Laser-induced damage threshold (LDT) is an important characterization to decide safe upper limit of laser intensity for nonlinear optical application of the crystal under investigation.⁴⁹ The threshold is affected by the presence of growth defects such as inclusions, chemical impurities and dislocations which reduce the damage threshold value.⁵⁰ We measured LDT for (100) LAP plate by “R on 1” method using 7 ns pulse width Nd:YAG laser.⁵¹ In this method multiple laser shots are fired at a particular site with ramped increase of intensity until damage occurs to the spot. The time interval between successive laser pulses was kept ~ 20 s for dissipation of thermal energy. The schematic of the optical set up for the LDT measurements is shown in Chapter 2 and is already reported.⁴⁰ A converging lens of 50 cm focal length was used to increase intensity at the sample surface. Initially the reflectivity of the beam splitter (BS) towards the first energy meter 1 (EM1) was determined with respect to the transmitted energy towards the sample or second energy meter (EM2). A neutral density filter was used for the safety of the EM2. This measurement was repeated at various laser energies and the average value of this ratio was 35.04. Subsequently a sample holder was fixed before the focal point of the beam using x-y-z translation stage. It was placed such that the distance of the front face of the sample remain constant from the converging lens. Before placing the sample for LDT

measurements, beam diameter was determined at this location using knife edge method⁵⁰ using a razor blade. The data was analyzed showing $1/e^2$ beam diameter of the beam to be 0.79 mm. Subsequently the LDT experiments were carried out with the (100) sample plate of LAP crystal by slowly increasing the laser pulse energy until the damage occur. The experiment was repeated at various locations of high and low EPD regions shown in Fig. 5.9 and the results are shown in and Table 5.3 and Table 5.4. A CCD camera was used to visualize the sample surface after each shot. The LDT values were calculated using the formula⁵²,

$$I_{Threshold} = \frac{\frac{1}{2}(E_{max}^{ND} + E_{min}^D)}{\tau \times A} \quad \text{---- (5.3)}$$

Where τ is laser pulse width, A is the area of the laser beam at the sample and E_{max}^{ND} and E_{min}^D denote the maximum non damaging energy and minimum damaging energy respectively. The experimental error was within $\pm 10\%$. The results are comparable with that reported in the literature.^{53,54}

Table 5.3 : LDT results obtained from various locations in low EPD region.

Location at crystal plate	$E_{max}^{ND} \times (35.04)^{-1}$ (mJ)	$E_{min}^D \times (35.04)^{-1}$ (mJ)	$I_{Threshold}$ (GW/cm²)
1	6.435	6.486	6.60
2	5.621	6.024	5.94
3	5.195	5.587	5.50

Table 5.4 : LDT results obtained from various locations in high EPD region.

Location at crystal plate	$E_{max}^{ND} \times (35.04)^{-1}$ (mJ)	$E_{min}^D \times (35.04)^{-1}$ (mJ)	$I_{Threshold}$ (GW/cm²)
1	4.825	4.996	5.01
2	4.688	4.808	4.84
3	4.808	4.988	4.99

5.5.5 Differential scanning calorimetry for thermal stability

Differential scanning calorimetry (DSC) measurement was carried out for a small piece of the LAP crystal in the range of 50 °C to 300 °C at a heating rate of 5° C per minute using the DSC systems described in Chapter 2. Fig. 5.15 show the obtained DSC curve between temperature and heat flow. It indicates an endothermic peak at 138 °C belong to melting of the material with onset temperature for the phase transitions ~ 110 °C. On further heating it shows further absorption of heat from 200 C onwards with several peaks related to the decomposition of the material.^{19,20} This study indicates that the safe upper limit for LAP crystal is ~ 100 °C.

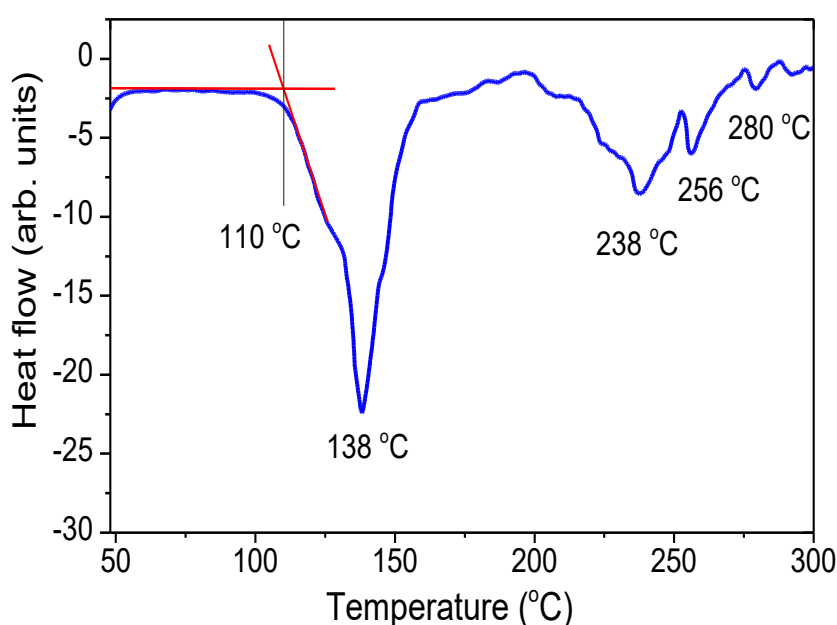


Fig. 5.15 Differential scanning calorimetric graph for LAP sample.

5.6 Growth kinetics studies of (100) faces of LAP crystal using birefringence interferometry

As per the above studies of crystal shape modification by seed orientation (Table 5.2) it is evident that one of the limiting feature to achieve exact isometric shape is low growth rate along (100) face. We therefore intended to study influence of supersaturation on the growth rate of this face because supersaturation is one of the main driving force to enhance growth rate. There are various optical techniques for determination of growth rates of crystals growing in solution.⁵⁵ We utilised birefringence interferometry technique because

it is applicable for those birefringent crystals which have large size parallel faces during growth.⁹ In our case, broad (100) faces are usually obtained in LAP crystal and hence growth kinetic studies are feasible. For this purpose, we have done following works,

- i. *Development of a small size growth unit,*
- ii. *Determination of the directions of principal axes with respect to the normal to the (100) face of LAP crystal, and*
- iii. *Setting up optical experiment based on birefringence interferometry for online measuring of crystal growth rates.*

These are described in following sections.

5.6.1 Design and fabrication of a small size growth unit for growth kinetics studies

For growth kinetics investigations of LAP crystal, a small size water bath of capacity ~ 1 liter was fabricated using perspex sheets to have plane transparent surfaces for exit and entry of the laser beam for birefringence interferometry. The bath was provided with heaters made using nichrome wire and connected to a *Eurotherm* make programmable PID temperature controller. The bath filled with water was placed on a magnetic stirrer. A teflon coated magnet was used at the bottom of this bath for stirring the water for homogenization of temperature. The rotation of the magnet was controlled by a magnetic stirrer placed below the bath. This design facilitated to achieve temperature stability of the order of ± 0.02 °C. For growth of crystals, a crystallizer was made using a borosilicate glass beaker of diameter ~ 40 mm. The beaker was covered with a lid made using teflon. A teflon rod of diameter ~ 25 mm was used for mounting seed crystal at its end for growth in the solution. Fig. 5.21 shows the fabricated growth unit for this purpose.

5.6.2 Determination of the orientations of the principal axes by laser conoscopy

LAP is a negative biaxial crystal where the relation between principal refractive indices is like $n_x < n_y < n_z$.³ Its indicatrix is a triaxial ellipsoid having two specific directions whose central sections are circular. These directions are called as optic axes (OA1 and OA2) and they lie within the x-z plane called as optic plane. The y-axis lies perpendicular to the optic plane and forms the optic normal. The bisectors of these optic axes corresponds to the dielectric axes x and z and are also called as acute and obtuse bisectrix depending on the angle being them to be acute or obtuse and are usually denoted by symbol 2V.

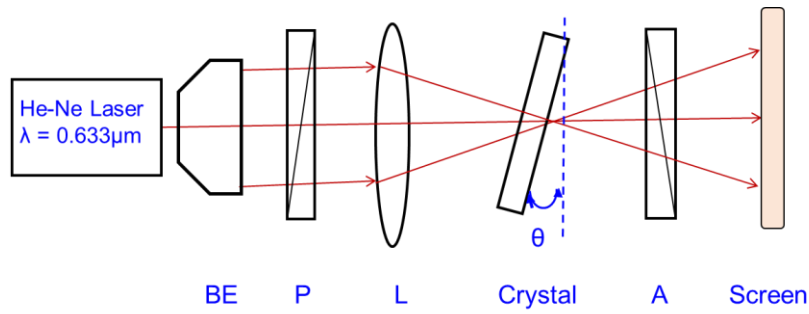


Fig. 5.16 Laser conoscopy set up for determination of directions of optic axes and bisectrix.

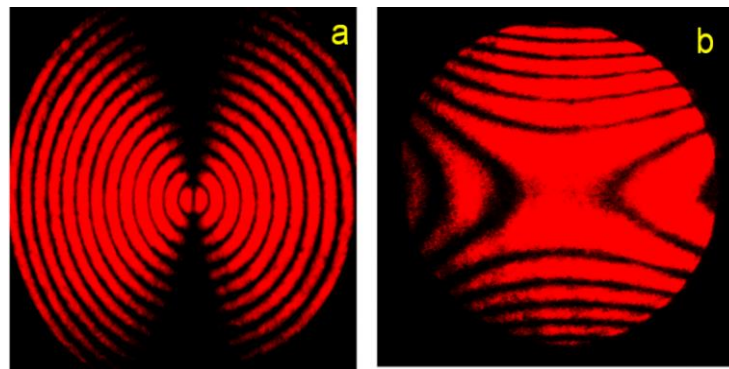


Fig. 5.17 Laser conoscopic interferograms obtained using (100) LAP plate. (a) for beam direction along one of the optic axis (OA1), and (b) for beam direction along its acute bisectrix.

The (100) LAP crystal plate was mounted between the cross polarizers (P and A) and passed converging laser beam using a convex lens of 100 mm focal length as shown in the Fig. 5.16. The plate was mounted such a way that its positive b-axis be vertically upward direction and the beam entering through (-100) face lies in the optic plane ca. The plane of polarizer was kept at 45° to the b-axis. The crystal was slowly rotated about the b-axis with simultaneous observation of the fringe movement at the screen. At a rotation angle of nearly 26° a characteristic conoscopic pattern of biaxial crystals for optic axis (OA1) was obtained as shown in Fig. 5.17 (a). The circular symmetric dark concentric fringes signify good optical homogeneity of the crystal while single isogyre oriented non-parallel to planes of the polarizers indicates the crystal to be biaxial. The number of circular fringes in the field of view depends on the sample thickness and the focal length of the lens for a given orientation. The number of fringes increases with increase in sample thickness and

with decrease of focal length of the lens. On further rotating the crystal about the b-axis another conoscopic pattern was obtained near 63° as shown in Fig. 5.17 (b). This is a characteristic biaxial conoscopic pattern belonging to direction along one of the bisectrix for a biaxial crystal.^{56,57}

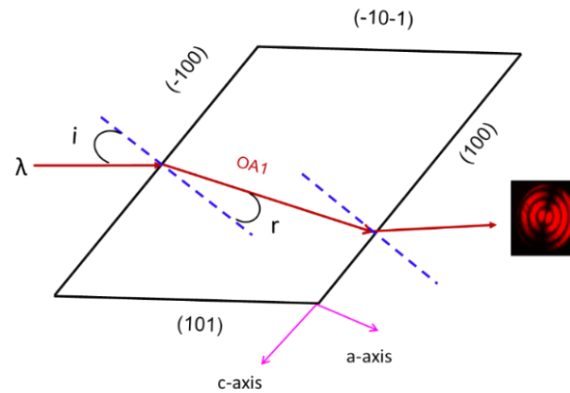


Fig. 5.18 Schematic ray diagram showing path of the central beam in the optic plane in laser conoscopy to calculate direction of optic axis (r).

These two external angles (say i from the normal to the entering face) can be used to calculate actual direction (say r) of the laser beam inside the crystal relative to the crystallographic axes as shown schematically in Fig. 5.18. The angle of refraction calculated using Snell's law of refraction giving the values of angle of refraction to be 16.4° and 35.0° for incident angles 26° and 63° respectively. The refractive index used for this purpose was calculated using the Sellmeier equations for $0.633 \mu\text{m}$ wavelength.^{3,58} For the two directions average of the three principal refractive indices was used.⁵⁴ The results show that OA1 direction is at 16.4° while that for the acute bisectrix is 35° . These values were used to derive directions of OA1, OA2, acute bisectrix and obtuse bisectrix with respect to the crystallographic directions as shown in Fig. 5.19 (a). Further the direction of the bisectrix belong to the principle axis of the crystal and hence depicted the x and z -axis. The third principal axis is y -axis which is along the crystallographic b -axis that lies normal to the optic plane (zx or ca) as shown in the Fig. 5.19 (a). This information is depicted in brief in Fig. 5.19 (b). The analysis show that crystallographic a -axis lies close ($\sim 8.4^\circ$ away) to the normal at the (100) face. The obtained values of the orientations of OA1 and OA2 and the bisectrix with respect to the crystallographic axes are quite close to that reported by Eimerl et al.³

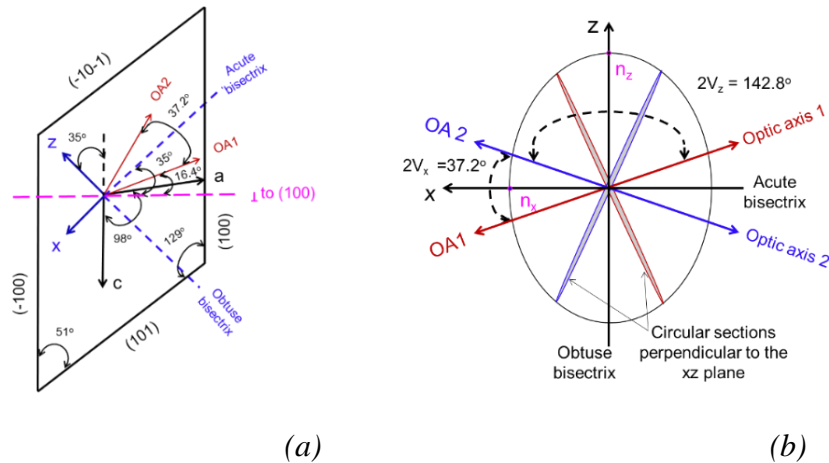


Fig. 5.19 (a) Orientations of acute and obtuse bisectrix inside the LAP crystal calculated from the observed external directions by laser conoscopy in the optic plane relative to habit faces of the crystal. The directions of crystallographic axes in this plane were determined using SHAPE software. (b) schematic of the corresponding sections of biaxial indicatrix viewed normal to zx - plane.

5.6.3 Growth kinetics studies of (100) face of LAP crystal using birefringence interferometry

The schematic of the optical set up based on birefringence interferometry for online measurement of growth rate of LAP crystal along the (100) face is shown in Fig. 5.20. We oriented the LAP seed crystal such that its y -axis be downward and the (100) plane face the laser beam. Now the seed is rotated about the y -axis so that the beam propagates along the x -axis of the crystal which can be aligned by visualizing the fringe movement under cross polars.⁹

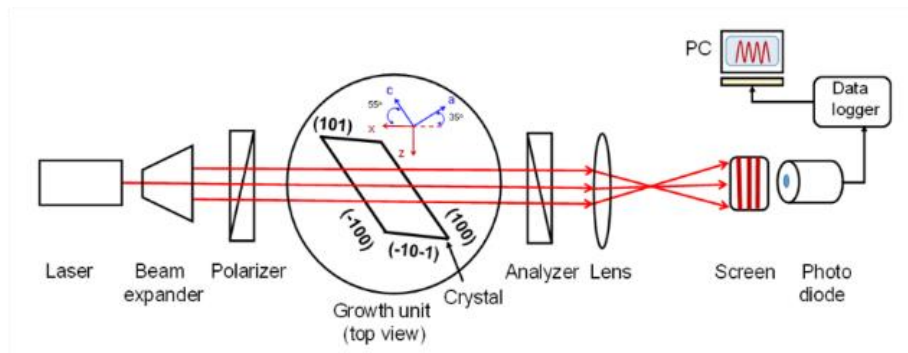


Fig. 5.20 Schematic of the optical set up used for growth rate measurement based on birefringence interferometry. The seed-crystal is shown with b -axis downward. Top view of the growth unit is depicted to show beam propagation in the optic plane with respect to its habit faces.

When monochromatic laser beam enters inside a birefringent crystal it splits in general into ordinary and extraordinary waves polarized 90° to each other and propagating with different speeds depending on their refractive indices determined by index ellipsoid. If the crystal is placed between a pair of crossed polarizers as shown in the Fig. 5.20, the transmitted intensity (I_T) depends on the interference between the components of the two waves along the plane of the analyzer given by,^{59,60,9}

$$I_T = \cos^2 \beta - \sin 2\alpha \sin 2(\alpha - \beta) \sin^2(\delta/2) \quad \text{---- (5.4)}$$

Where β is the angle between planes of polarizer and analyzer and α is the angle between the plane of the polarizer and one of the principal direction of the crystal lying in the plane normal to the beam, (here in our case is y -axis), while δ is the phase difference between the ordinary and extraordinary waves generated inside the crystal, given as

$$\delta = \left(\frac{2\pi}{\lambda}\right) \Delta n \times d \quad \text{---- (5.5)}$$

where λ is the wavelength of the laser beam and d and Δn are the thickness and the birefringence of the crystal along the direction of the beam inside it. The plane of the polarizer was kept at 45° to the y -axis simplifying the expression for transmitted intensity,

$$I_T = \sin^2(\pi \Delta n d / 2) \quad \text{---- (5.6)}$$

It shows that transmitted intensity varies sinusoidally as crystal thickness increases. If fringe to fringe average time interval is $\Delta\tau$ at a particular supersaturation or supercooling, growth rate expression can be written as,

$$R_x = \lambda / (2\Delta n \Delta\tau) \quad \text{---- (5.7)}$$

This is the expression for growth rate along the direction of the beam i.e. along the crystallographic x -axis. As the angle between c -axis and the a -axis is 35° the growth rate normal to (100) i.e. $R_{(100)}$ face can be written in terms of R_x as,

$$R_{(100)} = R_x \cos 35^\circ = 0.82 R_x \quad \text{---- (5.8)}$$

Combining Eq. and Eq.,

$$R_{(100)} = \frac{0.82\lambda}{2\Delta n \Delta\tau} \quad \text{---- (5.9)}$$

The value of the birefringence, Δn for $0.633\mu\text{m}$ wavelength laser beam along the x-axis was calculated using the Sellmeier coefficients. The computed value of the birefringence is Δn (along x-axis) = $(n_z - n_y) = 0.0083$.³⁰

It is to note that accurate determination of saturation temperature is a very important for growth kinetics measurements. We utilized laser shadowgraph technique to determine saturation temperature to be 44.1 ± 0.1 °C. After obtaining the state of saturation, the seed was oriented for interference fringes as per optical set up in Fig. 5.20. Fig. 5.22 (a) shows the typical interference fringes obtained after proper alignment. The photodiode was fixed at an interference fringe and recorded the variation of the transmitted intensity with time at corresponding growth temperature by a Pt-100 RTD sensor which were connected to a computer through a data acquisition unit. The data were recorded online using a software and recorded in a computer which can be displayed as shown in Fig. 5.22(b). The data was used to calculate average fringe to fringe time interval corresponding to the applied supercooling or supersaturation. Table 5.5 shows the obtained values which were plotted in terms of supercooling versus growth rate for (100) face of LAP crystal as shown in Fig. 5.23. The Fig. 5.24 show the as-grown crystal after the experiment. The growth run took place without any nucleation which is essential for accuracy of growth kinetic data.

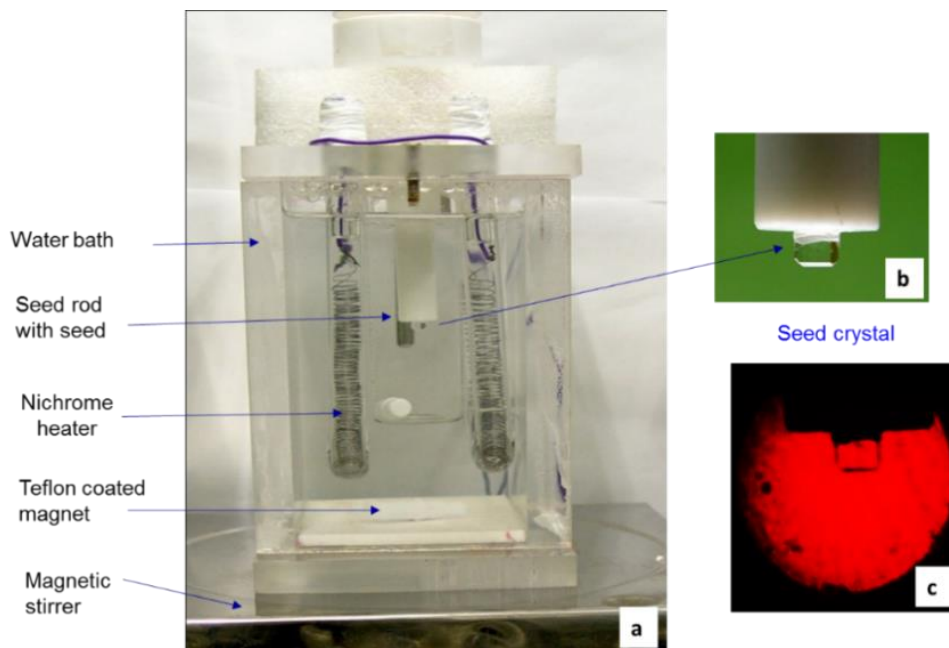


Fig. 5.21 Crystal growth unit (a), seed crystal at mount (b), and shadowgraph of seed showing saturation state (c).

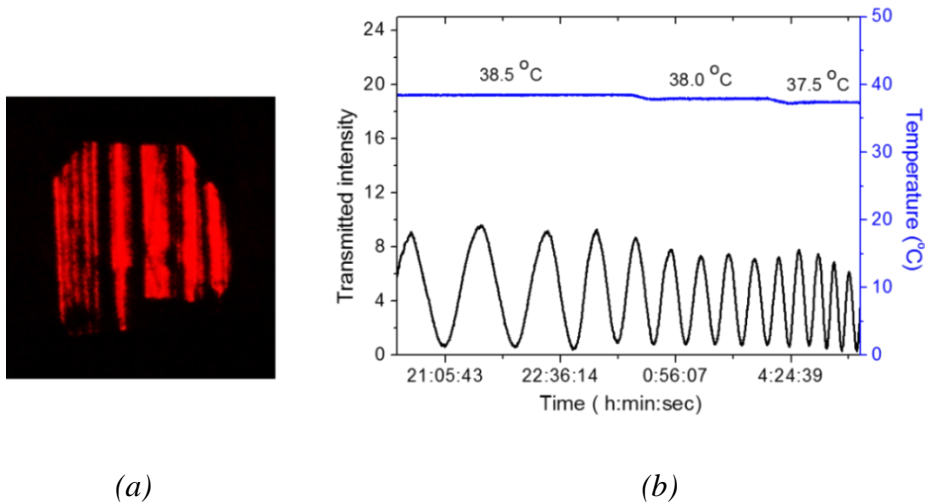


Fig. 5.22 (a) Image of birefringence fringes during growth, and (b) variation of transmitted intensity with time and temperature during the course of the experiment.

Table 5.5 Growth kinetics data determined at different undercooling for LAP crystal using birefringence interferometry.

S. No.	Under-cooling (°C)	Fringe to fringe av. Time interval (min)	$R_{(100)} \sim R_x \text{ Cos } 35^\circ$ (mm/day)
1	0.5	480	0.095
2	1	249	0.183
3	1.5	130	0.35
4	2	95	0.48
5	2.5	86	0.53
6	3	80	0.57
7	3.5	74	0.616
8	4	64	0.712
9	4.5	56	0.814
10	5	52	0.876
11	5.5	50	0.912
12	6	47	0.97
13	6.5	44	1.036
14	7	42	1.085
15	7.5	40	1.139
16	8	39	1.169

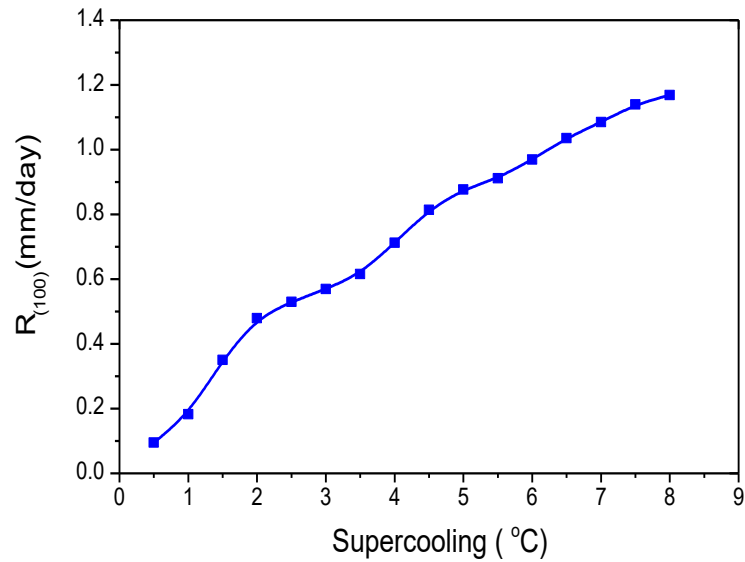


Fig. 5.23 Variation of growth rate of LAP crystal normal to the (100) face with supercooling.



Fig. 5.24 Photograph of the as-grown LAP crystal at the mount after the experiment.

The growth kinetics results indicate that growth rate of (100) face increases almost uniformly with supersaturation.¹⁰ The slope of increment is low therefore much higher supersaturation is required to enhance growth rate of (100) face of LAP crystal.

5.7 Summary and conclusion

Influence of seed orientation on growth rate and aspect ratio of LAP crystal is investigated to obtain isometric habit suitable for laser applications. For this purpose, LAP chemical was synthesized and crystalline phase was confirmed by powder X-ray diffraction. Solubility of the prepared chemical was determined at stoichiometric pH 4.3 in water in the temperature range of 34 °C to 66 °C. A growth unit was fabricated for growth of LAP crystals by slow cooling technique. LAP crystals were grown on a platform in the solution at four different seed orientations namely (100), (010), (001) and (011). The average growth rate of all these crystals along their crystallographic axes and their aspect ratio were calculated. The growth rate along the crystallographic axes follows the trend $R_b > R_c > R_a$ for each of the four orientations of LAP crystal. The relative variation in growth rate was correlated with the structure of the crystal. The aspect ratio of (011) oriented LAP crystal was found to be nearest to the isometric habit compared to the other three orientations making it more suitable for device fabrication. The (011) oriented LAP crystal was characterized for defects structures, dislocation density, optical quality, laser damage threshold, molecular functional groups and thermal stability. The optical transmittance for (100) plate was ~88% for 1064 nm as well as its higher harmonics (532 nm and 355 nm) indicating the usability of material for frequency conversion applications. The Mach-Zehnder interferometry showed good refractive index homogeneity of the crystal and the birefringence gradient normal to fringes obtained using birefringence interferometry was $1.86 \times 10^{-4} / \text{mm}$, again pointing towards high optical quality. The LDT values (4.8 to 6.6 GW/cm^2) show that the crystal is suitable for high power laser applications. Our results show that (011) oriented grown LAP crystal has high optical and structural quality and suitable for high power laser applications.

Growth kinetic studies were carried out for the slowest growing (100) face using birefringence interferometry. For it an experimental set up was developed including a small size water bath and a crystallizer. Principal axes of the LAP crystal were determined relative to crystallographic axes by laser conoscopy technique for proper alignment of seed crystal. Variation of growth rate of (100) face with change in supercooling/supersaturation was determined. The results show that growth rate of this face is slowly increases with supersaturation.

References:

- ¹ S. B. Monaco, L. E. Davis, S. P. Velsko, F. T. Wang, D. Eimerl, A. Zalkin, *J. Cryst. Growth*, 85 (1987) 252-255.
- ² A. Yokotani, T. Sasaki, K. Yoshida, S. Nakai, *Appl. Phys. Lett.*, 55 (1989) 2692-2993.
- ³ D. Eimerl, S. Velsko, L. Davis, F. Wang, G. Loiacono, G. Kennedy, *J. Quantum Electronics*, 25 (1989) 179-193.
- ⁴ D. Eimerl, S. Velsko, L. Davis, F. Wang, *Prog. Crystal Growth and Charact.*, 20 (1990) 59-113.
- ⁵ K. Aoki, K. Nagano, Y. Iitaka, *Acta Crystallogr.*, B27 (1971) 11-23.
- ⁶ D. Xu, M. Jiang, Z. Tan, *Acta Chim. Sinica*, 2 (1983) 230-233.
- ⁷ M. K. Singh, S. K. Sharma, Arup Banerjee, *CrystEngComm*, 15 (2013) 8493-8503.
- ⁸ G. Dhanaraj, T. Shripathi, H. L. Bhat, *J. Cryst. Growth*, 113 (1991) 456-464.
- ⁹ S. K. Sharma, Sunil Verma, B. B. Shrivastava, V. K. Wadhawan, *J. Cryst. Growth*, 244 (2002) 342-348.
- ¹⁰ G. Arunmozhi, E. De. M. Gomes, *Cryst. Res. Technol.*, 39 (2004) 34-39.
- ¹¹ Roger J. Davey and John Garside, *From molecules to Crystallizers: An Introduction to Crystallization*, Oxford University Press, Oxford. 2000.
- ¹² V. I. Bredikhin, V. P. Ershov, V. V. Korolikhin, V. N. Lizyakina, S. Yu. Potapenko, N. V. Khlyunev, *J. Cryst. Growth*, 84 (1989) 509.
- ¹³ A. Yeckel, Y. Zhou, M. Dennis, J. J. Derby, *J. Cryst. Growth*, 191 (1998) 206-226.
- ¹⁴ N. Zaitseva, L. Carman, I. Smolsky, *J. Cryst. Growth*, 241 (2002) 363-373.
- ¹⁵ S. Satapathy, S. K. Sharma, A. K. Karnal, V. K. Wadhawan, *J. Cryst. Growth*, 240 (2002) 196-202.
- ¹⁶ M. D. Aggarwal, J. Stephens, A. K. Batra, R. B. Lal, *J. Optoelect. Adv. Mater.*, 5 (2003), 552-562.
- ¹⁷ A. S. Hameed, C. Karthikeyan, G. Ravi, S. Rohani, *Physica B*, 406 (2011) 1363-1367.
- ¹⁸ B. Riscob, M. Shakir, N. Vijayan, K. K. Maurya, M. A. Wahab, G. Bhagavannarayana, *J. Appl. Cryst.*, 45 (2012) 679-685.

- ¹⁹ N. Kavitha, M. Arivanandhan, K. Ramamoorthy, K. Ragavendran, K. Sankaranarayanan, *Opt. Mater.*, 26 (2004) 275-280.
- ²⁰ A. S. Haja Hameed, G. Ravi, Md. M. Hossain, P. Ramasamy, *J. Cryst. Growth*, 204 (1999) 333-340.
- ²¹ S. K. Sharma, Yeshpal Singh, Sunil Verma, M. K. Singh, K. S. Bartwal and P. K. Gupta, *CrystEngComm*, 18 (2016) 6403-6410.
- ²² M. D. Aggarwal, J. Stephens, A. K. Batra, R. B. Lal, *J. Optoelect. Adv. Mater.*, 5 (2003) 552-562.
- ²³ Eric Dowty, Shape Software, 521 Hidden Valley Road, Kingsport, TN 37663.
- ²⁴ Russell G. Baughman, *J. Chem. Educ.*, 68 (1) (1991) A20.
- ²⁵ N. P. Zaitseva, L. N. Rashkovich, S. V. Bogatyreva, *J. Cryst. Growth*, 148 (1995) 276-282.
- ²⁶ Sunil Verma, K. Muralidhar, *Opt. Las. Eng.*, 49 (2011) 915-923.
- ²⁷ Y. Zhou, J. J. Derby, *J. Cryst. Growth*, 180 (1997) 497-509.
- ²⁸ N. A. Booth, T. Land, P. Erhmann, P. G. Vekilov, *Cryst. Growth Des.*, 5 (2005) 105-110.
- ²⁹ L. N. Rashkovich, G. T. Moldazhanova, *J. Cryst. Growth*, 151 (1995) 145-152.
- ³⁰ J. Herreros-Cedres, C. Hernandez-Rodriguez, B. Gonzalez-Diaz, R. Guerrero-Lemus, *Appl. Phys. B*, 77 (2003) 607-612.
- ³¹ A. A. Chernov, *Prog. Crystal Growth and Charact.*, 261 (1993) 121-151.
- ³² K. Sangwal, S. Veintemillas-Verdaguer, J. Torrent-Burgues, *J. Cryst. Growth*, 155 (1995) 135-143.
- ³³ Y. L. Geng, D. Xu, X. Q. Wang, G. H. Zhang, G. W. Yu, D. L. Sun, *J. Appl. Cryst.*, 38 (2005) 657-660.
- ³⁴ K. Wu, C. Liu, C. Mang, *Opt. Mater.*, 29 (2007) 1129-1137.
- ³⁵ R. Dovesi, R. Orlando, B. Civalleri, C. Roetti, V. R. Saunders, C. M. Zicovich-Wilson, *Z. Kristallogr.*, 220 (2005) 571-573.
- ³⁶ A. Kokalj, *Comp. Mater. Sci.*, 28 (2003) 155-168.
- ³⁷ K. Sangwal, S. Veintemillas-Verdaguer, J. Torrent-Burgues, *J. Cryst. Growth*, 155 (1995) 135-143.

- ³⁸ R. Docherty, G. Clydesdale, K. J. Roberts, P. Bennema, *J. Phys. D: Appl. Phys.*, 24 (1991) 89–99.
- ³⁹ B. K. Tanner, D. K. Bowen, *Characterization of Crystal Growth Defects by X-Ray Methods*, NATO advanced study institutes series: Series B, Physics; Vol. 63, Plenum Press, London, 1979.
- ⁴⁰ S. K. Sharma, Sunil Verma, Yeshpal Singh, K. S. Bartwal, M. K. Tiwari, G. S. Lodha, G. Bhagavannarayana, *Opt. Mater.*, 46 (2015) 329-338.
- ⁴¹ W. J. Liu, C. Ferrari, M. Zha, L. Zanotti, S. S. Jiang, *Cryst. Res. Technol.*, 35 (2000), 1215-1219.
- ⁴² Y. Ding, S. Nie, X. S. Wu, S. S. Jiang, X. B. Hu, S. Y. Guo, D. Xu, S. Y. Sun, J. H. Jiang, Y. L. Tian, *Ferroelectrics*, 251 (2001) 147-153.
- ⁴³ S. M. Rao, A. K. Batra, C. Rao, R. B. Lal, *J. Cryst. Growth*, 106 (1990) 481-482.
- ⁴⁴ F. Donald Bloss, *An Introduction to the Methods of Optical Crystallography*, Holtn Eichner, A. H. Guenther, E. Kiesel, R. Kuehnel, D. Milam, W. Ryseck, S. C. Seitel, A. F. Stewart, H. Weber, H. P. Weber, G. R. Wirtenson, R. M. Wood, *Appl. Opt.*, 23 (1984) 3743-3752.
- ⁴⁵ S. M. Rao, C. Rao, A. K. Batra, R. B. Lal, *Proc. SPIE*, 1557 (1991) 283-292.
- ⁴⁶ Sunil Verma, P. J. Shlichta, *Prog. Cryst. Growth Charact. Mater.*, 54 (2008), 1-120.
- ⁴⁷ Sunil Verma, S. Kar, K. S. Bartwal, *Interferometric techniques for investigating the refractive index homogeneity, birefringence and indicatrix of optical crystals*, Chapter 19, in: “*Interferometry Principles and Applications*”, Mark. E. Russo (Editor), Nova Science Publishers, New York, USA, 2012, 537-560.
- ⁴⁸ A. Mazumdar, T. Kar, S. P. S. Gupta, *Japanese J. Appl. Phys.*, 34 (1995) 5717-5720.
- ⁴⁹ Marvin J. Weber (Ed.), *CRC Handbook of Laser Science and Technology, Supplement 2: Optical Materials*, CRC Press Inc., Boca Raton, 1995, pp. 768-776.
- ⁵⁰ R. M. Wood, *Laser-induced Damage of Optical Materials*, Institute of Physics, Bristol, 2003.
- ⁵¹ K. H. Guenther, T. W. Humpherys, J. Balmer, J. R. Bettis, E. Casparis, J. Ebert, M. Eichner, A. H. Guenther, E. Kiesel, R. Kuehnel, D. Milam, W. Ryseck, S. C. Seitel, A. F. Stewart, H. Weber, H. P. Weber, G. R. Wirtenson, R. M. Wood, *Appl. Opt.*, 23 (1984) 3743-3752.
- ⁵² R. T. Bailey, F. R. Cruickshank, P. Kerkoc, D. Pugh, J. N. Sherwood, *Appl. Optics*, 37 (1985) 1239-1245.
- ⁵³ D. Eimerl, S. Velsko, L. Davis, F. Wang, *Prog. Crystal Growth Charact.*, 20 (1990) 59-113.

- ⁵⁴ G. C. Bhar, A. K. Chaudhary, P. Kumbhakar, *Applied Surface Science*, 161 (2000) 155-162.
- ⁵⁵ L. N. Rashkovich, O. A. Shustin, *Sov. Phys. Usp.*, 30 (1987) 280-283.
- ⁵⁶ L. Bergmann, C. Schaefer, in *Edi. "Optics of Waves and Particles"*, H. Niedrig (Ed.), Walter de Gruyter, Berlin, 1999.
- ⁵⁷ A. Puri, A. De, *J. Appl. Phys.*, 107 (2010) 083104-1 to 083104-5.
- ⁵⁸ V. G. Dmitriev, G. G. Gurzadyan, D. N. Nikogosyan, *Handbook of Nonlinear Optical Crystals*, Springer Verlag, Heidelberg, Germany, 1997.
- ⁵⁹ V. I. Bredikhin, V. P. Ershov, V. V. Korolikhin, V. N. Lizyakina, S. Yu. Potapenko, N. V. Khlyunov, *J. Cryst. Growth*, 84 (1987) 509-514.
- ⁶⁰ P. J. C. M. van Hoof, W. J. P. van Enkevort, M. Schoutsen, P. Bennema, X. Y. Liu, *J. Cryst. Growth*, 183 (1998) 641-652.

Chapter 6 Growth and characterization of ZCTC crystals

6.1 Introduction

Zinc cadmium thiocyanate, $\text{ZnCd}(\text{SCN})_4$ or in brief ZCTC is one of the important compound of bimetallic thiocyanate family for second order nonlinear optical applications.^{1,2} In comparison to KDP and LAP, it has about one order higher second order nonlinear coefficient, wider transparency range and less hygroscopicity however laser damage resistance is low.^{3,4} These features make it a potential candidate for frequency conversion of low power diode lasers.^{5,6} ZCTC was first reported in 1970 by Bergman et al.⁷ Wang et al. from 1999 onwards reported its properties and growth from solution in detail.¹ One of main limitation of this crystal is the difficulty in growing good quality moderate size crystals.⁸ In this chapter we report growth of optical quality crystals by precise control of evaporation rate. The grown crystals were subsequently characterized by various characterization tools for its crystalline structure, defect structure, optical quality, molecular structure, laser damage resistance and thermal stability. Further, refractive indices of the grown crystals were also determined for ordinary and extraordinary waves with wavelength and temperature and determined Sellmeier coefficients and thermo-optic coefficients. These results were further used to calculate phase matching angles for laser frequency conversion of Nd:YAG laser.

6.2 Chemical synthesis, phase identification and determination of solubility curve

6.2.1 Chemical synthesis

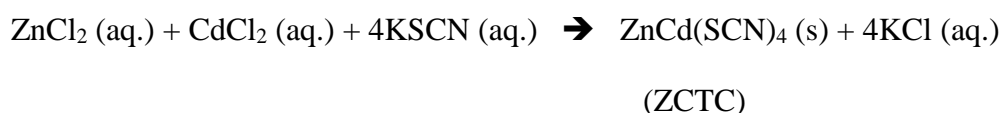
ZCTC chemical was synthesized by reacting analytical reagent grade zinc chloride, cadmium chloride and potassium thiocyanate chemicals with high purity demineralized water of 18.2 M Ω .cm resistivity obtained from a Milli-Q water purification system. The chemical reaction involves three steps: First to obtain a white colour precipitate by reacting zinc chloride, cadmium chloride and potassium thiocyanate in 1:1:4 molar ratios in the water. During this process of precipitation, the solution was stirred vigorously using teflon coated magnet controlled by a magnetic stirrer cum hot plate for homogenization of chemicals. Subsequently the precipitate was isolated by filtration through 0.2 μm porosity

nylon membrane filter under vacuum and also washed with fresh water repeatedly to remove unwanted chemicals. Lastly the precipitate was again dissolved in fresh demineralized water at higher temperature (~ 45 °C) for near saturation followed by filtration through the membrane filter. The prepared solution was then put for fast evaporation in an oven at moderate temperature (45-50 °C) to obtain ZCTC salt for crystal growth purpose.

The chemical preparation steps in short are depicted as:

Step 1: Chemical reaction

Stirring



Step 2: Washing

Room temperature Filtration



Step 3: Evaporation

Heat Filtration Evaporation



6.2.2 Powder X-ray diffraction for phase identification

The prepared salt was tested for its crystalline phase by powder X-ray diffraction technique. A small amount of the dried ZCTC salt was finely powdered in an agate mortar and used for the study. X-ray diffraction spectrum was taken using the Rigaku make X-ray diffractometer in the 2-theta range of 10° to 60° with angular steps of 0.01°. Fig. 6.1 shows the powder X-ray diffraction pattern of the prepared chemical. The peak positions of this spectrum match well with that of JCPDS card 89-6593 and with that reported in the literature^{1,9} for ZCTC. The crystal structure belongs to tetragonal crystal system, space group I4bar. The peak positions were identified using origin software and lattice parameters were calculated using another software. The obtained values are shown in Table 6.1 which matches closely with that reported in the literature.

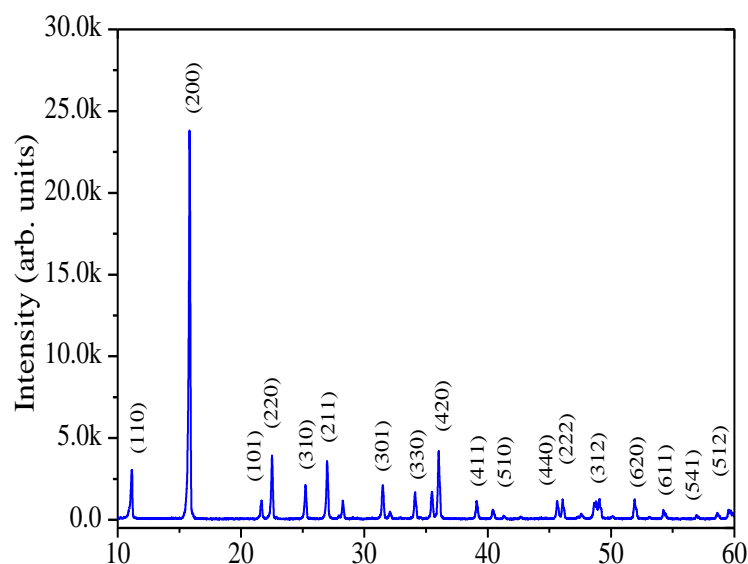


Fig. 6.1 Powder X-ray diffraction pattern for the prepared ZCTC chemical.

Table 6.1 A comparison of obtained lattice parameters with that reported in the literature.

S. No.	Lattice parameters (Å)		Reference no.
	a (= b)	c	
1	11.135	4.376	Wang et al. ¹
3	11.070	4.352	Kumari et al. ⁹
3	11.136	4.354	Present study

6.2.3 Determination of solubility curve in water

Determination of solubility is important to decide suitable technique of solution crystal growth. The prepared ZCTC powder was used to determine solubility at different temperatures. Saturated solution was prepared using high purity water in a glass bottle under rapid stirring by a teflon coated magnet in a water bath. After about 12 hours of stirring one or two drops of solution were taken in a weighing bottle through a syringe filter of 0.2 μm porosity. The concentration of ZCTC in the saturated solution was determined by gravimetric method. Table 6.2 shows the data of gravimetric analysis and the resulting saturation concentration at various temperatures. The pH of the solution was that of stoichiometric value 6.2.

Table 6.2 Saturation concentration of ZCTC salt in water for solubility curve.

Temperature (°C)	Mass of empty bottle W ₁ (g)	Mass of empty bottle and solution W ₂ (g)	Mass after evaporation of solvent, W ₃ (g)	Solubility (g /100g water)
30	24.7168	24.7764	24.7196	4.93
40	24.6345	24.7747	24.6415	5.26
45	24.5869	24.7067	24.5931	5.46
50	24.6244	24.7559	24.6317	5.88

This data is plotted to show solubility curve in Fig. 6.2. It shows that solubility of ZCTC varies almost linearly with temperature. This study show that solubility is small and increases slowly with temperature which is quite close to that reported in the literature.¹⁰ The temperature coefficient of solubility is also very low. These values of solubility curve indicate that growth of this crystal to large sizes will be difficult. However slow evaporation is a better technique compared to slow cooling based growth technique for solution growth of ZCTC.

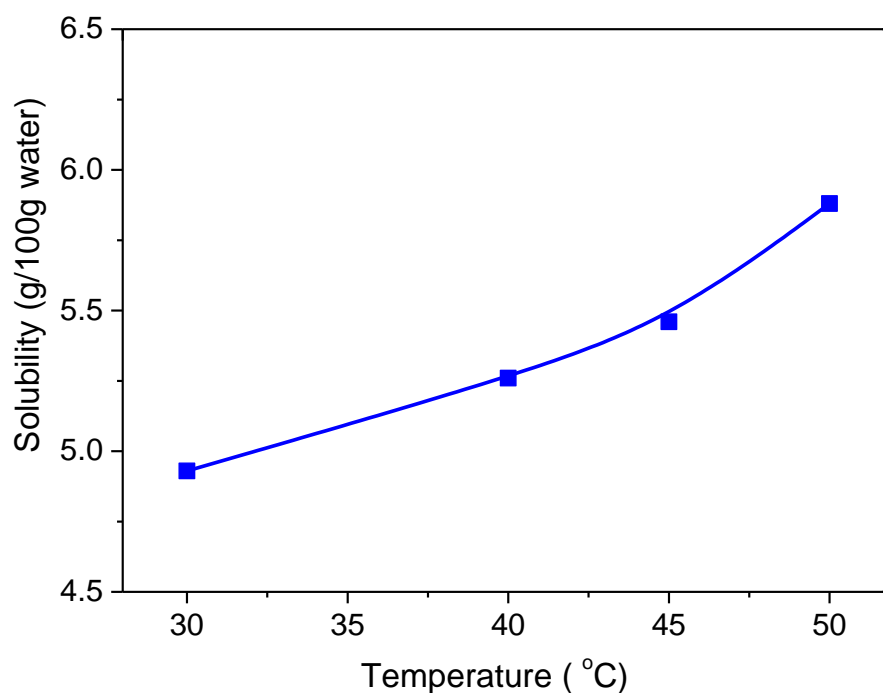


Fig. 6.2 Solubility curve for ZCTC chemical in water at stoichiometric pH value ~ 6.2.

6.3 Growth of ZCTC crystals by evaporation technique

Growth of ZCTC crystals from the prepared salt involve preparation of seed crystals, optimization of pH and development of a growth unit based on evaporation control. These are described in the following sub-sections.

6.3.1 Seed preparation and influence of solution pH

Seed preparation is an important part for seeded growth to obtain large size single crystals. For this purpose, small amount of saturated solution was prepared in a small glass beaker at room temperature. The solution was filtered through 0.2 μm porosity membrane by vacuum filtration technique. The filtered solution was left for slow evaporation for spontaneous nucleation. It was however observed that it ended with nucleation of small size crystallites spread all over the bottom of the beaker. On further continuation of the evaporation, it formed aggregates of randomly oriented small needle shape crystallites which were too small to use for seed. A lump of such an aggregate is shown in Fig. 6.3. The experiment was repeated many times but could not find good prismatic shape seed crystals. This situation of spontaneous nucleation at stoichiometric pH ~ 6.2 was similar to that observed by Wang et al.¹⁰

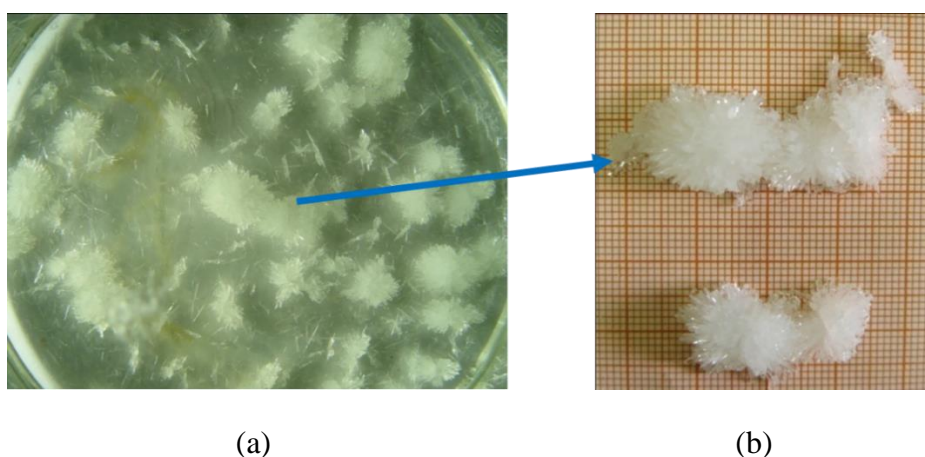


Fig. 6.3 (a) Needle shape nuclei and their aggregates formed at stoichiometric pH value 6.2, (b) an enlarged image of some aggregates.

Therefore, we tried with reduced pH of the solution using dilute HCl and obtained prismatic shape seed crystals. Fig. 6.4 (a) shows the prismatic shape crystals obtained at 2.3 pH value. Although they have some whitish inclusive portion at centre, however may be used as seed for crystal growth. For this purpose, the seed was wrapped by teflon tape

in such a way that all the seed covered except the clear pyramidal part as shown in Fig. 6.4 (b).

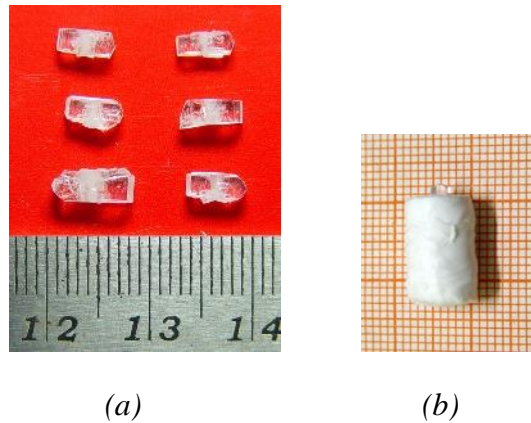


Fig. 6.4 (a) Prismatic shape seed crystals obtained at pH 2.3 by spontaneously nucleation by slow evaporation, and (b) a seed placed in a seed holder to mount at the platform for growth of ZCTC crystal.

6.3.2 Design and fabrication of a crystallizer to control evaporation rate of solvent

Controlling rate of evaporation of solvent from a solution to make it supersaturated for crystal growth is difficult compared to controlling rate of temperature reduction. It is because there are programmable PID temperature controllers readily available for precise control of temperature. While there are a few designs to control evaporation rate¹¹, however it has been difficult to isolate evaporation rate from temperature. Because for a same opening area evaporation rate depends on temperature difference between the solution and the condenser. We modified the design of the crystallizer in such a way that evaporation rate can be controlled easily at every temperature by controlling the opening area at the lid through which the vapour reaches at the condenser. It comprises of two concentric circular plates, the lower plate act as air tight lid for the glass beaker while the upper plate can be rotated on the outer plate about the central shaft of the platform. The inner plate is mounted with a conical shape glass condenser. Both the plates have open areas about the centre made in such a way that by rotating the upper plate, one can vary the opening area for the vapours to escape to the condenser. When this crystallizer is placed with solution in a water bath set at higher temperature than that of room temperature. The condensed water drops at the conical shape cooler surface slides down to the groove which is connected by a plastic pipe to a measuring cylinder placed outside. Fig. 2 (a) shows a schematic diagram of the crystallizer while Fig. 2(b) shows the actual crystallizer. The

crystallizer is suitable to obtain evaporation rate up to 20 ml/day at 42 °C temperature which can be lowered by controlling the opening area for the vapor to reach at the condenser wall. The crystallizer was used for growth of ZCTC crystals.

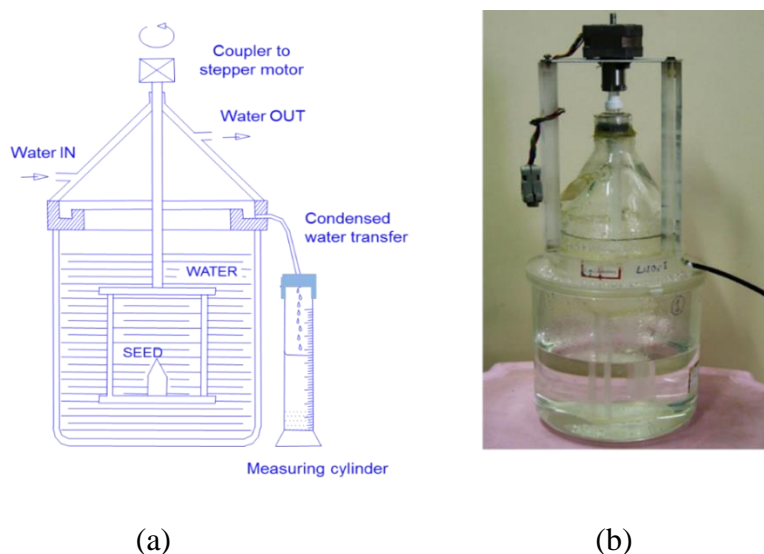


Fig. 6.5 (a) Schematic of a crystallizer based on controlled evaporation, and (b) actual photograph of the crystallizer based on controlling the rate of solvent evaporation.

6.3.3 Growth of ZCTC crystals

Saturated solution was prepared using the synthesized ZCTC salt in high purity water at ~ 42 °C by continuous mixing with excess salt at the magnetic stirrer using a teflon coated magnet. The pH of the solution was adjusted to ~ 2.3 by addition of hydrochloric acid (HCl). The solution was subsequently filtered using 0.2 μm porosity nylon membranes under vacuum. The filtered solution was transferred to the crystallizer where it was overheated by ~ 5 - 8 °C for nearly 12 hours. A perspex make platform was used for mounting a small transparent seed using teflon tape at the hole made at the center. The state of saturation was realized by manual observation of the seed crystal. After achieving the state of saturation the platform was rotated reversible at low RPM in the range of 20-30 by a stepper motor controller called as ACRT.¹²

We tried to optimize growth rate and quality of the crystal by varying evaporation rate for solutions with pH in the range of 2.0 to 3.0. The main problems faced were, inclusions, overgrowth, nucleation and coloration of the solution. It was observed that at higher evaporation rates (~ 8 to 15 ml /day) crystal cross section i. e. growth rate along its

prismatic faces $\{100\}$ also increased. However, it acquired inclusion and hence degraded the quality of the crystal as shown in Fig. 6.6 (i) and (ii). Another problem faced was that of overgrowth or nucleation at surface as shown in Fig. 6.6 (iii). At low evaporation rate of ~ 4 to 6 ml/day we obtained optically clear crystals of dimensions $\sim 2 \times 2 \times 14$ mm³ and $4 \times 1.5 \times 15$ mm³ as shown in Fig. 6.6 (iv) and (v) respectively. Many other crystals were also grown during the course of this work at a rate up to ~ 0.5 mm/day along $[001]$ direction. The growth details of one of the crystal shown at Fig. 6.6 (iv) are given in the Table 6.3.

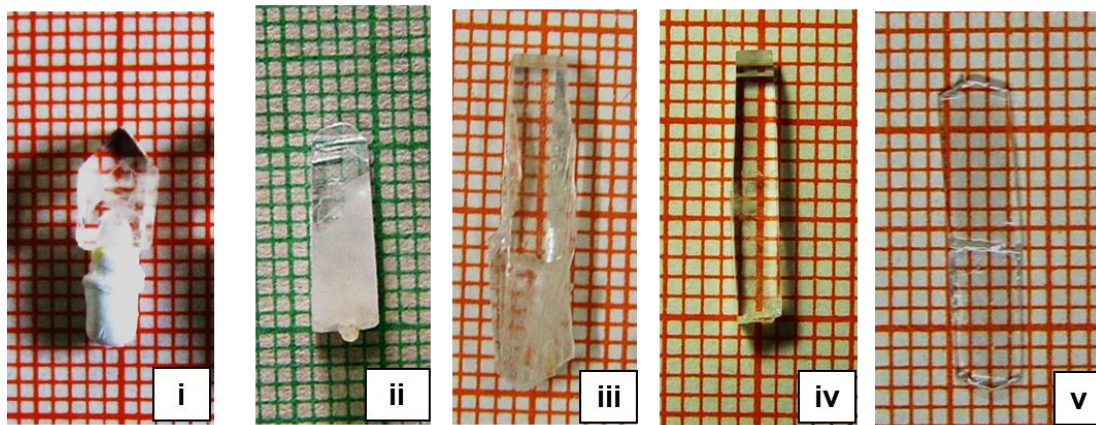


Fig. 6.6 As-grown ZCTC crystals from point seeds at low pH with approximate dimensions ($a \times b \times c$) as (i) $4 \times 4 \times 7$ mm³, (ii) $4 \times 3 \times 11$ mm³, (iii) $3 \times 2 \times 16$ mm³, (iv) $2 \times 2 \times 14$ mm³, and (v) $4 \times 1.5 \times 15$ mm³.

Table 6.3 Growth details of ZCTC crystal shown in Fig. 6.6(iv).

S. No.	Parameters	Values
1	Solution volume	~ 1.0 liter
2	Growth temperature	42 °C
3	Solution pH	2.3
4	Av. evaporation rate	~ 4 ml/day
5	Crystal size	$2 \times 2 \times 14$
6	Growth duration	30 days
7	Average $R_{(001)}$	~ 0.5 mm/day

6.4 Characterization of ZCTC crystals

6.4.1 Indexing faces of ZCTC crystal and preparation of samples plates

The faces of the as grown ZCTC crystals were indexed using SHAPE software by matching four-fold symmetry axis and interfacial angles.^{13,14} Fig. 6.7 shows the typical growth morphology of ZCTC crystals with respect to crystallographic directions. The crystal normally consists of eight faces (100), (-100), (010), (0 -10), (031), (-031), (3 -01) and (-0 -3 1) among which the first four are prismatic faces and the later four are pyramidal faces. The morphology is similar to that reported in the literature.^{15,16}

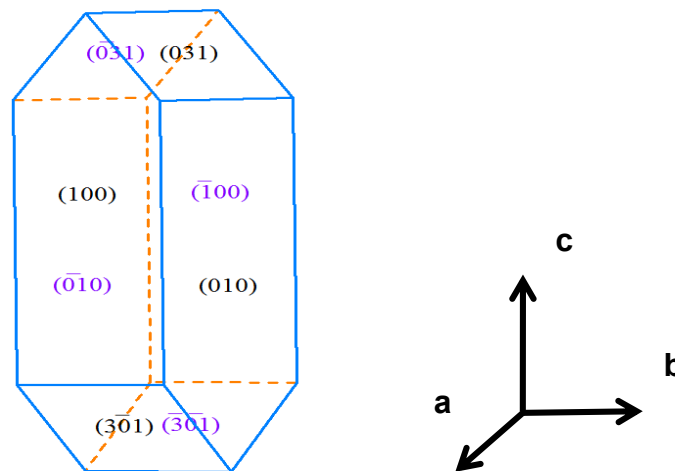


Fig. 6.7 Typical growth morphology of ZCTC crystal obtained by SHAPE software.

6.4.2 Optical quality by transmission spectroscopy

Transmission spectrum imparts useful information about the optical quality of the grown crystals. Optical quality of the grown crystals was assessed by measuring transmission spectra using *Jasco* make spectrophotometer in the range of 190 nm to 2200 nm. A small size (100) plate of ZCTC crystal was prepared for this purpose by careful polishing the sample plate. The thickness of the plate was nearly 1 mm. Fig. 6.8 shows the transmittance spectra for the plate without accounting for Fresnel reflection losses. It is evident that the crystal has wide transmission window extending from near UV to whole visible to mid IR range. The UV cut off was at ~290 nm showing the band gap to be ~ 4.28 eV. The results match well with that reported in the literature.^{3,5} The transmittance is in between 65 % to 75% for wavelength range 400 nm to 2000 nm. Transmittance at three specific

wavelengths 1064 nm, 532 nm and 355 nm are 75%, 67% and 57% respectively without accounting reflection losses.

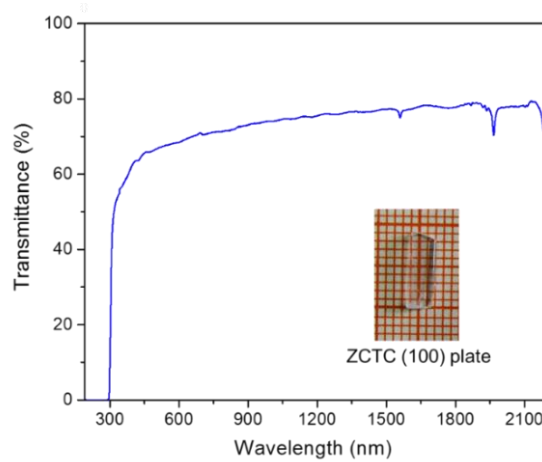


Fig. 6.8 Transmission spectrum of 1 mm thick (100) plate of ZCTC crystal without accounting for Fresnel reflection losses. Inset show the sample plate.

6.4.3 Birefringence homogeneity: Orthoscopy and conoscopy

Birefringence inhomogeneity test is useful for bulk assessment of optical homogeneity. The (100) sample plate of ZCTC crystal was placed between crossed polarizers and collimated light of He-Ne laser was passed through it. Fig. 6.9 (b) show the birefringence interferogram for the ZCTC plate Fig. 6.9 (a). It shows almost Equi-spaced interference fringes showing the good birefringence homogeneity of the crystal. Large number of fringes is an indication of slight wedge in the thickness. Localized dark spots indicate localized defects. The defect density is high near the seed region and it decreases away from the seed.

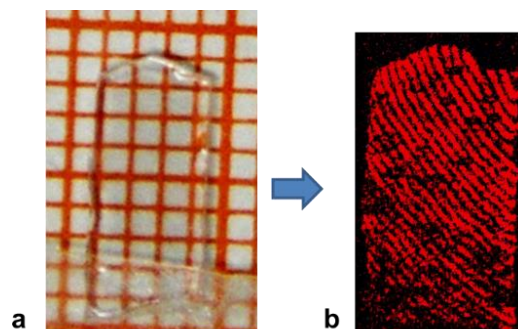


Fig. 6.9 (a) (100) sample plate of ZCTC crystal used for birefringence interferometry, and (b) birefringence interferogram for the plate in orthoscopic configuration.

6.4.4 X-ray diffraction topography for defects structures

The (100) sample plate of ZCTC crystals was further characterized using X-ray diffraction topography for defects structure and their distribution. Fig. 6.10 (b) shows the X-ray topograph for the sample plate shown in Fig. 6.10 (a). The plate was etched slightly by water for 30 to 60 second before X-ray topography to reduce unwanted defect features in topograph due to surface defects such as scratches, cracks etc. The resulting topograph shows that the region near edges contains more defects compared to the bulk. The region near the seed portion contains higher defect compared to that away from it. This observation corresponds to that observed by birefringence interferometry However there is no feature in topograph corresponding to the localized dark spots seen in the birefringence interferogram. It may be due to the fact that the X-ray topography provide surface defects while interferometry gives the overall effect of bulk defects.

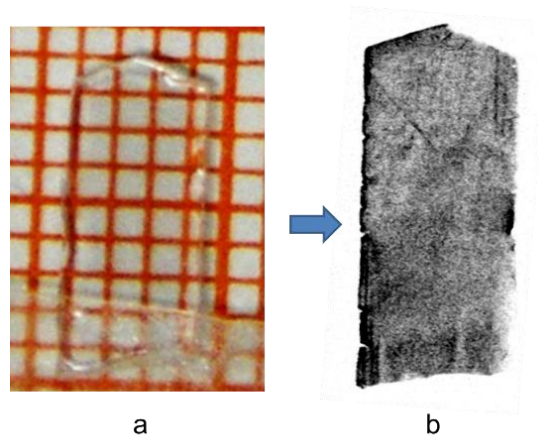


Fig. 6.10 (a) ZCTC sample plate used, and (b) X-ray diffraction topograph for (811) planes of (100) plate.

6.4.5 Chemical etching

Chemical etching is a simple technique used to delineate the dislocation sites their distribution and density. The (100) surface of ZCTC sample plate was used for this study. The surface was etched using ethylene glycol as an etchant and imaged by Olympus make optical microscope. Fig. 6.11 shows optical micrograph of the etched surface for ~ 60 s. The shape of etch pits was initially rectangular resembling to the surface symmetry of the (100) plane of ZCTC crystal.¹⁷ On further etching for longer duration it gets elongated along crystallographic c-axis, and tend to acquire a shape somewhat like triangular as shown in the Fig. 6.11. The etch pit density was of the order of 10^4 per cm^2 .

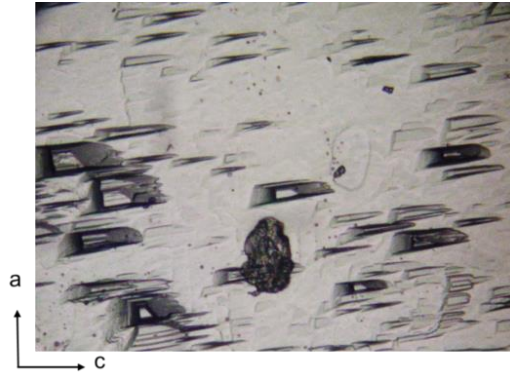


Fig. 6.11 Optical micrograph of etched (100) surface of ZCTC sample plate by ethylene glycol. (Magnification:50X)

6.4.6 Laser-induced damage threshold of ZCTC crystal

Laser damage resistance is an important property to decide the upper limit of laser intensity for the safety of crystal in case of frequency conversion applications. We utilized well-polished ZCTC (100) plate for this test. The plate was mounted at the nanosecond Nd:YAG laser workstation where convergent laser beam pulse was passed through the sample using a lens of 50 cm focal length. The other parameters for the experiments were similar to that used for LAP samples described in Chapter 5. Table 6.4 shows the LDT results obtained for various plates of ZCTC crystal. It shows that the LDT of ZCTC at 7 ns, Nd:YAG laser is nearly 1 GW/cm².

Table 6.4 LDT results measured at various locations of different (100) plates of ZCTC crystals.

S. No.	$E_{\max}^{ND} \times (35.04)^{-1}$ (mJ)	$E_{\min}^D \times (35.04)^{-1}$ (mJ)	$I_{\text{Threshold}}$ (GW/cm ²)
1	1.065	1.287	1.20
2	1.082	1.202	1.17
3	1.022	1.056	1.06
4	1.219	1.365	1.32
5	0.962	1.09	1.05

Further, it was observed that at the initiation of laser damage a whitish damage spot visibly seen at the crystal surface however if the pulse energy is slightly increased the crystal splits normal to the c -axis as shown for two sample plates in Fig. 6.12. This may be attributed to the anisotropic thermal expansion of this material along a and c axis.³ It is because ZCTC has high linear thermal expansion coefficient along c - axis while along a - or b -axis i.e. in the plane normal to c -axis it has negative thermal expansion coefficient. This anisotropic behaviour of thermal expansions leads to splitting of crystal normal to c -axis, if heat is absorbed in case of LDT measurements. The study shows that the value of LDT for ZCTC is lower compared to that obtained for KDP and LAP single crystals therefore ZCTC is not recommended for frequency conversion of high power lasers. However due to its high nonlinearity it is particularly suitable material for frequency conversion application of low power lasers such as diode lasers.^{5,6}

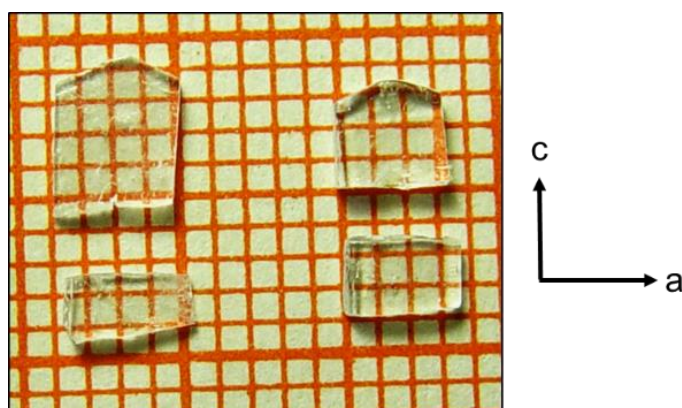


Fig. 6.12 ZCTC crystals splitted normal to c -axis at energy above the LDT.

6.4.7 Structural characterization by FTIR

The material was investigated using Fourier transform infrared (FTIR) spectroscopy for identification of its molecular functional groups. The experiment was carried out using *Jasco* make FTIR in the wavelength range of 400 cm^{-1} to 4000 cm^{-1} . There are various vibrating atomic groups in the ZCTC molecule such as CN, CS, SCN etc. which are IR active and hence absorb corresponding IR frequencies. Fig. 6.13 shows the FTIR spectrum obtained for ZCTC sample. The peak at 2156 cm^{-1} is highly absorbing it belongs to strong absorption by CN group. Peak at 785 cm^{-1} belongs to CS group while the absorption peaks at 475 cm^{-1} , 898 cm^{-1} and 945 cm^{-1} belong to vibrational modes of SCN group. These peak positions are in agreement with that reported in the literature.^{3,18}

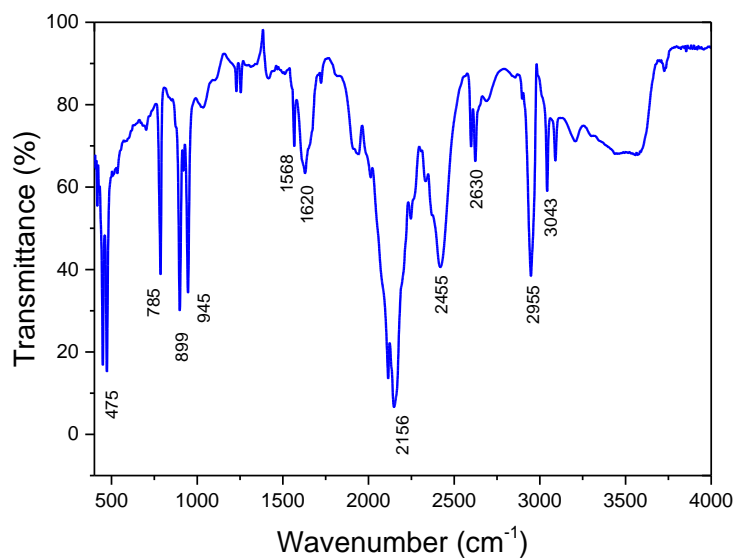


Fig. 6.13 FTIR spectrum of ZCTC crystal.

6.4.8 Differential scanning calorimetry of ZCTC

Differential scanning calorimetry was used to assess thermal stability of the ZCTC crystal. The experiment was carried out *Setaram* make DSC unit for room temperature to 500 °C at a heating rate of 5 °C/min. Fig. 6.14 shows the DSC curve for ZCTC crystal. It shows several exothermic peaks near to 357 °C, 377 °C and 405 °C. These peaks have been associated with the decomposition of ZCTC crystal structure.¹⁹ Hence ~ 325 °C may be suitably considered as upper limit of the material in use.

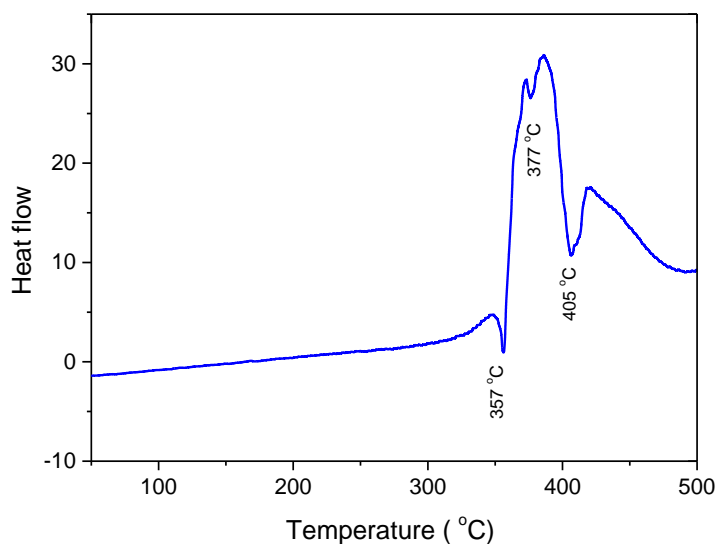


Fig. 6.14 DSC curve of ZCTC crystal.

6.4.9 Measurement of refractive indices of ZCTC and determination of Sellmeier coefficients and thermo-optic coefficients for ordinary and extraordinary waves

Determination of ordinary and extraordinary refractive indices of the grown single crystals with wavelength is an important characterization to get information about various parameters for nonlinear optical applications. This investigation includes determination of principal refractive indices with wavelength and temperature. Which can be used to derive various parameters such as: variation of birefringence with wavelength, nature of birefringence i.e. whether positive or negative, determination of Sellmeier coefficient for ordinary and extraordinary waves, determination of thermo-optic coefficients etc. This as a whole gives information about index ellipsoid which can be utilized to calculate phase matching angles for a given fundamental wavelength for type-I and type-II phase matching configurations. It also provides information about phase matching range beyond which phase matching could not be possible.

We used *Metricon* make (model 2100M) prism coupler for determination of refractive indices for ordinary and extraordinary waves for grown ZCTC crystal at five different wavelength covering 532 nm to 1551 nm. These wavelengths are obtained from specific laser diodes. The working principle of the instrument is based on the sharp change in reflected intensity at total internal reflection from the crystal-reference material interface. It occurs at a specific angle called as critical angle of internal reflection (i_c) for the material under study with respect to the reference material. Normally standard material is used in a shape of prism as shown schematically in the Fig. 6.15. The prism rotates smoothly about an axis normal to the plane formed by incident and reflected rays. Once the angle (i_c) is measured, refractive index of the material can be calculated using the formula,^{20,21}

$$n_s = n_p \sin i_c.$$

The instrument is capable of measuring refractive index for two polarization modes namely TE and TM. By proper selection of the orientation of the sample plate, it is possible to determine two or even three (if there) principal refractive indices of the material under study.²²

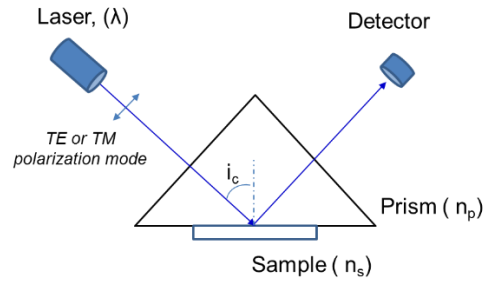


Fig. 6.15 Schematic depiction of principle of prism coupling method used for determination of refractive index of a sample plate.

We used well - polished (100) sample plate of ZCTC crystal for the investigations. The sample size of the plate was nearly $3 \times 7 \times 1 \text{ mm}^3$ ($a \times b \times c$). The plate was so selected that the two principal axes namely (a and c) lie in the plane of the plate and whose orientation can easily be identified by the edges of the crystal. The refractive indices of ZCTC lie somewhere in the range of 1.5 to 1.9, we therefore used GGG (gadolinium gallium garnet) prism. Initially the sample was put as c -axis horizontal and b -axis vertical it gave almost same value of refractive indices for both TE and TM modes showing this to be the ordinary index (n_o). This confirms it to be a uniaxial crystal. Now changed the sample orientation to c -axis vertical and b -axis horizontal. It showed different indices for TE and TM modes of polarizations. The obtained data is given in Table 6.5 and is quite close to that reported in the literature.⁶ The data show that the material is negative uniaxial.

Table 6.5 Extraordinary and ordinary refractive indices of ZCTC crystal at five different wavelengths at room temperature (30°C) and the resulted birefringence.

Wavelength (nm)	n_e (TE mode)	n_o (TM mode)	Birefringence ($n_e - n_o$)
407	1.7904	1.9481	- 0.1577
532	1.7500	1.8889	- 0.1389
828	1.7211	1.8481	- 0.127
1064	1.7138	1.8366	- 0.1228
1551	1.7071	1.8268	- 0.1197

The measured data was plotted as shown in Fig. 6.16 and fitted to Sellmeier equation for room temperature as,²³

$$n^2(\lambda) = A + \frac{B\lambda^2}{\lambda^2 - C}$$

Where A, B and C are Sellmeier coefficients and λ is the wavelength in micrometer. The results are summarized in Table 6.6.

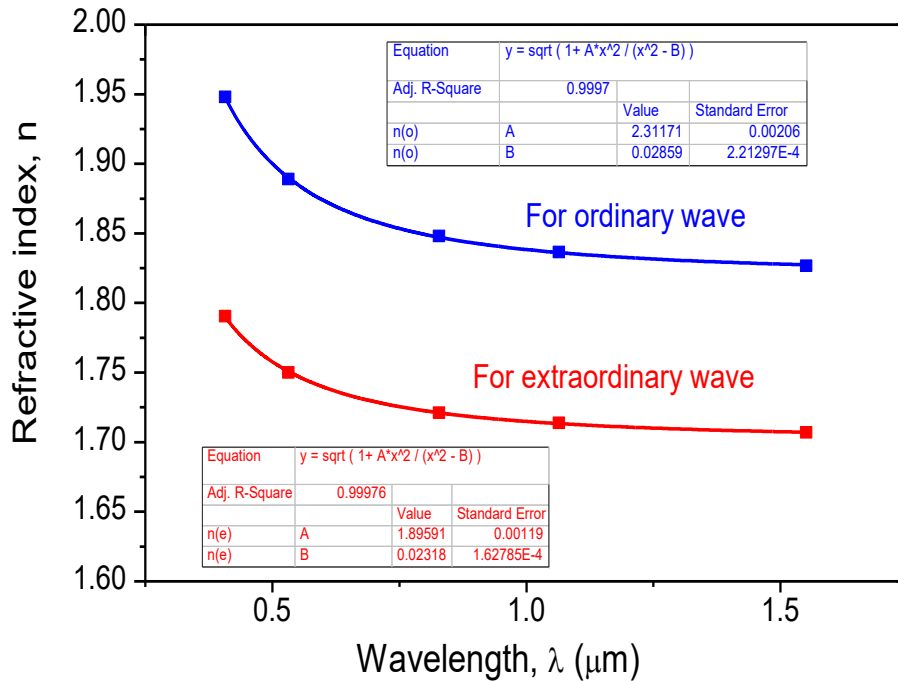


Fig. 6.16 Variation of ordinary and extra-ordinary refractive indices with wavelength, measured by prism coupling method at five different wavelengths at room temperature (30 °C).

Table 6.6 Sellmeier coefficients for the ZTC crystal.

Index	Sellmeier coefficients		
	A	B	C
n _o	1	2.31171	0.02359
n _e	1	1.89591	0.02318

Further the experiments were conducted to determine variation of ordinary and extraordinary refractive indices with temperature at a fixed wavelength to determine temperature coefficient of refractive index for o- and e-waves. The experiment was conducted at four specific wavelengths for ordinary and extraordinary refractive indices.

The results are given in Table 6.7. These are plotted with respect to temperature as shown in Fig. 6.17 and Fig. 6.18 to calculate thermos-optic coefficients. The calculated values of the thermo-optic coefficients at different wavelengths for ZCTC crystal are given in Table 6.8.

Table 6.7 Values of extraordinary and ordinary refractive indices with temperature measured by prism coupling method at four different wavelengths.

Temperature (°C) →		30	50	75	100	125	150
Wave-length ↓	Mode ↓						
532 nm	TE (n _e)	1.7501	1.7499	1.7498	1.7494	1.7489	1.7476
	TM (n _o)	1.8883	1.8872	1.8862	1.8846	1.8840	1.8831
828 nm	TE (n _e)	1.7211	1.7202	1.7196	1.7187	1.7181	1.7173
	TM (n _o)	1.8455	1.8443	1.8434	1.8417	1.8396	1.8386
1064 nm	TE (n _e)	1.7158	1.7130	1.7119	1.7113	1.7107	1.7101
	TM (n _o)	1.8375	1.8354	1.8340	1.8328	1.8308	1.8284
1551 nm	TE (n _e)	1.7062	1.7054	1.7050	1.7039	1.7034	1.7023
	TM (n _o)	1.8273	1.8262	1.8253	1.8227	1.8206	1.8189

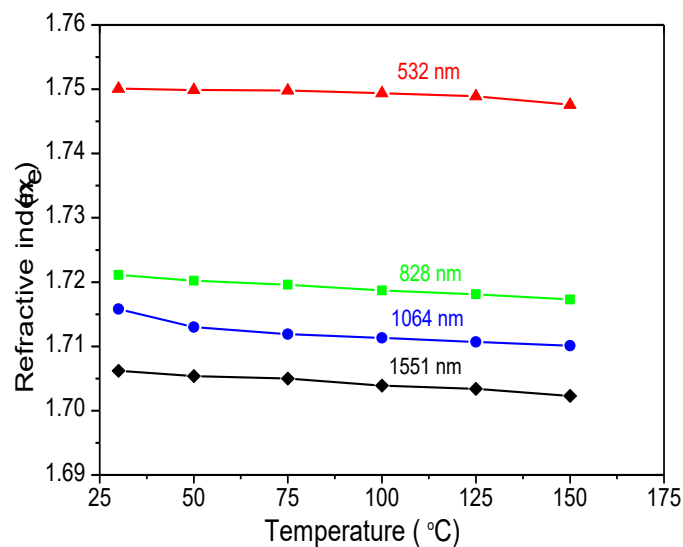


Fig. 6.17 Temperature dependent refractive index of extraordinary wave in ZCTC crystal at four different wavelengths.

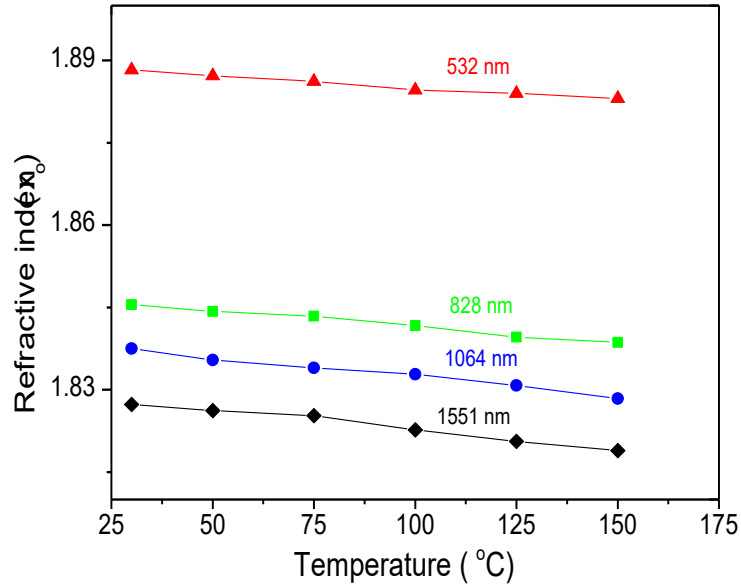


Fig. 6.18 Temperature dependent refractive index of ordinary wave in ZCTC crystal at four different wavelengths.

Table 6.8 Values of temperature coefficients of refractive indices for ordinary and extraordinary waves at different wavelengths.

Wavelength (nm)	(dn _e /dT) × 10 ⁵ (per °C)	(dn _o /dT) × 10 ⁵ (per °C)
532	- 1.88387	- 4.36774
828	- 3.07581	- 5.92419
1064	- 4.17742	- 7.10806
1551	- 3.12903	- 7.24355

6.4.10 Determination of phase matching angles for second harmonic generation

As per the Sellmeier coefficients given in Table 6.6, Sellmeier's equations for ZCTC can be written as,

$$n_o^2 = 1 + \frac{2.31171 \lambda^2}{\lambda^2 - 0.02859}$$

$$n_e^2 = 1 + \frac{1.89591 \lambda^2}{\lambda^2 - 0.02318}$$

Using these values in a software, the phase matching angles (from c-axis) for SHG in type-I and type-II configurations for ZCTC crystal were obtained at different wavelengths as given in *Table 6.9* and *Table 6.10* respectively. They are also depicted in *Fig. 6.19*.

Table 6.9 Phase matching angle with wavelength for ZCTC crystal in type-I SHG configuration.

Wavelength (μm)	Phase matching angle (in degrees)
0.7	64.9113
0.725	61.1092
0.750	57.9224
0.775	55.1693
0.800	52.7436
0.808	52.0245
0.825	50.5760
0.850	48.6185
0.900	45.2016
0.925	43.6949
0.950	42.2991
0.975	41.0009
1.000	39.7890
1.025	38.6542
1.050	37.5885
1.064	37.0194
1.075	36.5834
1.100	35.6386

Table 6.10 Phase matching angle with wavelength for ZCTC crystal in type-II SHG configuration.

Wavelength (μm)	Phase matching angle (in degrees)
0.900	72.7034
0.925	68.5483
0.950	65.2053
0.975	62.3711
1.000	59.8960
1.025	57.6926
1.050	55.7042
1.064	54.6695
1.075	53.8915
1.100	52.2259

Following graphs show variation of phase matching angle with wavelength for type-I and type-II SHG configurations for ZCTC crystal:

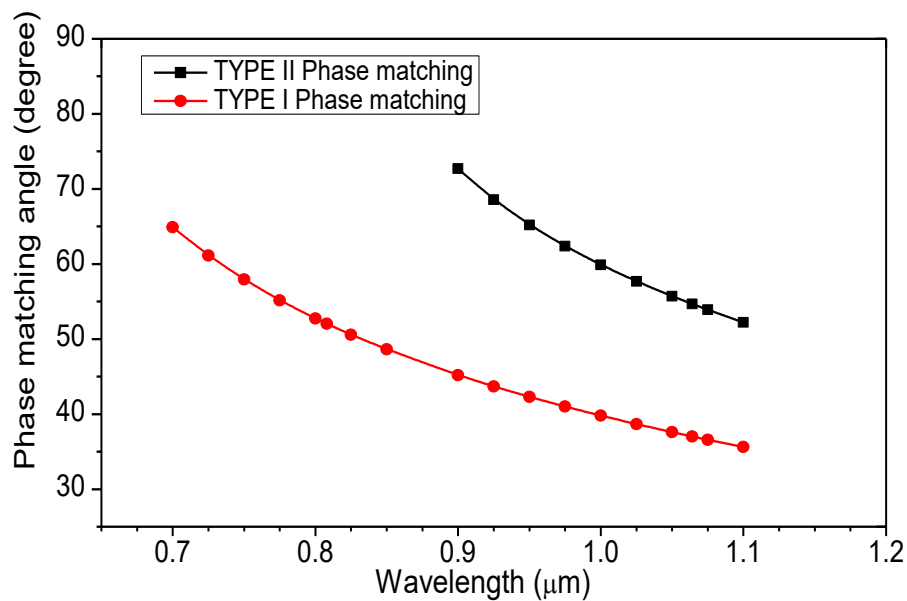


Fig. 6.19 Variation of phase matching angle with wavelength for ZCTC crystal in type-I and type-II phase matching configurations.

6.5 Unidirectional growth of ZCTC crystals

Nucleation and inclusions were found to be some of the main problems during growth of ZCTC which limits the size and quality of this crystal. We therefore also attempted to grow this crystal by using another technique namely solute feed based unidirectional growth technique described in Chapter 4. For this purpose, a small size glass ampoule was fabricated having diameter ~ 15 mm at top and tapered end at bottom for mounting a small size seed crystal using silicone sealant. Fig. 6.20 shows some of the crystals grown along [001] direction from point size seeds using this technique at a temperature gradient of ~ 10 °C. It was found that after some days of good growth crystal may acquire nucleation or inclusion that limit the crystal size. The crystal shown in Fig. 6.20 (c) was cut normal to growth direction and tested for optical quality and orientation using transmission spectroscopy and optical conoscopy techniques.

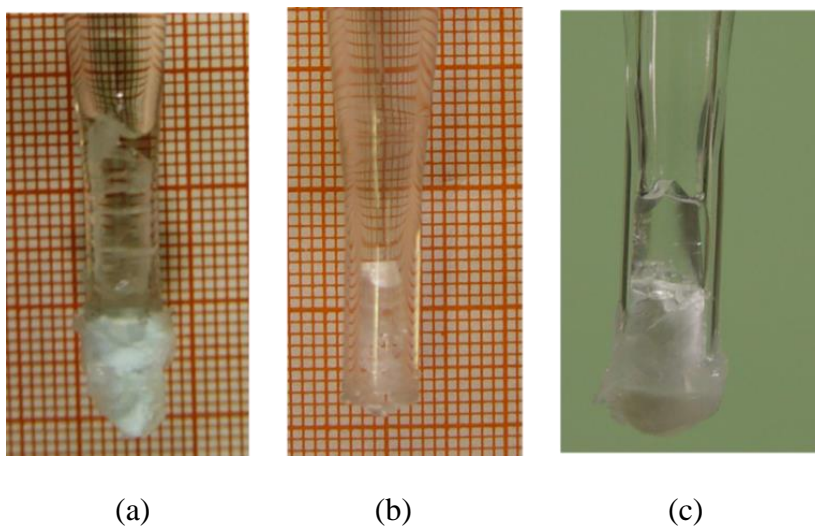


Fig. 6.20 Some of the ZCTC crystals, grown along [001] direction by solute-feed based unidirectional growth technique.

A small element cut normal to the growth axes and polished. The sample was characterized by transmission spectroscopy for optical quality and optical conoscopy for the orientation of the plate. Fig. 6.21 shows the transmission spectra for (001) in the range of 200 to 2200 nm range. It shows that crystal has ~ 60 % transmittance without accounting reflection losses for ~ 400 nm to 2200 nm range except some material specific localized absorption peaks.³ The transmittance is somewhat lower for (001) orientation compared to that along (100) orientation due to anisotropic structure of the material.

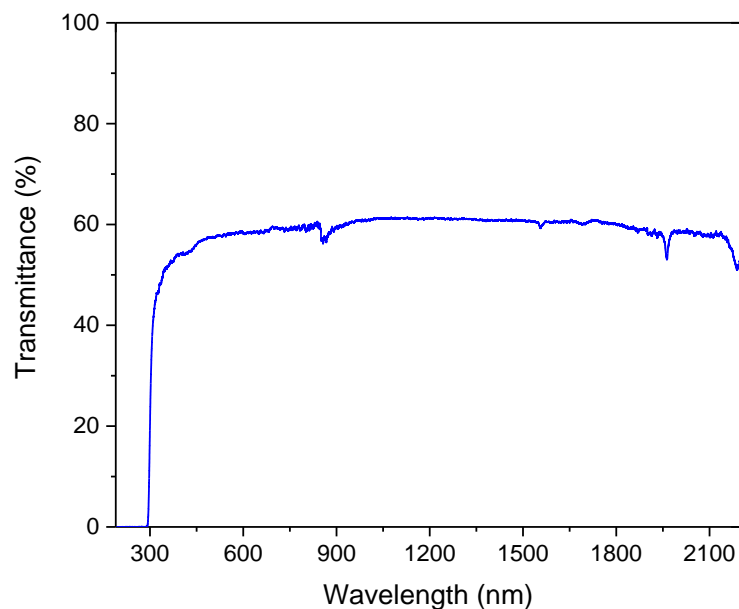


Fig. 6.21 Transmission spectrum for ~ 1mm thick (001) plate of ZCTC crystal grown by solute-feed based unidirectional growth technique.

Fig. 6.22 shows the optical conoscopic interferogram for the ZCTC plate using polarizing optical microscope. Concentric isochromes shows birefringence uniformity of the plate however there is a slight shift for the plate being exactly normal to the [001] axis. It may be due to slight error in seed mounting at the growth ampoule.

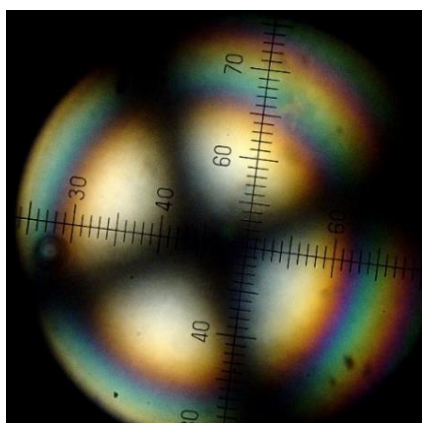


Fig. 6.22 Optical conoscopic image of ~ 1.0 mm thick (001) plate of ZCTC crystal.

6.6 Conclusion

In conclusion, ZCTC chemical was synthesized and prismatic shaped transparent crystals were obtained at optimized pH of the solution using controlled solvent evaporation

technique. A crystallizer was designed and fabricated for this purpose. Structural characterization of the grown crystals was made by powder X-ray diffraction technique and optical quality was assessed by transmission spectroscopy, birefringence interferometry, laser damage threshold and refractive index measurements. Dislocation density and their distribution was assessed by chemical etching technique and X-ray diffraction topography. The crystal was used to determine Sellmeier coefficients and determined thermo-optic coefficients and phase matching angles. The ZCTC crystal was also grown by solute feed based unidirectional technique. It shows that unidirectional growth of ZCTC crystal by solute feeding method is possible.

References:

- ¹ X. Q. Wang, D. Xu, D. R. Yuan, Y. P. Tian, W. T. Yu, S. Y. Sun, Z. H. Yang, Q. Feng, M. K. Lu, Y. X. Yan, F. Q. Meng, S. Y. Guo, G. H. Zhang, M. H. Jiang, *Mater. Res. Bull.*, 4 (1999) 2003-2011.
- ² T. R. Kumar, R. Jeyasekaran, S. M. R. Kumar, M. Vimalan, P. Sagayaraj, *Applied Surface Science*, 257 (2010) 1684-1691.
- ³ X. Wang, D. Xu, M. Lu, D. Yuan, G. Zhang, S. Xu, S. Guo, X. Jiang, J. Liu, C. Song, Q. Ren, J. Huang, Y. Tian, *Mater. Res. Bull.*, 38 (2003) 1269-1280.
- ⁴ C. Feng, G. Lu, X. Wang, P. Zhang, G. Zhou, H. Yang, *Phys. Status Solidi, B* 248 (2011) 1483-1489.
- ⁵ G. Zhang, D. Xu, M. Lu, D. Yuan, X. Wang, F. Meng, S. Guo, Q. Ren, M. Jiang, *Optics Laser Technol.*, 33 (2001) 121-124.
- ⁶ G. H. Zhang, D. Xu, Y. T. Chow, M. K. Lu, X. Q. Wang, D. R. Yuan, P. L. Chu, Q. Ren, X. G. Xu, *Opt. Comm.*, 233 (2004) 425-430.
- ⁷ J. G. Bergman, J. H. Mcfee, G. R. Crane, *Mater. Res. Bull.*, 5 (1970) 913-918.
- ⁸ X. N. Jiang, D. Xu, *J. Appl. Cryst.*, 36 (2003) 1448-1451.
- ⁹ P. N. S. Kumari, S. Kalainathan, N. A. N. Raj, *Mater. Lett.*, 61 (2007) 4423-4425.
- ¹⁰ X. Q. Wang, D. Xu, Y. T. Chow, G. H. Zhang, M. K. Lu, D. R. Yuan, H. P. Chan, H. Q. Sun, Y. L. Geng, C. K. Chow, Q. Ren, P. L. Chu, *J. Cryst. Growth*, 267 (2004) 263-269.

- ¹¹ J. F. Carvalho, A. C. Hernandez, F. D. Nunes, L. B. O. A. de Moraes, L. Misoguti, S. C. Zilio, *J. Cryst. Growth*, 173 (1997) 487- 491.
- ¹² A. K. Karnal, H. O. Mahawar, V. K. Wadhawan, *Indian J. Pure Appl. Phys.* 36 (1998) 587.
- ¹³ Eric Dowty, Shape Software, 521 Hidden Valley Road, Kingsport, TN 37663.
- ¹⁴ Russell G. Baughman, *J. Chem. Educ.*, 68 (1) (1991) A20.
- ¹⁵ X. Q. Wang, J. G. Zhang, D. Xu, M. K. Lü, D. R. Yuan, S. X. Xu, J. Huang, G. H. Zhang, S. Y. Guo, S. L. Wang, X. L. Duan, Q. Ren, G. T. Lü, *J. Cryst. Growth*, 235 (2002) 340-346.
- ¹⁶ X. N. Jiang, D. Xu, *J. Appl. Cryst.*, 36 (2003) 1448-1451.
- ¹⁷ K. Sangwal, “Etching of Crystals: Theory, Experiment, and Application”, North Holland, Amsterdam, 1987.
- ¹⁸ X. Q. Wang, D. Xu, G. W. Lu, M. K. Lu, D. R. Yuan, G. H. Zhang, G. T. Lu, Y. Chen, Y. Q. Zhou, *Chemical Physics Letters* 360 (2002) 573-578.
- ¹⁹ X. Wang, D. Xu, Y. T. Chow, W. Liu, S. Li, J. Huang, G. Zhang, M. Lu, D. Yuan, H. P. Chan, Q. Ren, P. L. Chu, *Mater. Res. Bull.*, 39 (2004) 1407-1416.
- ²⁰ H. Onodera, I. Awal, J. Ikenoue, *Appl. Opt.*, 22 (1983) 1194-1197.
- ²¹ D. Zhang, Q. Yang, P. Hua, H. Liu, Y. Cui, L. Sun, Y. Xu, E. Pun, *J. Op. Soc. Am. B*, 26 (2009) 620-626.
- ²² I. Bhaumik, R. Bhatt, S. Ganesamoorthy, A. Saxena, A. K. Karnal, P. K. Gupta, A. K. Sinha, S. K. Deb, *Apl. Opt.*, 50 (2011) 6006-6010.
- ²³ D. Meschede, *Optics, Light and Lasers*, Wiley-VCH Verlag GmbH & Co. KGaA, Weinheim, 2004, pp. 8-9.

Chapter 7 Summary and future scope

KDP is an important NLO material, widely used for second harmonic generation and electro-optic switching for high power Nd doped YAG or glass lasers mainly because of ease with which large size crystals of good optical quality can be grown. However, its natural growth morphology is such that it greatly limits the size of the device elements for laser applications. The main objective was to investigate shape modification techniques to be able to enhance usable volume fraction for device elements from the as grown KDP crystals. It resulted into development of two new growth methodologies for shape modification of crystals growing from solution namely “Flat-top growth technique” and “Solute feed based unidirectional growth technique”.

The “flat-top growth technique” is based on utilization of solution-air interface for habit modification of crystals for the first time. Several flat-top shape KDP crystals were grown without nucleation using [001] oriented spontaneously grown point seeds. The dimension of the largest size flat-top KDP was 116x92x116 mm³. The crystallization yield for this crystal was ~50% which is almost two times higher compared to the crystal if grown to similar height of 116 mm by conventional platform technique. The usable volume fraction for Pockels cell elements in the grown flat-top KDP crystal was enhanced by more than 11 % as compared to that obtained from a pyramidal shape crystal of similar cross-section. The device purpose volume fraction for SHG elements in the flat-top grown KDP crystals was although enhanced compared to that obtained from a pyramidal shape crystal but is still quite low because its habit faces are neither parallel nor perpendicular to the phase matching directions for Nd:YAG laser. This issue was solved by developing a technique of orienting natural morphology KDP point seed at the platform. Type-I and type-II SHG oriented KDP crystals of dimensions 40x47x65 mm³ and 57x60x66 mm³ were grown from point seeds using this technique along with flat-top methodology to enhance device purpose yield. The device purpose volume fractions were 48% and 56% for type-I and type-II SHG oriented KDP crystals respectively, which are much higher than those obtained from crystals grown by conventional platform technique and also higher than that reported (30 % and 50%) by parallel plate technique. The flat-top KDP crystals were characterized in detail for structural perfection, optical quality, impurity concentration and defect structure and the results show that abrupt termination of crystal top by solution - air interface do not degrade the crystal quality. Laser damage threshold

(LDT) was measured using 7 ns pulse width Nd:YAG laser for sample plates prepared from different growth sectors of the flat-top KDP crystal. The LDT values were lying in the range of 2.4 to 3.9 GW/cm² which are comparable with those reported in the literature. The SHG oriented flat-top KDP crystals were used to fabricate SHG elements and cells for Nd:YAG laser. The SHG conversion efficiency measured using 7 ns pulse width Nd:YAG laser was ~30% at the pulse intensity of ~ 900 MW/cm².

LAP crystal is of interest because of having about 2 times higher NLO coefficient and laser damage threshold compared to that for KDP. However, a major limitation with LAP is due to large growth asymmetry along crystallographic axes which results into a morphology having low usable volume fraction for device elements. Investigations were mainly aimed to reduce growth anisotropy of LAP crystal by studying influence of seed orientation on growth morphology. Influence of seed orientation on growth rate and aspect ratio of LAP crystals was studied for crystals grown by platform technique. Our investigations showed that growth with (011) oriented seed leads to significantly better aspect ratio of LAP compared to that by (100), (010) and (001) oriented seeds. The (011) oriented LAP crystal was characterized in detail for crystal structure, optical quality, defect structure and laser damage threshold. The obtained values for optical transmittance (~88% for 355 nm to 1100 nm), birefringence inhomogeneity (1.86×10^{-4} per mm at 632 nm), LDT (4.8 to 6.6 GW/cm² at 7 ns Nd:YAG laser) and orientations of optic axes were comparable to that reported in the literature. Growth kinetics studies of slow growing (100) face of LAP crystal was carried out using birefringence interferometry. The results show the growth rate of (100) face increases almost linearly with supersaturation.

ZCTC is another important crystal due to having more than 15 times higher NLO coefficient compared to KDP. The main difficulty with this crystal was very low growth rate due to low solubility with small value of temperature coefficient of solubility. A crystallizer was therefore developed having facility of controlling solvent evaporation rate. ZCTC crystals were grown up to 15 mm length along [001] direction with high average growth rate of ~ 0.5 mm/day comparable to the best reported in the literature. The crystals were characterized for optical quality, structural defects and determined principle refractive indices along two crystallographic axes. The refractive indices were measured at five different wavelengths and determined Sellmeier coefficients. The data was further used to calculate phase matching angles for SHG in type-I and type-II configurations with

wavelength. The obtained values of phase matching angles were quite close to that reported in the literature. The laser-induced damage threshold was measured for (100) plate of ZCTC crystal showing it to be nearly 1 GW/cm² at 7 ns, Nd:YAG laser. The crystal was also grown successfully by solute-feed based unidirectional growth technique.

A new methodology was also developed for seed protection during overheating stage of solution in the presence of seed crystal to reduce chances of spurious nucleation during crystal growth. The technique was successfully used to prevent nucleation during growth of KDP and LAP crystals.

The possible future scope of the above work may be in the direction of extending the two shape modification techniques to other solution grown crystals to modify their shape for enhancing their usable volume fraction and crystallization yield. The other direction is to investigate growth kinetics of the crystals grown by these two techniques preferably using optical interferometry techniques to optimize growth parameters for enhancing growth rate along desired directions.

